

Geology and Geochemistry of Ultramafic Rocks in the Lake of the Woods Greenstone Belt

Chanelle Boucher

Submitted in partial fulfillment of the requirements for the degree of

Master of Science in Geology

Supervisors: Dr. Pete Hollings (Lakehead University)

and Dr. Derek Wyman (University of Sydney)

Department of Geology
Lakehead University
Thunder Bay, Ontario
October 2019

Abstract

The Archean komatiites of the Lake of the Woods greenstone belt, Kenora, Ontario formed on the western extension of the Superior Province southern margin and have not been studied using modern analytical methods. Although Archean plate tectonic processes have been the subject of decades of research, the nature of these processes remains the subject of considerable debate. Recent work has investigated the link between komatiites and Archean subduction zones. Komatiites are widespread in Archean terranes and together with spatially associated tholeiitic basalts form an important part of many Late Archean greenstone belts, therefore a better understanding of Archean geodynamic processes and comparison to modern day processes is required.

Detailed mapping in the Upper Keewatin Assemblage identified komatiites on the southern margin of the Long Bay Group. The komatiites are typically metamorphosed to upper greenschist facies and include a variety of schists that do not show any preserved primary textures or mineralogy. Polyhedrally jointed flow tops were observed in rare locations. Mineral assemblages include dominantly anthophyllite-tremolite-chlorite and serpentine-tremolite-chlorite schists, as well as lesser talc-tremolite-chlorite schists. These units are moderately to intensely foliated with chlorite and lesser amphibole defining the foliation and also include randomly oriented bladed amphibole grains that typically have tremolite cores and anthophyllite rims. The amphiboles show a chemical transition from core to rim with a loss in Ca as anthophyllite appears. Accessory phases include chromite, magnetite, ilmenite and apatite. Ultramafic rocks are very fine-grained and mineralogy has been described using a compilation of petrography, x-ray diffraction and scanning electron microscope analysis.

Whole-rock geochemical analyses were conducted on 110 samples. The Upper Keewatin Assemblage is composed of dominantly mafic to intermediate volcanic rocks that are typically of tholeiitic affinity with rare calc-alkalic units. A total of 41 samples were determined to be ultramafic in which the komatiite units are Al-undepleted komatiites that display major and trace element concentrations consistent with melts derived from above the garnet stability zone. They can be subdivided into three suites with primitive mantle patterns that display strong Th and Nb depletions with flat HREEs (heavy rare earth elements), weak Th and Nb depletions with flat HREEs and enriched Th with moderate Nb depletions and flat HREEs. Neodymium isotope analyses, in conjunction with trace element geochemistry, suggests that some units have been weakly to moderately contaminated. Mafic tholeiitic units have low- and high-Ti varieties, in which most units are dark grey to black amphibolites and rare chlorite-tremolite schists. The mafic units shows similar contamination trends to the ultramafic units.

The tectonic setting of the Upper Keewatin Assemblage requires voluminous mafic magmatism with relatively sporadic ultramafic magmatism in a subaqueous setting given

the widespread pillow basalts. The belt evolution is interpreted to represent an initial primitive oceanic arc with subaqueous tholeiitic magmatism followed by calc-alkalic dominant magmatism following arc evolution. Tholeiites originating from the primitive arc display weak Nb depletions, and through geochemical modelling it is possible that they are the contaminant that produced Th-enriched komatiites. Although a hydrous source could not be confirmed for the Nb-depleted komatiites, contamination cannot account for the variation in trace elements. It is likely that plume-arc interactions have occurred, similar to scenarios documented in the Superior Province; however, the mechanisms cannot be determined. Deep-penetrating fractures can accommodate along-strike variations in the dip of subduction zones, which typically segment island arcs into various belts. Large-scale crustal weaknesses would act as potential magma conduits for ascending plumes, resulting in a chemical and isotopic difference between the upwelling asthenosphere and arc magmatism. This would result in likely interaction between the rising plume and subduction-derived fluids, producing the Nb-depletions present in komatiite samples within the assemblage.

ACKNOWLEDGMENTS

First and foremost, I would like to thank both Dr. Pete Hollings and Dr. Derek Wyman for the many discussions, insight, and support throughout this MSc project. The complex questions faced throughout the project could not have been solved without their guidance. I am thankful to the Ontario Geologic Survey for providing the means to conduct geochemical analyses of my samples, as well as the funding provided by NSERC. Thank you to everyone at the Geoscience Labs in Sudbury for all the analytical work performed on samples throughout both field seasons. I appreciate all the help with the SEM as well as XRD analyses from Dr. Wu, Mike Sorokopud and Dr. Zurevinski.

Thank you to Craig Ravnaas and Kristen Wiebe of the ENDM Kenora Resident Geologist Program for their introduction to the area, guidance to accessing specific field areas, and for putting on a rescue mission when the boat broke down. Thank you to Michael Lewinsky for assisting with the first field season and not hating me after we sat in the boat stranded in the rain for a full afternoon.

Thank you, Anne Hammond, Kristi Tavener, and Jonas Valiunaas, for preparing perfect thin sections, even when I kept coming back with more after I insisted I wouldn't bring anymore samples down.

Thank you to everyone in the department that have shown nothing but support and interest in everything that I've encountered throughout the two years. A number of students made my Graduate Assistantship an amazing experience, I hope the passion and drive to continue to learning lives on.

Most of all, I would like to thank my father Curtis Boucher for being the greatest field assistant a graduate student could ask for. A huge thank you also goes out to the rest of my family for their continuous support, even though they were not super keen on me being a professional student.

Table of Contents

ABSTRACT	I
ACKNOWLEDGMENTS	III
TABLE OF CONTENTS	IV
LIST OF FIGURES	VI
LIST OF TABLES	VIII
CHAPTER 1: INTRODUCTION	1
1.1 Objective	1
1.2 Location	2
1.3 Komatiites	3
1.3.1 Aluminum Undepleted Komatiites	9
1.3.2 Aluminum Depleted Komatiites	9
1.3.3 Komatiite Genesis	10
1.4 Previous Work	11
CHAPTER 2: REGIONAL GEOLOGY	12
2.1 Superior Province	12
2.2 Wabigoon Terrane	13
2.2.1 Western Wabigoon Terrane	17
2.2.2 Eastern Wabigoon Terrane	17
2.3 Lake of the Woods Greenstone Belt	18
2.3.1 Lower Keewatin Assemblage	18
2.3.2 Upper Keewatin Assemblage	20
2.3.3 Electrum Assemblage	21
2.3.4 Plutonic Complexes	21
CHAPTER 3: METHODOLOGY	22
3.1 Field Techniques	22
3.2 Analytical Techniques	22
3.2.1 Petrographic Analysis	23
3.2.2 Whole-Rock Geochemistry Analysis	23
3.2.3 Scanning Electron Microprobe	24
3.2.4 X-Ray Diffraction	25
3.2.5 Radiogenic Isotopes	25
CHAPTER 4: FIELD OBSERVATIONS AND PETROGRAPHY	27
4.1 Falcon Island Stratigraphy	27
4.1.1 Felsic Metavolcanic Rocks	29
4.1.2 Intermediate to Mafic Metavolcanic Rocks	29
4.1.3 Mafic to Ultramafic Intrusive Rocks	30
4.1.4 Felsic Intrusive Rocks	32
4.1.5 Clastic Metasedimentary Rocks	34
4.1.6 Falcon Island Stock	35
4.1.7 Mafic Metavolcanic Rocks	36
4.1.8 Ultramafic Metavolcanic Rocks	40

4.2 Cliff Island Stratigraphy	41
4.2.1 Felsic Metavolcanic Rocks	42
4.2.2 Intermediate to Mafic Metavolcanic Rocks	44
4.2.3 Mafic Intrusive Rocks	46
4.2.4 Felsic Intrusive Rocks	48
4.2.5 Clastic Metasedimentary Rocks	50
4.2.6 Mafic Metavolcanic Rocks	51
4.2.7 Ultramafic Metavolcanic Rocks	53
4.3 Mineral Chemistry	54
4.4 X-Ray Diffraction	57
CHAPTER 5: GEOCHEMISTRY AND RADIOGENIC ISOTOPES	59
5.1 Whole Rock Geochemistry	59
5.1.1 Ultramafic metavolcanic rocks	65
5.1.2 Mafic metavolcanic rocks	70
5.1.3 Intermediate metavolcanic rocks	76
5.1.4 Intrusive Rocks	77
5.2 Mineral Chemistry	82
5.2.1 Pyroxene Chemistry	82
5.2.2 Amphibole Chemistry	82
5.2.3 Accessory Phase Chemistry	84
5.2.3.1 Chromite Chemistry	84
5.2.3.2 Ilmenite	84
5.2.3.3 Apatite	84
5.3 Samarium-Neodymium Isotopes	84
CHAPTER 6: DISCUSSION	87
6.1 Mineralogy and Field Observations	87
6.1.1 Mafic to Ultramafic Volcanic Rocks	87
6.1.2 Textural Variability in Amphibolites	89
6.1.3 Metamorphism and Deformation of Ultramafic Rocks	90
6.2 Whole-Rock Geochemistry and Radiogenic Isotopes	93
6.2.1 High- and Low-Ti Tholeiitic Mafic Volcanic Rocks	93
6.2.2 Calc-Alkalic Mafic Volcanic Rocks	99
6.2.3 Ultramafic Rock Discrimination	100
6.2.4 Komatiites	104
6.2.4.1 N-MORB Pattern	104
6.2.3.2 Nb Depletion	106
6.2.3.3 Th Enrichment	116
6.2.5 Petrogenesis	118
6.2.6. Tectonic Environment	122
CHAPTER 7: CONCLUSIONS	131
REFERENCES	135
APPENDIX A: FIELD SAMPLE DESCRIPTIONS	147
APPENDIX B: WHOLE-ROCK GEOCHEMISTRY	0
APPENDIX C: SAMARIUM-NEODYMIUM ISOTOPE DATA	22

List of Figures

Figure 1.1. Location of Kenora, Ontario. A: Map of Ontario. B: Close up of Kenora region	2
Figure 1.2. Map of islands chosen for the study	3
Figure 1.3. Layered komatiite flow with spinifex texture A-zone and cumulate B-zone	6
Figure 1.4. Schematic diagram showing position of AUK and ADK	8
Figure. 2.1. Geological map of Ontario subdivided into terranes	17
Figure. 2.2. Geological map of western Wabigoon terrane	17
Figure. 2.3. Geological map of eastern Wabigoon terrane	18
Figure. 2.4. Geological map of the Lake of the Woods greenstone belt	20
Figure 4.1. Geological map of Falcon Island	28
Figure 4.2. Field photographs of felsic metavolcanic units	30
Figure 4.3. Field photos and photomicrographs of intermediate to mafic metavolcanic rocks	31
Figure 4.4. Field photos and photomicrographs of mafic to ultramafic intrusive units	32
Figure 4.5. Field photos and photomicrographs of felsic intrusive units	33
Figure 4.6. Field photographs of metasedimentary units	34
Figure 4.7. Field photos and photomicrographs of the Falcon Island stock	35
Figure 4.8. Field photographs of black to dark grey non-foliated mafic metavolcanic rocks	36
Figure 4.9. Photomicrographs in transmitted light of mafic metavolcanic rocks	37
Figure 4.10. Field photographs of light grey to grey non-foliated metavolcanic rocks	37
Figure 4.11. Photomicrographs in transmitted light of grey to light grey metavolcanic rocks	38
Figure 4.12. Field photos and photomicrographs of grey to dark green foliated metavolcanic rocks	39
Figure 4.13. Field photographs of grey to dark green foliated ultramafic metavolcanic rocks	40
Figure 4.14. Field photographs of ultramafic metavolcanic rocks	41
Figure 4.15. Photomicrographs of ultramafic metavolcanic rocks	41
Figure 4.16. Geological map of Cliff Island	43
Figure 4.17. Field photographs of felsic metavolcanic units	44
Figure 4.18. Field photographs of intermediate metavolcanic units	45
Figure 4.19. Field photograph of a sedimentary and pyroclastic contact	45
Figure 4.20. Photomicrograph in transmitted light of intermediate tuffaceous unit	46
Figure 4.21. Field photographs of mafic intrusive rocks	47
Figure 4.22. Photomicrograph in transmitted light of gabbroic unit	47
Figure 4.23. Field photos and photomicrographs of felsic intrusive samples	49
Figure 4.24. Field photos and photomicrographs of porphyritic felsic unit	50
Figure 4.25. Field photographs of clastic sedimentary rocks	51
Figure 4.26. Field photographs of mafic metavolcanic rocks	52
Figure 4.27. Field photograph of mafic pillowed flows	52
Figure 4.28. Photomicrographs of a mafic metavolcanic sample	53
Figure 4.29. Field photograph of ultramafic metavolcanic rocks	54
Figure 4.31. Photomicrograph of cumulate sample LOW17C76	54
Figure 4.32. Photomicrograph of sample LOW17CB79	55
Figure 4.33. Photomicrograph of sample LOW17CB62	56
Figure 4.34. Photomicrograph of samples composed as subhedral amphibole	57
Figure 5.1. Bivariate plots of TiO ₂ versus major element oxides	60
Figure 5.2. Bivariate plots of Nb (ppm) versus trace elements	61

Figure 5.3. Rock classification diagram after Le Maitre et al. (1989)	62
Figure 5.4. Rock classification diagram after Pearce (1996)	63
Figure 5.5. AFM diagram differentiating magmatic affinity	64
Figure 5.6. Jensen plot after Rollinson (2013)	64
Figure 5.7. Harker diagrams with SiO ₂ plotted against major element oxides	65
Figure 5.8. Bivariate diagram of MgO versus Cr and Ni	66
Figure 5.9. Element immobility diagrams for ultramafic metavolcanic rocks	70
Figure 5.10. Magmatic affinity diagrams after Ross and Bédard (2009)	70
Figure 5.11. Primitive mantle normalized diagrams of ultramafic volcanic rocks	70
Figure 5.12. Harker diagram of SiO ₂ vs major element oxides for mafic metavolcanic rocks	70
Figure 5.13. Element immobility diagrams for mafic metavolcanic rocks	71
Figure 5.14. Magmatic affinity diagrams after Ross and Bédard (2009) for mafic volcanic rocks.	72
Figure 5.15. Primitive mantle normalized diagram of low Ti tholeiitic mafic volcanic rocks	74
Figure 5.16. Primitive mantle normalized diagram of high-Ti tholeiitic mafic volcanic rocks	74
Figure 5.17. Bivariate plot of Ti/Ti* versus Nb/Nb* for mafic metavolcanic rocks.	75
Figure 5.18. Primitive mantle normalized diagram of calc-alkalic mafic volcanic rocks	76
Figure 5.19. Magmatic affinity diagrams after Ross and Bédard (2009)	77
Figure 5.20. Primitive mantle normalized diagram of intermediate volcanic rocks	77
Figure 5.21. Harker diagrams for intrusive rocks	78
Figure 5.22. Silica versus total alkalis diagram after Middlemost (1994)	79
Figure 5.23. Magmatic affinity diagrams after Ross and Bédard (2009) for intrusive rocks	80
Figure 5.24. Primitive mantle normalized diagram of intrusive rocks	81
Figure 5.25. Primitive mantle normalized diagram of Falcon Island Stock syenites	81
Figure 5.26. Pyroxene classification diagram	82
Figure 5.27. BSE image of amphibole grains	83
Figure 5.28. Primitive mantle normalized diagram with ϵ_{Nd} values	85
Figure 6.1. Jensen cation plot after Rollinson (2013)	88
Figure 6.2. Geological map of Falcon Island with degree of foliation and geochemical classifications	89
Figure 6.3. Amphibole porphyroblast mineral chemistry	91
Figure 6.4. Geological map of Falcon Island showing distribution of various volcanic rocks	93
Figure 6.5. Bivariate plots of MgO vs metal abundances of tholeiitic volcanic rocks	94
Figure 6.6. Bivariate diagrams of Zr versus Nb, La, Ti, Th, Gd and Yb	95
Figure 6.7. Diagram of La/Sm _{pm} versus [Th/La] _{pm} and Nb/La _{pm}	96
Figure 6.8. Bivariate plot of Ti/Ti* versus [Nb/La] _{pm} and [Th/La] _{pm} .	97
Figure 6.9. Diagram after Pearce (2014) of tholeiitic volcanic rocks	98
Figure 6.10. Diagram after Pearce (2014) of calc-alkalic mafic volcanic rocks	99
Figure 6.11. Bivariate diagram of MgO versus Cr and Ni	101
Figure 6.12. Bivariate diagram of CaO versus LOI for komatiite samples	102
Figure 6.13. Komatiite classification diagrams	102
Figure 6.14. Primitive mantle diagram of komatiites from various greenstone belts	103
Figure 6.15. Bivariate diagrams of Zr (ppm) versus various trace elements for komatiites and komatiitic basalts	105
Figure 6.16. Bivariate diagrams of [Th/La] _{pm} versus LOI % and [Nb/La] _{pm} versus Eu/Eu*	106
Figure 6.17. Komatiite and komatiitic basalt samples from this study compared to Abitibi komatiites	107
Figure 6.18. Komatiite bivariate diagrams with trend lines (arrows) pointing in the general direction of increasing crustal contamination	110
Figure 6.19. Results of AFC modelling plotted on primitive mantle normalized diagrams to produce Nb-depleted komatiites	111

Figure 6.20. Binary mixing modelling on a primitive mantle normalized diagram to produce Nb-depleted komatiites	112
Figure 6.21. Results of AFC modelling plotted on primitive mantle normalized diagrams to produce Nb-depleted komatiites	113
Figure 6.22. Binary mixing modelling on a primitive mantle normalized diagram to produce Nb-depleted komatiites	113
Figure 6.23. A) Diagram after Pearce (2008)	114
Figure 6.24. Plot of Ce/Nb versus Th/Nb	115
Figure 6.25. Results of AFC modelling plotted on primitive mantle normalized diagrams to produce Th-enriched komatiites	116
Figure 6.26. Binary mixing modelling on a primitive mantle normalized diagram to produce Th-enriched komatiites	117
Figure 6.27. Results of AFC modelling plotted on primitive mantle normalized diagrams to produce Th-enriched komatiites	118
Figure 6.28. Diagram after Pearce (2014)	120
Figure 6.29. Th/Nb versus Th (ppm) of ultramafic and mafic volcanic rocks	121
Figure 6.30. ϵ_{Nd} versus $^{147}Sm/^{144}Nd$ modified after Henry et al., (1997)	122
Figure 6.32. Bivariate diagrams of Al_2O_3/TiO_2 versus TiO_2 and Al_2O_3/TiO_2 versus Al_2O_3 of mafic volcanic rocks	124
Figure 6.33. Reconstruction of the geodynamic setting for tholeiitic dominant magmatism	125
Figure 6.34. Reconstruction of the geodynamic setting for calc-alkalic dominant magmatism	126
Figure 6.35. Idealized section through an oceanic arc	127
Figure 6.36. Primitive mantle normalized diagram	128
Figure 6.37. Reconstruction of plume-related komatiite and tholeiite magmatism	128
Figure 6.38. Reconstruction of possible pathways for an ascending plume	130

List of Tables

Table 4.1. Minerals identified using XRD	59
Table 5.1. Results of radiogenic isotope analyses	86
Table 6.1. Partitioning coefficients of ultramafic and mafic magmas	111

Chapter 1: Introduction

1.1 Objective

Although there have been decades of research into Archean plate tectonic processes, the nature of these processes remains the subject of considerable debate. The current discussion concerning Archean plate tectonics has focused on determining if these processes are dominantly horizontal or vertical, with many authors evoking a uniformitarian approach (Abbott et al., 1994; Hollings et al., 1999; Polat and Kerrich, 2002; Wyman and Kerrich, 2009) and others arguing that modern day tectonics are fundamentally different from those that operated in the Archean (Bleeker, 2002; Thurston, 2015; Bedard, 2018). Komatiites are ultramafic rocks that are widespread in Archean terranes and together with spatially associated tholeiitic basalts form an integral part of many Late Archean greenstone belts (Kerrich et al., 1999; Hollings and Kerrich, 1999). Although komatiites are widely associated with plume magmatism, it has been speculated that komatiites may be associated with subduction related processes (Grove and Parman, 2004). Komatiite magmatism was widespread from 3.5 to 1.5 Ga but mantle geodynamics have progressed to conditions that very rarely produce komatiites and the Gorgona Island occurrence is the only confirmed Phanerozoic example (Arndt et al., 2008). Key questions are: Is the mantle's heat budget responsible for the lack of komatiites as they require high eruption temperatures, and have subduction-related processes contributed, as the association between komatiites and subduction-related rocks throughout the Superior Province are still poorly understood. This project evaluated komatiitic units within the Lake of the Woods greenstone belt (LWGB) in order to investigate accretionary processes along the southwestern margin of the Superior Province at ~2.7 Ga. This was achieved by a combination of detailed geological mapping, petrography, geochemical analysis, scanning electron microprobe (SEM) and radiogenic isotope studies. This project allows for the interpretation of the geodynamic processes that dominated the Superior Province at *circa* 2.7 Ga and consequent comparison to modern day processes.

1.2 Location

The Lake of the Woods greenstone belt is located near Kenora, Ontario and extends both into Manitoba, Canada and Minnesota, United States. Kenora is situated roughly 485km northwest of Thunder Bay, Ontario (Fig. 1.1). Access to the field locations was achieved by boat on Lake of the Woods. The field area accessed in 2017, Falcon Island, is located approximately 50km southwest of Kenora (Fig. 1.2). The field areas accessed in 2018, Cochrane Island and Cliff Island, are approximately 46km southwest and 31km south of Kenora, respectively (Fig. 1.2). The mapping portion of the project consisted of inland traversing with variable degrees of exposure and shoreline mapping that consisted of well-exposed areas throughout.

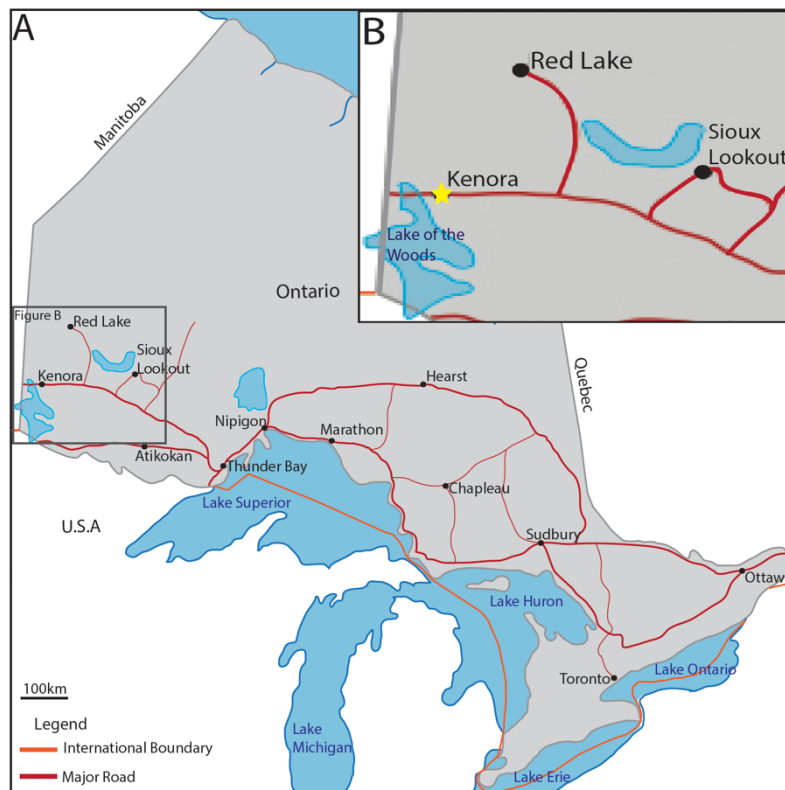


Figure 1.1. Location of Kenora, Ontario. A: Map of Ontario. B: Close up of Kenora region.



Figure 1.2. Map of islands chosen for the study (modified from Google Earth, 2018).

1.3 Komatiites

Komatiites are highly magnesian ultramafic rocks that are interpreted to have formed from high degrees of partial melting (30-50%) of an anhydrous peridotite mantle with eruption temperatures of up to 1600°C (Dostal, 2008). They erupted in large volumes from 3.5 to 1.5 Ga, but only rarely since, with the youngest komatiite occurrence at 90 Ma on Gorgona Island, Columbia (Grove and Parman, 2004). These ultramafic rocks are widespread in Archean terranes globally (Arndt, 1994; Hollings and Kerrich, 1999; Sossi et al., 2016). Komatiites were first recognized in the Barberton greenstone belt, South Africa in the late 1960s and were named for their type locality to the Komati River (Viljoen and Viljoen, 1969).

Komatiite flow nomenclature includes the division into the A zone consisting of the upper flow top and spinifex layers and the B zone consisting of the basal chill zone and cumulate layers (Fig. 1.3). The term spinifex texture is characterized by large, skeletal, platy blades of olivine or acicular needles of pyroxene typically found in the upper parts of komatiitic flows (Arndt et al., 2008). The origin of spinifex texture is often debated, but likely encompasses a mixture of a unique cooling history and high thermal gradient (7-35°C/cm; Shore and Fowler, 1999; Faure et al., 2006). Producing a model for the formation of spinifex texture has been challenging as producing results through experimental methods is difficult. Proposed models of spinifex texture include those of Turner et al. (1986) who proposed that spinifex resulted from rapid cooling caused by vigorous internal convection, Aitken and Echeverria (1984) and Arndt (1994) who proposed that spinifex texture resulting from crystallization of komatiitic magma that had become superheated during its rapid ascent from the mantle source, and Grove et al. (1994, 1996) and Parman et al. (1997) who proposed spinifex forming during crystallization of hydrous, intrusive komatiite magma that formed sill complexes at depths of roughly 6km (Faure et al., 2006).

Until the work of Faure et al. (2006), preferentially oriented crystals typical of platy olivine spinifex had never been produced in laboratory experiments. Donaldson (1982) attributed the differences in olivine morphology between the various spinifex layers to be dependent on the content of MgO where olivine spinifex would only occur in highly magnesian magmas. The recently proposed model by Faure et al. (2006) utilizes the difference in cooling rates and thermal gradients throughout the flow to explain the variations in olivine spinifex; however, it is dominantly the thermal gradient that dictates the morphology of the crystals and their preferred orientation. Deep within the flow interior, the cooling rate diminishes rapidly, therefore leaving the thermal gradient as the dominant effect controlling crystallization (Donaldson, 1982). This corresponds to the uppermost spinifex layers (A₁ and A₂) of randomly oriented fine-grained olivine whereas the spinifex layer is composed of coarse-grained parallel aligned olivine crystals controlled by the variations in the thermal gradient (Faure et al., 2006). The experiments conducted by Faure et al. (2006) demonstrated that randomly oriented spinifex occurs when cooling rates are not too high (<10°C/hour) with high thermal gradients (>25°C/cm). A transition occurs

where olivine spinifex orients itself perpendicular to the cooling front in parallel arrangements, and is no longer randomly oriented, when the thermal gradient decreases to 20-25°C/cm (Faure et al., 2006). The orientation of olivine perpendicular to the cooling front originates from the thermal anisotropy of olivine in which the a-axis demonstrates the highest thermal conductivity (Shore and Fowler, 1999). The geometry of the crystal front aligns itself so that the a-axis forms perpendicular to the cooling front to allow for efficient loss of the latent heat causing vertical crystal growth along the c-axis (Shore and Fowler, 1999).

Komatiite flows that are well-differentiated typically host olivine and/or spinifex-textured upper zones and cumulate lower zones dominated by olivine ad-, ortho- or meso-cumulates (Arndt et al., 2008). Pyroxene spinifex contains augite, pigeonite or rare orthopyroxene as complex skeletal needles that are typically 1 to 5 cm long and 0.5 mm wide, however these primary phases, as well as primary olivine in olivine spinifex layers, are usually replaced by serpentine, chlorite, tremolite, talc, epidote, albite or metamorphic olivine (Arndt et al., 2008). Low grade metamorphism of komatiites produces a mineral assemblage dominated by serpentine-antigorite, chlorite, talc, tremolite, magnesite-dolomite and magnetite. At higher metamorphic grades they contain anthophyllite, enstatite, olivine and diopside (Dostal, 2008). However, it is common for komatiites to occur as massive units with no differentiation into an upper olivine spinifex and lower olivine cumulate zone but contain un-layered olivine phenocrysts and exhibit polyhedral jointing within the upper chill margin (Arndt et al., 2008).

The total thickness of komatiite flows can range from <10 m with well-differentiated units as thin as 50cm, to roughly 100m and when intercalated with tholeiitic sequences complete sequences can be up to 500m thick (Arndt et al., 1979; Arndt et al., 2008). Due to their highly fluid state and extremely low viscosity they would be expected to form rather thin flows, so thick units were likely ponded or thickened by inflation due to repeated flow pulses (Dann 2001; Dann and Grove 2007). Alternatively, thick flows may represent lower effusion rates and dominate proximal to the vent as eruption wanes, whereas thin flows likely developed in distal environments as part of a complex system of lava tubes or toes (Perring

et al., 1995). Distal environments in which thinner komatiite flows crystallize often have no cumulate zones (Hill et al., 1995).

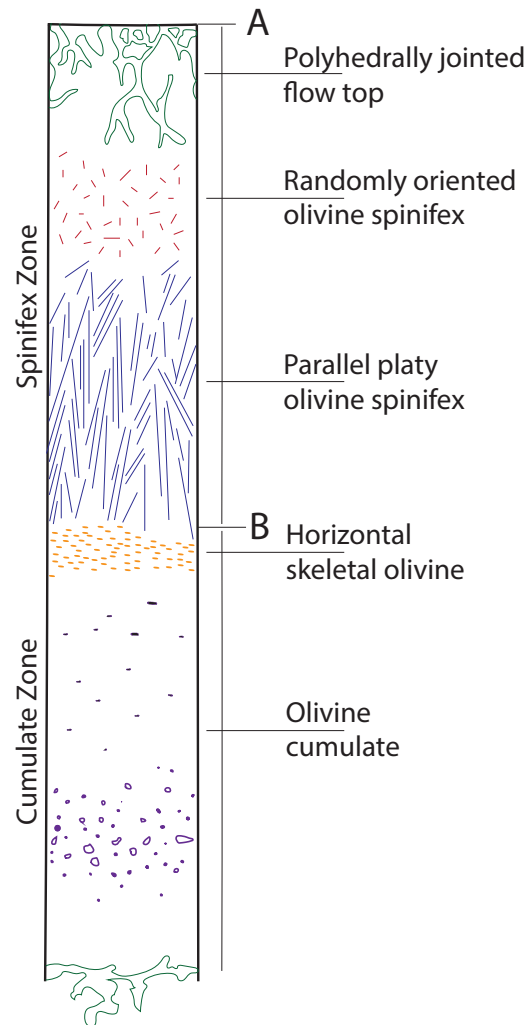


Figure 1.3. Layered komatiite flow with spinifex texture A-zone and cumulate B-zone (modified from Arndt et al., 2008).

The upper 1 to 10 cm of komatiite flows often consist of a chilled margin (A_1) that hosts fine (0.1 mm) polyhedral olivine phenocrysts set in a matrix of elongate, platy, randomly oriented skeletal olivine grains that is commonly deemed a microspinifex texture (Fig. 1.3; Arndt et al., 2008). The matrix can also be composed of glass or a microcrystalline groundmass depending on the flow. The flow tops are also typically polyhedrally jointed and can range in thickness from 5 to 150 cm (with an average thickness of 15 cm; Arndt et al.,

2008). The polyhedral joints are comparable to columnar jointing seen in basalts and originate from the contracting and cooling of the solidifying magma (Arndt et al., 2008).

It is common to subdivide the spinifex zone into A_2 for the randomly oriented fine-grained olivine spinifex and A_3 for the parallel aligned coarse-grained olivine spinifex. Spinifex texture consists of both randomly oriented and parallel aligned olivine or pyroxene grains that are typically in the form of dendritic, platy, or skeletal depending on their location within the flow (Fig. 1.3). The grain size of olivine grains typically increases from the top to the base of the spinifex layer where it is demonstrated that the top layer consists of randomly oriented skeletal olivine grains 1 to 2 mm long and 0.5 mm thick and the base consists of coarser parallel olivine blades (Arndt et al., 2008). The modal abundance of olivine decreases from the top to the base of the spinifex layer with the most dramatic changes occurring in thicker flows (Arndt et al., 2008). In many cases the transition from randomly oriented spinifex to platy parallel spinifex is abrupt (Arndt et al., 2008). Deeper in the flow, spinifex grains can reach 1m in length.

The B_1 layer consists of a pyroxene-glass matrix with elongate skeletal olivine phenocrysts often 1-3mm long aligned parallel to flow direction (Arndt et al., 2008). There is often an abrupt contact present between the spinifex and cumulate layers in which it can be observed that skeletal olivine grains grow upwards from the top B_1 layer, suggesting that the B_1 cumulate layer consolidates before the growth of spinifex olivine crystals is complete (Fig. 1.3; Arndt et al., 2008). The lower B_1 contact is typically gradational and corresponds to a gradual increase in the proportion of solid polyhedral grains and a decrease in the proportion of elongate hopper grains (Arndt et al., 2008). The modal abundance of olivine within layer B_1 is intermediate between spinifex olivine concentrations and the cumulate B_2 - B_4 layers.

The cumulate B_3 or 'knobby peridotite' layer, forms in the lower third of the cumulate layer and is distinguished from the underlying and overlying layers by the presence of knobs, or patches, 1 cm across of pyroxene-glass matrix material (Fig. 1.3; Arndt et al., 2008). The knobby patches within this unit preferentially withstands weathering compared to olivine and therefore stands out relative to the groundmass. The remaining cumulate layers typically consist of adcumulate or orthocumulate olivine layers (cumulate olivine from 70-

95 %) in which the olivine occurs as equant to tabular grains, 0.3 to 0.6 mm wide, often with rounded edges and minor skeletal olivine (Arndt et al., 2008).

The basal chill zone comprises 2-3 cm of most komatiite flows with textures resembling those of overlying cumulate layers in that they normally consist of polyhedral olivine grains in a finer pyroxene-glass matrix (Arndt et al., 2008). Olivine grains within this zone are much smaller at 0.1 to 0.3 mm wide and are far less abundant (5-30 modal%; Arndt et al., 2008). The variation from the upper chill margin is that the microscopic spinifex texture is rarely present within the basal chill margin (Arndt et al., 2008).

Komatiites are often characterized by having at least 18 wt% MgO with komatiitic basalts, or basaltic komatiites, having lower concentrations of 12 to 18 wt% MgO (Dostal, 2008). They also have low SiO₂ of 40 to 45 wt% and TiO₂ less than 1% (Gurenko et al., 2016). Komatiites are commonly subdivided into aluminum depleted komatiites (ADK) and aluminum undepleted komatiites (AUK) based on differing Al₂O₃/TiO₂. This variation relates to the komatiite depth of origin where ADK komatiites are aluminum depleted because of Al retention in garnet when the magma liquids developed and AUK komatiites are sourced from above the garnet stability field, or at great depth below the mantle transition zone, resulting in their lack of Al depletion (Dostal, 2008). It has been suggested that AUKs are derived from the plume head and ADK from the plume tail (Fig. 1.4; Sproule et al., 2003).

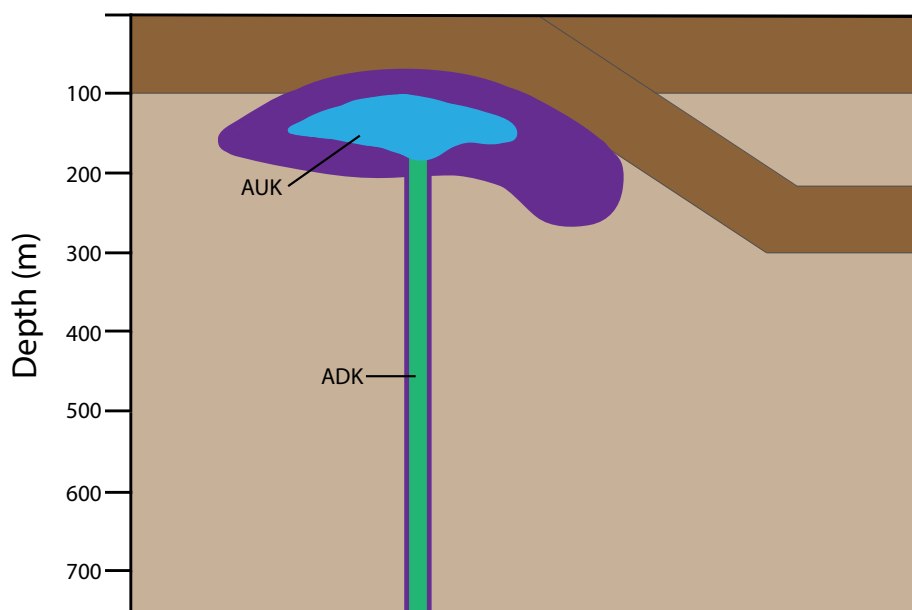


Figure 1.4. Schematic diagram showing position of AUK and ADK relative to an ascending plume modified from Sproule et al. (2003).

The flows display a fractionated heavy rare earth element (HREE) pattern on a primitive mantle normalized diagram if the magma originates from the garnet stability field, as garnet preferentially retains HREE versus the melt. There is also internal variation of MgO within flow units, in which the olivine cumulate layers will display higher concentrations of MgO relative to the spinifex layers (Arndt, 1986). The variation in crystal composition correlates with olivine fractionation within the flow, which modifies the composition of the komatiite liquid (Dostal, 2008).

1.3.1 Aluminum Undepleted Komatiites

Although there is no specific temporal constraint on aluminum depleted or undepleted komatiites (AUK), the AUK variety are prevalent in Neoproterozoic terranes, occurring only rarely pre-3Ga, and are named Munro-type after their type locality in the Abitibi greenstone belt of the Archean Superior Province (Dostal, 2008). Aluminum undepleted komatiites are thought to have been derived from high degrees of partial melting (up to 50% at low pressures) at depths of 100-350 km (5 to 8.5 GPa) or depths greater than 660 km in which perovskite is the stable mantle phase (Campbell et al., 1989; Ringwood, 1982; Dostal, 2008). The shallow origin corresponds to a depleted source, therefore resulting in the light rare earth element (LREE) depletion of AUK komatiites (Arndt et al., 1998). AUKs are characterized by chondritic $\text{Al}_2\text{O}_3/\text{TiO}_2$ ratios of ~ 20 , $\text{CaO}/\text{Al}_2\text{O}_3$ of ~ 1 , and unfractionated $[\text{Gd}/\text{Yb}]_{\text{PM}}$ of ~ 1 (Sossi et al., 2016).

1.3.2 Aluminum Depleted Komatiites

Aluminum depleted komatiites (ADK), or Barberton komatiites, occur dominantly in the Paleoproterozoic and are named for their type locality in the Barberton greenstone belt in South Africa where they were first documented by Viljoen and Viljoen (1969; Dostal, 2008). The source for ADK is thought to be in the garnet stability field at 300 to 660 km with pressures of 8 to 13 GPa (Sossi et al., 2016). The presence of residual garnet sequesters Al and the heavy rare earth elements (HREE) resulting in a depletion in these elements (Sossi et al., 2016). Geochemical indicators of aluminum depleted komatiites include: subchondritic ratios of $[\text{Gd}/\text{Yb}]_{\text{PM}}$ of ~ 1.3 - 1.6 , $\text{CaO}/\text{Al}_2\text{O}_3$ of ~ 1.5 and $\text{Al}_2\text{O}_3/\text{TiO}_2$ of < 12 (Sossi et al., 2016;

Dostal, 2008). They typically have high concentrations of light rare earth elements and depletions in Al, Sc and V, and commonly have small negative Zr-Hf anomalies (Sossi et al., 2016). Aluminum depleted komatiites are interpreted to result from roughly 30% partial melting derived often from plume tails (Fig. 1.4; Campbell et al., 1989; Dostal, 2008).

1.3.3 Komatiite Genesis

Komatiites are commonly considered to have been derived from anhydrous partial melting of the mantle, however alternative models include high-degree partial melting of mantle peridotite at relatively low pressures (Nisbet & Walker, 1982), lower degrees of partial melting at very high pressures in mantle plumes (Ohtani, 1990; Hertzberg, 1992) or hydrous melting of mantle peridotite at low pressures in a subduction zone setting (Grove et al., 1997; Parman et al., 1997). The arguments in support of the model of hydrous komatiites include: the depression of the liquidus that results in the reduction of temperatures required to induce komatiite melting (Allègre, 1982; Kawamoto et al., 1996), the occurrence of vesicles and the occurrence of pyroclastic komatiites indicating volatiles were present in the source (Parman et al., 1997) and moderate water contents observed in olivine and chromite melt inclusions (Shimizu et al., 1997). Grove et al. (1996) proposed that spinifex texture required water in the source; however, melting experiments by Parman et al. (1997) have replicated spinifex texture under both hydrous and anhydrous conditions. Arndt et al. (1998) have argued that the presence of water in komatiites could also be derived from a mantle source or was perhaps assimilated from hydrated oceanic crust. This assimilation would result in little change to the trace element geochemistry but may still enrich the komatiite in water. More recently, Arndt et al. (2008) have suggested that moderate amounts of water (0.6 wt%) were entrained into Archean plumes as they crossed the Mantle Transition Zone (Sobolev et al., 2016).

The possible implications of a strongly hydrous source for komatiite genesis would include changing the interpreted temperature of the Archean mantle, in which the temperature variation from modern mantle may not be as high as the proposed $\sim 200^{\circ}\text{C}$ difference (Condie, 2016). The presence of mantle-sourced water present in komatiites could implicate a subduction origin for komatiites. The addition of water can cause a

depression in the komatiite liquidus by roughly 150°C, and demonstrates that lower temperatures can produce highly magnesian lavas, but would require water contents from 10 to 20 wt% (Green et al., 1974). The subduction models for komatiites has been discussed by Parman et al. (1997) and Parman et al. (2004) who invoked analogies between Archean komatiite geochemistry and modern boninite occurrences derived from supra-subduction zone settings.

1.4 Previous Work

Although studied in the 1990's, komatiites in the Lake of the Woods greenstone belt have subsequently received little study utilizing modern methods. Ayer's (1998) PhD thesis analyzed the Lake of the Woods greenstone belt to investigate the petrogenesis and tectonic evolution of the Neoproterozoic greenstone belt. Related studies based on geochronology, geochemistry, and radiogenic isotope data by Ayer and Davis (1997) and Ayer and Dostal (2000) argued that the Lake of the Woods komatiites were generated by a high degree of partial melting of a relatively shallow source, therefore indicating they are aluminum undepleted komatiites. Although there have been previous studies on the LWGB, the goal of this study specifically is to enlarge the high-precision geochemical data base for LWGB komatiites and to propose a genetic model consistent with revised interpretations of the Superior Province.

Chapter 2: Regional Geology

2.1 Superior Province

The Superior Province is the largest Archean craton globally at 1.4×10^6 km and forms the core of the Canadian Shield (Percival et al., 2012). It is bounded by the Grenville Province to the southeast and by the Trans-Hudson Orogen to the north, with thrust and transcurrent faulting along province boundaries subsequent to the Superior Province accretion (Fig. 2.1; Card, 1990). The Superior Province was created by the amalgamation of volcanic, plutonic, volcanic-plutonic, high-grade gneissic, and metasedimentary terranes, domains and tectonic assemblages from 2.74–2.65 Ga and has been tectonically stable since ~ 2.6 Ga, occupying a lower plate setting during the Paleoproterozoic and Mesoproterozoic tectonism that affected its margins (Card and Ciesielski, 1986; Percival et al., 2006; Polat, 2008). Specifically, five accretionary events in the central and western Superior Province have been linked with the assembly of continental and oceanic crust fragments to form a coherent craton by 2.6 Ga (Percival et al., 2006). These five events exhibit similar cycles at ~ 10 million-year intervals including: cessation of arc magmatism, early deformation, synorogenic sedimentation, sanukitoid magmatism, bulk shortening, regional metamorphism, late transpression, orogenic gold mineralization, emplacement of crustally-derived granites, and postorogenic cooling (Percival et al., 2006).

Early attempts to subdivide the Canadian Shield have relied heavily on variations in structural trends and styles with less emphasis using isotopic ages from lithologies and geologic events (Card and Ciesielski, 1986). Prior to the work of Stott et al. (2010), the subprovince classification utilized features, or a combination of features, such as structural style and trends, metamorphic grade, lithology, absolute and relative ages of rock units and events, metallogenesis and geophysical attributes as summarized by Card and Ciesielski (1986). This classification constructed a number of litho-tectonic domains including volcano-plutonic, metasedimentary, plutonic, and high-grade gneissic subprovinces (Card and Ciesielski, 1986). Each subprovince was considered a primary component in the Late Archean assemblage of the Superior Province. Although the subprovince classification is widely used as a geologic reference throughout the Superior Province, the classification

scheme has been superseded for tectonic analysis (Stott et al., 2010). The progression to a new terrane classification stemmed from substantial developments in regional bedrock geology mapping coupled with geophysical surveys and interpretations, widespread geochronological applications, and geochemical and isotopic syntheses (Stott et al., 2010). Stott et al. (2010) described terranes as being tectonically bounded regions with internal characteristics distinct from those in adjacent regions prior to Superior Province assemblage, and domains as typically being the younger and lithologically distinct part of a terrane, either with juvenile crust or sharing a common basement. It is the amalgamation of two or more terranes before the Neoproterozoic assembly of the Superior Province that defines a superterrane, for example, the North Caribou superterrane and Northern Superior superterrane (Fig. 2.1).

Additional work utilizing isotopic and zircon inheritance studies revealed five fundamental age domains across the Superior Province (Percival et al., 2006). These Mesoproterozoic terranes are recognized despite pervasive overprinting by Neoproterozoic magmatism, metamorphism, and deformation (Percival et al., 2006). The oldest remnants of continental crust occur in the Northern Superior superterrane with rocks as old as 3.7 Ga, whereas to the south the North Caribou superterrane has continental remnants ~3.0 Ga in age and both the Winnipeg River and Marmion terranes are composed of relatively small continental fragments dating back to 3.0 and 3.4 Ga, respectively (Fig. 2.1; Beakhouse, 1991; Stott and Corfu, 1991; Skulski et al., 2000; Percival et al., 2006). The North Caribou superterrane is thought to be the core to which subsequent terranes were accreted (Percival et al., 2006). Individual orogenic (deformation) events young southward across the Superior Province with the Hudson Bay and North Caribou terranes experiencing common deformation at 2.72 Ga in the north, whereas juvenile submarine volcanism was underway in the Wabigoon, Wawa and Abitibi terranes in the south (Percival et al., 2012).

2.2 Wabigoon Terrane

The Wabigoon terrane is a 900 km long by 150 km wide granite-greenstone terrane situated in the southwestern Superior Province (Fig. 2.1; Blackburn et al., 1991). It is a composite terrane comprising volcanic-dominated domains with a central axis of plutonic

rocks with variable ages (Davis and Jackson, 1988; Percival et al., 2002). The terrane is commonly subdivided into the western and eastern Wabigoon terranes, separated by domains of Mesoarchean age (the eastern Winnipeg River terrane and Marmion domain; Tomlinson et al., 2004). The Marmion terrane, formerly included as part of the south-central Wabigoon terrane, is now recognized to be a distinct metamorphically complex domain that is distinguishable from the western and eastern Wabigoon terranes (Easton, 2000; Percival and Easton, 2007). Several small greenstone belts with ages between 2.99 and 2.78 Ga formed on the 3.01 to 2.99 Ga Marmion tonalite basement (Tomlinson et al., 2004; Percival and Easton, 2007). The Winnipeg River terrane now includes the former central Wabigoon granitoid complex and Winnipeg River meta-plutonic terrane (Percival and Easton, 2007). The Winnipeg River-type crust is ~3.4 Ga while the Marmion terrane appears to have been juvenile at 3.0 Ga and is proposed to have accreted to the Winnipeg River terrane by *circa* 2.92 Ga (Percival and Easton, 2007).

The Marmion terrane, formerly included as part of the south-central Wabigoon terrane, consists of 3.01 to 2.99 Ga Marmion tonalite basement that has undergone a complex metamorphic history relative to the surrounding western and eastern Wabigoon terranes (Tomlinson et al., 2004; Percival and Easton, 2007). The boundary between the Quetico and western Wabigoon terranes is defined as the Seine River-Rainy River Lake fault, whereas the boundary between the Quetico and eastern Wabigoon terranes appears to be an imbricate zone with an earlier history of structural telescoping (Devaney and Williams, 1989; Tomlinson et al., 1996; Percival and Easton, 2007).

2.2.1 Western Wabigoon Terrane

The western Wabigoon domain is dominated by mafic volcanic rocks with large tonalite-granodiorite plutons (Fig. 2.2; Blackburn et al., 1991). It is characterized by interconnected, arcuate, metavolcanic greenstone belts that largely conform to elliptical batholiths (Blackburn et al., 1991). The volcanic rocks are generally 2.74 and 2.72 Ga with rare older (2.775 Ga) and younger (2.713-2.70 Ga) volcano-sedimentary sequences (Corfu and Davis, 1992). The volcanic rocks range in composition from calc-alkaline to tholeiitic and

have been interpreted to represent arc and ocean floor or plateau environments, respectively (Ayer and Davis, 1997; Ayer, 1998; Ayer and Dostal, 2000; Wyman et al., 2000).

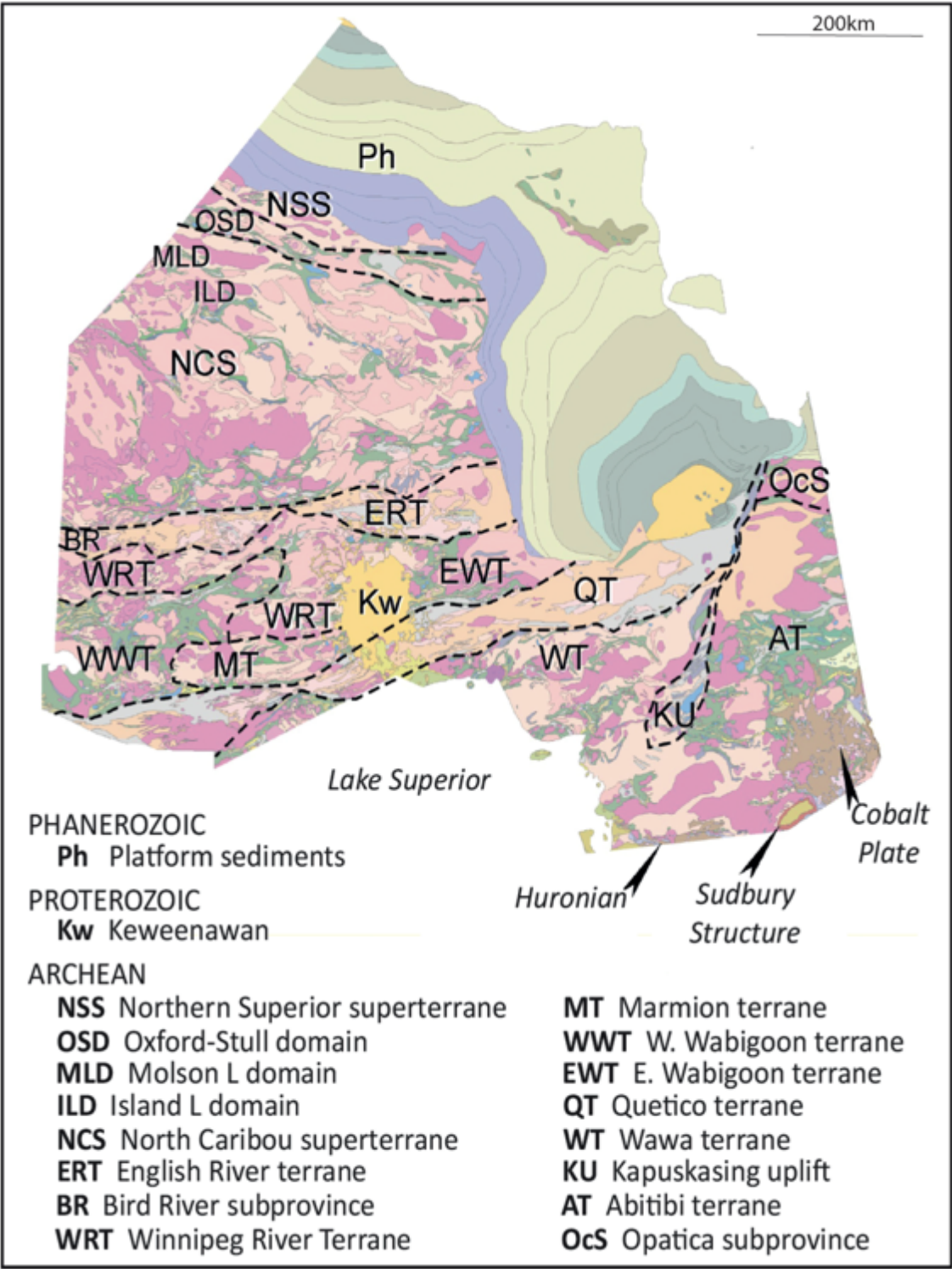


Figure. 2.1. Geological map of Ontario subdivided into terranes defined by Percival and Easton (2007).

They are dominantly juvenile, submarine tholeiitic basalts through calc-alkaline basalt-andesite-dacite sequences (Percival et al., 2012). The calc-alkaline volcanic rocks and coeval plutons within the terrane are consistent with back-arc settings, associated with local massive sulphide accumulations (Galley et al., 2000, Percival et al., 2012). Plutonic rocks range from broadly synvolcanic batholiths of tonalite-diorite-gabbro (2.73-2.72 Ga) to younger granodiorite batholiths and plutons (2.71 Ga), monzodiorite plutons of sanukitoid affinity (~2.69 Ga) and plutons and batholiths of monzogranite (2.69-2.66 Ga; Corfu and Davis, 1992; Ayer et al., 1998; Melnyk et al., 2000; Whalen et al., 2004; Percival et al., 2006; Melnyk et al., 2006). Clastic metasedimentary sequences preserved in narrow belts within volcanic sequences are commonly younger than the volcanic rocks with locally unconformable relationships and geological constraints indicating deposition between 2.71 and <2.69 Ga (Fralick, 1997; Fralick and Davis, 1999; Sanborn-Barrie and Skulski, 2006). The western Wabigoon terrane likely evolved as a small ocean basin in a complex microplate environment (Percival et al., 2004, 2012).

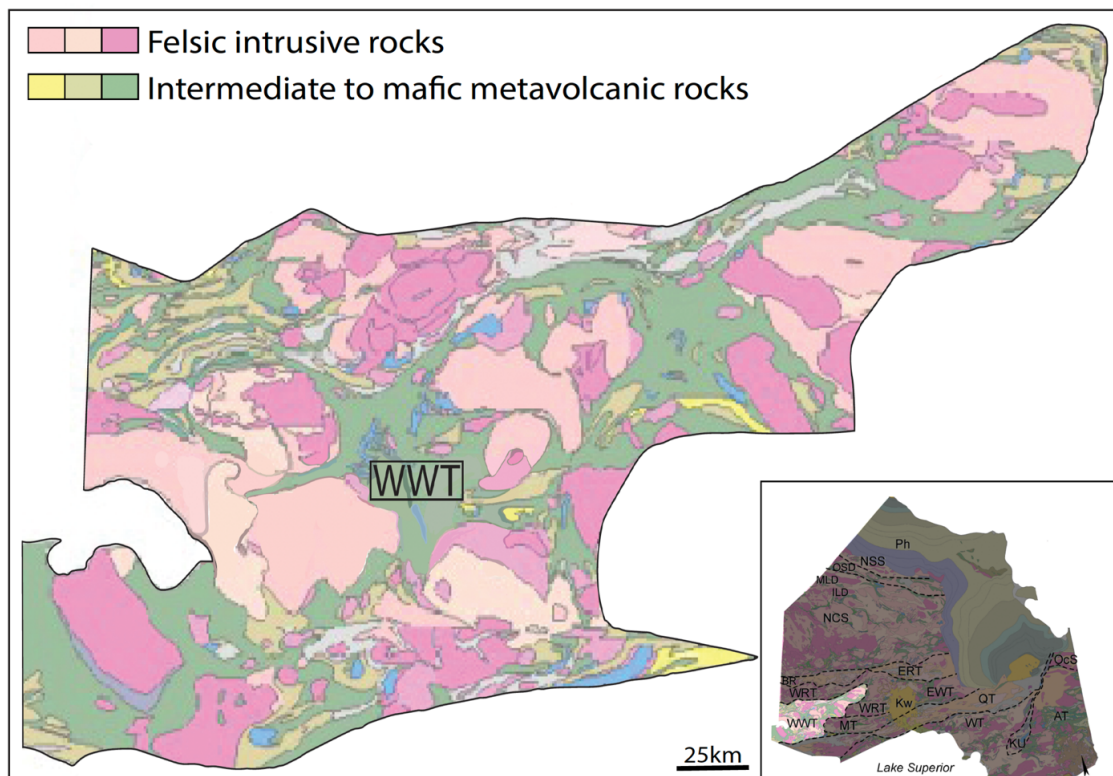


Figure. 2.2. Geological map of western Wabigoon terrane (WWT; modified after Ontario Geological Survey, 2011) and location within the Superior Province.

Two deformation phases have affected the supracrustal rocks of the western Wabigoon terrane with deformation starting pre-2.709 Ga in the Lake of the Woods greenstone belt to ~2.70 Ga in the Sioux Lookout-Savant area in the east (Blackburn et al., 1991; Davis and Smith, 1991; Ayer and Davis, 1997; Melnyk et al., 2006; Percival et al., 2006; Sanborn-Barrie and Skulski, 2006). The Sturgeon-Savant greenstone belt occurs at the contact between the western Wabigoon and the Winnipeg River terranes (Percival et al., 2006).

2.2.2 Eastern Wabigoon Terrane

The eastern Wabigoon terrane is a composite terrane with greenstone belts and intervening granitoid plutons of Mesoarchean and Neoproterozoic age (Fig. 2.3; Percival et al., 2006). The supracrustal rocks have been divided into several assemblages based on lithology, age, and geochemistry (Percival and Easton, 2007). The assemblages include continental margin sequences, tholeiitic rocks of oceanic affinity, calc-alkaline rocks of continental affinity, and clastic rocks that unconformably overly the assemblage (Stott et al., 2002; Tomlinson et al., 2004; Percival et al., 2006). The northwest part of the terrane includes the Toronto and Tasho assemblages (3.0-2.92 Ga), interpreted to represent a continental margin sequence built on the Winnipeg River terrane (Percival and Easton, 2007). The central part of the terrane is dominated by juvenile pillowed basalts and calc-alkalic rocks of the 2.78 to 2.738 Ga Onaman and Willet assemblages and 2.725 to 2.715 Ga Metcalfe-Venus assemblage. The southern part of the terrane is dominated by the calc-alkalic Elmhirst-Rickaby assemblage (2.78-2.74 Ga; Percival and Easton, 2007).

At least two deformation events affected the eastern Wabigoon terrane. Firstly, an event that created east-striking structures at approximately 2.706 Ga and a second event causing east-striking, dextral transpressive shear zones with a lower age limit of 2.694 Ga provided by the Deeds Lake pluton (Stott et al., 2002).

2.3 Lake of the Woods Greenstone Belt

The Lake of the Woods greenstone belt (LWGB) is situated along the Northwestern margin of the Wabigoon terrane, bounded to the north by the Winnipeg River and English River

terrane and to the south by the Quetico terrane (Ayer and Davis, 1997). It consists of a northeast trending metavolcanic plutonic belt that extends for 900km and is about 150km wide (Fig. 2.4; Ayer and Davis, 1997). The LWGB is divided into three supracrustal assemblages: a lowermost mafic volcanic Lower Keewatin assemblage; a compositionally diverse, predominantly volcanic middle Upper Keewatin assemblage; and a predominantly sedimentary uppermost Electrum assemblage (Ayer and Davis, 1997). The assemblages are regional units in which each assemblage is characterized by similar lithology, geochemistry, facies associations, geophysical signatures, structural style and age (Fig. 2.2B; Ayer and Davis, 1997). The supracrustal assemblages are intruded by granitic batholiths which divide the terrane into eastern and western regions (Ayer and Davis, 1997).

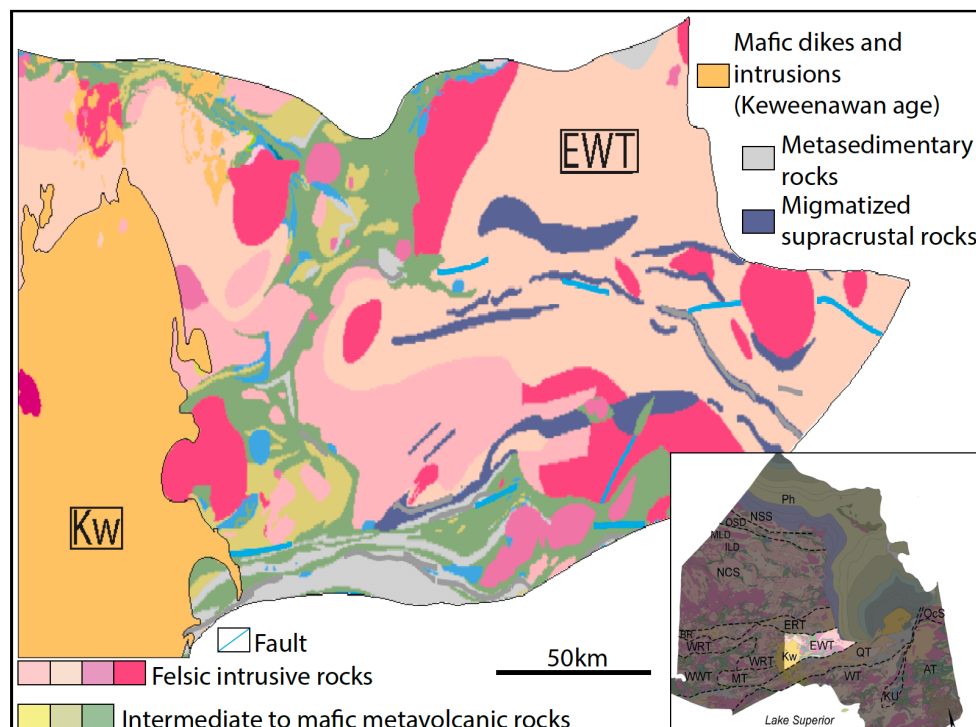


Figure. 2.3. Geological map of eastern Wabigoon terrane (EWT) and a component of the Keweenaw terrane (Kw; modified after Ontario Geological Survey, 2011) and location within the Superior Province.

2.3.1 Lower Keewatin Assemblage

The Lower Keewatin assemblage occupies the lowermost stratigraphic position within the LWGB with a maximum preserved thickness of approximately 10 km (Ayer and Davis, 1997). It consists of five geographically isolated mafic volcanic groups, correlated on

the basis of stratigraphy, lithological and geochemical similarities, and geochronology (Ayer and Davis, 1997). These are the Deception Bay, Bigstone Bay, Cedar Island, Barrier Islands and Snake Bay groups (Blackburn et al., 1991; Ayer and Davis, 1997). The Bigstone Bay and Snake Bay groups yield ages of *circa* 2738 Ma and >2732 Ma, respectively (Blackburn et al., 1991; Ayer and Davis, 1997). Concentrated in the uppermost part of the assemblage are aphyric pillowed to massive mafic flows with local plagioclase megacrystic mafic flows, variolitic flows, vesicular flows and columnar-jointed mafic flows (Ayer and Davis, 1997).

The volcanic rocks within the assemblage are tholeiites with the uppermost part of the assemblage consisting of Fe-tholeiites and lowermost part of the assemblage consisting of Mg-tholeiites (Ayer and Davis, 1997). Rare magnesian volcanic flows, present within the Cedar Island group in the Shoal Lake area, have MgO contents up to 14 wt% and Mg numbers up to 70 and are described as basaltic komatiite by Ayer and Davis (1997; Smith, 1987).

2.3.2 Upper Keewatin Assemblage

The Upper Keewatin assemblage is the most extensive unit of the LWGB and consists of three distinct rock associations with a total estimated maximum stratigraphic thickness of approximately 10 km. The Upper Keewatin assemblage consists of 1) mafic to felsic metavolcanic rocks of calc-alkalic affinity, 2) ultramafic to mafic metavolcanic rocks of komatiitic to tholeiitic affinity, and 3) turbiditic metasedimentary rocks (Ayer and Davis, 1997). The assemblage consists of the informal Clearwater Bay group (*circa* 2719 Ma) consisting dominantly of calc-alkaline mafic to felsic flows and pyroclastic rocks, the Indian Bay group of tholeiitic mafic flows, the Andrew Bay (*circa* 2723 Ma) group of calc-alkaline mafic to felsic volcanic rocks, the Monument Bay group of calc-alkaline mafic to felsic volcanic rocks, the Royal Island and Warclub groups (*circa* 2715 Ma) consisting of turbidites, the Long Bay (*circa* 2719 Ma) group of calc-alkaline mafic to felsic volcanic rocks and lastly the Windigo Islands group of calc-alkaline mafic to felsic volcanic rocks (Blackburn et al., 1991; Ayer and Davis, 1997). Tholeiitic to komatiitic metavolcanic units up to 50 km long and 2 km thick are intercalated with calc-alkalic mafic to felsic metavolcanic units (Ayer and Davis, 1997). The ultramafic metavolcanic units are considered to be coeval with the calc-alkalic metavolcanic units based on the presence of conformable contacts that are typically

abrupt, demonstrating a lack of unconformities (Ayer and Buck, 1989; Ayer, 1991; Ayer et al., 1991). These contacts can also be marked by fine-grained felsic metatuffs and turbiditic metawackes. Aphyric mafic and ultramafic flows host rare intercalations of intermediate metatuff and fine-grained epiclastic metasedimentary rocks (Ayer and Davis, 1997). The Upper Keewatin assemblage is interpreted to be the result of shallow submarine eruption and deposition because of the presence of intercalations of epiclastic sediments and highly vesicular pillowed flows (Ayer and Davis, 1997).

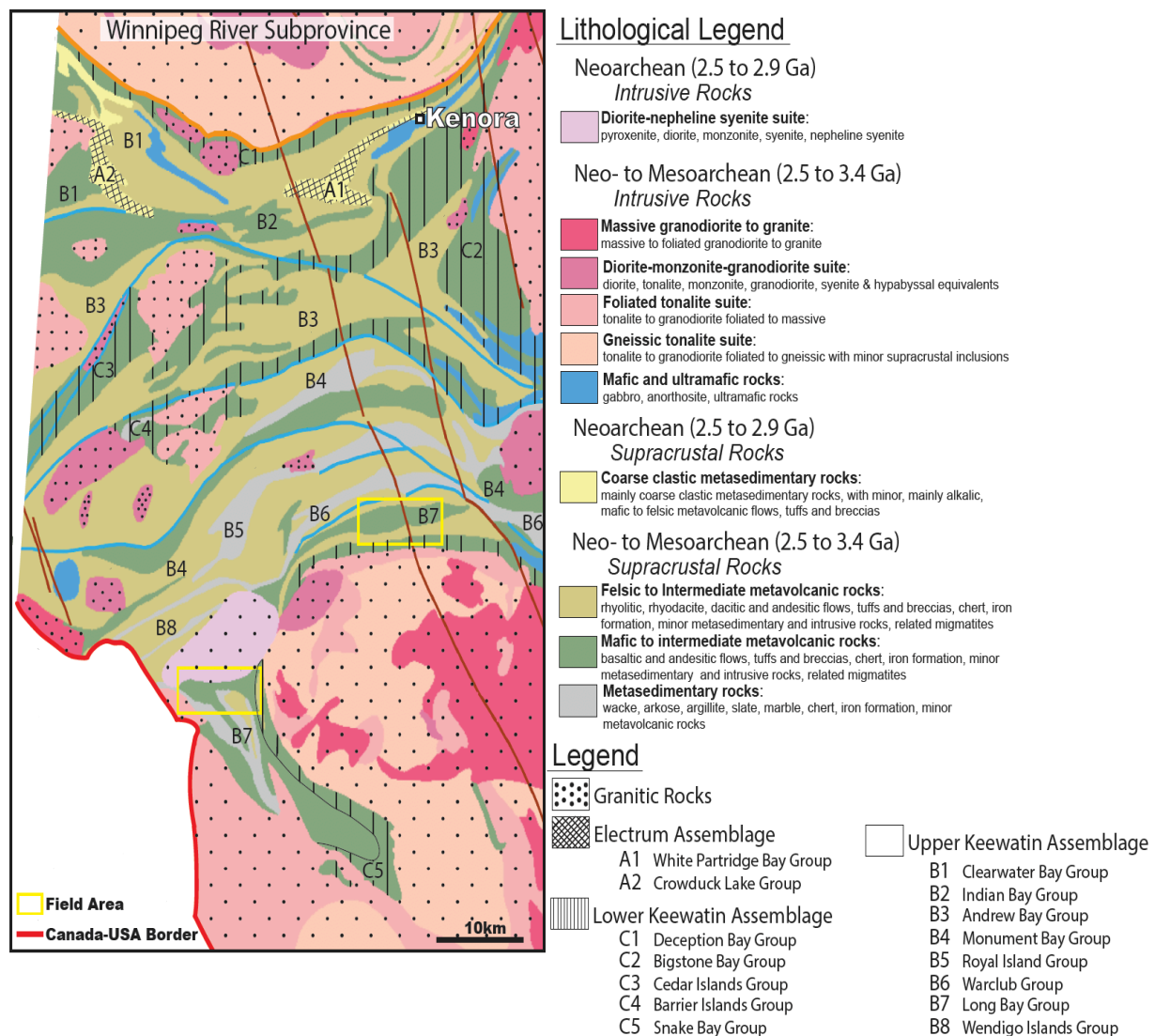


Figure. 2.4. Geological map of the Lake of the Woods greenstone belt (modified after Ontario Geological Survey, 2011).

2.3.3 Electrum Assemblage

The Electrum assemblage, located in the northern part of the LWGB (Fig. 2.4), contains the informal Crowduck Lake (<2699 Ma) and White Partridge Bay (2709 Ma) groups composed of clastic metasedimentary rocks with subordinate metavolcanic units (Ayer and Davis, 1997). The metasedimentary rocks within the Electrum assemblage host ancient detrital zircons with ages greater than 3.0 Ga, indicating ancient source regions (Percival et al., 2006). Zircons collected from a debris flow within the Crowduck Lake group put an upper limit on deposition of the group of 2699 ± 2 Ma (Ayer and Davis, 1997). Metavolcanic rocks of the Crowduck Lake group consist predominantly of felsic and intermediate flows and intermediate pyroclastic rocks, however, turbiditic sandstones and subordinate felsic pyroclastic rocks are present within the lower Crowduck Lake (Ayer and Davis, 1997). Both the Crowduck Lake and White Partridge Bay groups contain metaconglomerates that host granitoid and supracrustal rock clasts (Ayer and Davis, 1997).

2.3.4 Plutonic Complexes

There are three main episodes of plutonism in the LWGB (Fig. 2.4; Ayer and Davis, 1997). The first event consists of predominantly tonalitic intrusions that are contemporaneous with Upper Keewatin assemblage volcanism including the Sabaskong batholith (2723–2724 Ma), the early phases of the High Lake stock (2727 ± 2 Ma), and the Aulneau Batholith (2717 ± 3 Ma). The second event includes syntectonic to post-tectonic, mainly granodioritic intrusions, including the Canoe Lake stock (2709 ± 1 Ma) and the late phases of the High Lake stock (2711 ± 2 Ma) and the Aulneau Batholith ($2710 +4/-2$ Ma). The third and last event comprises alkalic plutons interpreted to be coeval with Electrum assemblage volcanism (<2699 Ma).

Chapter 3: Methodology

3.1 Field Techniques

Sampling for this study was focused on mafic to ultramafic metavolcanic units present throughout the Upper Keewatin Assemblage of the LWGB. Field mapping was conducted in the summer of 2017 on Falcon Island and in the summer of 2018 on Cliff and Calendar Islands. The field seasons consisted of two two-week periods in which inland traversing as well as shoreline mapping was completed. A total of 99 samples were taken during the first field season from a total of 270 stations. Geological maps were created from the field mapping at a scale of 1:5000 on each island. The mapping strategy was to target mafic to ultramafic metavolcanic units previously documented by Ayer (1997). Field observations included primary and secondary mineralogy, alteration type and strength, primary structures and deformation. Due to the lack of primary mineralogy and structures as a result of metamorphism and likely hydrothermal alteration, regional interpretations and classification of lithologies relied heavily on geochemistry. Field sample descriptions are provided in Appendix A.

The Falcon Island area mapped in 2017 consisted of an irregularly shaped quadrant that included one large island and a number of small surrounding islands with an approximate total surface area of 15.5km². The islands mapped in 2018 focused on mapping the main islands with little to no mapping of surrounding islands and covered an approximate total surface area of 2.3km² on Calendar Island and 13km² on Cliff Island.

3.2 Analytical Techniques

The following section outlines the variety of analytical techniques utilized in this project in order to characterize the ultramafic units within the LWGB. Whole rock geochemical analyses consisted of inductively coupled plasma-mass spectrometry (ICP-MS) to gather trace element concentrations, and X-ray fluorescence (XRF) to gather major element concentrations. Mineral compositions were analyzed using a scanning electron microscope with an energy dispersive spectrometer (SEM).

3.2.1 Petrographic Analysis

A total of 52 samples were prepared at the Lakehead University lapidary facility consisting of 12 polished thin sections to be analyzed under both transmitted and reflected light and 40 thin sections to be analyzed under transmitted light. The grain size classification utilized in this study is as follows: very fine-grained <0.1 mm, fine-grained <1 mm, medium-grained 1-3 mm and coarse-grained >3 mm. Felsic plutonic rocks were classified using a QAPF discrimination diagram in which modal percentages of plagioclase, potassium feldspar and quartz are normalized to 100% and plotted.

3.2.2 Whole-Rock Geochemistry Analysis

Whole-rock geochemistry was used to differentiate lithological units in conjunction with petrographic observations. Geochemical analysis was conducted using a variety of methods including loss on ignition, nickel sulphide fire assay, X-ray fluorescence spectrometry (XRF) and inductively coupled plasma-mass spectrometry (ICP-MS). Geochemical analysis was conducted at the Geoscience Laboratories (Geo Labs) of the Ministry of Northern Development Mines in Sudbury, Ontario. Raw whole-rock geochemistry of each sample is provided in Appendix B.

Samples were first crushed using an agate mill to reduce contamination by Cr, Fe and Al. Samples were reduced to 88 μm . The samples were analyzed for loss on ignition firstly at a temperature of 105°C under nitrogen atmosphere and then at a temperature of 1000°C under oxygen atmosphere. Samples were then fused with a borate flux to produce a glass bead for XRF major oxide analysis of the fused disk, in which abundances are presented as oxide percent and have been recalculated to a 100% volatile-free value. X-ray fluorescence was also utilized to analyze trace element geochemistry with samples prepared as pressed pellets and analyzed using optimized parameters for various elements. Analysis of trace elements utilizing both XRF and ICP-MS allow for comparison of data from both methods. Major elements analyzed through XRF are reported as oxide percentages in which Al_2O_3 , BaO , CaO , Cr_2O_3 , Fe_2O_3 , K_2O , MgO , MnO , Na_2O , P_2O_5 , SiO_2 and TiO_2 are provided. The limits for major oxide percentages on average range from a detection limit of 0.01 wt% and an upper limit of 47 wt%; however, many elements including Al_2O_3 , CaO , Fe_2O_3 and SiO_2 can be

analyzed up to 100 wt%. Trace elements analyzed through XRF are reported in parts per million (ppm) and include As, Br, Cu, Ga, Pb, Mo, Rb, Sr, Th, U, Y, Zn, Ni, Zr and Nb. The limits for this procedure range from 0.7 ppm as a detection limit and 7000 ppm as an upper limit, element dependent.

Samples analyzed by ICP-MS underwent closed vessel multi-acid digestion to completely dissolve the silicate rock samples. This method is utilized to analyze rare earth elements, high field strength elements and large ion lithophile elements. Lower limits for this procedure are 0.0018 ppm and upper limits are 25 000 ppm, element dependent. A lead fire-assay method was used to determine gold, platinum and palladium, in which the metals collected in the fire-assay procedure are quantified by ICP-MS. The Au, Pd, and Pt had an average lower detection limit of 0.27 ppb and Au/Pd had upper limits of 5000 ppb and Pt 11,000 ppb. Carbon and sulphur methods measure the total carbon, expressed as CO₂, and total sulphur, expressed as either S or SO₃. Combustion of samples in an oxygen-rich environment oxidizes the carbon and sulphur present, which is then measured by infrared absorption. The lower limits for CO₂ and S are 0.023 wt% and 0.003 wt% and upper limits 110 wt% and 54 wt%, respectively.

3.2.3 Scanning Electron Microprobe

Samples were chosen for detailed analysis by standard petrographic methods and back-scattered electron (BSE) imagery and energy dispersive X-ray spectrometry using a Hitachi SU-70 scanning electron microscope (SEM) at the Lakehead University Instrumentation Laboratory. The Hitachi SU-70 Schottky Field Emission SEM was used to conduct quantitative analyses of the minerals, with a 15mm working distance and an accelerating voltage of 20kV via the Oxford Aztec 80mm/124 eV electron dispersive X-ray spectrometer (EDX) on the SEM. Point analysis was conducted on the carbon coated SEM discs in order to constrain qualitative mineral chemistry of crystals to determine if variation exists between the mineralogy and komatiite classification. The following well characterized mineral, metal, and synthetic standards were used: jadeite (Na), periclase (Mg), corundum (Al), garnet (Si), orthoclase (K), wollastonite (Ca), ilmenite (Ti), chromite (Cr), olivine (Ni), manganese (Mn), zirconium (Zr), palladium (Pd), and platinum (Pt).

3.2.4 X-Ray Diffraction

X-ray diffraction (XRD) was utilized to determine the mineralogy of the very fine-grained groundmass present throughout the samples. The identified mineralogy was compared to various textures and geochemistry. Samples were crushed at Lakehead University as well as the Geoscience Laboratories in Sudbury, Ontario. Powdered samples crushed by agate mill at the Geoscience Laboratories in Sudbury were sent to Lakehead University following geochemical analyses. Samples crushed at Lakehead University were first milled using a 46 alumina mortar and pestle to achieve a very fine grainsize. Samples were then crushed using an agate mill with silica sand used between samples to ensure no contamination occurred. The homogenous powder was loaded into XRD mounts in a non-oriented fashion to prevent preferred orientation of crystal bias in the results. Nine samples were assessed at the Lakehead University Instrumentation Laboratory (LUIL) using the PANalytical Expert Pro Diffractometer. The analyses were conducted on a continuously spinning stage using a Cu anode material with a generator of 40 mA and 45 kV. The scan took place from $6.0331^{\circ}2\theta$ to $96.9291^{\circ}2\theta$ with a step size of $0.0260^{\circ}2\theta$ and step time of 37.74s. The results were analyzed using XPert Highscore Plus software to determine mineralogy present within each sample.

3.2.5 Radiogenic Isotopes

Twelve samples were submitted as whole rock powders for Sm-Nd isotope analyses at Memorial University of Newfoundland, St. John's, Newfoundland and Labrador. They were dissolved in Savilex® Teflon capsules using an 8 ml (4:1) mixture of 29 M HF – 15 M HNO₃. Prior to acid digestion, a mixed ¹⁵⁰Nd/¹⁴⁹Sm spike is added to each sample. After five days of acid digestion on a hotplate, the solution was then evaporated to dryness, taken back up in 6M HCl for 4 to 5 days. The sample was finally dried down and then re-dissolved in 2.5 M HCL. Samples were then loaded into a column containing cation exchange resin AG-50W-X8, H⁺ form, 200-400 mesh where a Sr fraction can be isolated followed by collection of bulk rare earth elements (REEs). This bulk solution was then dried and taken up in 0.18 M HCl and loaded on a second column containing Eichrom® Ln resin (50-100 mesh) to isolate Sm and Nd separately from the other REEs. All reagents were purified in order to ensure a low contamination level.

Samarium and Nd concentrations and isotopic compositions were determined using a multi-collector Finnigan Mat 262 mass spectrometer in static mode for concentration determination, and dynamic mode for isotopic composition determination. Instrumental mass fractionation of Sm and Nd isotopes were corrected using a Raleigh law relative to $^{146}\text{Nd}/^{144}\text{Nd} = 0.7219$ and $^{152}\text{Sm}/^{147}\text{Sm} = 1.783$. The reported $^{143}\text{Nd}/^{144}\text{Nd}$ ratio was corrected for the deviation of repeated duplicates of the JNdi-1 standard from the accepted value of $^{143}\text{Nd}/^{144}\text{Nd} = 0.512115$ (Tanaka et al., 2000). The current mean value of Jndi-1 analyses is $^{143}\text{Nd}/^{144}\text{Nd} = 0.512092 \pm 8$ (1SD, n=20).

Chapter 4: Field Observations and Petrography

This section presents the results of geological mapping, petrography, SEM and XRD analyses. Visual examination was used to estimate modal abundances and crystal sizes. Crystal size was defined as being very fine-grained (<0.1mm), fine-grained (0.1 to 1mm), medium-grained (1 to 5mm) and coarse-grained (>5mm). During the field mapping, protolith names were given when possible, in order to subdivide the metavolcanic rocks in the area. The rocks in the area have been subjected to greenschist facies metamorphism, therefore metamorphic names were given once petrography was completed.

4.1 Falcon Island Stratigraphy

Field mapping of Falcon Island occurred during the summer of 2017 with 99 samples taken from 270 stations. The mapping area consisted of an irregularly shaped quadrant of roughly 6 by 4 km with a resulting surface area of ~15.5 km² (Fig. 4.1). Work in this area consisted of mapping Falcon Island and a small number of smaller surrounding islands.

There were no direct contacts observed between lithological units, therefore contact boundaries are all inferred. The Falcon Island Stock (quartz-saturated intermediate to mafic intrusive rocks; Fig. 4.1) is located in the north of the mapping quadrant and was sparsely sampled. The field area was composed primarily of mafic to ultramafic metavolcanic rocks, which ranged from fine- to medium-grained lithologies and demonstrated a pervasive east-west striking schistosity with an average dip of 62°N. Minor components in the field area consisted of mafic intrusive rocks, felsic to intermediate metavolcanic rocks, intermediate to mafic metavolcanic rocks, felsic to intermediate intrusive rocks and clastic metasedimentary rocks. The northeast section of the field area within the felsic to intermediate metavolcanic units showed the only occurrence of a northeast-southwest striking foliation with an average dip of 55°N. When metavolcanic units occur as bedded tuffs, observed as compositional banding of siliceous and biotite-rich layers, the schistosity follows the strike of the bedding.

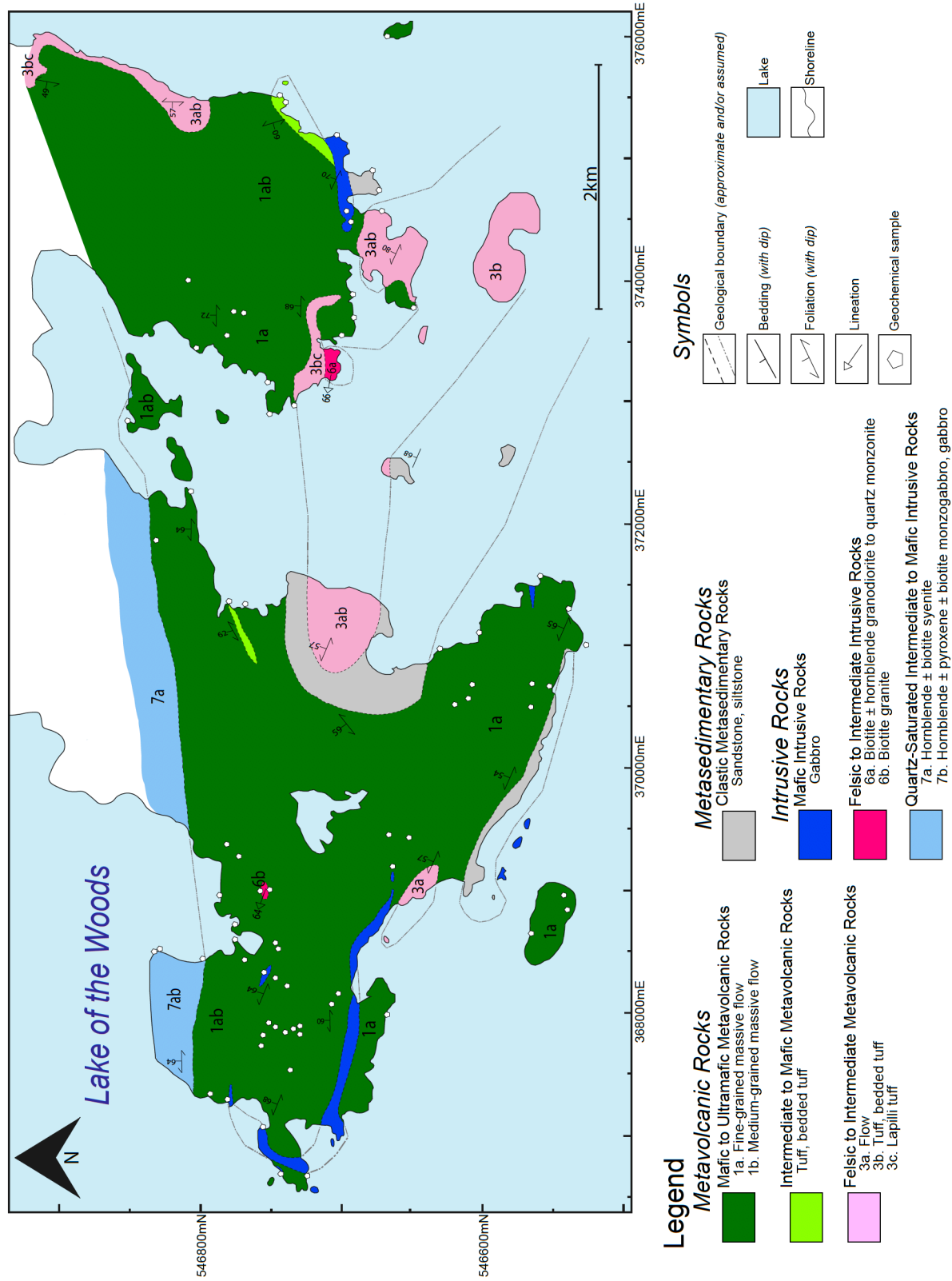


Figure 4.1. Geological map of Falcon Island completed in 2017. The UTM co-ordinates are provided in Zone 15 using NAD83.

4.1.1 Felsic Metavolcanic Rocks

The felsic metavolcanic rocks in the Falcon Island map area are pyroclastic with a lapilli tuff and tuffaceous unit that was bedded or massive (Fig. 4.1). The absence of flow textures indicates a likely pyroclastic origin. The lapilli tuff unit has an aphyric matrix with angular to sub-angular quartz and feldspar phyrlic clasts (Fig. 4.2A). The feldspar and quartz grains are not aligned, and thus indicate no defining foliation. The matrix is similar in composition and appearance to that of the tuff unit. The clasts range in size from 1 to 15 cm, with the larger clasts possessing angular boundaries. The quartz and feldspar subhedral grains are 1 to 3 mm wide, with phenocrysts composing up to 80 modal% of the clasts (Fig. 4.2B). Clasts show slight elongation in east-west orientation.

The tuff is light grey, fine-grained, siliceous, and is commonly quartz phyrlic (Fig. 4.2C). Recognizable beds commonly have greater quartz contents relative to other layers, resulting in white and grey layering. Tuff layers are locally interlayered with mafic flows that are commonly strongly altered and schistose. The tuff is not intensely deformed; however, biotite phenocrysts up to 3 mm long define a weak to moderate foliation when present. Alteration in the tuff unit is dominantly silicification, with local epidote alteration commonly present as veins with surrounding potassic alteration, defining a propylitic alteration (Fig. 4.2D).

4.1.2 Intermediate to Mafic Metavolcanic Rocks

The intermediate to mafic metavolcanic rocks comprise a small portion on the eastern side of the study area (Fig. 4.1). The rocks are pyroclastic with common occurrences of bedded tuffs that have dark and light grey layering characterized by an abundance of quartz in light grey layers (Fig. 4.3A). Layers are typically 10 to 40 cm thick. The unit is fine-grained and weakly to moderately siliceous. Darker grey layers with greater abundance of biotite and/or hornblende display greater schistosity relative to siliceous layers. Samples that are non-foliated are characterized by a very fine-grained grey groundmass and are typically moderately silicified (Fig. 4.3B). Biotite is present within the siliceous layers; however, it does not define a strong foliation (Fig. 4.3C).

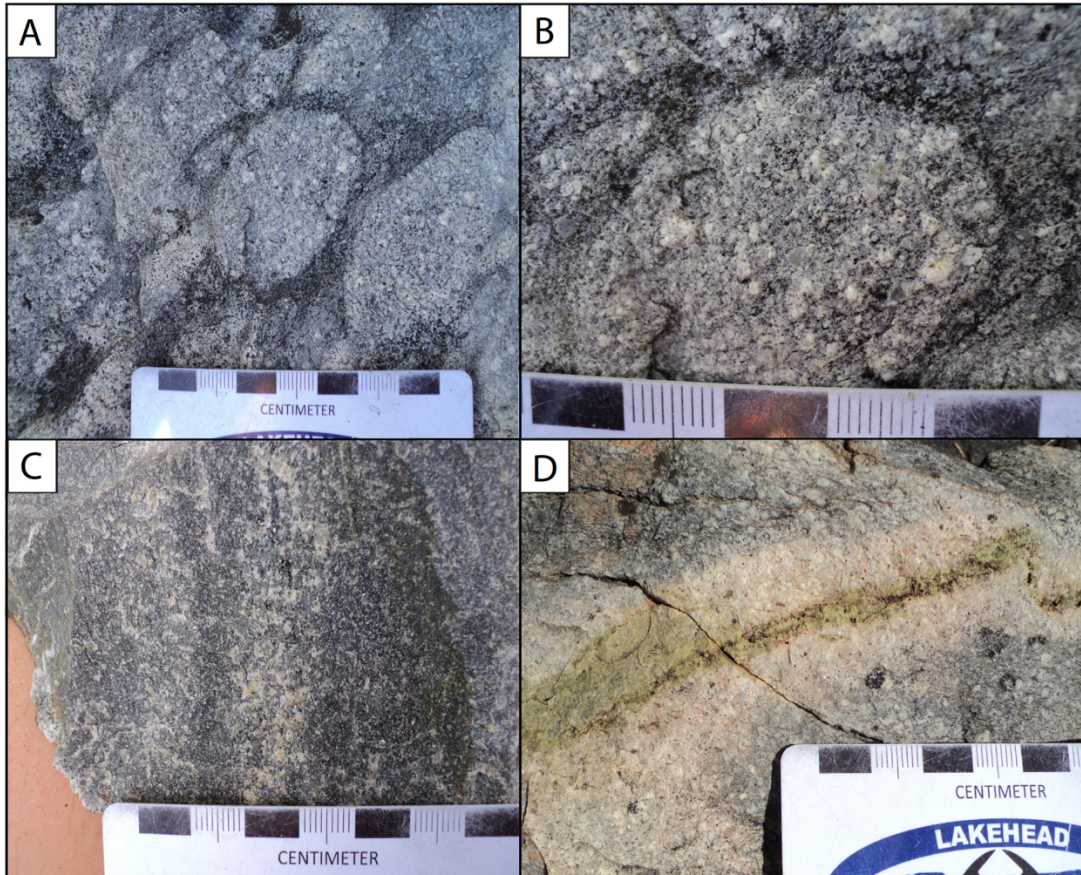


Figure 4.2. Field photographs of felsic metavolcanic units. A (Station 9/8 15U 374559 5466781): Felsic lapilli tuff with clasts up to 7cm long. B (Station 9/8 15U 374559 5466781): Quartz and feldspar phyric clast with grains up to 2mm wide. C (Station 9/12 15U 373464 5467159): Layered unit with variation in silica content seen by darker and lighter grey banding. D (Station 9/14 15U 373126 5467167): Propylitic alteration of host felsic metavolcanic unit.

Fine-grained subhedral amphibole and fine- to medium-grained plagioclase are present within a quartz dominated groundmass with minor chlorite (Fig. 4.3D). Plagioclase grains exhibit moderate fine-grained sericite alteration and polysynthetic twinning. Only a minor population of quartz grains exhibit hematite dusting.

4.1.3 Mafic to Ultramafic Intrusive Rocks

The gabbroic units in the Falcon Island map area are closely associated with mafic metavolcanic flows (Fig. 4.1). Gabbros are dark, medium- to coarse-grained with a moderate to strong foliation. Amphibole crystals up to 1 cm long are elongated, defining a foliation and are commonly 2 to 3 mm wide (Fig. 4.4A). Plagioclase laths comprise up to 20 modal% of the gabbro, and are typically 5 mm long parallel to foliation. Plagioclase laths commonly exhibit weak sericite alteration. Samples range in composition with amphibole consisting of 40 to

60 modal% of the unit, with the remaining rock mass composed of a quartz and plagioclase dominated groundmass. Alteration consists of moderate silicification (~30%) and weak chloritization (~10%; Fig. 4.4B).

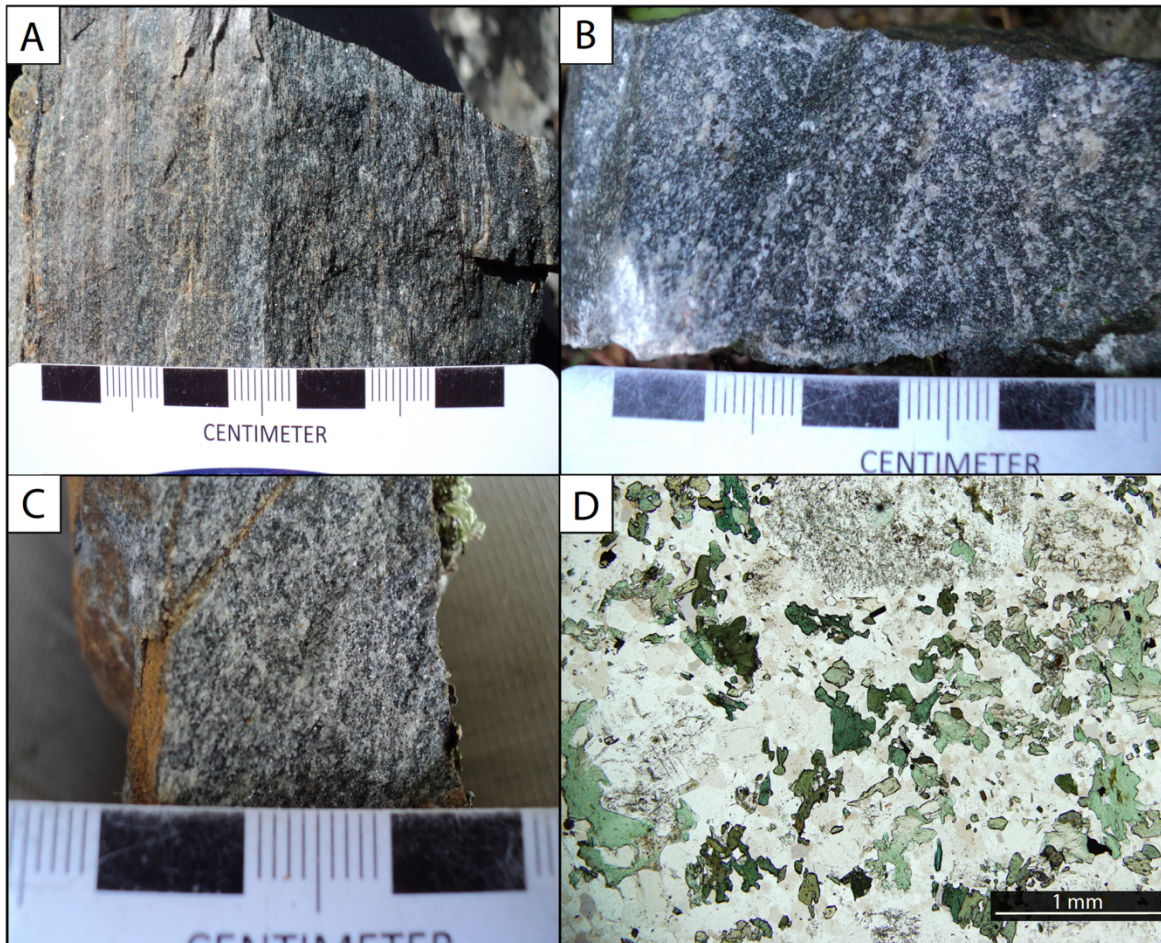


Figure 4.3. Field photos and photomicrographs of intermediate to mafic metavolcanic rocks. A (LOW17CB02 15U 375465 5467424): Bedded tuff with lighter and darker bands representing silica content. B (Station 11/5 15U 373805 5467092): Metavolcanic unit with weak to moderate silicification. C (Station 7/9 15U 371531 5467409): Unit containing quartz, plagioclase and biotite. D (LOW17CB17 15U 373779 5466660): Photomicrograph of intermediate to mafic metavolcanic rock with moderate contents of chlorite and secondary amphibole, quartz with some hematite staining, and feldspar.

Cumulate samples are present within the field area, but are not extensive. Outcrops typically exhibited preferential weathering of the matrix with robust cumulates creating a knobby texture (Fig. 4.4C). The unit contains grains, or cumulates, up to 7 mm wide and were sub- to euhedral within a dark matrix composed of fine-grained plagioclase, quartz and amphibole. Cumulate grains on the weathered surface are demonstrated to be hornblende

and, possibly, actinolite based on petrographic analysis (Fig. 4.4D). It is likely that the amphiboles are metamorphic, potentially after pyroxene.

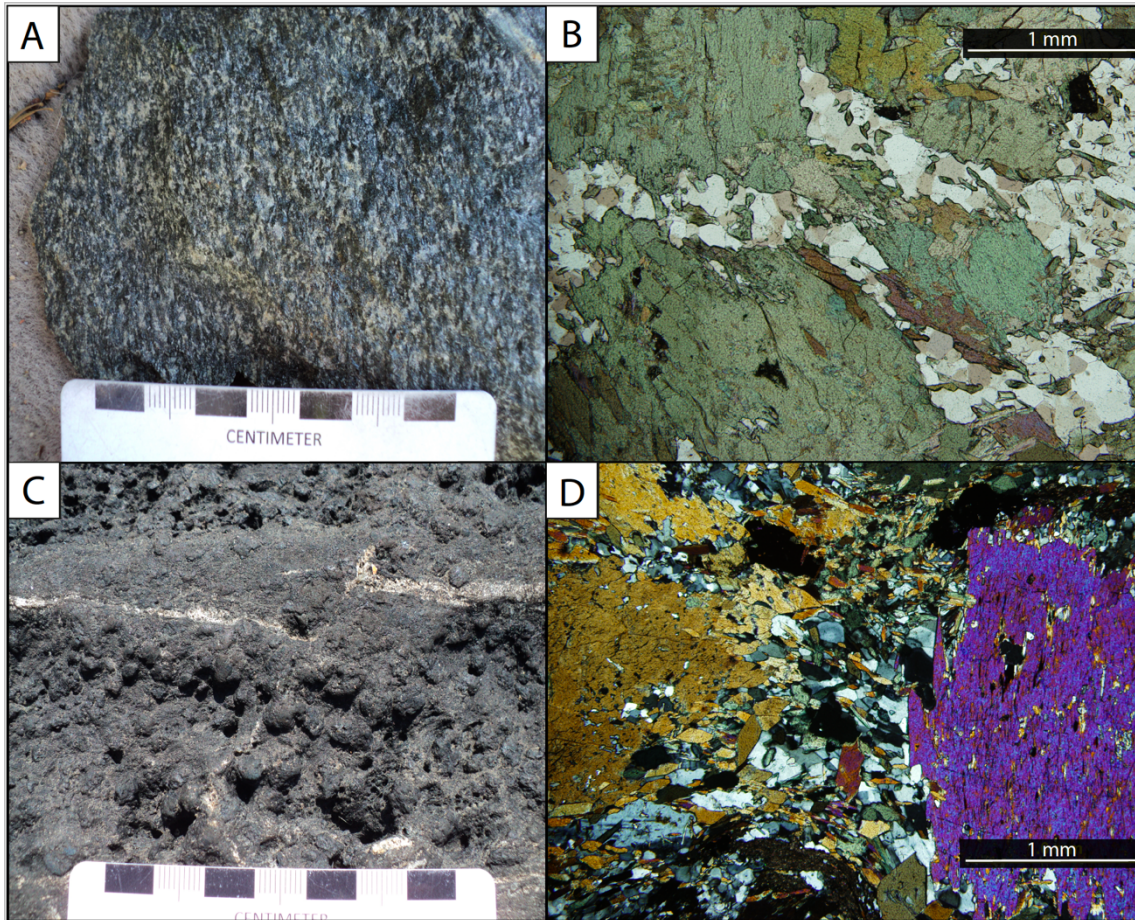


Figure 4.4. Field photos and photomicrographs of mafic to ultramafic intrusive units. A (Station 9/4 15U 374530 5466876): Gabbro with elongate grains in direction of regional foliation. B (LOW17CB61 15U 368042 5467038): Photomicrograph of coarse-grained secondary amphibole and minor medium-grained biotite in a groundmass of dominantly quartz. C (LOW17CB03 15U 375465 5467428): Intrusive unit with preferentially eroded matrix and knobby grains of pyroxene and/or secondary amphibole. D (LOW17CB06 15U 374872 5466791): Cumulate secondary medium-grained amphibole in a matrix of finer-grained secondary amphibole and quartz.

4.1.4 Felsic Intrusive Rocks

The granodiorites within the field area are white to grey, with minor pink, fine- to medium-grained inequigranular varieties (Fig. 4.5A). The groundmass is dominantly quartz and plagioclase with a combined modal abundance of 40 to 60%, and up to 10% subhedral, medium-grained potassium feldspar. Fine-grained biotite comprises approximately 15 to 20 modal% of the rock, and commonly defines a lineation with grains approximately 0.3 mm thick and 1 cm long (Fig. 4.5B;D). Weak sericite alteration occurs within the feldspar grains, occurring as fine-grained blades of sericite along cleavage planes.

The monzonites to quartz monzonites are dominantly inequigranular, medium-grained, grey and black rocks with rare pink varieties (Fig. 4.5C). The groundmass consists predominantly of biotite, likely replacing hornblende, and medium-grained plagioclase and potassium feldspar. Plagioclase grains are typically blocky 5 mm laths, although rare laths up to 8 mm long are present. Plagioclase comprises approximately 35 to 40 modal% of the groundmass. Potassium feldspar crystals are subhedral with an average length of 3 mm, and commonly rim the plagioclase crystals, with potassium feldspar comprising 25 to 35 modal% of the groundmass. The fine-grained biotite is typically interstitial to the feldspar.

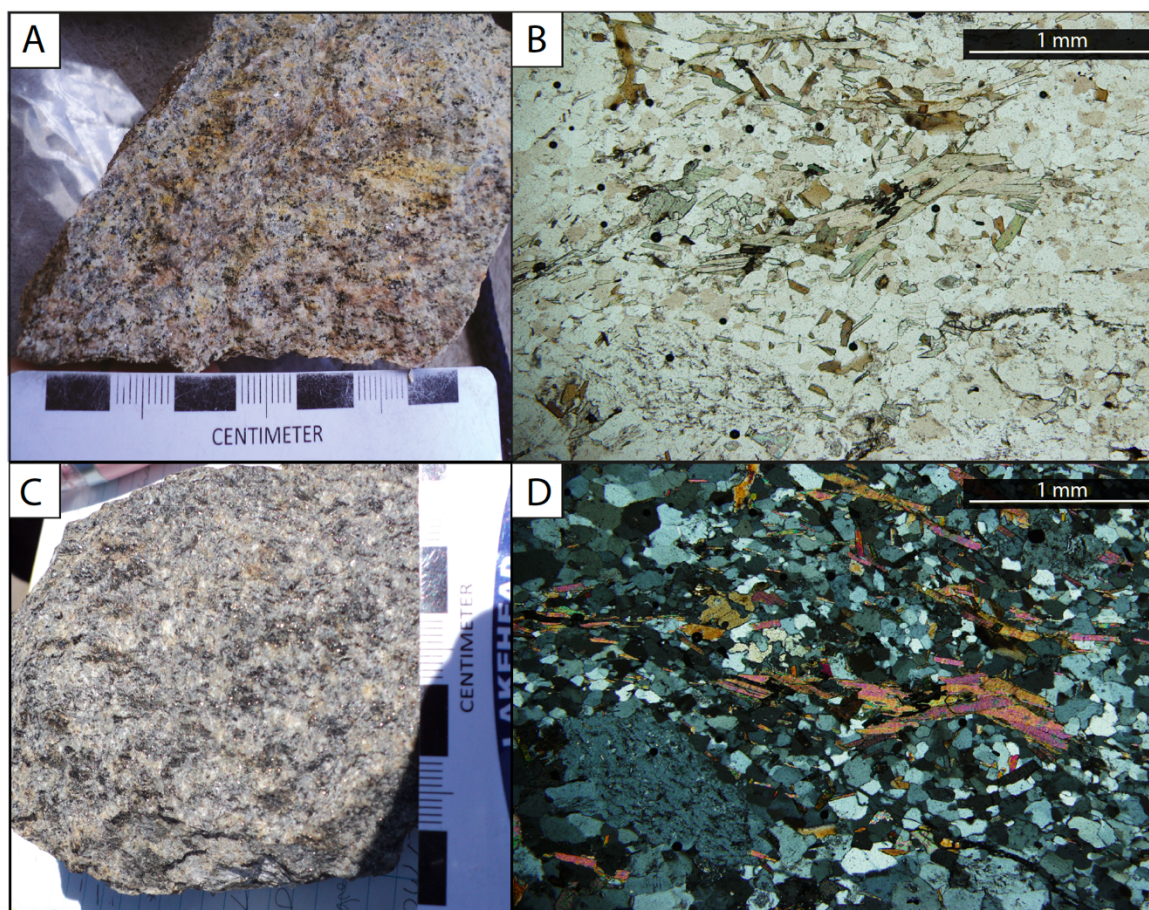


Figure 4.5. Field photos and photomicrographs of felsic intrusive units. A (Station 9/13 **15U 373345 5467041**): Medium-grained granite composed of plagioclase, potassium feldspar and quartz. B and D (**LOW17CB08 15U 374703 5466751**): Photomicrograph in transmitted light in plain polarized (B) and cross polarized (D) light. Groundmass consists of fine-grained quartz and plagioclase with fine to medium-grained potassium feldspar with weak sericite alteration. Biotite present as fine- to medium-grained laths. C (**LOW17CB08 15U 374703 5466751**): Medium-grained granodiorite composed of dominantly quartz and plagioclase with fine-grained biotite and muscovite.

4.1.5 Clastic Metasedimentary Rocks

The metasedimentary rocks in the Falcon Island map area consist of mudstones to siltstones. The rocks are commonly silicified and the intensity of foliation is quite varied. Biotite, when present, commonly defines a moderate foliation (Fig. 4.6A). Siltstones are fine- to very fine-grained and moderately siliceous (Fig. 4.6B). The unit is massive with no obvious bedding, however in one location, cross-bedding was observed at orientations of 27° and 35° to the original bedding of east-west in surrounding beds (Fig. 4.6C). When bedding was observed, it consisted of grey to red layers averaging 2 to 4 mm in width (Fig. 4.6D). Quartz grains often have rounded grain boundaries. Trace fine-grained pyrite is locally associated with the metasedimentary units.

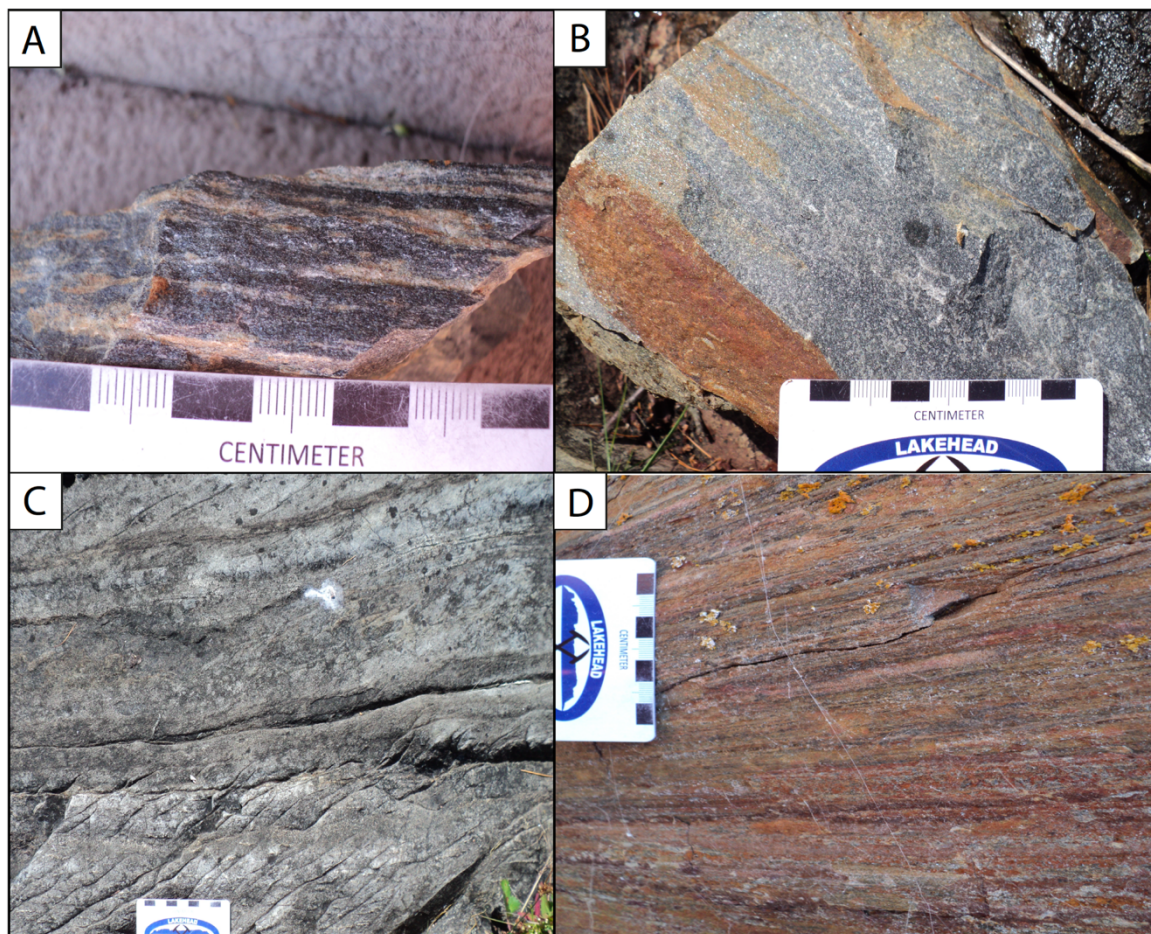


Figure 4.6. Field photographs of metasedimentary units. A (Station ISL/G1 **15U 368880 5465923**): Biotite schist with minor siliceous bands. B (OW17CB07 **15U 374865 5466786**): Grey fine-grained metasedimentary unit with weak to moderate silicification. C (Station ISL/I **15U 372514 5465838**): Metasedimentary unit showing cross-bedding at 27° to original bedding surface on upper contact and 35° to original bedding on lower contact. D (Station 5/12 **15U 370733 5465438**): Highly layered unit composed of red, black and grey beds.

4.1.6 Falcon Island Stock

The syenite intrusive rocks throughout the Falcon Island map area are black and pink, moderately equigranular, and vary from fine- to medium-grained (Fig. 4.7A). The syenites contain from 55 to 70 modal% potassium feldspar, often medium-grained, with minor fine-grained quartz \pm biotite (Fig. 4.7B). The samples also contained 20 to 40 modal% hornblende. A few samples had high mica content, with up to 15 modal% biotite and muscovite, whereas the majority of samples contained approximately 5 modal% biotite. Veinlets occur sporadically throughout the unit, consisting of aligned hornblende grains from 3 to 12 mm. Potassium feldspar is concentrated as halos to the veinlets and infilling gaps in the veinlets (Fig. 4.7C).

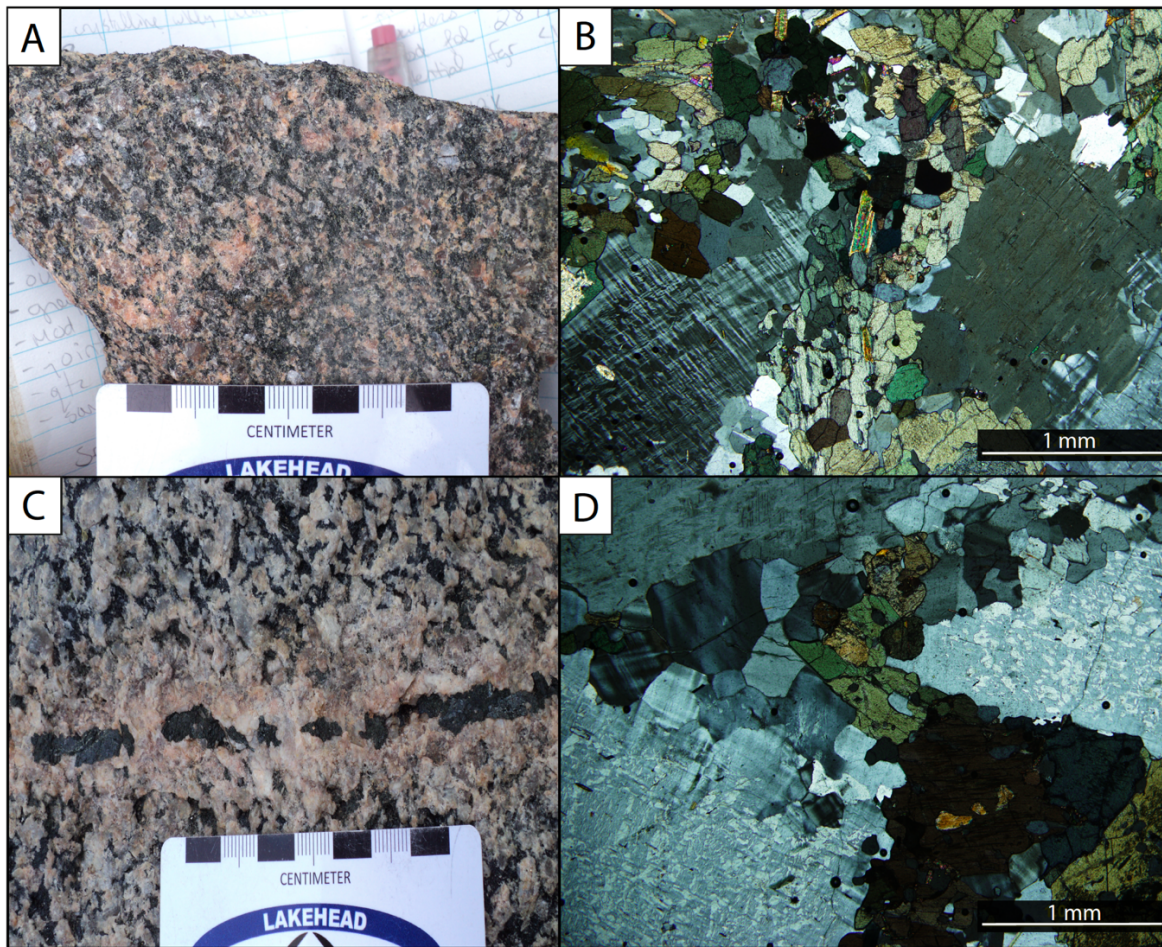


Figure 4.7. Field photos and photomicrographs of the Falcon Island stock. A (Station 12/6 15U 373008 5468534): Medium-grained amphibole syenite. B (LOW17CB31 15U 368412 5468343): Photomicrograph in transmitted cross polarized light with coarse-grained microcline and fine-grained amphibole and quartz. C (LOW17CB31 15U 368412 5468343): Medium-grained amphibole band within syenite unit with potassium feldspar along the rim. D (LOW17CB31 15U 368412 5468343): Photomicrograph in transmitted cross polarized light with coarse-grained microcline exhibiting perthitic exsolution and fine-grained amphibole and quartz occurring in the groundmass.

The unit is weakly deformed with deformation of microcline tartan twinning, quartz subgrain formation and undulatory extinction (Fig. 4.7B). Feldspars often had weak sericite alteration as well as hematite dusting. Microcline scattered throughout exhibited moderate perthitic exsolution (Fig. 4.7D).

4.1.7 Mafic Metavolcanic Rocks

Mafic metavolcanic flows comprise the majority of the Falcon Island map area. Flows are typically massive, aphanitic to fine-grained with varied degrees of chlorite alteration and weak silicification. The mafic metavolcanic rocks include dark grey to black, grey to light grey, and green tinted varieties. Rare occurrences of fine-grained subhedral pyrite occur disseminated throughout the flows in a few outcrops, which vary from amphibolites to schists.

Units that are dark grey to black may exhibit rare occurrences of east-west striking foliation in which biotite, when present, defines a weak foliation (Fig. 4.8A). Alteration present within this unit consists of weak to no silicification (Fig. 4.8B). Petrographic analysis of the dark metavolcanic rocks demonstrates a matrix of fine-grained quartz with minor plagioclase interstitial to medium- to fine-grained randomly oriented amphiboles that comprise approximately 60 modal% of the section (Fig. 4.9A). Amphiboles are typically poikilitic with fine-grained inclusions of quartz present throughout (Fig. 4.9B).

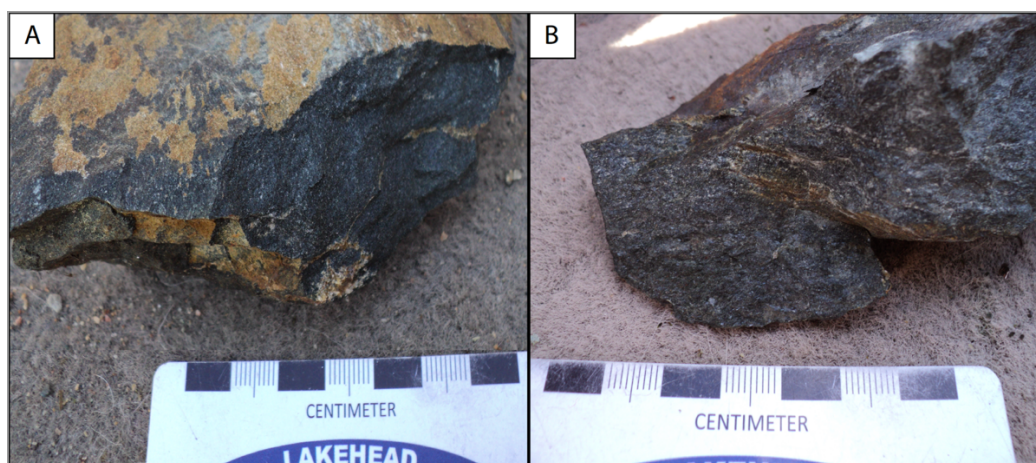


Figure 4.8. Field photographs of black to dark grey non-foliated mafic metavolcanic rocks. A (LOW17CB47 15U 366531 5467256): Very fine-grained black metavolcanic rock with weak to no silicification. B (LOW17CB81 15U 372919 5467356): Very fine-grained dark grey metavolcanic rock with weak to moderate silicification.

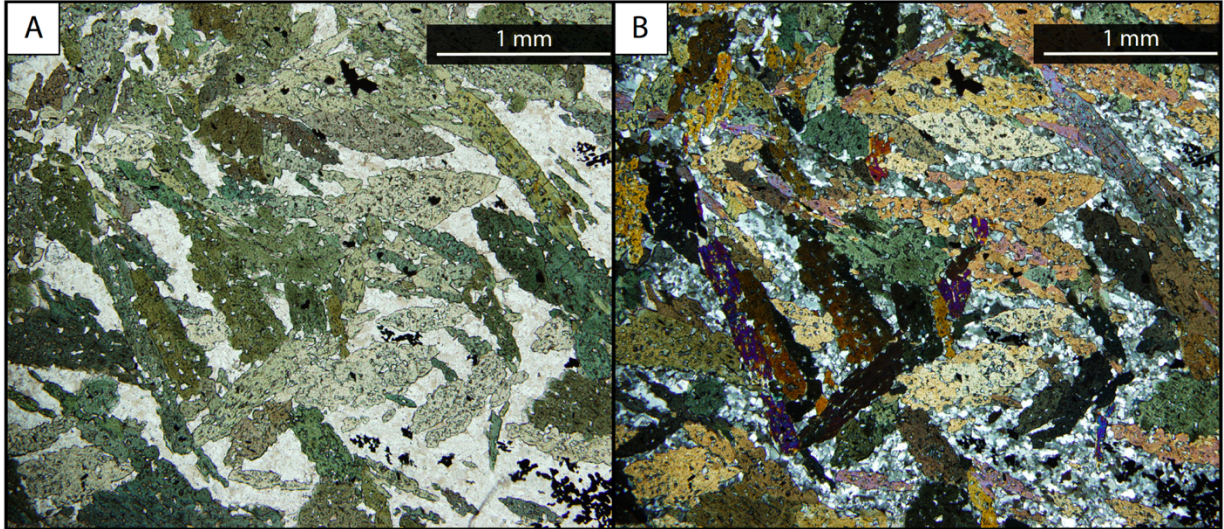


Figure 4.9. Photomicrographs in transmitted light of black to dark grey mafic metavolcanic rocks of sample LOW17CB48 (15U 367863 5466684). A: Plain-polarized light photomicrograph consisting of up to 60% randomly oriented amphibole laths. B: Cross-polarized light photomicrograph of poikiloblastic actinolite with trace tremolite within a quartz dominated groundmass.

Light grey to grey units are typically devoid of foliation and exhibit weak to moderate silicification (Fig. 4.10A). Greater degrees of silicification create the lighter grey appearance of the units (Fig. 4.10B). The samples contain either fine-grained subhedral amphibole present within a quartz dominated matrix or randomly oriented acicular to bladed amphibole grains within a quartz dominated matrix (Fig. 4.11).

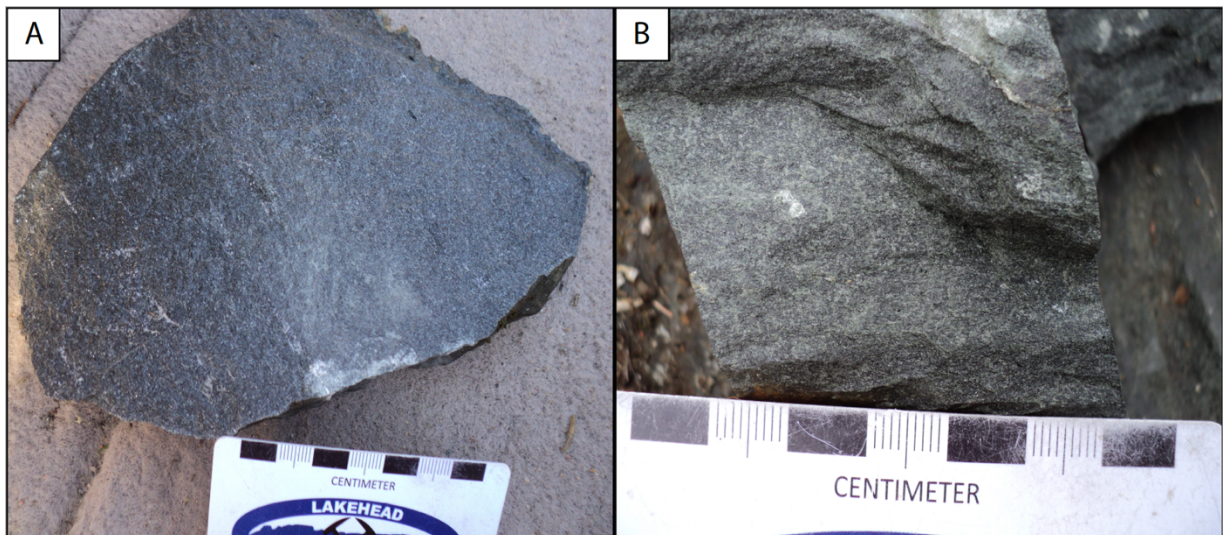


Figure 4.10. Field photographs of light grey to grey non-foliated metavolcanic rocks. A (LOW17CB48 15U 367863 5466684): Massive, grey very fine-grained metavolcanic rock. B (LOW17CB94 15U 375983 5466692): Very fine-grained light grey, moderately siliceous metavolcanic rock.

The fine-grained samples typically contain approximately 50 modal% subhedral actinolitic amphibole with the remaining mass of the rock composed of quartz, with minor plagioclase and opaque minerals (Fig. 4.11A). Fine-grained plagioclase shows rare polysynthetic twinning, with minor pinching of the twins in some grains. Plagioclase grains occur interstitial to amphibole grains and are often void of polysynthetic twinning (Fig. 4.11B). Quartz comprises less than 5 modal% of the groundmass.

The units with medium-grained, randomly oriented, amphibole blades contain approximately 60 modal% amphibole with the remaining rock mass consisting of a groundmass dominated by quartz and subhedral fine-grained amphibole as well as minor plagioclase and biotite (Fig. 4.11C). Amphibole within the unit consists dominantly of hornblende with minor tremolite (Fig. 4.11D).

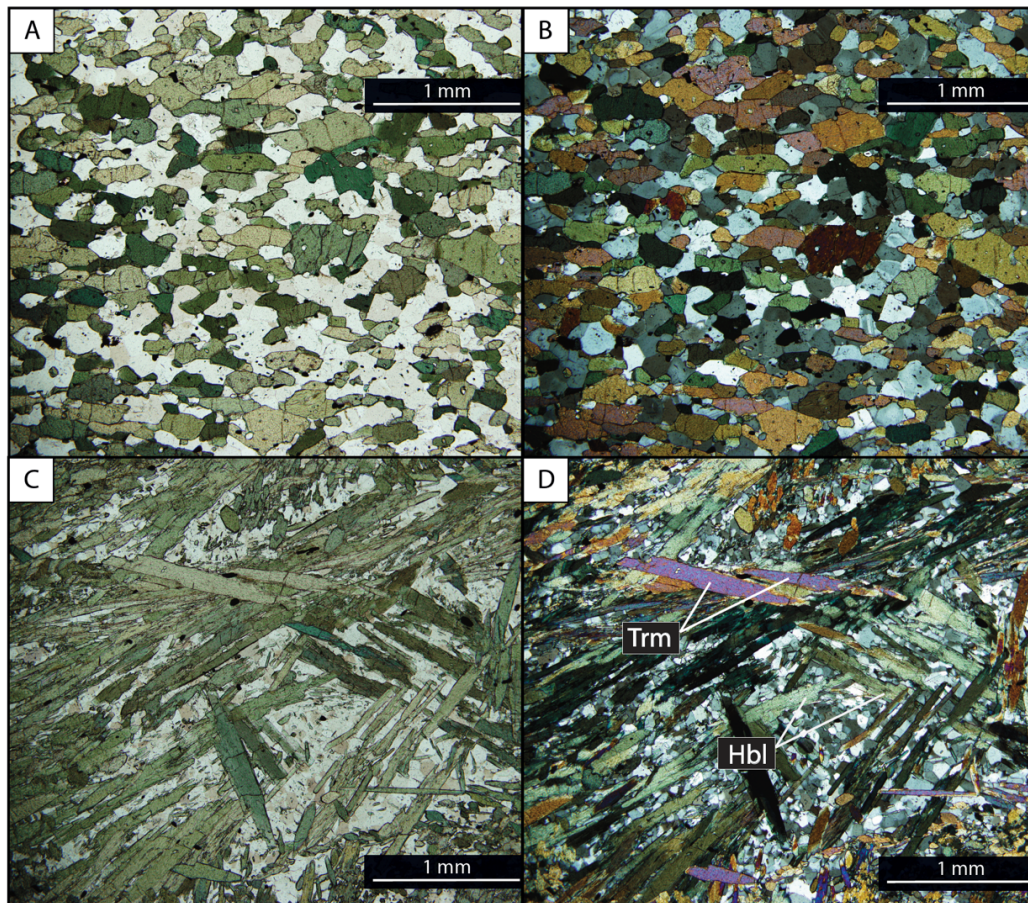


Figure 4.11. Photomicrographs in transmitted light of grey to light grey metavolcanic rocks. A (LOW17CB34 15U 367218 5467948): Plain-polarized light photo of subhedral amphibole grains. B (LOW17CB34 15U 367218 5467948): Cross-polarized light photo of C (LOW17CB63 15U 369333 5466535): Plain-polarized light photo of randomly oriented amphibole laths with minor cross-sectional views demonstrated as hexagonal crystals. D (LOW17CB63 15U 369333 5466535): Cross-polarized light photo of actinolite and trace tremolite blades with a quartz dominated groundmass. **Trm**: tremolite. **Hbl**: hornblende.

Mafic metavolcanic rocks in the area also consist of grey to grey-greenish units with varying degrees of foliation (Fig. 4.12A). The grey-greenish samples are commonly moderately foliated with amphibole and chlorite defining the foliation (Fig. 4.12B). Fine-grained blades of amphibole are weakly aligned within a fine- to very fine-grained groundmass (Fig. 4.12C). The groundmass contains a combination of amphibole, chlorite and very minor quartz (Fig. 4.12D). The unit consists of tremolite-chlorite amphibolites as well as tremolite-chlorite schists.

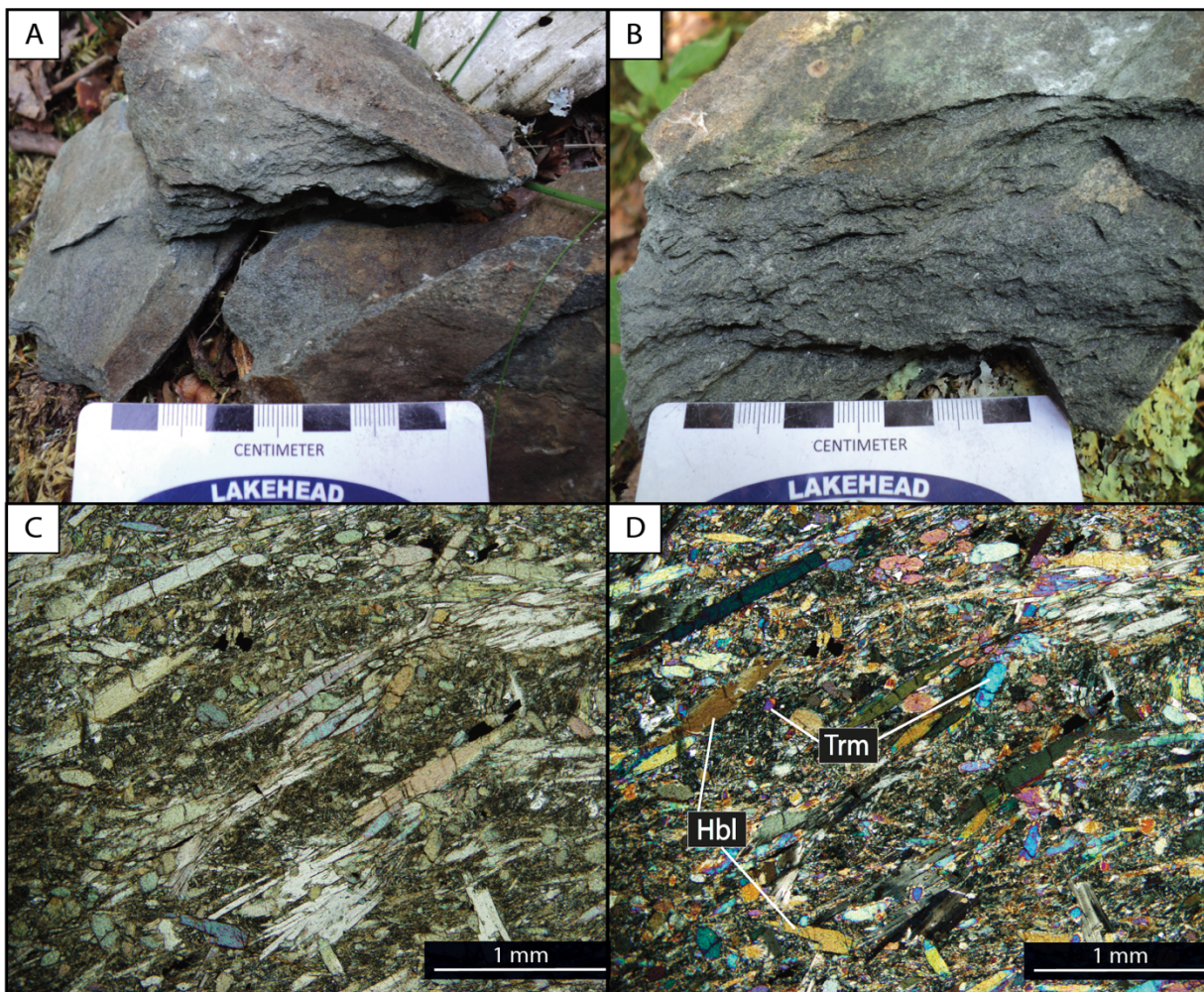


Figure 4.12. Field photos and photomicrographs of grey to dark green foliated metavolcanic rocks. A (LOW17CB41 15U 367718 5467404): Grey with green tint, very fine-grained, highly foliated mafic rock. B (LOW17CB59 15U 369175 5467749): Dark grey to green highly foliated, very fine-grained mafic rock. C (LOW17CB87 15U 370606 5466078): Amphibole blades and clusters within a very fine-grained groundmass. D (LOW17CB87 15U 370606 5466078): Amphibole consists of hornblende and minor tremolite. **Trm**: Tremolite. **Hbl**: Hornblende.

4.1.8 Ultramafic Metavolcanic Rocks

Ultramafic metavolcanic rocks are fine-grained, sometimes aphanitic, and are commonly grey with varied degrees of chlorite alteration creating a green tint (Fig. 4.13A). Rare varieties exhibited talc alteration, resulting in a lighter grey appearance and red staining along foliation planes and/or fracture planes (Fig. 4.13B).

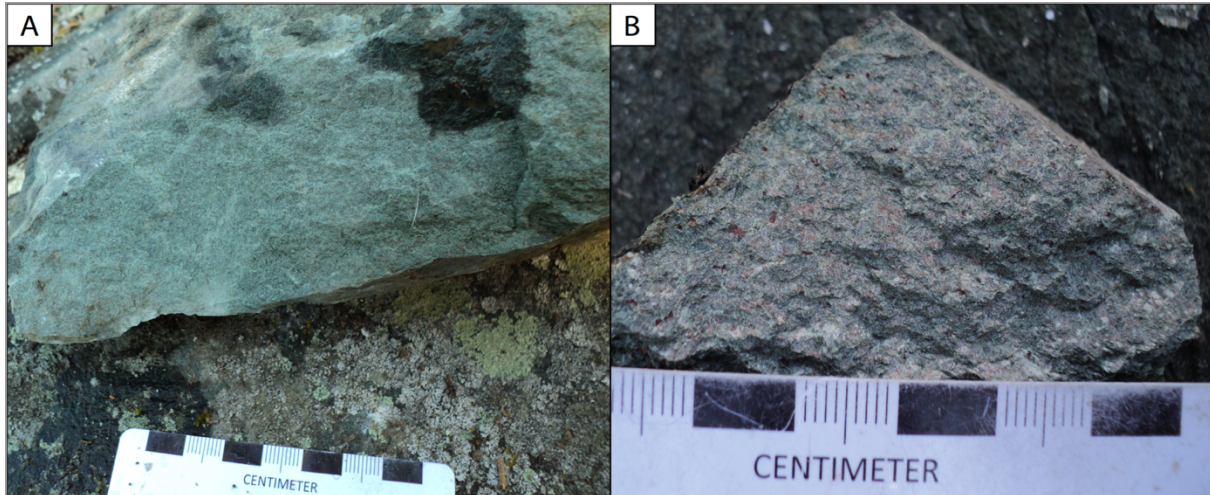


Figure 4.13. Field photographs of grey to dark green foliated ultramafic metavolcanic rocks. A (LOW17CB19 15U 368614 5467778): Pervasive chlorite creates deep green color and moderate foliation. B (LOW17CB92 15U 368861 5465424): Talc alteration with red staining along strong foliation planes.

Samples present within this unit often contained amphibole crystals that are rarely in the same orientation as the main fabric (Fig. 4.14A). The blades are approximately 1 to 3 mm long and commonly 1 mm thick. Polyhedral jointing was observed in very few exposures of ultramafic rocks, with polygonal joints 10 to 30 cm in width (Fig. 4.14B).

The ultramafic rocks are dominated by a combination of very fine- to fine-grained amphibole and a matrix composed of chlorite or lesser serpentine, with rare samples containing talc throughout the matrix. The groundmass is commonly very fine-grained with brown to beige color in plain polarized light (Fig. 4.15A). Needles observed in thin section consist of tremolite and anthophyllite, and are randomly oriented, cross-cutting the dominant foliation (Fig. 4.15B). Samples without a pervasive foliation demonstrate a randomly oriented arrangement of amphibole grains with fine-grained ilmenite scattered throughout (Fig. 4.15C). Sections cut perpendicular to the long axis of the crystals demonstrate a hexagonal habit (Fig. 4.15D). In rare cases, medium-grained serpentine clusters in a linear form following the orientation of foliation. The ultramafic metavolcanic

unit consists of a variety of rocks including talc-tremolite-chlorite schists, tremolite-chlorite schists, and tremolite-serpentine-chlorite schists.

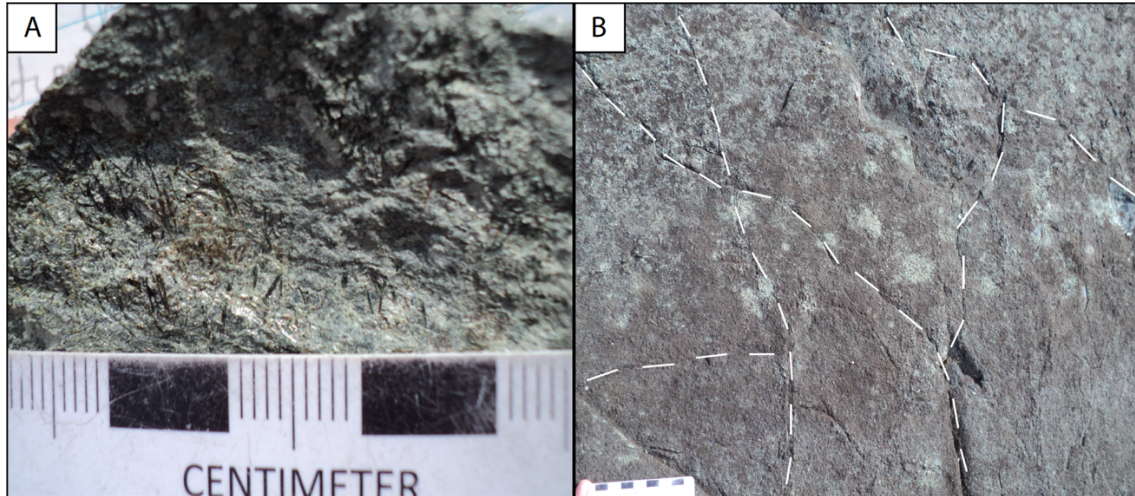


Figure 4.14. Field photographs of ultramafic metavolcanic rocks. A (LOW17CB83 15U 373108 5467542): Randomly oriented amphibole grains oblique to the foliation defined by chlorite. B (LOW17CB83 15U 373108 5467542): Polyhedrally jointed surface of an ultramafic outcrop.

4.2 Cliff Island Stratigraphy

Mapping of Cliff Island and proximal islands occurred in the summer of 2018 with 50 samples taken over 238 stations. The mapping area consisted of the elongate irregular Cliff Island that is 9 km long with a range of widths, resulting in an approximate surface area of 12 km². Smaller islands were mapped surrounding Cliff Island, including Calendar Island to the west. Calendar Island is 2 by 0.6 km with a resulting surface area of 1.2 km².

The field area consisted of fine-grained intermediate to ultramafic metavolcanic rocks with pervasive east-west striking schistosity (Fig. 4.16). The average dip observed in the intermediate to mafic metavolcanic rocks is 86° dominantly towards the south, whereas the mafic to ultramafic rocks demonstrated an average dip of 80° and dipped to both the north and the south. When present, biotite displayed a west to southwest lineation with dips of 80°SW to 86°SW. Minor components in the field area included clastic metasedimentary rocks, mafic intrusive rocks, felsic to intermediate metavolcanic rocks, and a diabase dyke. When metavolcanic units occur as bedded tuffs, the schistosity follows the strike of the bedding.

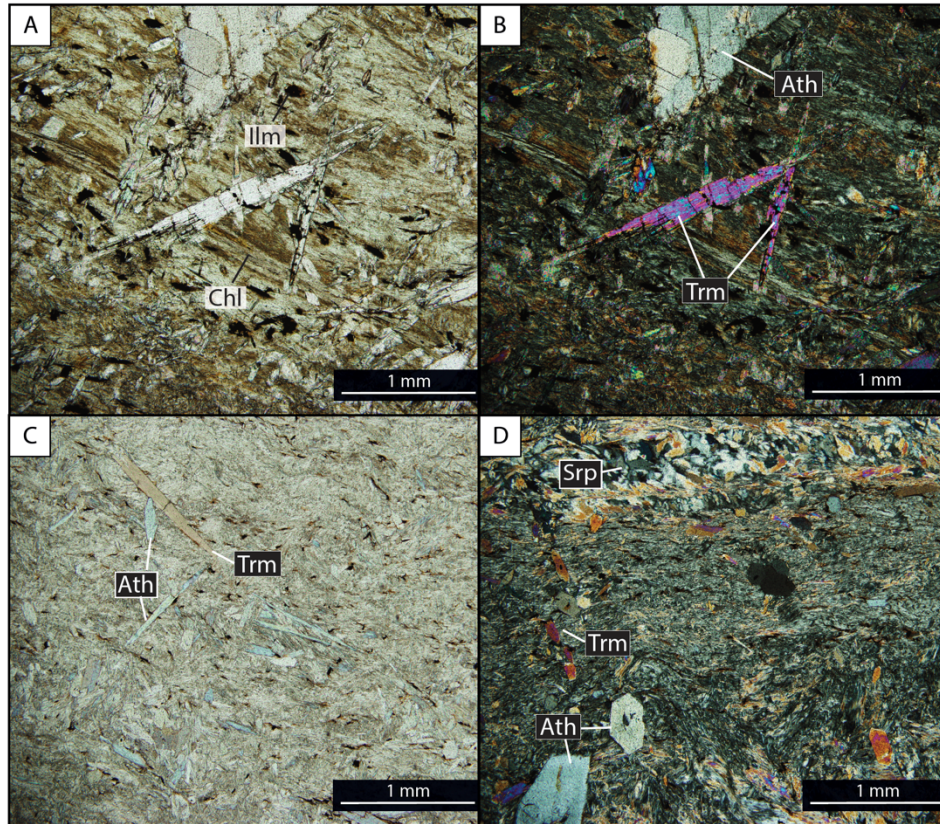


Figure 4.15. Photomicrographs of ultramafic metavolcanic rocks. A (LOW17CB79 15U 373647 5466898): Very fine-grained groundmass composed of chlorite with dispersed fine-grained slightly rounded ilmenite grains. B (LOW17CB79 15U 373647 5466898): Tremolite blade cross-cutting foliation defined by chlorite. C (LOW17CB83 15U 373108 5467542): Hexagonal amphibole grains dispersed throughout with rare subhedral and bladed varieties. D (LOW17CB83 15U 373108 5467542): Tremolite and anthophyllite within a chlorite dominated groundmass, with clusters of serpentine occurring in linear masses. **Ath:** Anthophyllite. **Trm:** Tremolite. **Ilm:** Ilmenite. **Chl:** Chlorite. **Srp:** Serpentine.

Direct contacts in the field area were commonly observed between the intermediate metavolcanic and felsic porphyritic rocks occurring in the northern part of the field area. The average orientation of these contacts is $253^{\circ}/80^{\circ}$, dipping to the north. Contacts were also observed between the mafic to ultramafic metavolcanic rocks and the granodiorite intrusion. Contacts observed on the northern most portion of the felsic intrusion exhibit a strike of $\sim 264^{\circ}$, with near vertical dips ranging from 84° to 86° . Granodiorite to diorite dykes often occur as narrow intrusions into mafic metavolcanic rocks at a common orientation of $128^{\circ}/76^{\circ}$.

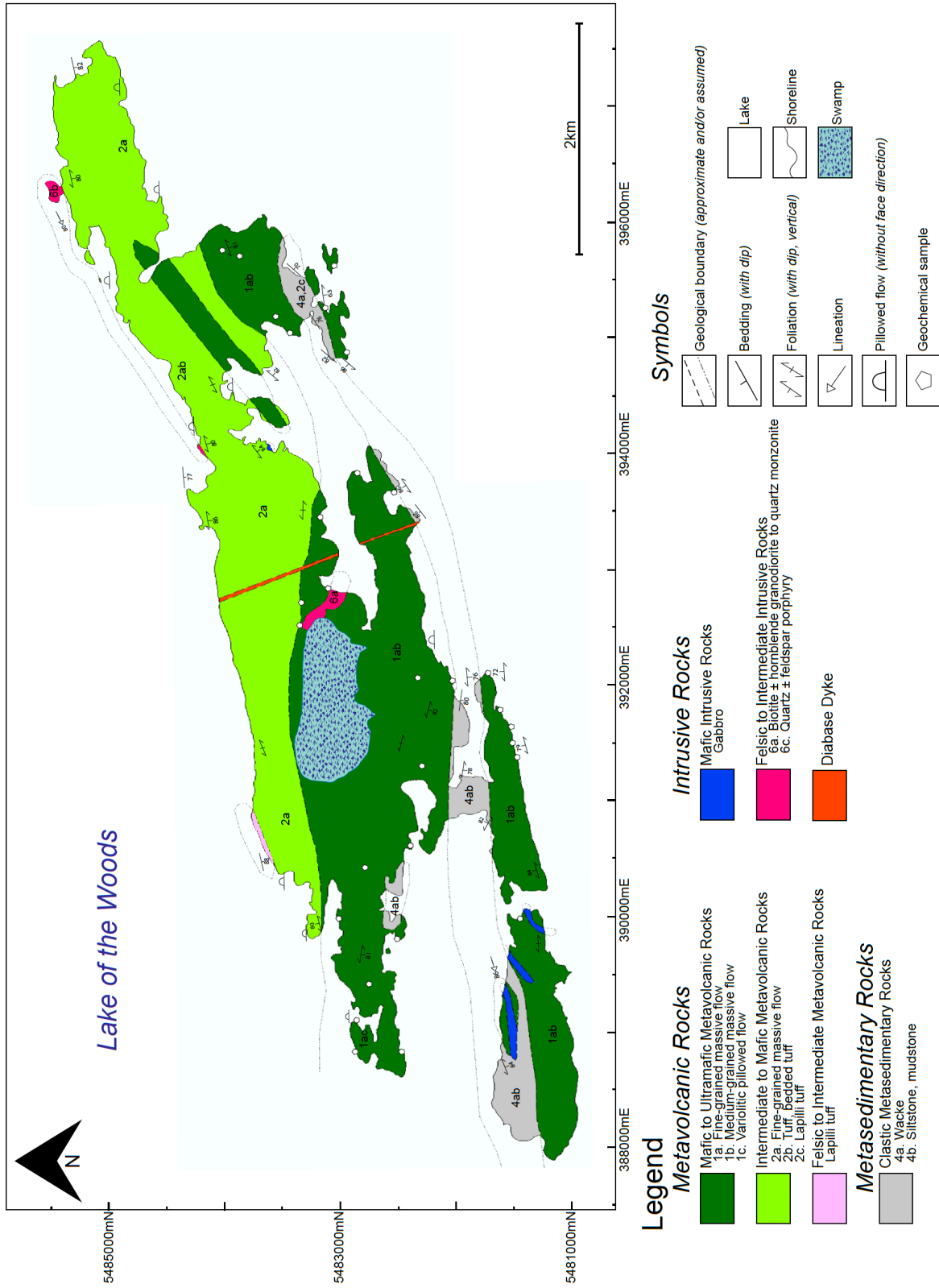


Figure 4.16. Geological map of Cliff Island completed in 2018. The UTM co-ordinates are provided in Zone 15 using NAD83.

4.2.1 Felsic Metavolcanic Rocks

The felsic metavolcanic rocks comprise only a small portion of the Cliff Island map area, where a lapilli tuff unit was identified. The tuff is grey to white, fine-grained, siliceous and is quartz and feldspar phyrlic (Fig. 4.17A). The matrix is composed of quartz and feldspar with angular to subangular clasts (Fig. 4.17B). The clasts range in size from 3 cm to 35 cm, with larger clasts being more angular. The quartz and feldspar subhedral grains within the lapilli clasts range in size from 1 to 3 mm wide, with phenocrysts comprising up to 60 volume % of the clasts.



Figure 4.17. Field photographs of felsic metavolcanic units. A (Station 7/11 15U 390582 5483661): Highly siliceous felsic metavolcanic host rock. B (Station 7/10 15U 390409 5483531): Felsic lapilli tuff with clasts up to 15 cm long.

4.2.2 Intermediate to Mafic Metavolcanic Rocks

The intermediate metavolcanic rocks in the Cliff Island map area are commonly massive to layered flows and pillowed, with rare occurrences of a pyroclastic lapilli tuff occurring with clastic metasedimentary rocks. The massive flows are grey to light grey, fine-grained, moderately siliceous and include rare quartz-phyric units. In layered flows, recognizable beds are differentiated by lighter grey more siliceous layers and mafic layers indicated by a green tint reflecting chlorite alteration (Fig. 4.18A). These sequences demonstrate an alternating light grey and green layering that also hosts minor 1 to 3 mm vesicles dispersed throughout. The vesicles comprise approximately 5 modal% of the outcrop. Weak to moderate foliation is present throughout the area; however, foliation is

seen more prominently in layered flow units. Pillowed flows range in size with some outcrops consisting of pillows 10 to 30 cm across and other outcrops consisting of pillows 70 cm to 1 m in length (Fig. 4.18B). Selvages are consistently 1 to 5 mm throughout the field area and are commonly thicker on the north and south side of the pillows.

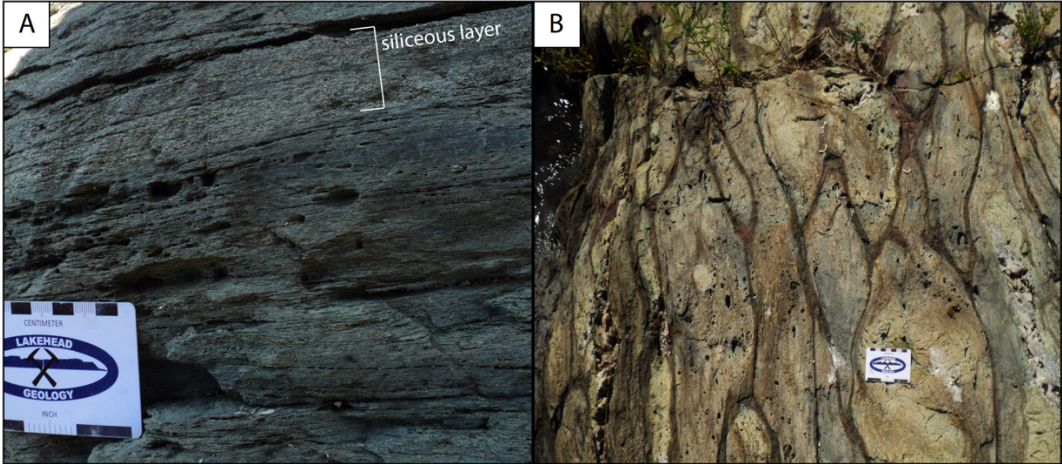


Figure 4.18. Field photographs of intermediate metavolcanic units. A (Station 7/5 15U 389685 5483098): Layered flow with siliceous layers averaging 5 cm wide and chloritic layers up to 30 cm wide. B (Station 7/24 15U 395608 5484997): Irregular pillowed flow with pillows from 7 cm to 30 cm wide and up to 1 m long with selvages of 1 to 5 cm.

The intermediate lapilli tuff unit has an aphyric grey matrix with angular to subangular feldspar phyrlic clasts. The matrix consists of feldspar and quartz. The clasts range in size from 1 to 3 mm consisting of subhedral feldspar grains. The tuffaceous layer is in contact with layered clastic metasedimentary rocks, in which the contact is sharp and irregular (Fig. 4.19).



Figure 4.19. Field photograph of the contact between a layered sedimentary horizon and an intermediate pyroclastic unit (Station 2/2 15U 395107 5483041).

The unit comprises feldspar, and minor quartz, phenocrysts within a groundmass dominated by fine-grained quartz, feldspar, biotite, and epidote (Fig. 4.20A). Fine-grained biotite laths define a weak foliation and often bend around coarse phenocrysts. Plagioclase and quartz phenocrysts typically host weak hematite dusting, whereas grains within the groundmass are generally free of alteration. Alteration of plagioclase grains consists of fine-grained sericite blades concentrated along cleavage planes, as well as fine-grained subhedral calcite and epidote (Fig. 4.20B). Fine- to medium-grained epidote occurs throughout the groundmass as sub- to euhedral crystals.

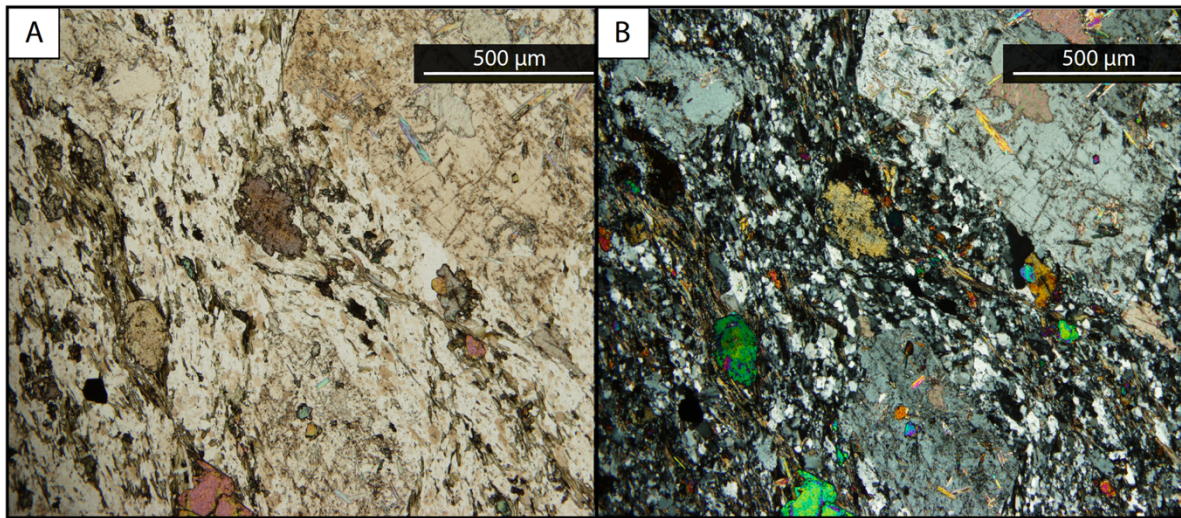


Figure 4.20. Photomicrograph in transmitted light of intermediate tuffaceous unit (Station 2/2 15U 395107 5483041). A: Plain-polarized photomicrograph demonstrating epidote associated with biotite in the groundmass while biotite defines a weak foliation. B: Cross-polarized photomicrograph demonstrating sericite, calcite, and epidote alteration of plagioclase grains.

4.2.3 Mafic Intrusive Rocks

The gabbroic unit in the study area occurs on the neighbouring Calendar island approximately 200m from Cliff Island, with only a trace occurrence on the main island. The gabbro is medium-grained and grey, with weak foliation due to the elongation of pyroxene grains (Fig. 4.21A). The unit is pyroxene and/or amphibole phyric with crystals up to 3 mm long and commonly 2 mm wide. Plagioclase laths comprise up to 40 modal% of the gabbro, and are typically 3mm long. Alteration consists of weak silicification and moderate chloritization. One locality displayed a random orientation of amphibole grains 3 mm long with rare grains up to 7 mm long that were typically bladed to lath-like with rare elongated rhombohedral grains (Fig. 4.21B).

The gabbroic units were dominated by actinolite and hornblende occurring as medium-grained bladed to lath-like crystals as well as thin needles randomly oriented within the groundmass (Fig. 4.22A). Hornblende grains commonly have simple twinning (Fig. 4.23B). The groundmass is composed of fine- to very fine-grained plagioclase and chlorite with minor quartz.

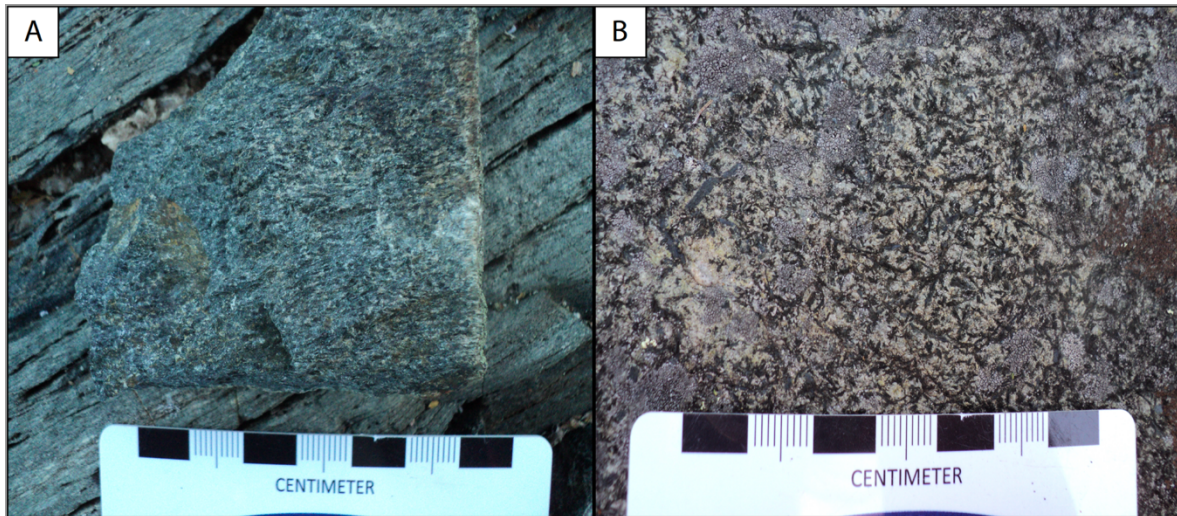


Figure 4.21. Field photographs of mafic intrusive rocks. A (Station 1/12 15U 389985 5481252): Fine-grained gabbro with dark slightly elongated pyroxene grains from 2 to 4 mm long in a plagioclase dominated groundmass. B (LOW18CB07 15U 395275 5482805): Surface of a gabbroic unit with randomly oriented amphibole blades up to 7 mm long.

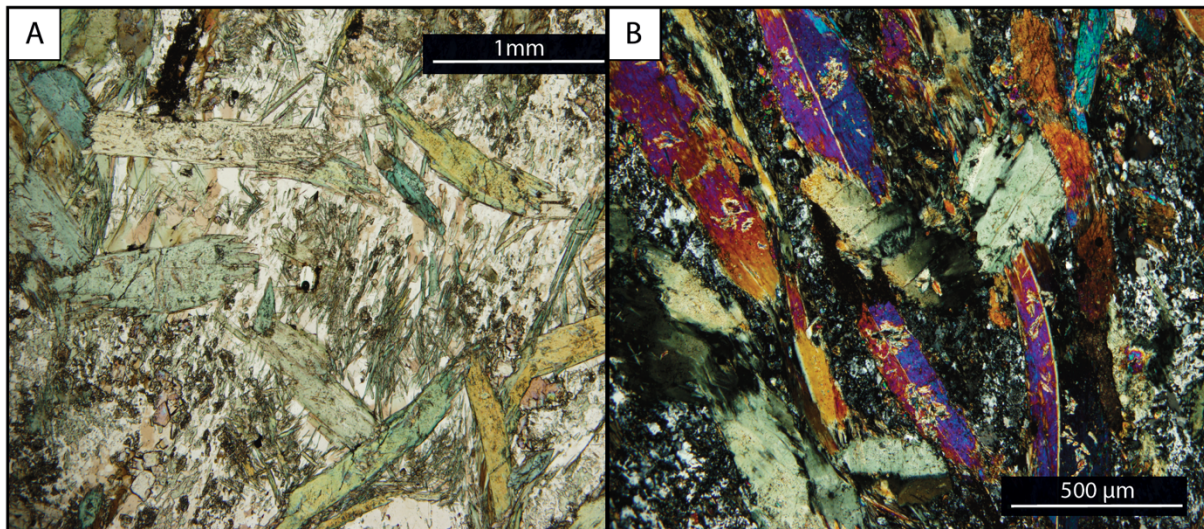


Figure 4.22. Photomicrograph in transmitted light of gabbroic unit (LOW18CB07 15U 395275 5482805). A: Subhedral medium-grained amphibole phenocrysts scattered throughout, as well as fine-grained acicular amphibole occurring in clusters within the groundmass. B: Subhedral amphibole occur within a groundmass dominated by fine- to very fine-grained plagioclase and quartz. These grains often display simple twinning.

4.2.4 Felsic Intrusive Rocks

The biotite granodiorites to quartz monzodiorite are dominantly inequigranular, medium-grained, grey to white and black rocks with rare pink varieties. The groundmass consists dominantly of quartz, plagioclase, biotite with minor potassium feldspar (Fig. 4.23A). Quartz and feldspar grains are often 3-5 mm in width with 1-2 mm interstitial biotite grains between the feldspar phases. Plagioclase grains are rarely seen as blocky laths, however when present they are approximately 3 mm long. Quartz and plagioclase combined comprise 60 to 70 modal% of the rock, with biotite and potassium feldspar both typically composing 10 % of the modal abundance each, with rare samples containing up to 15 modal% potassium feldspar. Biotite often defines a weak lineation.

Along the margins between the granodiorite to monzodiorite and the mafic to ultramafic metavolcanic rocks, there is concentrated potassium feldspar, in which potassium feldspar comprises approximately 60 modal% of the rock (Fig. 4.23B). Biotite in these areas remains consistent at approximately 10 modal% and 2 mm in width. The intrusion of the granodiorite to monzodiorite weakly brecciated the surrounding host rock. This results in angular fragments of host material up to 50 cm in width occurring within the felsic intrusive body (Fig. 4.23C).

The feldspar grains are weakly to moderately altered by sericite, calcite and epidote. Deformation of microcline grains is demonstrated by the pinching of tartan twins (Fig. 4.23D). Minor medium-grained biotite grains are often associated with zoisite. Biotite commonly hosts fine-grained zircon that produces narrow radiation halos. The groundmass is composed of fine-grained quartz with fine-grained amphibole, clinozoisite, and minor feldspars scattered throughout. Trace fine-grained euhedral titanite occurs throughout (Fig. 4.23E). Plagioclase is often weakly sericitized (Fig. 4.23F).

A felsic porphyritic unit occurs to the north of the field area as rare thin layers no greater than 75 cm within the intermediate metavolcanic units. The contact between the two units is consistently oriented at approximately $280^{\circ}/80^{\circ}$ (Fig. 4.24A). Feldspar and biotite phenocrysts occur in a very fine-grained grey groundmass of quartz (Fig. 4.24B). Phenocrysts of plagioclase and potassium feldspar are approximately 2 to 3 mm in width and biotite grains are dominantly 1 mm in width. Plagioclase feldspar grains are commonly concentrically zoned and demonstrate weak sericite alteration (Fig. 4.24C).

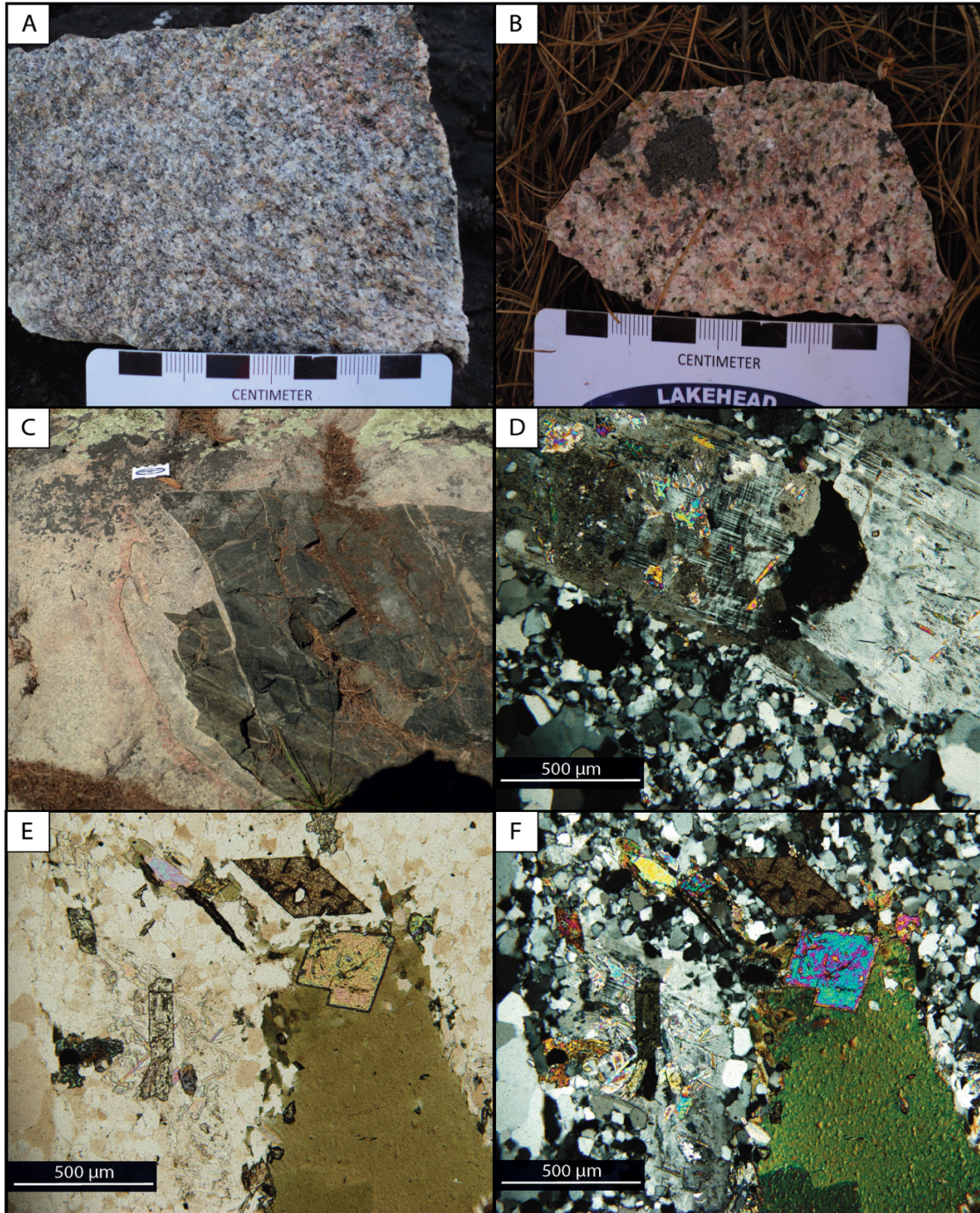


Figure 4.23. Field photos and photomicrographs of felsic intrusive samples. A (Station 3/7 15U 390302 5482583): Granodiorite sample consisting of fine- to medium-grained quartz, plagioclase and minor potassium feldspar and biotite. B (LOW18CB18 15U 392866 5483032): Highly potassic sample residing near the contact between the granodiorite and surrounding mafic metavolcanic rocks. C (LOW18CB18 15U 392866 5483032): Brecciated mafic host rock up to 50cm wide within felsic intrusion. D (LOW18CB18 15U 392866 5483032): Cross-polarized transmitted light photo of feldspar phenocrysts within a fine-grained quartz groundmass that demonstrate weak sericite and epidote alteration. Microcline demonstrates slight pinching of tartan twins. E (LOW18CB18 15U 392866 5483032): Plain-polarized transmitted light photo of a fine-grained euhedral titanite grain, medium-grained biotite, and fine-grained euhedral zoisite and clinozoisite. F (LOW18CB18 15U 392866 5483032): Groundmass consists dominantly of quartz subgrains with minor fine-grained sericite alteration of plagioclase.

Some grains demonstrate a disruption in zoning by the brittle fracturing of the grains (Fig. 4.24D). Feldspar phenocrysts constitute approximately 15 modal% whereas biotite occurs scattered throughout the groundmass at approximately 5 modal%.



Figure 4.24. Field photos and photomicrographs of porphyritic felsic unit (Station 2/16 15U 395816 5484204). A: Sharp contact between the porphyritic unit and surrounding intermediate metavolcanic rocks. B: Minor potassium feldspar, plagioclase, and biotite phenocrysts within a very fine-grained grey quartz matrix. C: Concentrically zoned plagioclase feldspar phenocryst within a very fine-grained groundmass of quartz, minor feldspar and opaque minerals. Feldspar grains demonstrate weak sericite and calcite alteration. D: Fracturing of feldspar phenocryst shows disruption of zoning.

4.2.5 Clastic Metasedimentary Rocks

The metasedimentary rocks in the area consist of turbiditic siltstones to sandstones with observable bedding occurring in rare outcrops. Bedding, when present, typically demonstrates gradational textures with a basal sandstone layer and upper mud-rich shale layer (Fig. 4.25A). In rare cases the mud-rich layers occur on a millimetre scale and sand-rich layers dominate the unit (Fig. 4.25B). The rocks are commonly moderately siliceous and a

lighter grey relative to units with lesser silicification. Fine-grained biotite, when present, often defines the foliation and occurs as blades up to 3 mm long and approximately 1 mm wide. Trace fine-grained pyrite mineralization is locally associated with mudstones and siltstones with lesser silicification.

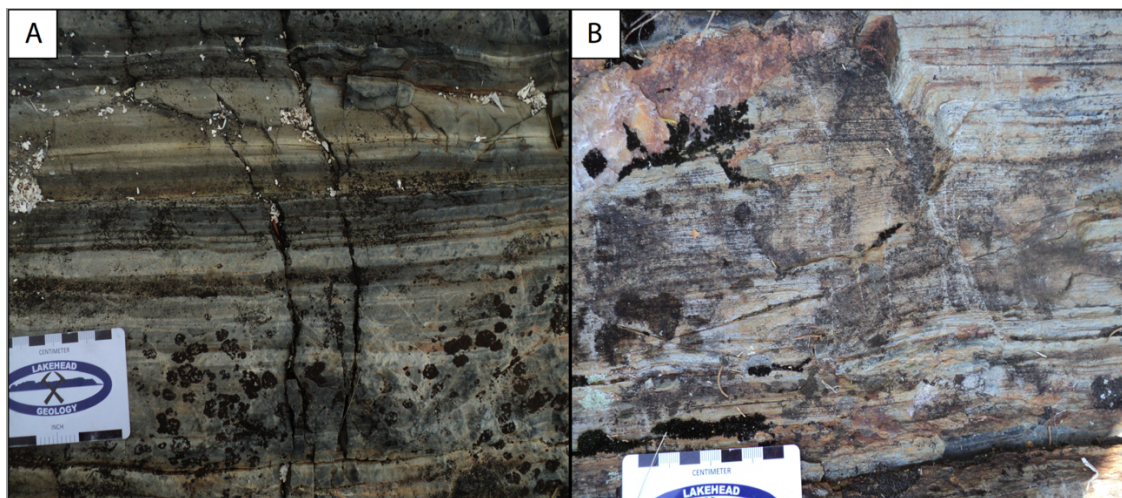


Figure 4.25. Field photographs of clastic sedimentary rocks. A (Station 5/5 15U 391860 5481902): Gradational bedding from sand-rich basal layer to mud-rich top layer. B (Station 2/10 15U 395602 5483272): Sandstone dominated unit with thin <1 mm mud-rich layers.

4.2.6 Mafic Metavolcanic Rocks

Mafic metavolcanic flows comprise the majority of the Cliff Island map area. Flows are typically massive, very fine-grained and grey; however, pillows were observed at three occurrences within the field area. Massive flows are dark grey, aphanitic to fine-grained with weak chlorite and silicification present (Fig. 4.26A). Foliation in the mafic metavolcanic rocks ranges from weak to moderate, with fine-grained biotite and chlorite commonly defining foliation (Fig. 4.26B).

Pillows range in size from 30 cm to 1.2 m long and 20 cm to 70 cm in width with 2 to 4 cm selvages surrounding the pillows. Pillowed flows were typically aphyric, however, rare outcrops displayed variolitic pillows with an abundance of varioles concentrated towards the interior of the pillow and dissipated towards the selvages (Fig. 4.27A). These varioles are elongated in an east-west direction, and are typically rounded and 1 to 4 mm in length. Selvages are commonly irregular and often thicker on the northern and southern sides of the pillows, possibly the result of compression. The direction in which the pillows faced was

generally inconclusive due to deformation and poor exposure; however, one outcrop demonstrated a southward facing direction (Fig. 4.27B).

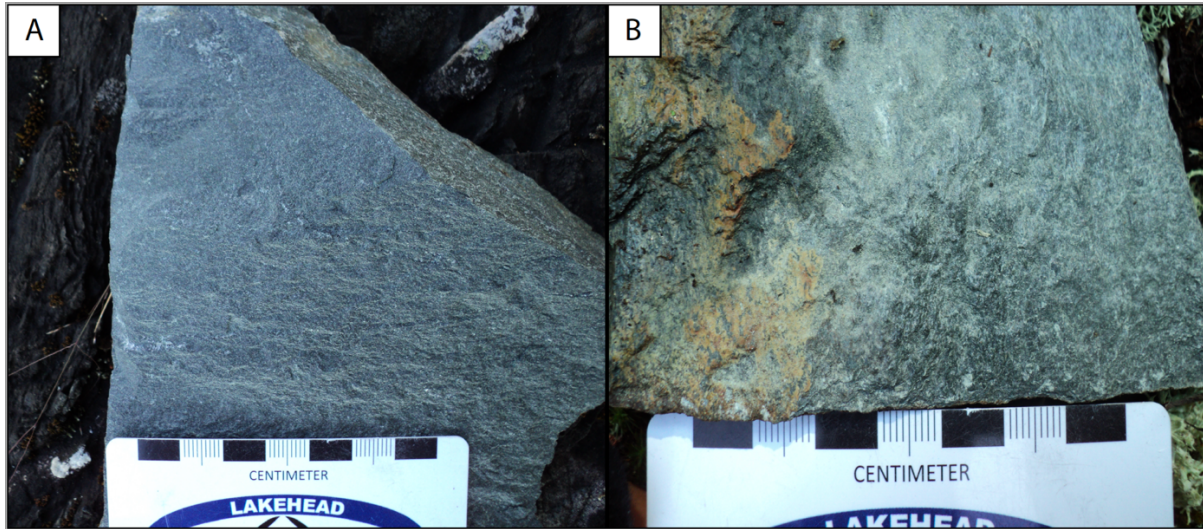


Figure 4.26. Field photographs of mafic metavolcanic rocks. A (Station 4/1 15U 393532 5483126): Massive very fine-grained grey rock. B (LOW18CB12 15U 389507 5482741): Weakly to moderately foliated grey/green rock.

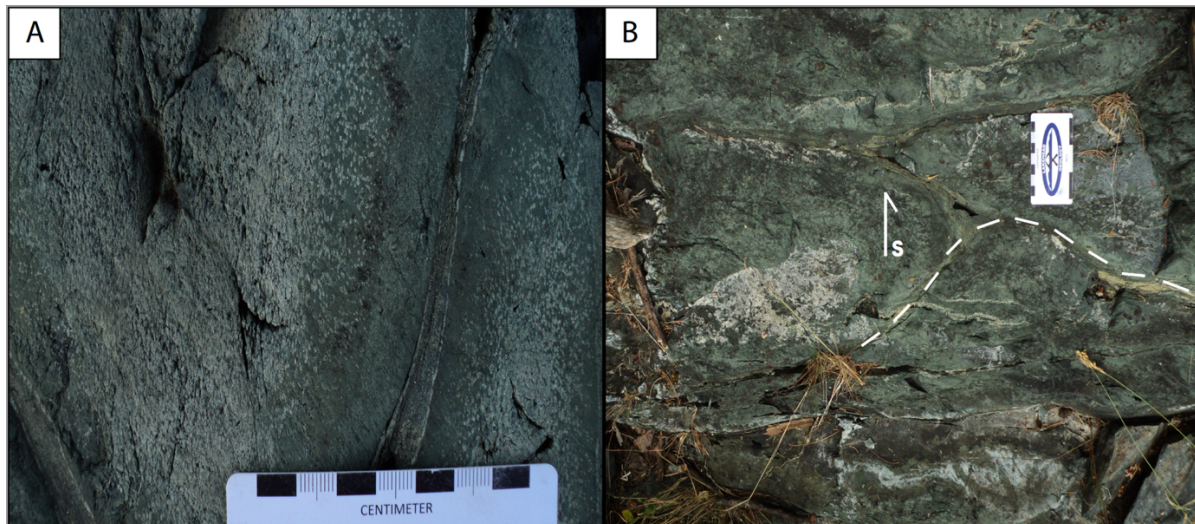


Figure 4.27. Field photograph of mafic pillowed flows. A (LOW18CB42 15U 389132 5482903): Pillow unit with varioles up to 2 mm elongated in an east-west orientation concentrated towards the interior of the pillow. B (Station 5/3 15U 392369 5482197): Pillowed flow with bulbous head demonstrating possible facing direction towards the south.

Tremolite and actinolite are the main amphibole species present. Tremolite occurs as fine elongate grains typically lath-like in habit (Fig. 4.28A). Actinolite occurs as subhedral grains with remnant rhombohedral shape. Crystals are typically fine-grained and host rare very fine-grained quartz inclusions. The groundmass is dominated by chlorite occurring as

subhedral grains associated with amphibole. Minor quartz subgrains occur interstitially to tremolite and actinolite (Fig. 4.28B).

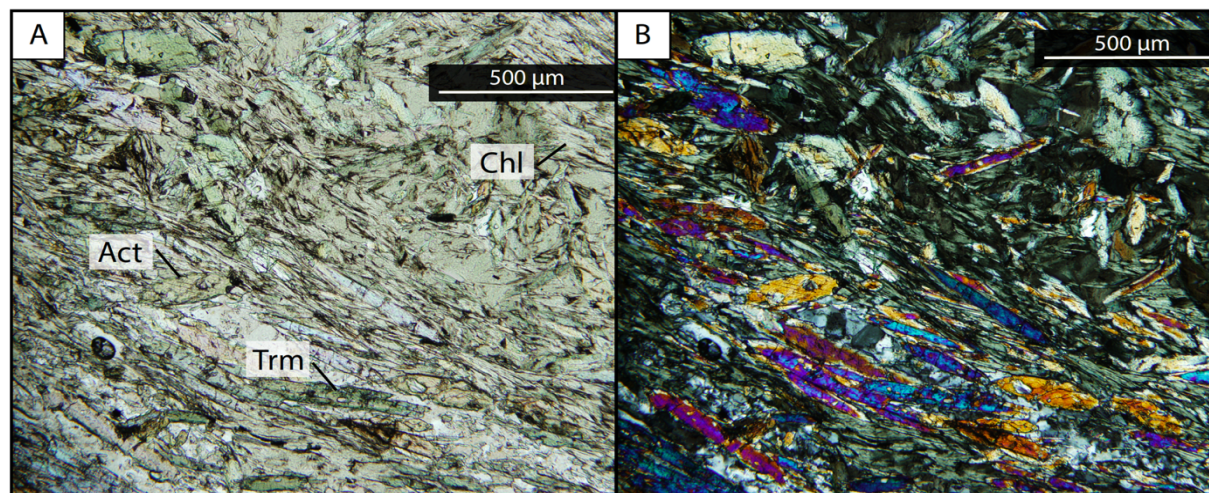


Figure 4.28. Photomicrographs of mafic metavolcanic sample LOW18CB37 (15U 391629 5481462). A: Transmitted plain-polarized light of fine-grained subhedral to elongated tremolite and actinolite grains. B: Transmitted cross-polarized light of amphibole present within a chlorite dominated groundmass with very fine-grained quartz occurring interstitially to tremolite and actinolite.

4.2.7 Ultramafic Metavolcanic Rocks

Ultramafic metavolcanic rocks on Cliff Island were identified based on the presence of strong chlorite and/or talc alteration. The flows are fine-grained, often aphanitic, and exhibit various tints of green created by chlorite alteration (Fig. 4.29A). Rare samples are highly foliated, light grey and aphanitic, suggesting a lesser degree of chlorite alteration and higher degree of talc and/or potential serpentine alteration. Polyhedral jointing was observed in few of the outcrop exposures towards the south of the island (Fig. 4.29B).

4.3 Mineral Chemistry

Scanning Electron Microscope-Energy Dispersive X-ray Spectroscopy (SEM-EDS) was used to determine the mineral chemistry of units within the Falcon Island mapping area. Mafic to ultramafic rocks and a representative sample of a cumulate unit were chosen to investigate the groundmass constituents and mineral chemistry of amphibole, olivine and/or pyroxene present. The cumulate sample exhibits both subhedral amphibole grains present within cumulates as well as fine- to medium-grained laths throughout, likely after primary cumulate pyroxene (Fig. 4.30A). The groundmass consisted of abundant plagioclase,

with annealing textures along grain boundaries, and minor amounts of quartz (Fig. 4.30B). Mineralogy of the cumulate unit consists tschermakitic hornblende and lesser tschermakite. Fine-grained ilmenite is associated with amphibole grains and is often subhedral to rounded.

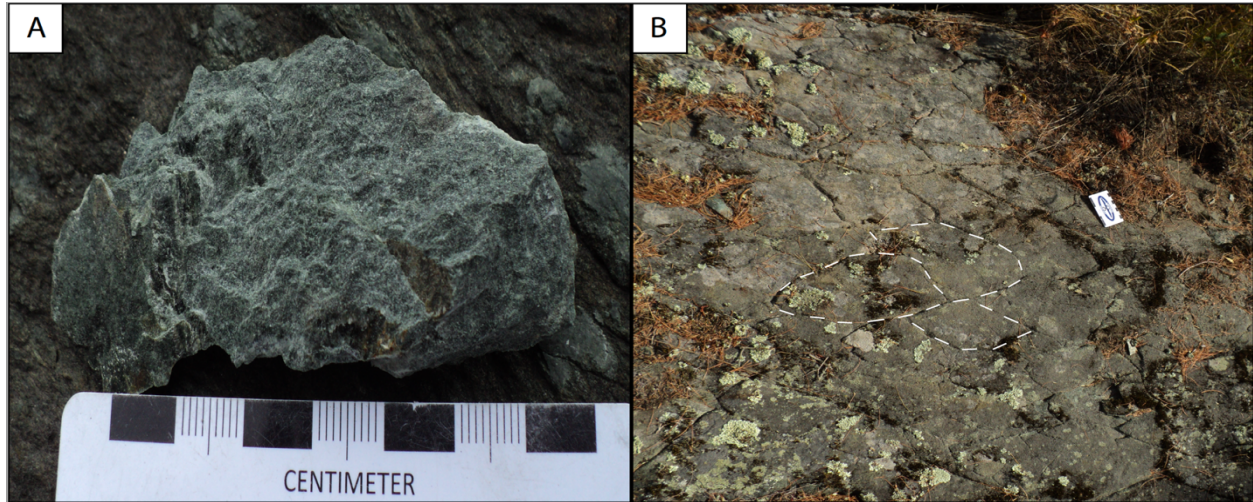


Figure 4.29. Field photograph of ultramafic metavolcanic rocks. A (LOW18CB21 15U 395242 5483449): Grey/green unit with moderate foliation defined by chlorite and amphibole. B (LOW18CB35 15U 392100 5481657): Polyhedral jointing with dimensions of approximately 20 by 10 cm.

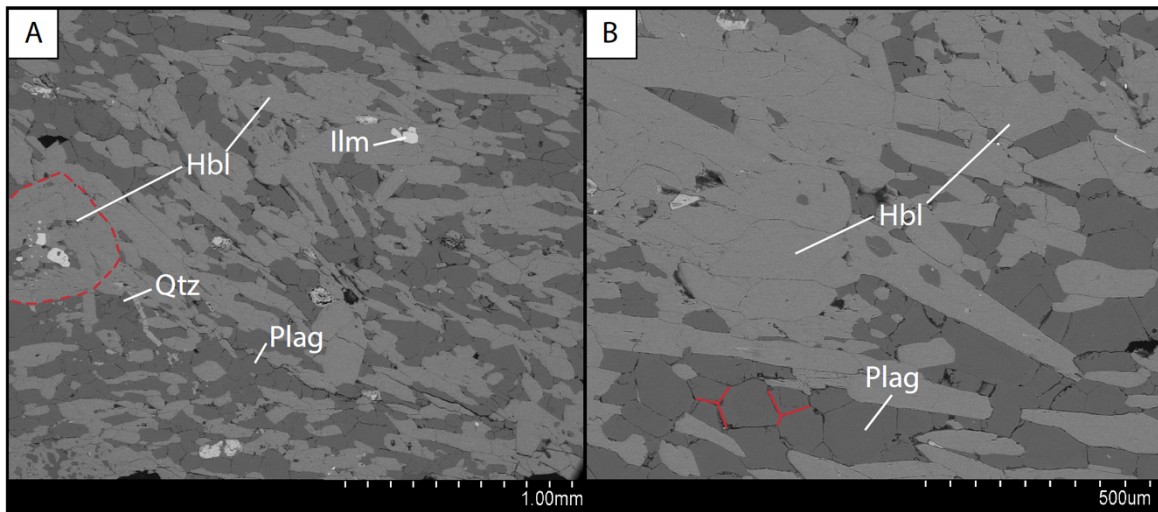


Figure 4.30. Photomicrograph of amphibole cumulate sample LOW17C76. A: Cumulate of hornblende subgrains (shown in red circle) as well as subhedral hornblende within a matrix of plagioclase and quartz. Ilmenite occurs dominantly with hornblende. B: Hornblende within a groundmass of plagioclase with annealed grain boundaries. **Ilm**: Ilmenite. **Qtz**: Quartz. **Plag**: Plagioclase. **Hbl**: Hornblende.

There were minor differences between the mafic to ultramafic rocks of the area. Two mineralogical and textural varieties existed. These include 1) bladed to lath-like amphibole

within a very fine-grained matrix of amphibole and chlorite \pm talc, and 2) thin needles of pyroxene and medium-grained subhedral amphibole present within a groundmass of chlorite and serpentine with dispersed fine-grained magnetite. There were trace minerals identified in modal abundances of $<3\%$ in two samples, consisting of apatite and chromite.

The first variety included tremolite blades and laths with irregular anthophyllite rims, as well as fine grains completely replaced by anthophyllite. Compositional variation is indicated by the lighter and darker grey coloration of the amphibole grains, in which the lighter grey represents anthophyllite and darker grey tremolite (Fig. 4.31A). Talc, when present, is a pseudomorph of fine blocky and lath-like grains (Fig. 4.31A). Ilmenite occurs as fine- to very fine-grained subhedral to rounded grains scattered throughout the groundmass and as rare inclusions in tremolite (Fig. 4.31B).

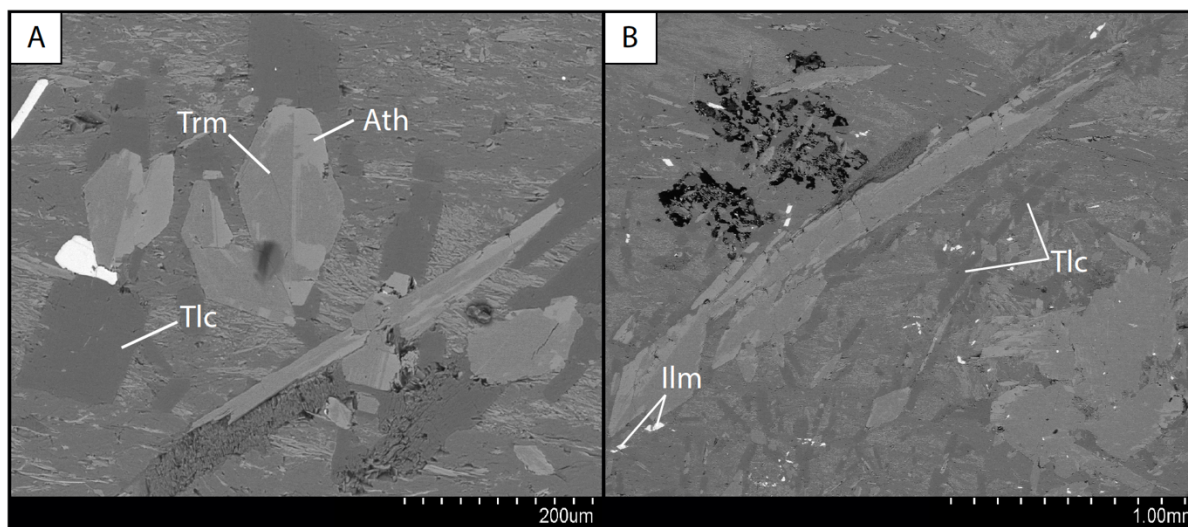


Figure 4.31. Photomicrograph of sample LOW17CB79. A: Anthophyllite and tremolite grains as blades. Fine-grained blocky talc and very fine-grained laths occur dispersed in a hydrous groundmass. B: Ilmenite occurs dispersed throughout as subhedral to rounded fine grains, often associated with amphibole crystals. Amphibole grains can also occur up to 2 mm long with cross sections up to 3 mm wide. Talc occurs dispersed as fine elongated laths. **Trm:** Tremolite. **Ath:** Anthophyllite. **Tlc:** Talc. **Ilm:** Ilmenite.

The second variety consists of randomly oriented thin pyroxene blades as well as subhedral amphibole in a very fine-grained groundmass consisting of chlorite and serpentine (Fig. 4.33). Magnetite is often rounded and dispersed throughout the thin section, however when present within the chlorite matrix it is elongated in the direction of foliation defined by chlorite (Fig. 4.32A). Amphiboles also occur as fine- to medium-grained subhedral crystals as well as rare blades, commonly as tremolite and anthophyllite. Amphibole grains often cross-cut pyroxene grains (Fig. 4.32B). Serpentine occurs

interstitially to pyroxene grains as well as subhedral masses scattered throughout (Fig. 4.32).

Rare occurrences of apatite occur in ultramafic sample LOW17CB62 as very fine-grained subhedral to rounded crystals occurring within the groundmass (Fig. 4.33A). Ilmenite occurs as fine- to very fine-grained subhedral to rounded grains associated with hornblende and minor tremolite phenocrysts scattered throughout the groundmass. Chromite appears in ultramafic sample LOW17CB43 interstitial to amphibole phenocrysts within the groundmass, as well as very fine-grained inclusions within tremolite grains (Fig. 4.33B). Sample LOW17CB43 has the highest abundance of Cr (ppm) at 3450ppm.

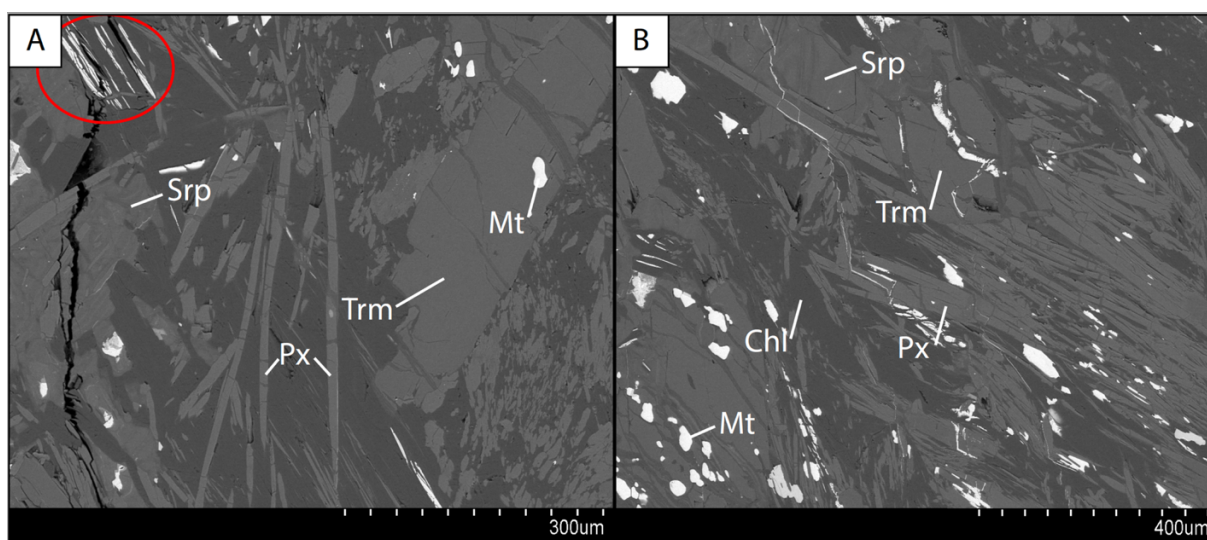


Figure 4.32. Photomicrograph of sample LOW17CB62. A: Acicular pyroxene and subhedral fine-grained tremolite in a chlorite dominated matrix with minor serpentine. Magnetite occurs as rounded grains within the matrix, as inclusions in amphibole grains, and as a replacement. Red circle denotes magnetite elongated in the direction of foliation. B: Subhedral pyroxene with irregular bladed edges with tremolite grains that have been fractured. Tremolite appears to cross-cut pyroxene grains. **Srp:** Serpentine. **Px:** Pyroxene. **Trm:** Tremolite. **Mt:** Magnetite. **Chl:** Chlorite.

4.4 X-Ray Diffraction

XRD was utilized to understand the constituents of the groundmass that were unidentifiable using petrography and SEM. Samples were chosen on the basis of various amphibole species identified in SEM, as well as represent a range of trace element compositions (See Section 5.1.1). XRD analysis identified clinocllore as the main constituent of the groundmass in all mafic and ultramafic metavolcanic samples that were analyzed.

Clinocllore existed as magnesium- and chromium-rich varieties. Amphibole analyzed through the XRD are often consistent with amphibole chemistry produced by SEM analyses.

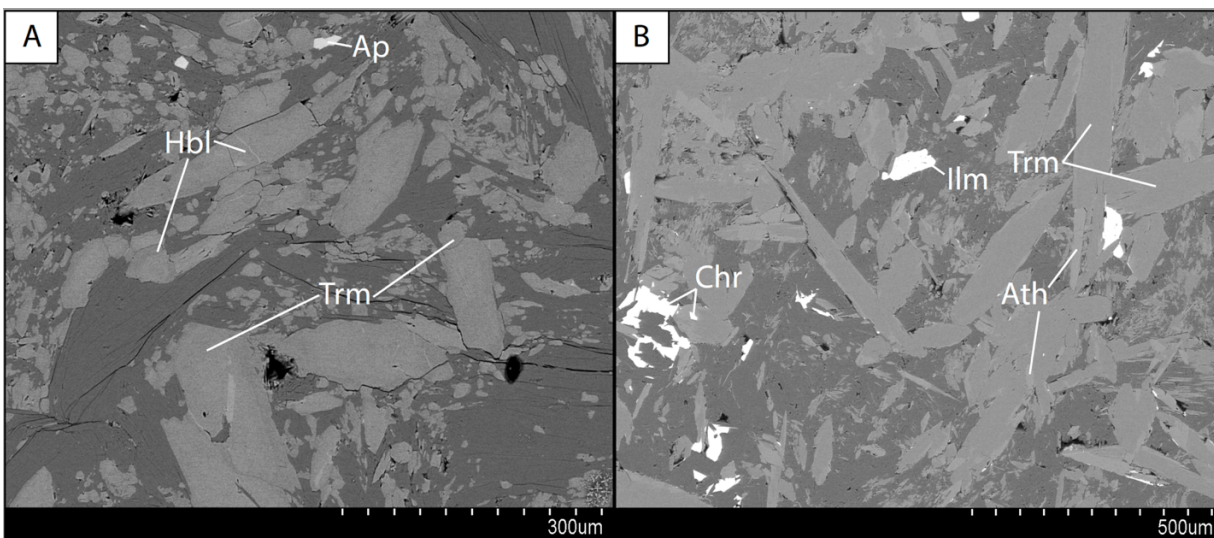


Figure 4.33. Photomicrograph of samples composed as subhedral amphibole. A (LOW17CB67): Hornblende and tremolite grains within a hydrous groundmass. Fine-grained subhedral apatite occurs dispersed throughout. B (LOW17CB43): Tremolite and actinolite subhedral grains, with rare laths, with fine-grained subhedral ilmenite occurring along amphibole boundaries. Chromite occurs interstitial to tremolite grains, as well as inclusions. **Hbl**: Hornblende. **Trm**: Tremolite. **Ap**: Apatite. **Chr**: Chromite. **Ilm**: Ilmenite. **Ath**: Anthophyllite.

Typical results identifying hornblende as the main phase with minor tremolite were consistent between SEM and XRD analyses. Samples containing tremolite with anthophyllite rims as well as fine-grained anthophyllite did not show anthophyllite through XRD analyses. Anthophyllite is a minor phase relative to tremolite, and due to similarity in crystal structure of both amphibole phases, this is likely why anthophyllite did not appear during XRD analyses. One sample contained both clinocllore and serpentine as groundmass phases, along with both amphibole and enstatite, and these results were consistent with those produced by the SEM. The cumulate sample consisted of tschermakitic and magnesium-rich hornblende with a groundmass dominated by plagioclase.

Table 4.1. Minerals identified using XRD. UMV: ultramafic volcanic. MV: mafic volcanic. C: cumulate.

Sample	Rock Type	Main Mineral Phases
LOW17CB28	Tremolite-Chlorite Schist (UMV)	Cr-rich Clinocllore $(\text{Mg, Fe, Al})_6(\text{Si, Cr})_4\text{O}_{10}(\text{OH})_8$ Tremolite $\text{Ca}_2\text{Mg}_5\text{Si}_8\text{O}_{22}(\text{OH})_2$
LOW17CB43	Tremolite-Chlorite Schist (UMV)	Clinocllore $(\text{Mg, Fe})_6(\text{Si, Al})_4\text{O}_{10}(\text{OH})_8$ Tremolite $\text{Ca}_2\text{Mg}_5\text{Si}_8\text{O}_{22}(\text{OH})_2$ Anthophyllite $(\text{Mg, Fe}^{2+})_7\text{Si}_8\text{O}_{22}(\text{OH})_2$
LOW17CB62	Tremolite-Serpentine-Chlorite Schist (UMV)	Cr-rich Clinocllore $(\text{Mg, Fe, Al})_6(\text{Si, Cr})_4\text{O}_{10}(\text{OH})_8$ Enstatite $\text{Mg}_{1.04}(\text{SiO}_3)$ Chrysotile (serpentine) $\text{Mg}_3\text{Si}_2\text{O}_5(\text{OH})_4$ Tremolite $\text{Ca}_2\text{Mg}_5\text{Si}_8\text{O}_{22}(\text{OH})_2$
LOW17CB67	Tremolite-Hornblende-Chlorite Schist (MV)	Magnesiohornblende $\text{Ca}_2(\text{Mg, Fe})_5(\text{Si, Al})_8\text{O}_{22}(\text{OH})_2$ Tremolite $\text{Ca}_2\text{Mg}_5\text{Si}_8\text{O}_{22}(\text{OH})_2$ Clinocllore $(\text{Mg, Fe})_6(\text{Si, Al})_4\text{O}_{10}(\text{OH})_8$
LOW17CB68	Tremolite-Chlorite Schist (UMV)	Tremolite $\text{Ca}_2\text{Mg}_5\text{Si}_8\text{O}_{22}(\text{OH})_2$ Clinocllore $(\text{Mg, Fe})_6(\text{Si, Al})_4\text{O}_{10}(\text{OH})_8$
LOW17CB69	Tremolite-Chlorite Schist (UMV)	Tremolite $\text{Ca}_2\text{Mg}_5\text{Si}_8\text{O}_{22}(\text{OH})_2$ Cr-rich Clinocllore $(\text{Mg, Fe, Al})_6(\text{Si, Cr})_4\text{O}_{10}(\text{OH})_8$
LOW17CB76	Hornblende-phyric cumulate (C)	Magnesiohornblende Tschermakite Albite $(\text{Na, Ca})\text{Al}(\text{Si, Al})_3\text{O}_8$
LOW17CB92	Tremolite-Chlorite Schist (UMV)	Tremolite $\text{Ca}_2\text{Mg}_5\text{Si}_8\text{O}_{22}(\text{OH})_2$ Cr-rich Clinocllore $(\text{Mg, Fe, Al})_6(\text{Si, Cr})_4\text{O}_{10}(\text{OH})_8$
LOW17CB96	Tremolite-Hornblende-Chlorite Schist (MV)	Magnesiohornblende $(\text{Ca, Na})_{2.26}(\text{Mg, Fe, Al})_{5.15}(\text{Si, Al})_8\text{O}_{22}(\text{OH})_2$ Clinocllore $(\text{Mg, Fe})_6(\text{Si, Al})_4\text{O}_{10}(\text{OH})_8$ Tremolite $\text{Ca}_2\text{Mg}_5\text{Si}_8\text{O}_{22}(\text{OH})_2$

Chapter 5: Geochemistry and Radiogenic Isotopes

5.1 Whole Rock Geochemistry

Major and trace element geochemistry analyses of 109 samples were used to subdivide and characterize units from the two field areas in order to produce a petrogenetic model and evaluate the tectonic environment in which they formed. Sample geochemistry has been calculated to a 100% volatile free basis to account for loss on ignition (LOI).

The field area is situated within a greenstone belt in which metamorphism and alteration have greatly affected the rocks, therefore geochemical interpretation must be made cautiously. Rocks that have been subjected to hydrothermal alteration or metamorphism are likely to suffer from element mobility (Rollinson, 1993). Typically, high-field strength elements (HFSE) are immobile during alteration, including the rare earth elements, Al, Sc, Y, Th, Hf, Ti, Nb, Ta and P, whereas the large ion lithophile elements (LILE) including Cs, Sr, K, Rb, Ba are mobile (Pearce, 1983; Hollings et al., 1998). At high temperatures Cr, Ni, Co and V are also considered immobile whereas Mn, Zn and Cu tend to be mobile (Rollinson, 1993). Bivariate diagrams plotting TiO_2 versus SiO_2 , Al_2O_3 , MgO , Na_2O , K_2O and CaO and Nb versus La, Zr, Yb, Th, TiO_2 and Y can be used to evaluate element mobility. Element immobility and/or mobility of trace elements, aluminum and titanium, is identified by analyzing the linear trend or scatter shown by the trace element ratios of those that are typically immobile (Fralick, 2003). There is large scatter observed in Na_2O and weak scatter in CaO (Fig. 5.1). The large scatter in Na_2O suggests element mobility during metamorphism and alteration. Figure 5.2 displays the relative immobile nature of trace elements demonstrated by plotting Nb versus La, Zr, Yb, Th, TiO_2 , and Y. Calc-alkalic metavolcanic rocks commonly differ from the linear trend established by the intermediate to ultramafic metavolcanic rocks, especially Nb versus Th and La (Fig. 5.2). There is weak scatter of Th in which there appears to be two trends defined by the low-Ti tholeiites and one high-Ti tholeiite sample. Scatter is also observed in La versus Nb, most dominantly in the high-Ti tholeiites. The relative immobility of the trace elements will ensure confidence when utilizing rock classification diagrams and inferring tectonic setting and magmatic history.

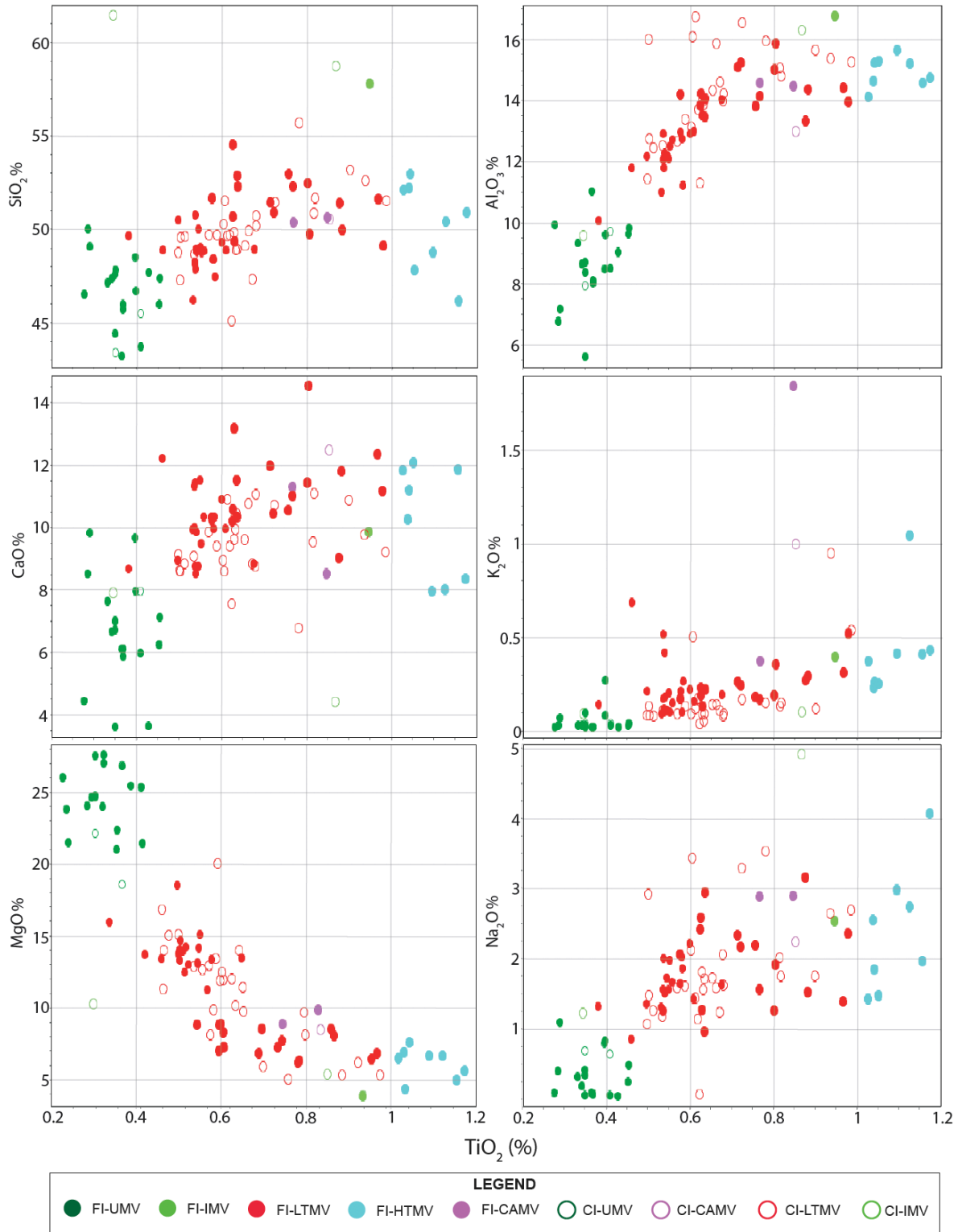


Figure 5.1. Bivariate plots of TiO_2 versus major element oxides. **FI:** Falcon Island. **CI:** Cliff Island. **UMV:** Ultramafic metavolcanic rocks. **IMV:** Intermediate metavolcanic rocks. **LTMV:** Low Ti metavolcanic rocks. **HTMV:** High Ti metavolcanic rocks. **CAMV:** Calc-alkalic metavolcanic rocks.

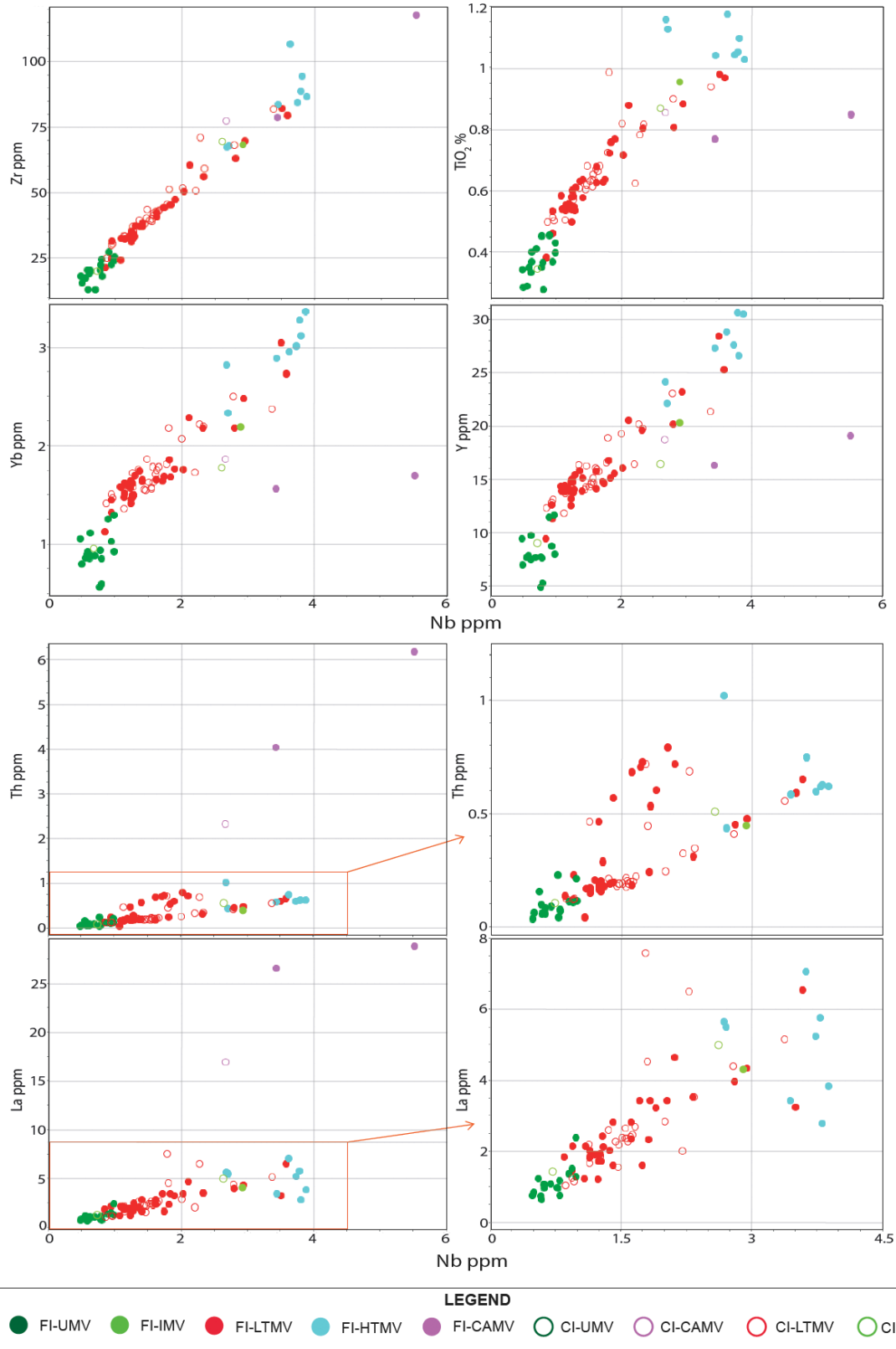


Figure 5.2. Bivariate plots of Nb (ppm) versus trace elements. **FI:** Falcon Island. **CI:** Cliff Island. **UMV:** Ultramafic metavolcanic rocks. **IMV:** Intermediate metavolcanic rocks. **LTMV:** Low Ti metavolcanic rocks. **HTMV:** High Ti metavolcanic rocks. **CAMV:** Calc-alkalic metavolcanic rocks.

During field work, rocks were subdivided by protolith when metamorphism and alteration had not obscured the primary textures and mineralogy, however in most cases for mafic to ultramafic volcanic rocks, mineralogy is entirely metamorphic. Geochemical analyses can be used to further classify the units by major and trace element geochemistry.

As previously mentioned, Na_2O demonstrated considerable scatter, and K_2O weak scatter, when plotted against TiO_2 , this likely accounts for scatter observed on the classification diagram after Le Maitre et al. (1989; Fig. 5.3). The three samples plotting within the picrobasalt field are ultramafic rocks classified as serpentine-chlorite schists and an anthophyllite-tremolite-chlorite schist. The clastic metasedimentary unit plots as an outlier in the intermediate-felsic realm.

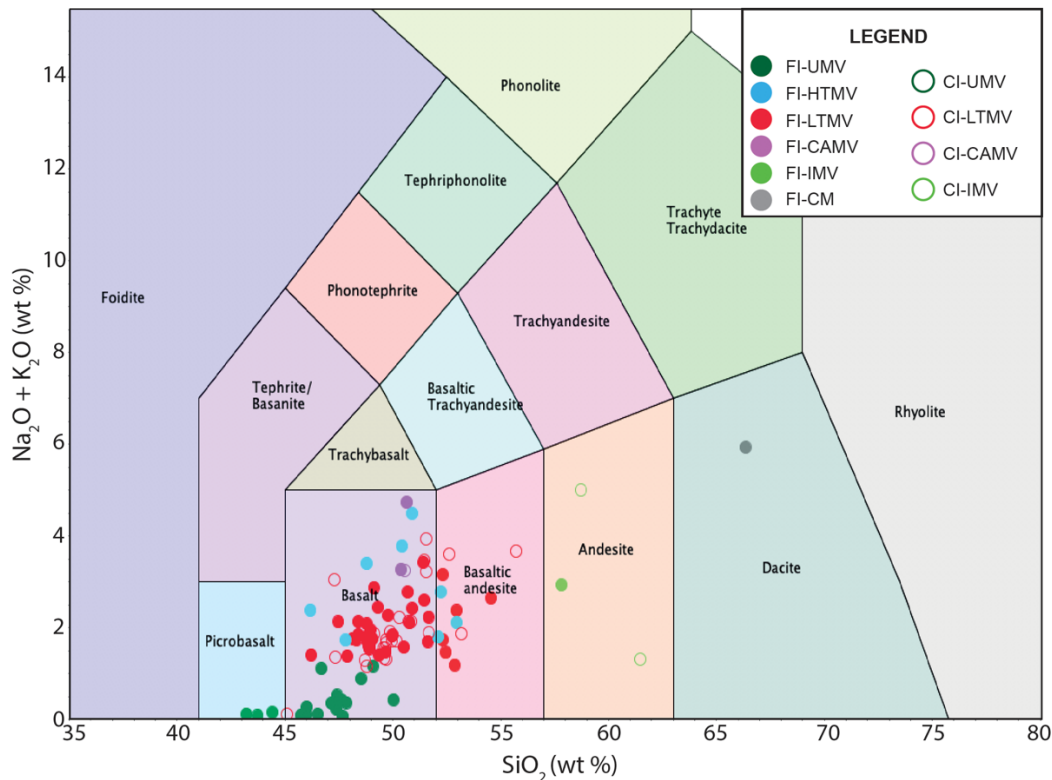


Figure 5.3. Rock classification diagram after Le Maitre et al. (1989) utilizing SiO_2 versus $\text{Na}_2\text{O} + \text{K}_2\text{O}$ (total alkalis) of the volcanic and sedimentary samples present within the Long Bay Group. **FI:** Falcon Island. **CI:** Cliff Island. **UMV:** Ultramafic metavolcanic rocks. **IMV:** Intermediate metavolcanic rocks. **LTMV:** Low Ti metavolcanic rocks. **HTMV:** High Ti metavolcanic rocks. **CM:** Clastic metasedimentary rocks. **CAMV:** Calc-alkalic metavolcanic rocks.

The classification diagram of Pearce (1996) provides a more precise classification of the units as it uses the immobile elements Nb, Zr, Ti and Y (Fig. 5.4). This diagram minimizes any geochemical variance caused by metamorphism and/or alteration that may have

affected the major element oxides. The majority of samples plot within the basalt field, including the intermediate metavolcanic rocks, with the exception of one calc-alkalic rock and the clastic metasedimentary sample. This is different to the TAS diagram in which a larger scatter in classification occurs, ranging from picrobasalt to basaltic andesite for mafic to ultramafic rocks and andesite for intermediate rocks.

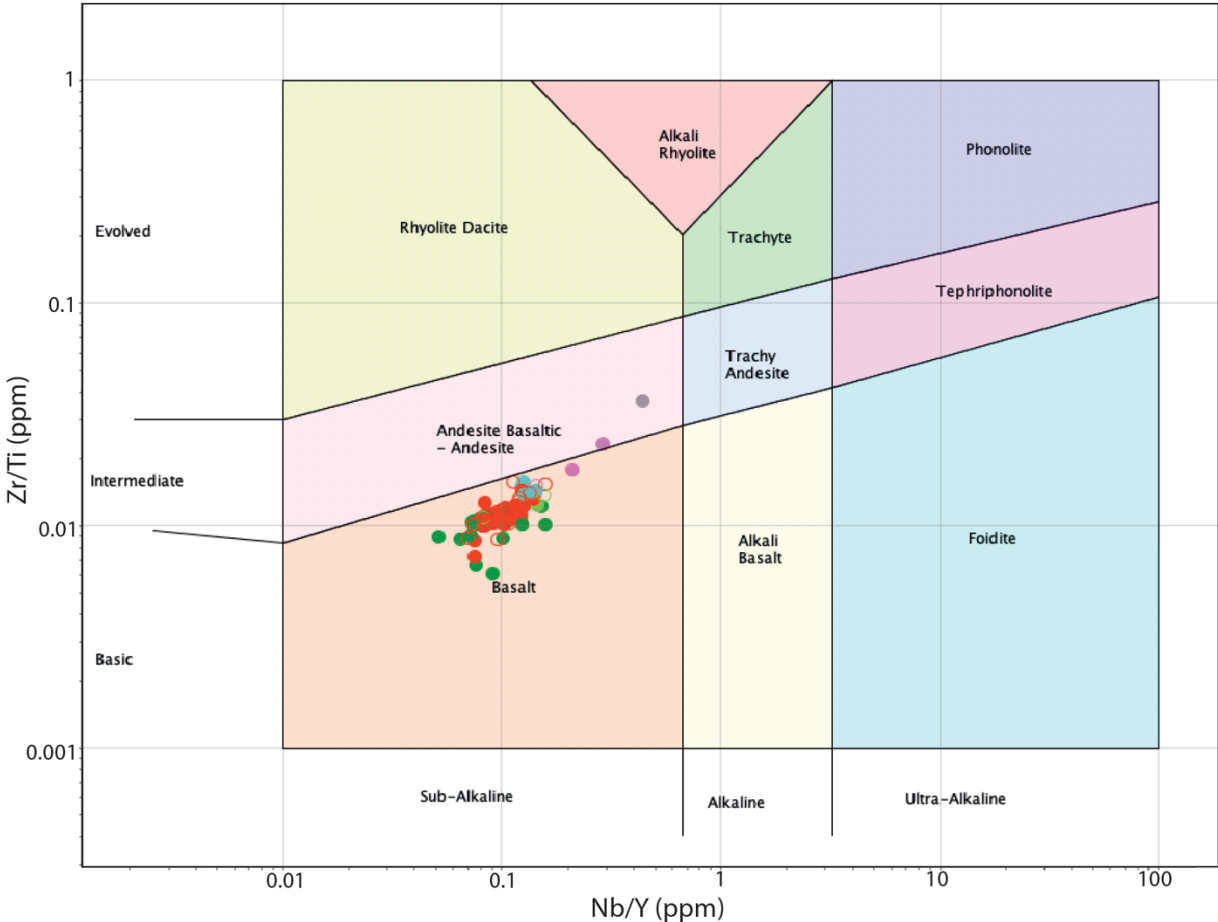


Figure 5.4. Rock classification diagram after Pearce (1996) utilizing Nb/Y versus Zr/Ti of the volcanic and sedimentary samples present within the Long Bay Group. Symbols same as in Figure 5.3.

The magmatic affinity of volcanic and plutonic rocks can be evaluated using an AFM diagram after Rollinson (1993; Fig. 5.5). The calc-alkalic and tholeiitic differentiation produces a tholeiitic to calc-alkalic classification. There is scatter surrounding the tholeiitic trend lines in both volcanic and intrusive diagrams, therefore in order to confirm magmatic affinity, the trace elements Th, Zr, Y, and Yb were plotted following the methods of Ross and Bédard (2009) for ultramafic and mafic metavolcanic rocks, and intrusive rocks in the following sections due to their immobile nature. To further classify magmatic affinity, Jensen

plots after Rollinson (2013) were utilized to characterize volcanic rocks (Fig. 5.6). Ultramafic volcanic rocks consistently remain in the komatiite domain whereas the mafic metavolcanic rocks reside in the komatiitic basalt, high-Mg tholeiite, high-Fe tholeiite and some samples within the calc-alkalic basalt domain.

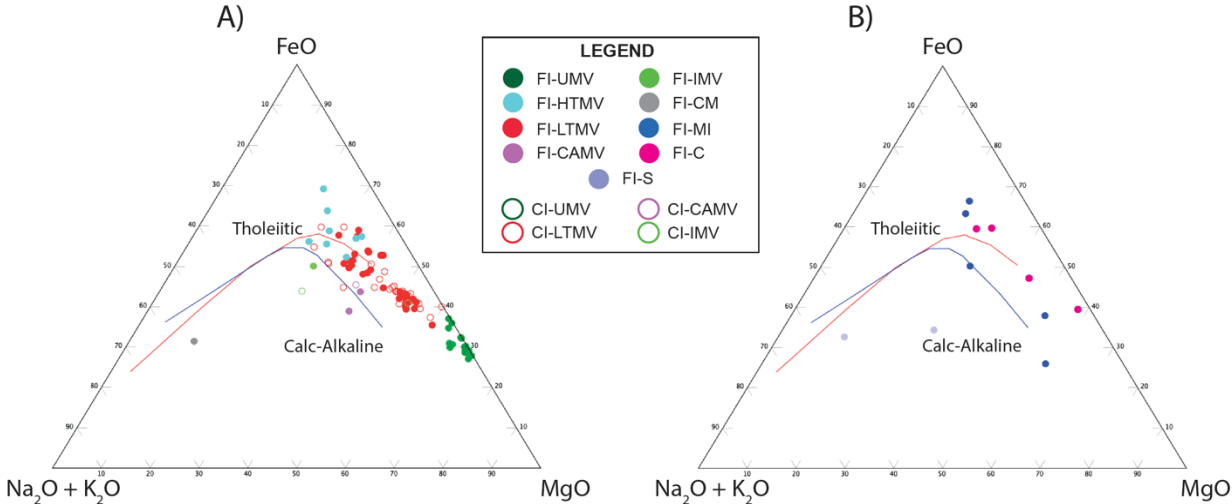


Figure 5.5. AFM diagram differentiating magmatic affinity of A) volcanic and B) plutonic rocks. Trend lines, **red – tholeiitic and blue – calc-alkalic**, from Kuno (1968) and Irvine and Baragar (1971). **FI:** Falcon Island. **CI:** Cliff Island. **UMV:** Ultramafic metavolcanic rocks. **IMV:** Intermediate metavolcanic rocks. **LTMV:** Low Ti metavolcanic rocks. **HTMV:** High Ti metavolcanic rocks. **CM:** Clastic metasedimentary rocks. **CAMV:** Calc-alkalic metavolcanic rocks. **C:** Cumulate. **MI:** Mafic intrusive rocks. **S:** Syenite.

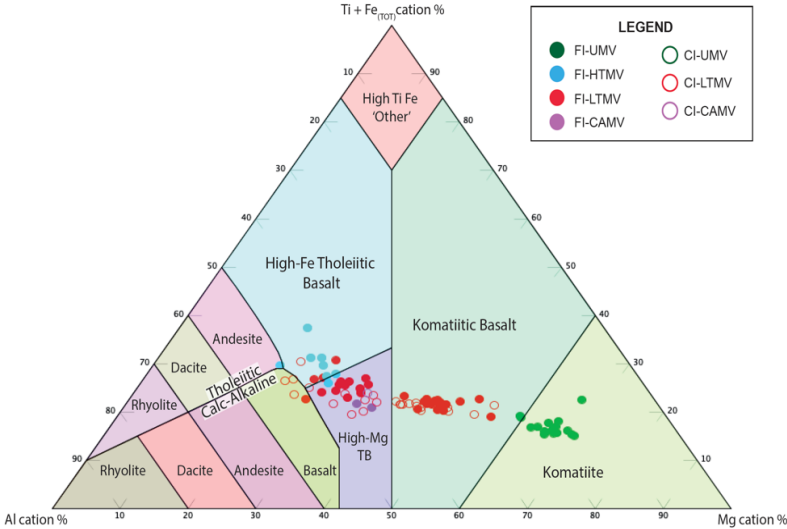


Figure 5.6. Jensen plot after Rollinson (2013) plotting mafic to ultramafic volcanic rocks. **FI:** Falcon Island. **CI:** Cliff Island. **UMV:** Ultramafic metavolcanic rocks. **LTMV:** Low Ti metavolcanic rocks. **HTMV:** High Ti metavolcanic rocks. **CAMV:** Calc-alkalic metavolcanic rocks.

5.1.1 Ultramafic metavolcanic rocks

The ultramafic volcanic rocks are largely subdivided based on geochemistry as they occur as a variety of schists and amphibolites in the field area. Collected samples exhibit similar geochemical compositions and signatures. Ultramafic volcanic rocks in the area typically have SiO_2 values <50 wt% with the majority of samples <48 wt% and reaching as little as 43 %. The MgO content ranges from 21 to 27.6 wt%. Major elements CaO and TiO_2 show no correlation with SiO_2 content; however, a positive correlation exists between $\text{Na}_2\text{O}+\text{K}_2\text{O}$ and negative correlation exists between Fe_2O_3 , Al_2O_3 and SiO_2 (Fig. 5.7). There is a positive correlation between both Ni (580 to 1,311 ppm) and Cr (1,734 to 3,451 ppm) against MgO (Fig. 5.8). Samples with the highest MgO concentrations have Cr contents up to 3,451 ppm and Ni contents up to 1,311 ppm.

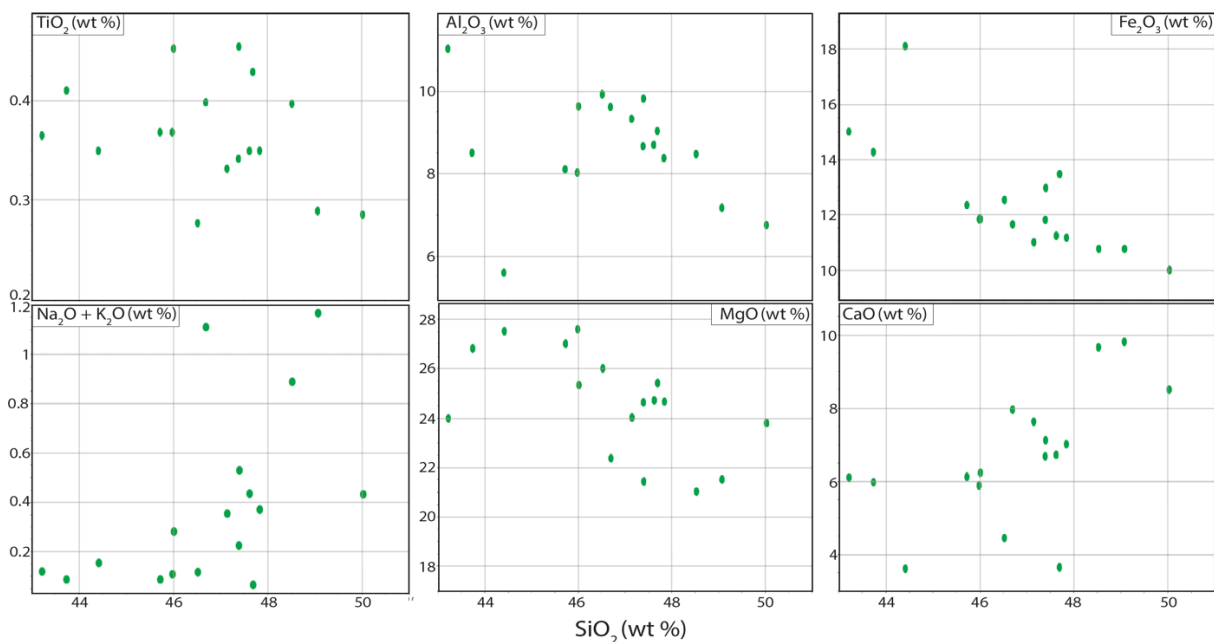


Figure 5.7. Harker diagrams with SiO_2 plotted against major element oxides for ultramafic metavolcanic samples.

The samples plot within both picobasalt and basalt field on the TAS classification diagram and plot consistently within the basalt field on the trace element classification diagram after Pearce (1996; Figs. 5.3;5.4). On the Jensen plot the majority of samples remain within the komatiite field; however, two samples trend towards the komatiitic basalt domain (Fig. 5.6).

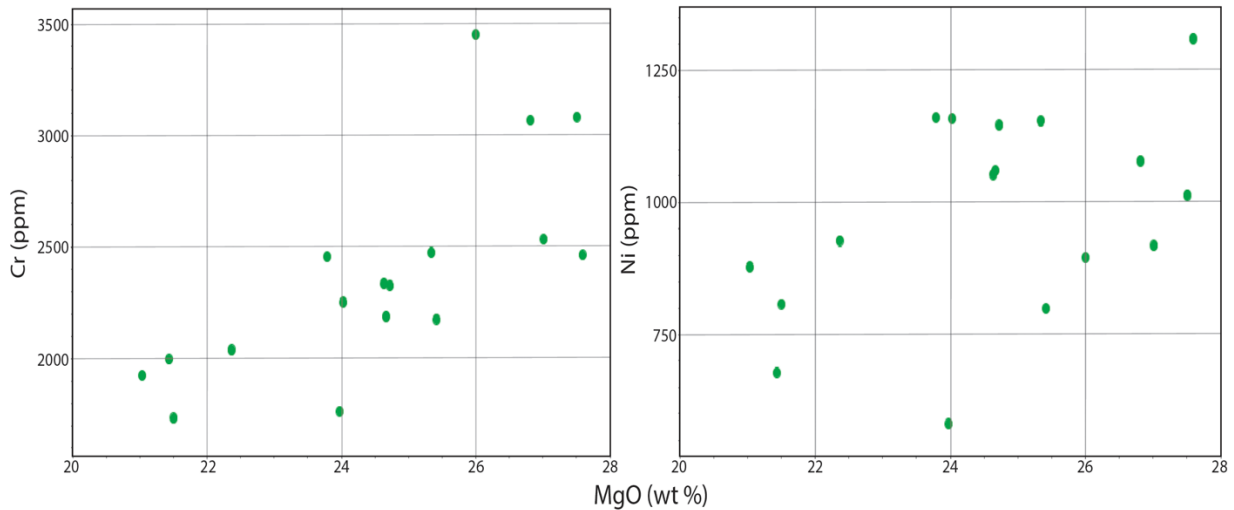


Figure 5.8. Magnesium oxide versus Cr and Ni to evaluate metal content of ultramafic volcanic rocks.

Linear trends on trace element bivariate plots reflect element immobility, whereas increasing scatter reflects element mobility (MacLean and Barrett, 1993). Bivariate plots of Zr versus Nb, La, Th, Gd, Yb (ppm) and TiO_2 wt% are constructed to test element mobility throughout (Fig. 5.10). Within the ultramafic volcanic lithology there is no linear trend between Zr and Nb demonstrated by an r^2 value of 0.51. Very weak correlation exists between Zr and La, TiO_2 and Gd (r^2 values of ~ 0.19 to 0.3), with a few outliers causing slight scatter. There is greater scatter with Zr versus Th and Yb % resulting in a poor linear correlation. The results reflect an overall mobile nature or a genetic variation distinguished by the scatter observed in many trace elements (Fig. 5.9).

The diagrams of Ross and Bédard (2009) are utilized to investigate the magmatic affinity of the samples (Fig. 5.10). Overall, the rocks plot within the tholeiitic field with one outlier plotting within the transitional domain on the Th/Yb versus Zr/Y diagram but within the tholeiitic field on the La versus Yb diagram. The results coincide with the samples plotting along the tholeiitic trend in Figure 5.5A.

There are three distinct primitive mantle normalized patterns present within the ultramafic volcanic unit, based on light rare earth element (LREE), Th, and Nb concentrations (Fig. 5.11). Samples exhibit: a light rare earth depletion and flat heavy rare earth elements, a light rare earth enrichment with Nb depletion, or have an overall flat light and heavy rare earth pattern with depleted Th and Nb.

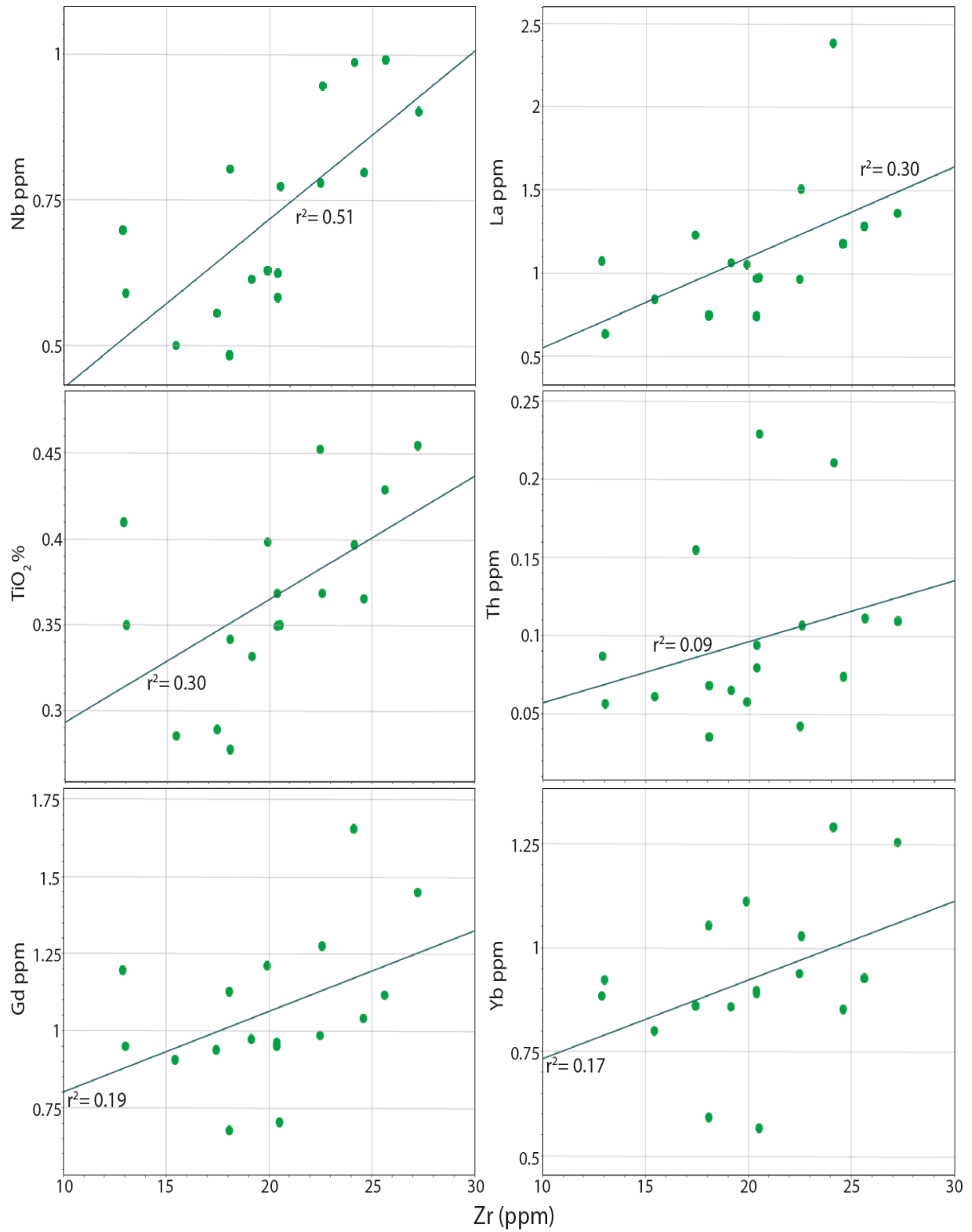


Figure 5.9. Element immobility diagrams for ultramafic metavolcanic rocks. Regression values given for the line of best fit.

Values of $[La/Sm]_{pm}$ range from 1.5 to 3.1 (average 2.25) indicating a slight LREE enrichment in most samples. Although values for Nb/Nb^* range from 0.37 to 1.16, the average value within the unit is 0.67 and moderate Nb depletions occur within most patterns whereas weakly positive anomalies are rare. In some samples, Th and Nb exist as similar values in which a near straight horizontal line can be drawn between the elements. The heavy rare earth elements (HREE)s exhibit flat to weakly fractionated slopes with $[Gd/Yb]_{pm}$ values of 1.25 to 1.64 (average 1.39). There is an overall positive correlation with $[Gd/Yb]_{pm}$ and $[La/Sm]_{pm}$ values as samples display increased LREE enrichment with slightly fractionated HREE, apart from one outlier that has the highest $[Gd/Yb]_{pm}$ value of 1.64 while shows a moderate LREE enrichment below the average for the ultramafic samples ($[La/Sm]_{pm} = 1.89$). There are rare strong positive and negative Eu anomalies, however weak to zero Eu anomalies are common ($Eu/Eu^* = 0.43$ to 1.61; average of 0.97).

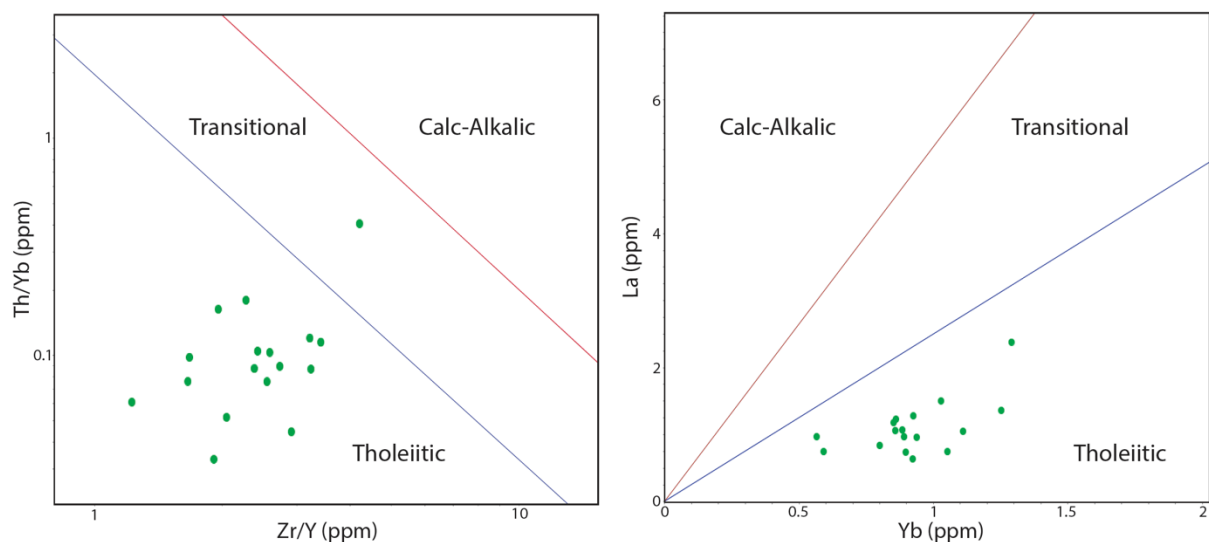


Figure 5.10. Magmatic affinity diagrams after Ross and Bédard (2009) for ultramafic volcanic rocks.

5.1.2 Mafic metavolcanic rocks

The mafic volcanic rocks consist of three distinct varieties: low-Ti tholeiitic basalts (<1 wt% TiO_2), high-Ti tholeiitic basalts (>1 wt% TiO_2), and calc-alkalic basalts. The TAS volcanic classification diagram shows considerable scatter of mafic volcanic rocks in which

the three varieties of basalts plot within the basalt, and basaltic andesite fields; however, considerable mobility exists with Na and K, therefore the classification is not representative (Fig. 5.3).

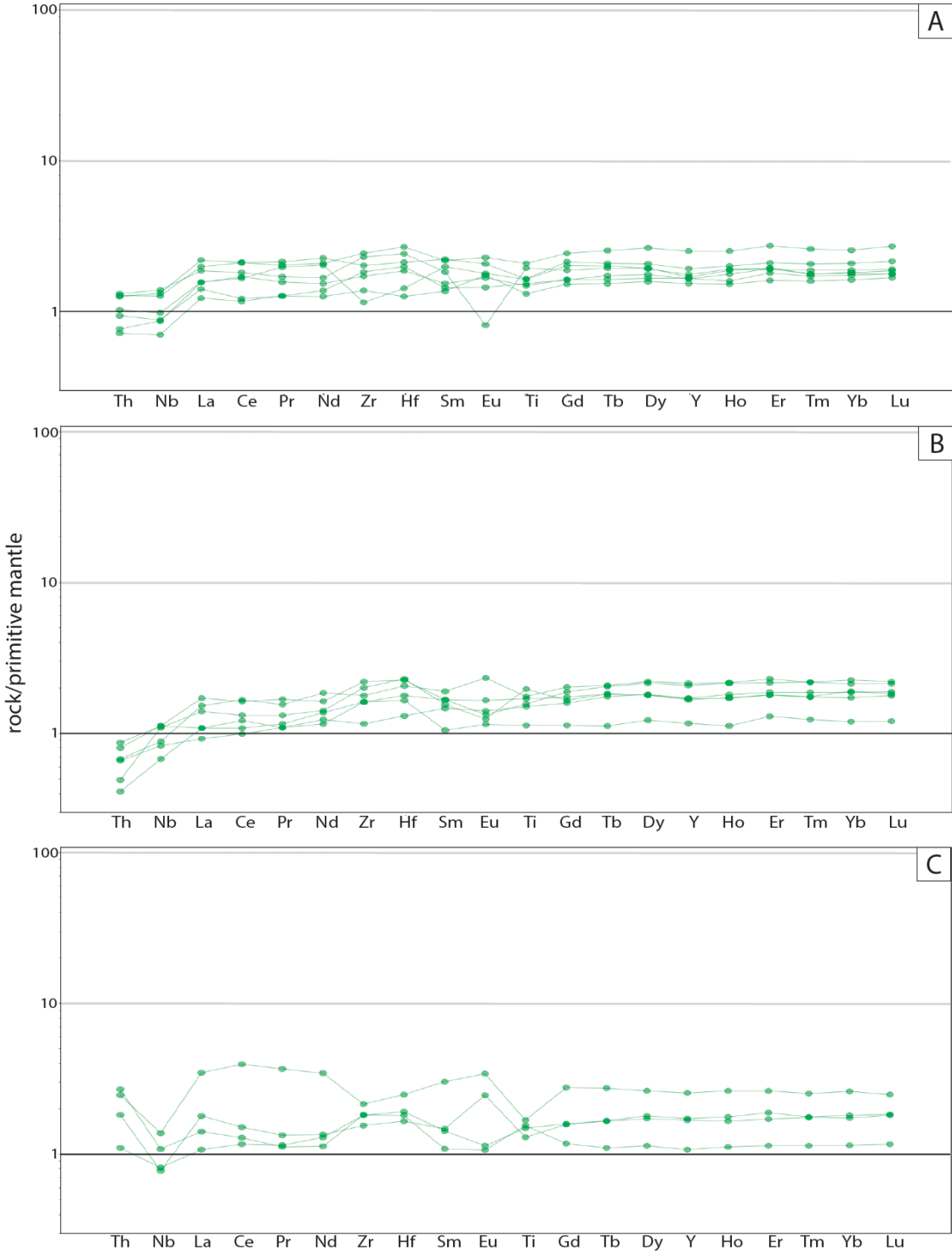


Figure 5.11. Primitive mantle normalized diagrams of ultramafic volcanic rocks. Normalizing values from Sun and McDonough (1989).

On the Nb/Y versus Zr/Ti rock classification diagram however, rocks are defined more specifically in the basalt field with only one sample of calc-alkalic basalt plotting within the andesite to basaltic andesite field (Fig. 5.4). On the Jensen cation plot, the low-Ti basalts plot consistently within the high-Mg tholeiitic and komatiitic basalt field. The high-Ti basalts plot in the high-Fe tholeiitic field, with slight scatter into surrounding fields, and the calc-alkalic rocks are restricted to the high-Mg tholeiitic field (Fig. 5.6).

Mafic volcanic rocks in the area typically have SiO₂ values of 46 to 48 wt% with outliers as low as 44 and as high as 51 wt%. There is no major correlation between SiO₂ and any of the oxides, however negative correlation is observed between SiO₂ and MgO in the low-Ti basalts (Fig. 5.12). The high-Ti basalts have consistent MgO contents of approximately 6 to 7 wt% with variations in SiO₂ from 45 to 49 wt%.

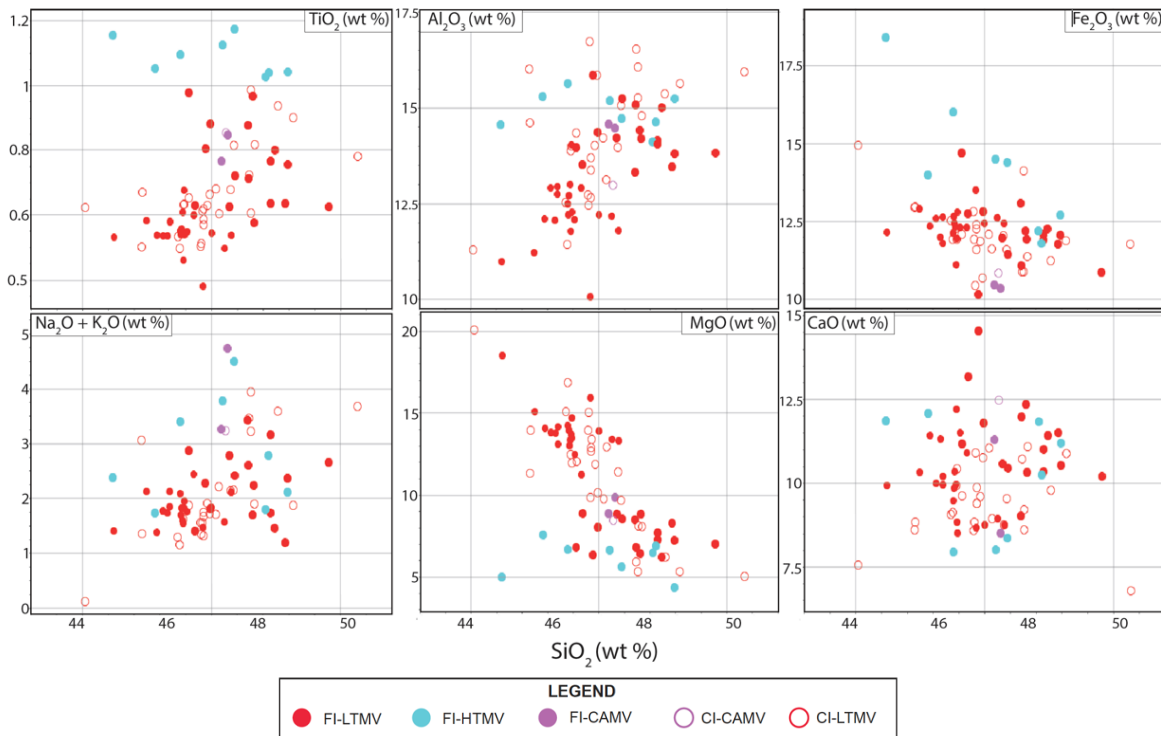


Figure 5.12. Harker diagram of SiO₂ vs major element oxides for mafic metavolcanic rocks.

Trends are much tighter when plotted as bivariate plots with trace elements and TiO₂ plotted against Zr (Fig. 5.13). Linear regression and trend lines are given for both calc-alkalic and tholeiitic suites. Distinct linear trends exist within the tholeiitic rocks between Zr and Nb, Gd, and Yb, in which r² values are >0.90. TiO₂ also has a strong linear correlation with r² = 0.87. The remainder of the trace elements, La and Th, have moderately linear trends with

r^2 values of 0.59 and 0.50, respectively, and support element immobility. The calc-alkalic rocks demonstrate strong linear trends between Nb and Gd versus Zr in which r^2 values are ≥ 0.94 . A strong trend is also observed in Th versus Zr ($r^2 = 0.83$), and a weak trend in La versus Zr ($r^2 = 0.44$). No correlation exists between TiO_2 and Yb versus Zr as r^2 values are 0.12 and 0.01, respectively, although these statistics are weak as there are only three calc-alkalic samples present. This demonstrates an overall element immobility between the trace elements, with the exception of TiO_2 and Yb within the calc-alkalic rocks, and the variation in trends defined by tholeiitic and calc-alkalic samples justifies the geochemical grouping. It is likely that TiO_2 mobility is a result of Ti-magnetite and/or ilmenite fractionation.

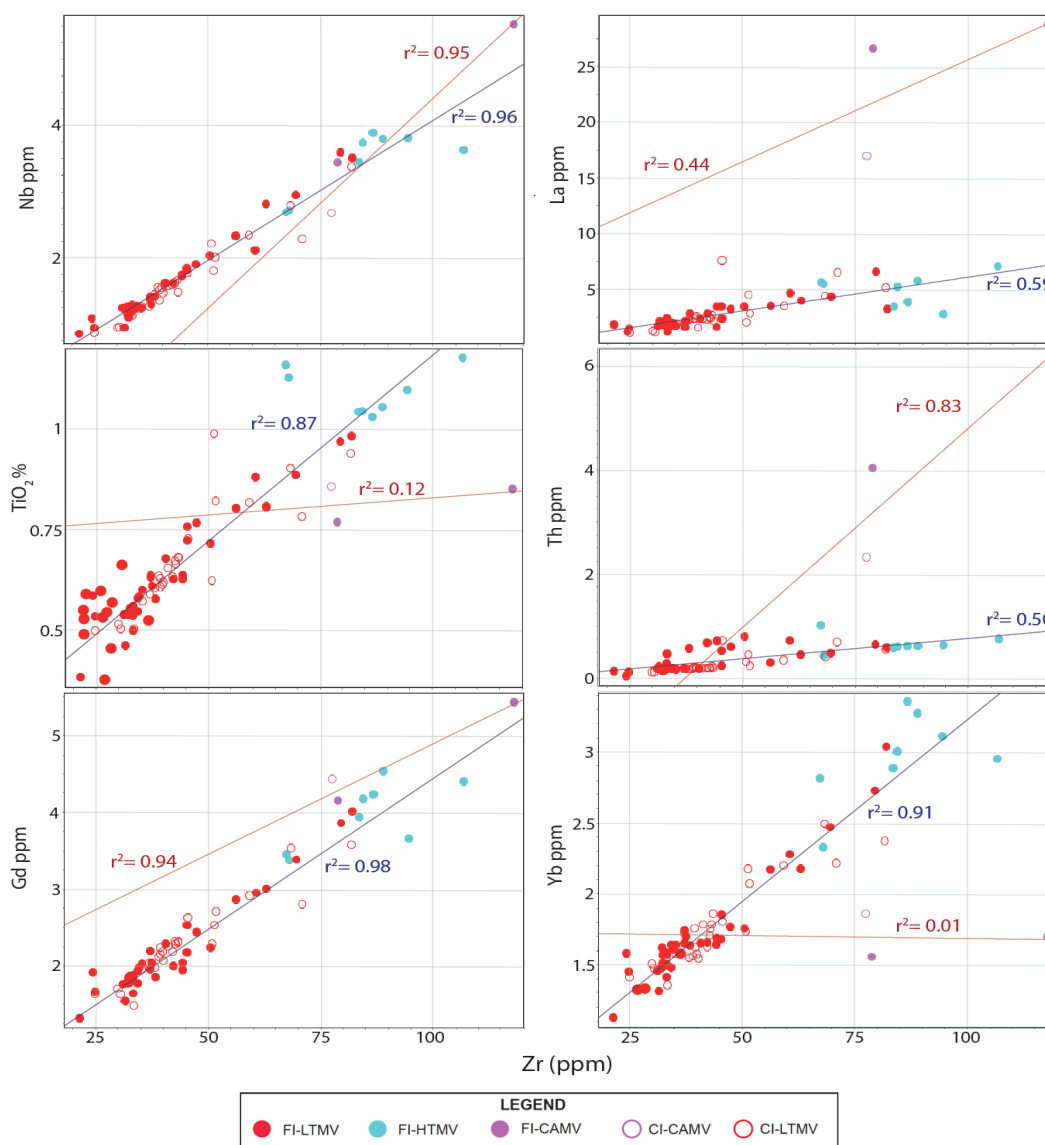


Figure 5.13. Element immobility diagrams for mafic metavolcanic rocks. Regression values given for the line of best fit on each diagram. Blue line: tholeiitic mafic rocks. Red line: Calc-alkalic mafic rocks.

The discrimination diagrams from Ross and Bédard (2009) use element pairs that demonstrate immobility under most alteration conditions because it is assumed that fractional crystallization does not separate one immobile element from the other and post-crystallization alteration can change the proportions of these elements but not their ratios. For this reason, it is likely that alteration processes have resulted in a tholeiitic classification on the Jensen diagram whereas rocks remain in the calc-alkalic domain on magmatic affinity diagrams (Figs. 5.5, 5.14).

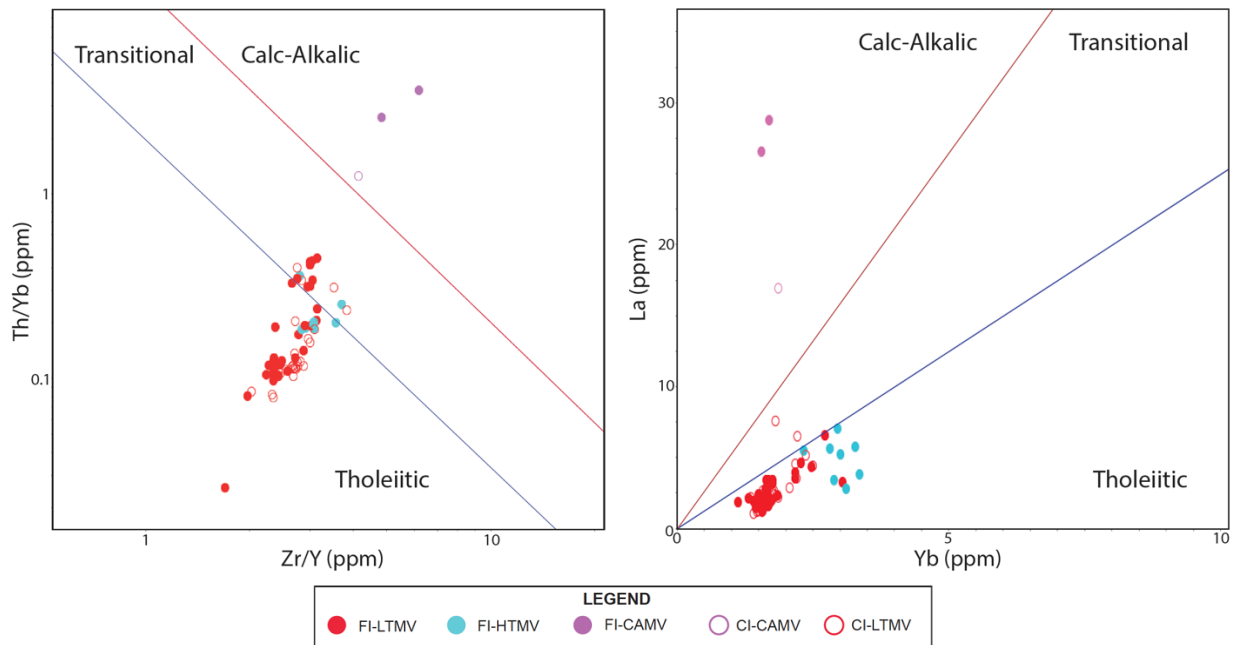


Figure 5.14. Magmatic affinity diagrams after Ross and Bédard (2009) for mafic volcanic rocks.

Primitive mantle normalized diagrams provided a distinction between tholeiitic and calc-alkalic rocks. The low-Ti tholeiites exhibit similar variations in primitive mantle patterns as the ultramafic metavolcanic rocks. These consist of samples with a zero to weak depletion in Nb, more pronounced depletion in Nb, and a LREE depletion (Fig. 5.15). The low-Ti basalts exhibit weak Nb anomalies with one sample with a more pronounced depletion, and one sample with a distinct Zr-Hf enrichment (Fig. 5.16). Low-Ti tholeiites exhibit a flat LREE pattern to weak LREE enrichment with $[La/Sm]_{pm}$ values of 1.48 to 3.52 with an outlier up to 4.86. Overall, samples exhibit flat HREEs ($[Gd/Yb]_{pm} = 1.32$ to 1.82). The majority of samples show a range in Nb anomalies ($Nb/Nb^* = 0.2$ to 1.09), however, there also positive Nb anomalies present within few samples in which a strong depletion of Th

occurs ($Nb/Nb^* = 1.31$; Fig. 5.17). A range in Ti anomalies exists with no correlation to the Nb anomalies, shown by the large scatter between Nb/Nb^* versus Ti/Ti^* (Fig. 5.17). Negative Ti anomalies exist over a range of Nb anomalies ($Ti/Ti^* = 0.25$ with $Nb/Nb^* = 0.46$ to 1.59). Some units exhibit positive and negative Eu anomalies ($Eu/Eu^* = 0.74$ to 1.82), however the majority of samples demonstrate zero to weak anomalies in Eu. Negative and/or positive Ti and Nb anomalies do not correlate to Eu anomalies.

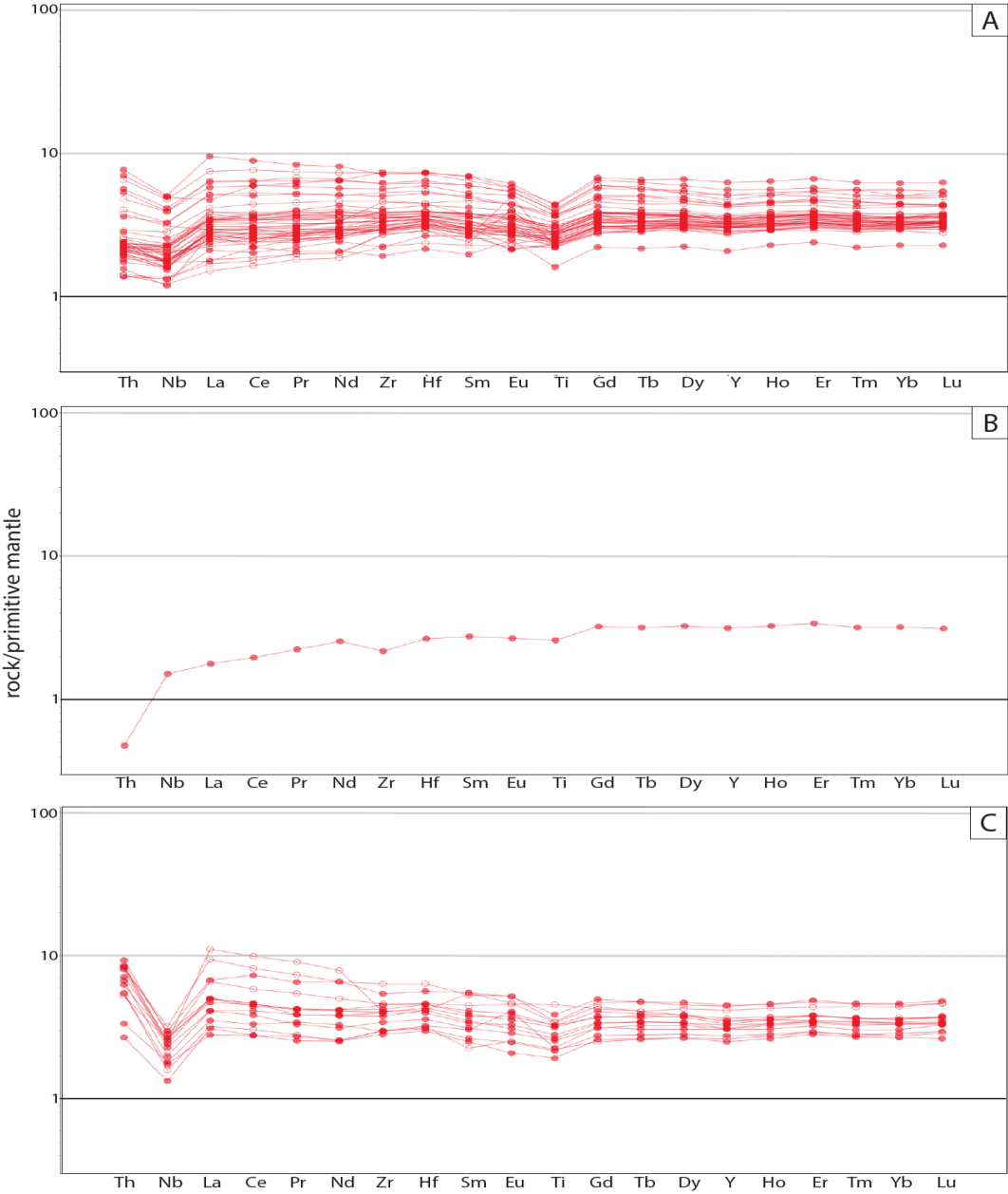


Figure 5.15. Primitive mantle normalized diagram of low Ti tholeiitic mafic volcanic rocks following normalizing values of Sun and McDonough (1989). A) Samples with weak Nb depletions. B) Samples with Th depletion. C) Samples with strong Nb depletion.

Primitive mantle patterns for high-Ti tholeiites do not differ greatly from low-Ti tholeiites (Fig. 5.16). They show moderately negative to weakly positive Nb anomalies and moderate to weak negative Ti anomalies ($Nb/Nb^* = 0.33$ to 1.59 ; $Ti/Ti^* = 0.62$ to 0.88 ; Fig. 5.17). They have a flat HREE pattern ($[Gd/Yb]_{pm} = 1.42$ to 1.80) and flat to enriched LREE ($[La/Sm]_{pm} = 1.72$ to 3.09).

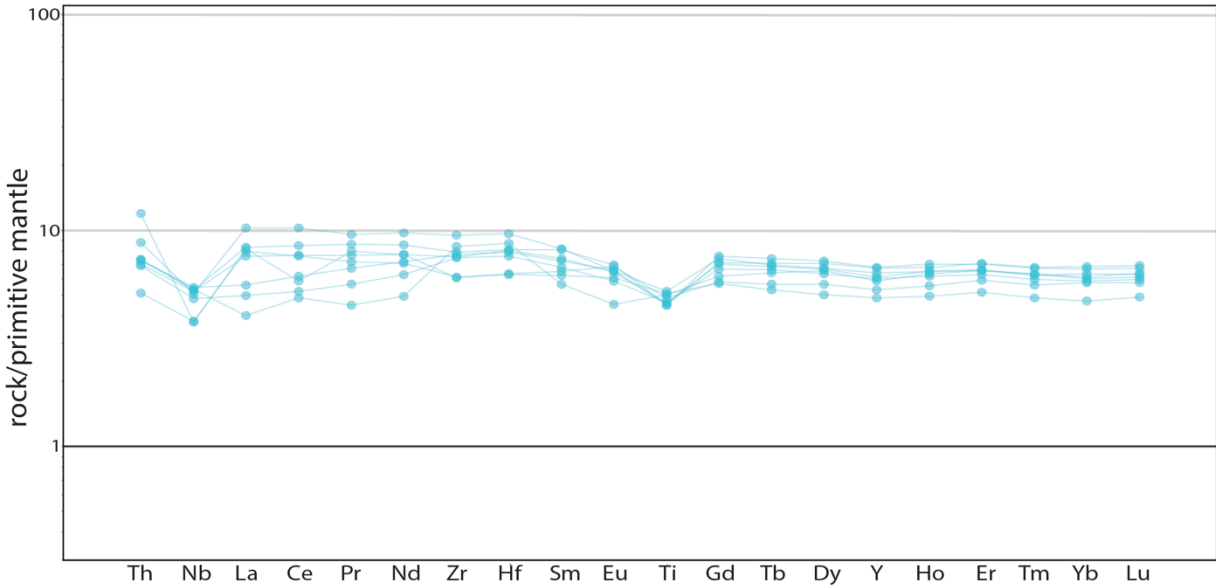


Figure 5.16. Primitive mantle normalized diagram of high-Ti tholeiitic mafic volcanic rocks following normalizing values of Sun and McDonough (1989).

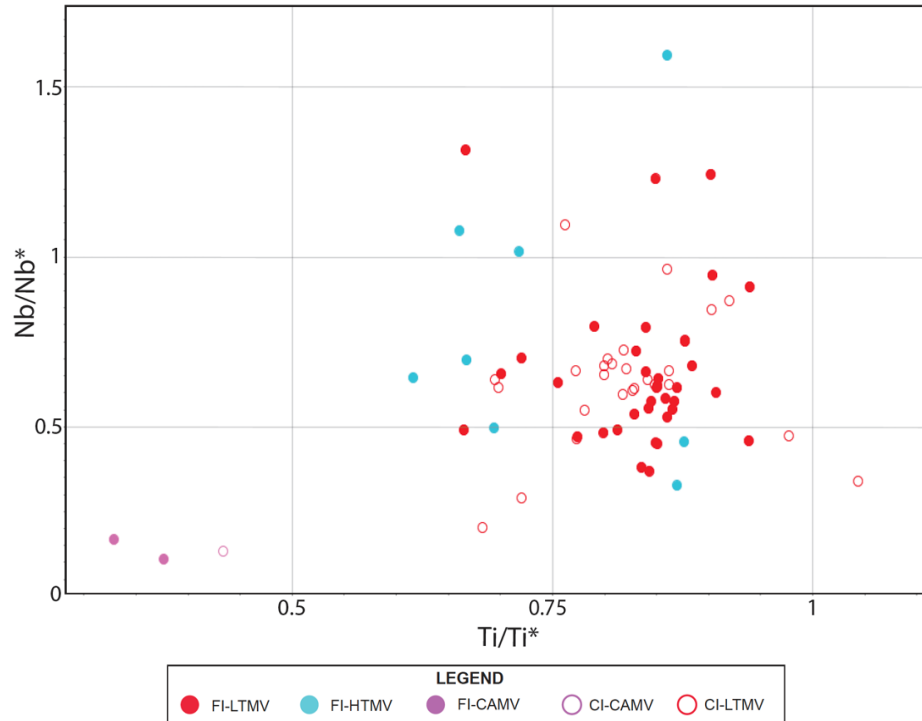


Figure 5.17. Bivariate plot of Ti/Ti^* versus Nb/Nb^* for mafic metavolcanic rocks.

Calc-alkalic rocks differ from tholeiitic rocks as they are typically LREE enriched with moderate LREE enrichment ($[La/Sm]_{pm} = 5.34$ to 7.31) relative to tholeiitic basalts, as well as depleted in Zr-Hf and have fractionated HREEs ($[Gd/Yb]_{pm} = 2.88$ to 3.87 ; Fig. 5.18). Strong negative Nb anomalies are observed ($Nb/Nb^* = 0.11$ to 0.17) and are accompanied by strong Ti depletions ($Ti/Ti^* = 0.32$ to 0.43 ; Fig. 5.17). Eu anomalies are not present in calc-alkalic units ($Eu/Eu^* = 0.94$ to 0.99).

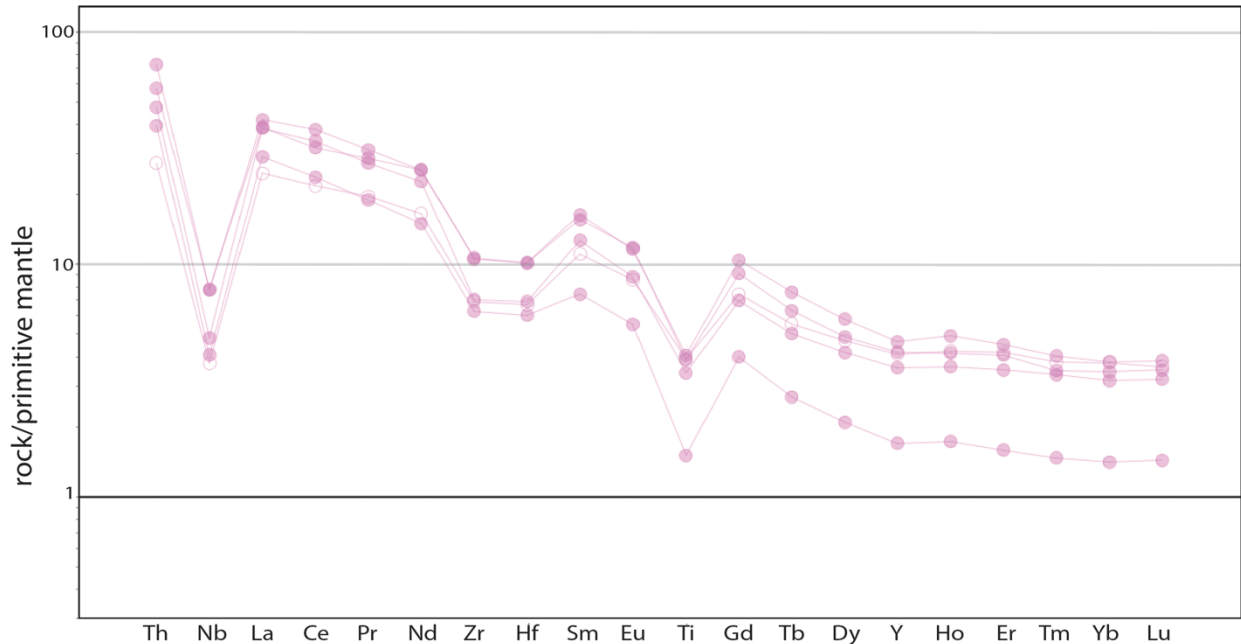


Figure 5.18. Primitive mantle normalized diagram of calc-alkalic mafic volcanic rocks following normalizing values of Sun and McDonough (1989).

5.1.3 Intermediate metavolcanic rocks

The intermediate volcanic rocks in the area were differentiated in the field by their siliceous nature relative to mafic volcanic rocks. On the rock classification after Le Maitre et al. (1989; Fig. 5.3), the intermediate rocks plot within the andesite field, however, on the classification diagram after Pearce (1996; Fig. 5.4) the rocks plot within the basalt field, suggesting silica alteration has affected the TAS diagram classification.

Intermediate rocks typically have SiO₂ contents of 57.8 to 61.7 wt%. There is a positive correlation between SiO₂ and MgO and negative correlation between SiO₂ and TiO₂ as well as Al₂O₃. The MgO content ranges from 3.9 to 10.3 wt% with increasing silica, a trend typically opposite of what is observed in previously mentioned lithologies. Trace element chemistry indicate a tholeiitic affinity with one sample plotting partially into the transitional field (Fig. 5.19).

On a primitive mantle normalized diagram, the intermediate rocks are characterized by a fairly flat overall pattern (Fig. 5.20). Weak negative Nb anomalies (Nb/Nb* = 0.44 to 0.66) are often accompanied by weak to zero negative Ti anomalies (Ti/Ti* = 0.77 to 0.90). The LREE show a relatively flat to slightly fractionated pattern ([La/Sm]_{pm} = 2.62 to 3.73) whereas the HREE maintain a fairly flat pattern within all samples ([Gd/Yb]_{pm} = 1.53 to 1.83).

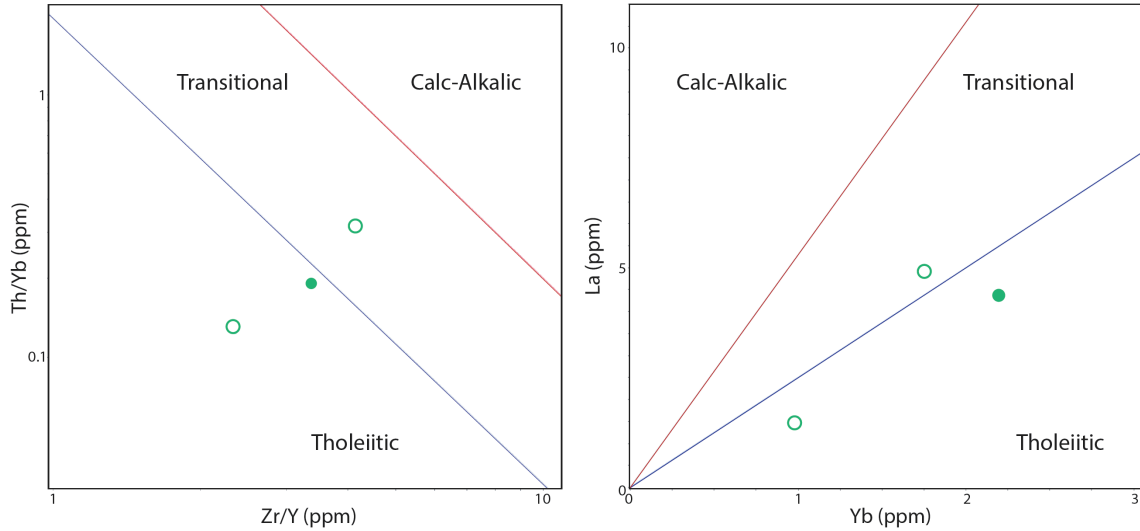


Figure 5.19. Magmatic affinity diagrams after Ross and Bédard (2009) for intermediate volcanic rocks.

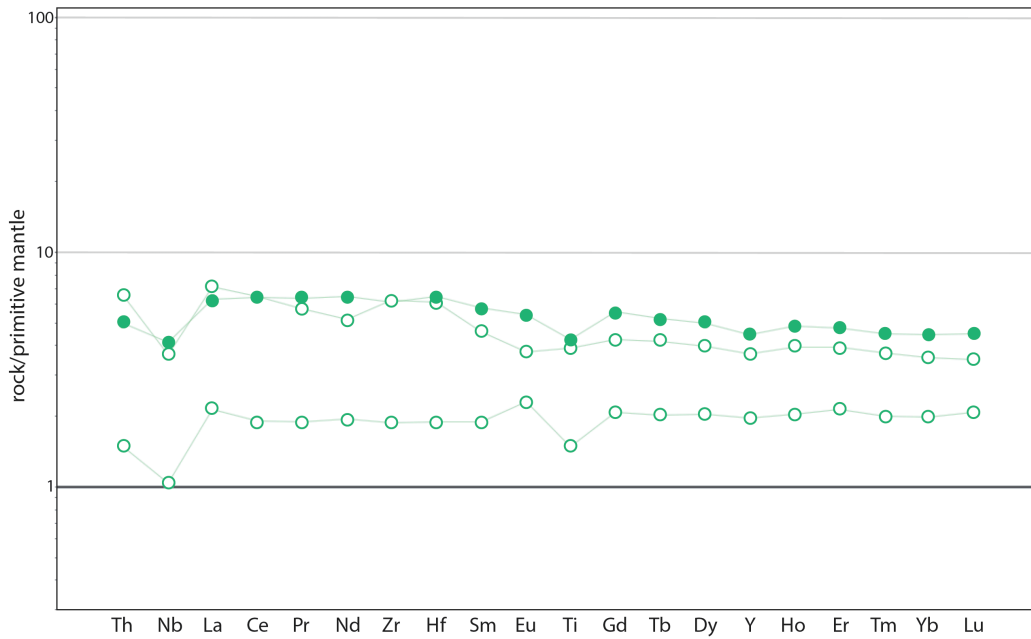


Figure 5.20. Primitive mantle normalized diagram of intermediate volcanic rocks. Normalizing values from Sun and McDonough (1989).

5.1.4 Intrusive Rocks

Intrusive rocks in the field area include 2,719 Ma gabbroic and cumulate intrusions as well as the 2694 ± 3 Ma Falcon Island Stock (syenite; Ayer and Davis, 1997). There is no correlation between most of the major element oxides and SiO_2 , however, there is a weak negative correlation between Fe_2O_3 and SiO_2 and a positive correlation with the alkali elements (Fig. 5.21). The gabbroic and cumulate samples range from 47 to 52 wt% SiO_2 with

one gabbroic sample reaching 55 wt%. The syenite samples have 53 and 57 wt% SiO₂ and generally have low concentrations of MnO, TiO₂, Fe₂O₃ and MgO (Fig. 5.21).

On a TAS diagram the gabbroic and cumulate samples plot in the gabbro to gabbroic diorite fields and the syenite samples plot within the monzodiorite and monzonite fields (Fig. 5.22). The mafic intrusive units show a weak variance in Na₂O + K₂O with a change in SiO₂ of over ~8 wt%, therefore producing the gabbro to gabbroic diorite classification (Figs. 5.21; 5.22). The Falcon Island Stock syenites have a concentration of Na₂O + K₂O and SiO₂ that is less than is characteristic syenite rocks, and therefore they plot as a monzonite and monzodiorite (Fig. 5.22). There is minimal variation in Na₂O + K₂O and SiO₂ concentrations of cumulate rocks and they consistently plot in the gabbro field (Fig. 5.22).

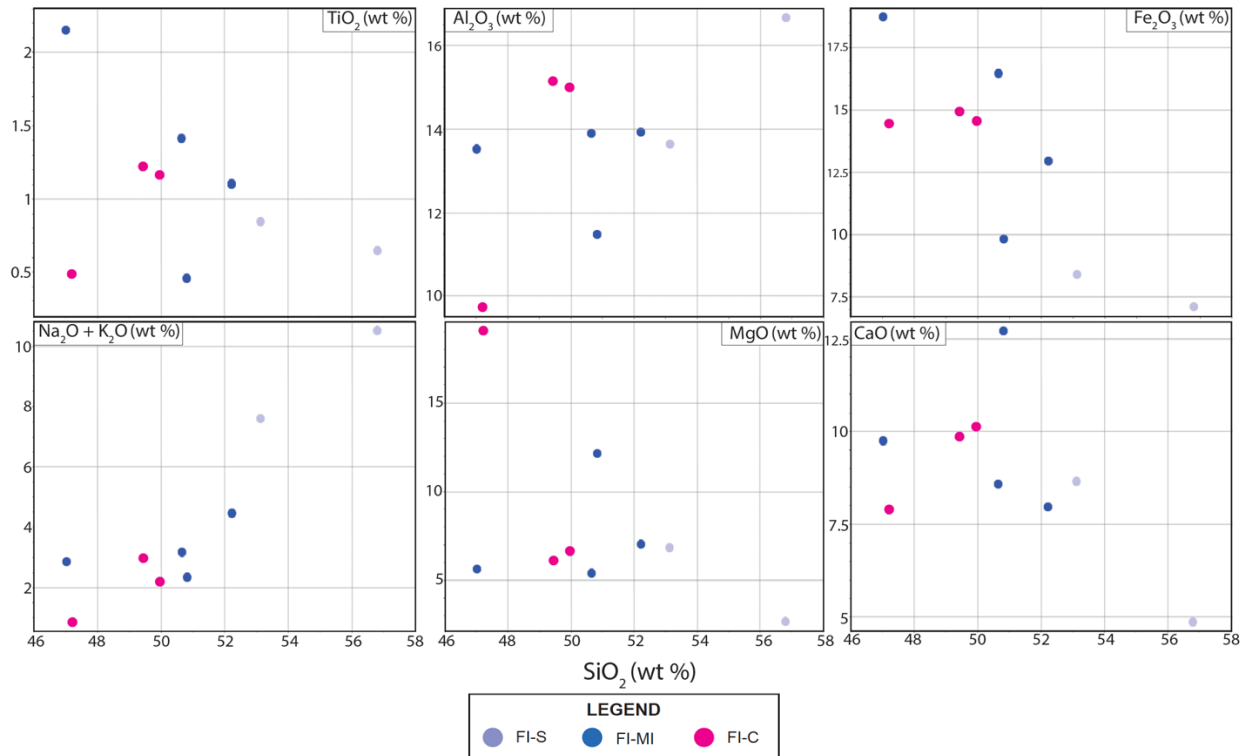


Figure 5.21. Harker diagrams for intrusive rocks. **FI**: Falcon Island. **S**: Syenite. **MI**: Mafic intrusive. **C**: Cumulate.

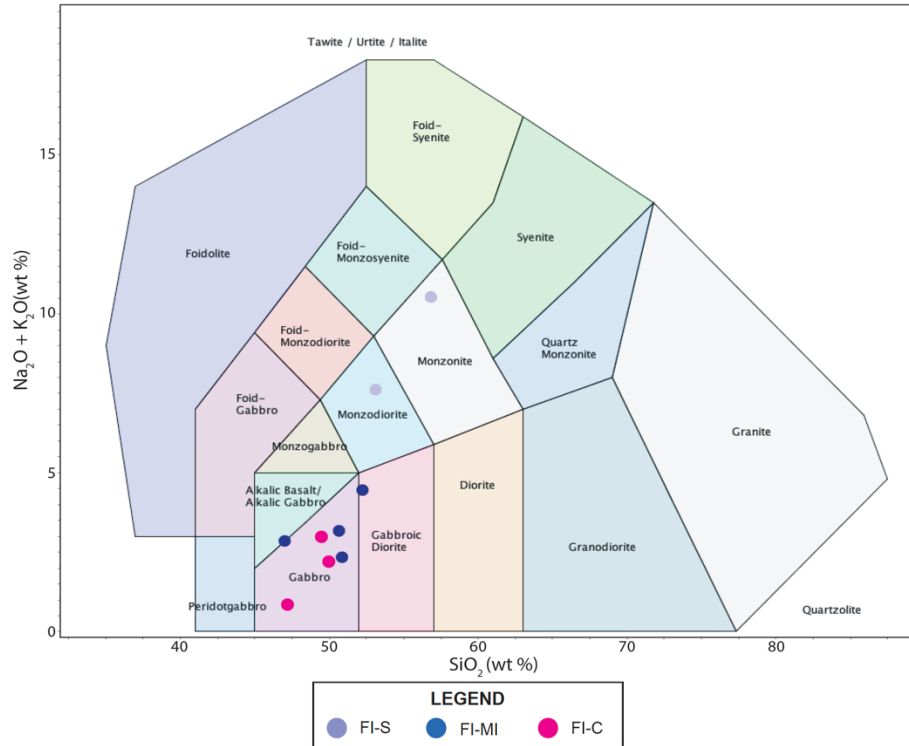


Figure 5.22. Silica versus total alkalis diagram after Middlemost (1994) for intrusive rock classification. **FI:** Falcon Island. **S:** Syenite. **MI:** Mafic intrusive. **C:** Cumulate.

The syenite samples plot within the calc-alkalic affinity field along with a gabbroic and cumulate sample on both diagrams after Ross and Bédard (2009; Fig. 5.23), however, only the syenite samples plot in the calc-alkalic regime when plotted on the AFM diagram (Fig. 5.5B). The gabbroic and cumulate samples follow the tholeiitic trend on the AFM diagram and plot in the calc-alkalic field on magmatic affinity diagrams, therefore indicating some likely mobility of the major elements as element pairs utilized in diagrams after Ross and Bédard (2009) are immobile under most alteration conditions. One cumulate sample plots in the transitional field on both diagrams; however, one gabbroic sample plots in the transitional field only on the Th/Yb versus Zr/Y.

There is great variability amongst primitive mantle normalized patterns of gabbroic and cumulate samples. Samples exhibit a variety of primitive mantle normalized patterns (Fig. 5.24). Some samples show strong negative Nb and Ti anomalies with enriched LREE and fractionated to flat HREE, whereas other samples exhibit weak Ti anomalies (both positive and negative anomalies) with weak to moderate negative Nb anomalies, and relatively flat rare earth elements (Fig. 5.24). Intrusive units that have calc-alkalic affinity

exhibit strong negative Nb ($Nb/Nb^* = 0.11$ and 0.16) and Ti anomalies ($Ti/Ti^* = 0.29$ and 0.34). Overall, the calc-alkalic intrusive rocks demonstrate a LREE enrichment relative to the tholeiitic intrusive units and a moderate LREE ($[La/Sm]_{pm} = 5.69$ to 9.39) and HREE fractionation ($[Gd/Yb]_{pm} = 4$ to 4.14). There is a moderate depletion in Zr and Hf relative to the LREEs seen within the HREE fractionated samples. One cumulate sample has a strong negative Nb anomaly ($Nb/Nb^* = 0.24$; however, it has a fractionated LREE and relatively flat HREE pattern ($[La/Sm]_{pm} = 3.77$; $[Gd/Yb]_{pm} = 1.72$). The tholeiitic intrusive rocks exhibit a moderate negative to zero Nb anomaly ($Nb/Nb^* = 0.58$ to 1.15) and dominantly weak to moderate negative Ti anomalies with one strong positive anomaly ($Ti/Ti^* = 0.67$ to 2.07). They exhibit a slight variability in their LREEs ($[La/Sm]_{pm} = 1.79$ to 2.36), but have a generally flat pattern. The HREEs exhibit the similar flat nature as $[Gd/Yb]_{pm}$ values range from 1.56 to 1.75 .

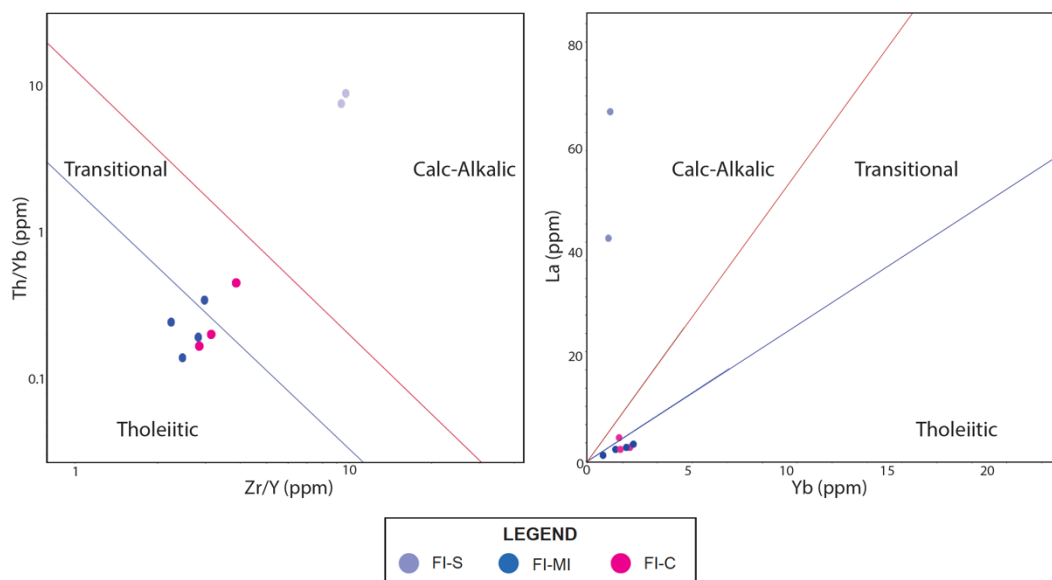


Figure 5.23. Magmatic affinity diagrams after Ross and Bédard (2009) for intrusive rocks.

The syenites of the Falcon Island Stock are characterized by a strong fractionation of the LREEs ($[La/Sm]_{pm} = 7.55$ and 9.74) and the HREEs ($[Gd/Yb]_{pm} = 6.97$ and 7.80 ; Fig. 5.25). The two samples have strong negative Nb and Ti depletions ($Nb/Nb^* = 0.08$ and 0.21 ; $Ti/Ti^* = 0.15$ and 0.19). Zirconium and Hf exhibit a depletion relative to surrounding elements, similar to the depletion present within the HREE depleted calc-alkalic intrusive

rocks. There is no spatial correlation to the intrusive rocks that plot as calc-alkalic rocks and the Falcon Island Stock.

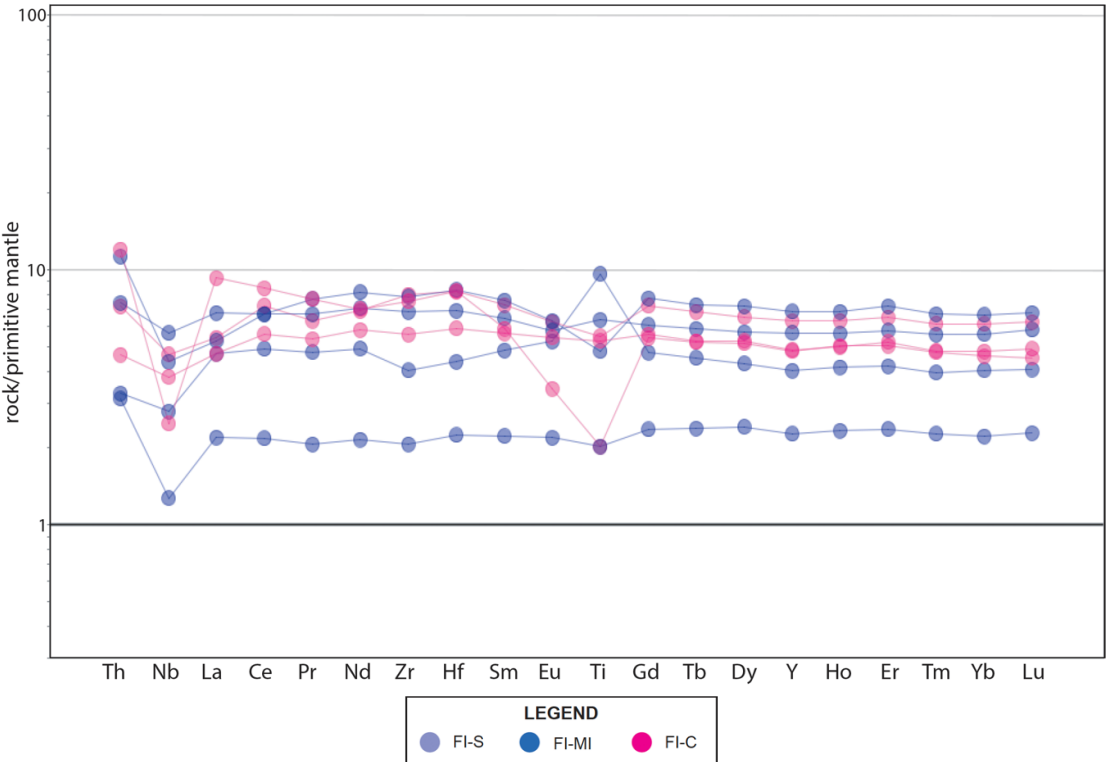


Figure 5.24. Primitive mantle normalized diagram of intrusive rocks following normalizing values of Sun and McDonough (1989).

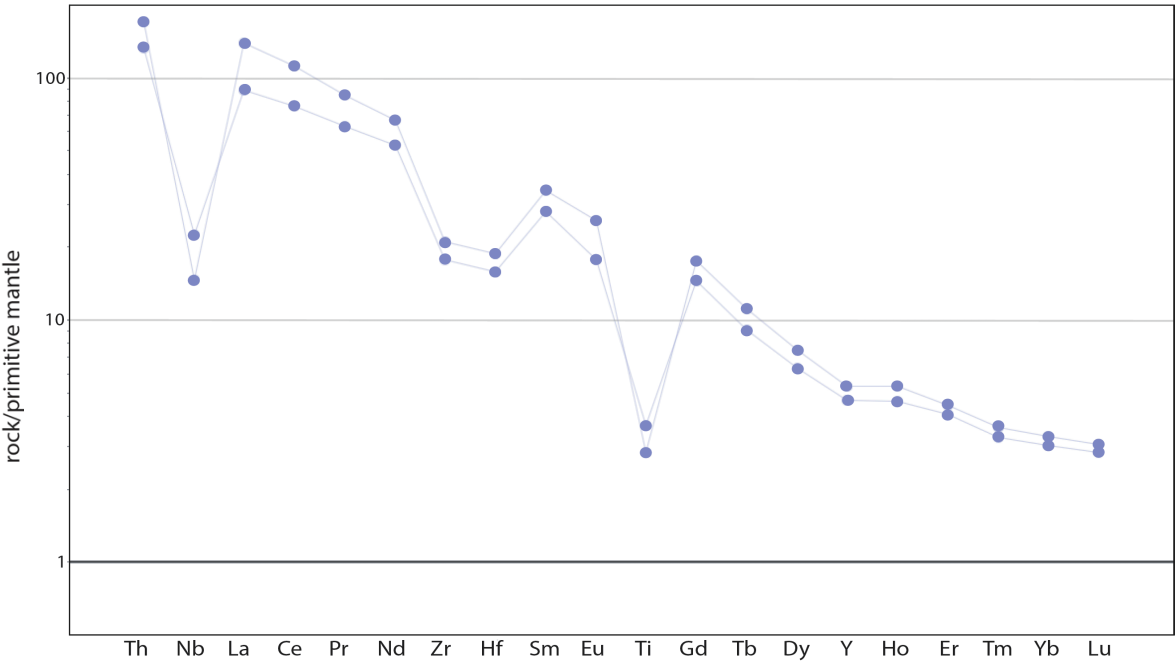


Figure 5.25. Primitive mantle normalized diagram of Falcon Island Stock syenites following normalizing values of Sun and McDonough (1989).

5.2 Mineral Chemistry

The main phase in the majority of samples was amphibole which occurred in many Fe- to Mg-rich varieties, with one sample containing both pyroxene and amphibole as major phases. The groundmass consisted predominantly of chlorite and chloritoid minerals. Anomalous samples consisted of pyroxene, talc, apatite, chromite, and serpentine. Ilmenite was common throughout all samples often associated with amphibole phases as well as dispersed throughout the groundmass. Detailed mineral chemistry can be found in Appendix D.

5.2.1 Pyroxene Chemistry

One ultramafic sample contained pyroxene grains as randomly oriented thin needles. A total of 33 pyroxene grains were analyzed. The pyroxene grains plot within the enstatite field (Fig. 5.26). The average formula for pyroxene within the sample is $\text{Ca}_{0.04}(\text{Mg}_{1.53}\text{Fe}_{0.87}\text{Mn}_{0.03})\text{Si}_{1.76}\text{O}_6$ with an average Mg number of 75.79 (range from 74.92 to 77.26).

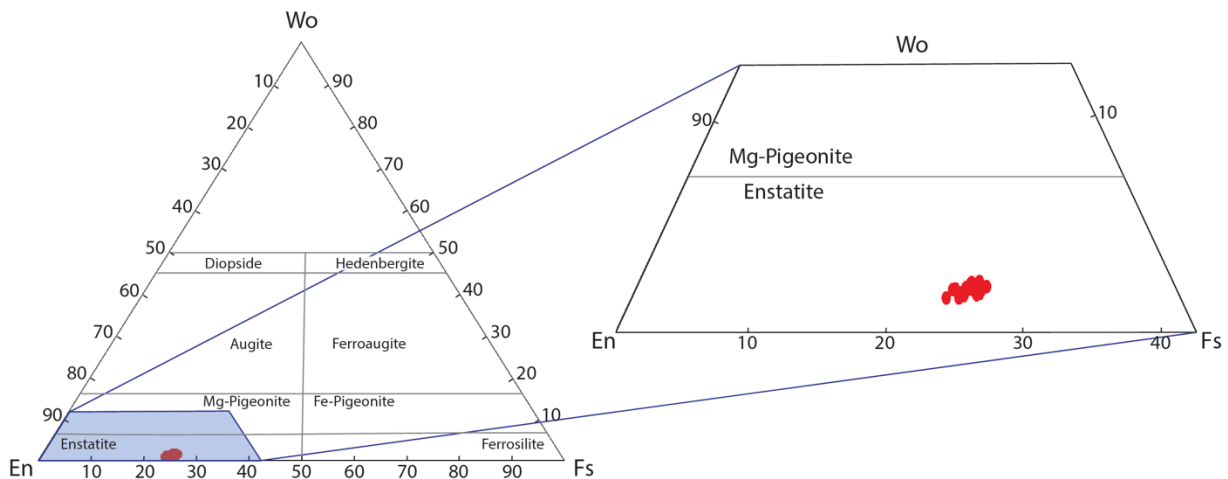


Figure 5.26. Pyroxene classification diagram (modified after Sushchevskaya et al., 2008).

5.2.2 Amphibole Chemistry

Amphibole species throughout the analyzed samples varied considerably. Samples with higher concentrations of MgO were composed of highly magnesian amphibole species (e.g., tremolite and anthophyllite) whereas more mafic samples contained Fe-rich amphibole species. Amphibole classification follows the methods and nomenclature of Leake et al. (1997). The range in chemical formulas for each amphibole species is given in Table 4.1.

Ultramafic samples contained grains that exhibited cores with tremolite composition and irregular rims with anthophyllite composition (Fig. 5.27). The presence of anthophyllite rims indicates a loss in calcium from core to rim as anthophyllite has a lesser concentration of CaO relative to tremolite. The average tremolite chemical formula is $(\text{Ca}_{1.82}\text{Na}_{0.04})(\text{Mg}_{4.34}\text{Fe}^{3+}_{0.63}\text{Fe}^{2+}_{0.12})(\text{Si}_{7.84}\text{Al}_{0.17})\text{O}_{22}(\text{OH})_2$ and anthophyllite is $(\text{Ca}_{0.15}\text{Mg}_{1.85})(\text{Mg}_{3.05}\text{Fe}^{3+}_{0.58}\text{Fe}^{2+}_{1.32}\text{Mn}_{0.06})(\text{Si}_{7.92}\text{Al}_{0.06})\text{O}_{22}(\text{OH})_2$. In the sample that hosts pyroxene and serpentine, tremolite hosts up to 6.33 wt% Cr_2O_3 , a concentration that is not seen in other samples. One ultramafic sample (LOW17CB67) is composed of actinolite and actinolitic- to tremolitic-hornblende and exhibits higher SiO_2 and lower in MgO whole-rock geochemistry than other ultramafic samples that are typically composed of tremolite and anthophyllite (Fig. 4.34). The average chemical formula for actinolite is $(\text{Ca}_{1.8}\text{Na}_{0.36})(\text{Mg}_{3.81}\text{Fe}^{3+}_{0.80}\text{Fe}^{2+}_{0.24})(\text{Al}_{0.06}\text{Si}_{7.36})_{22}(\text{OH})_2$. Rare grains of tremolite are scattered throughout.

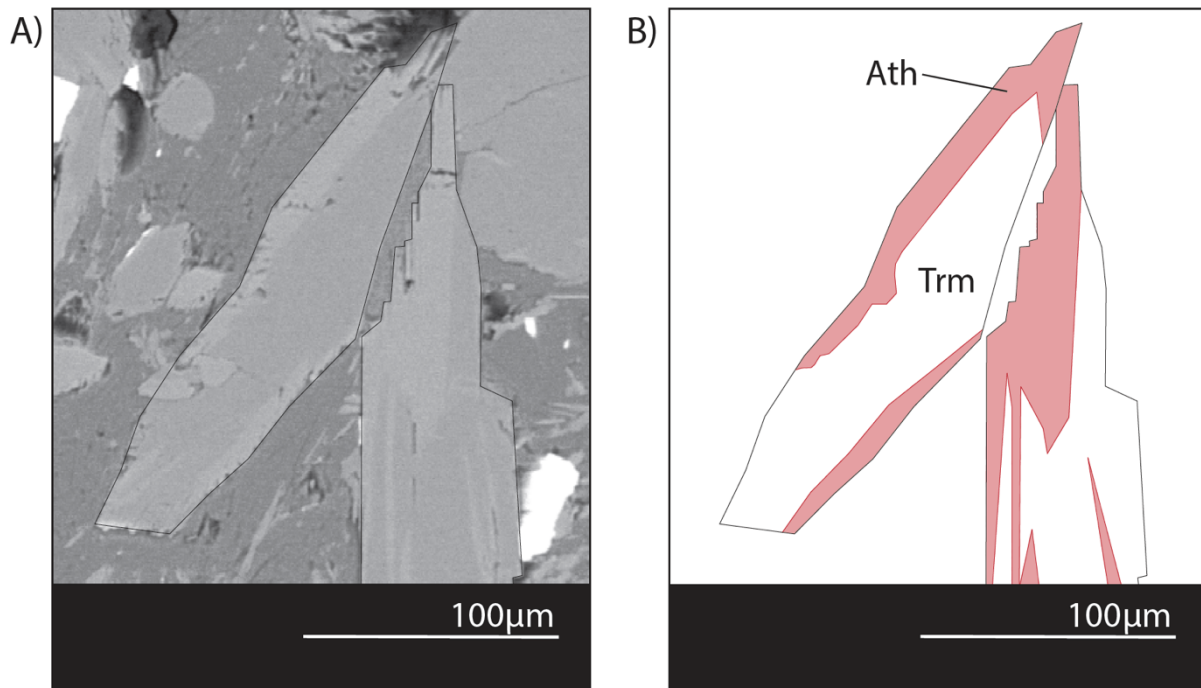


Figure 5.27. Amphibole grains demonstrating tremolite (grey) and anthophyllite (lighter grey) compositions. A: BSE image of two amphibole grains. B: A Schematic diagram illustrating the change in amphibole species throughout the grains.

The cumulate sample that was analyzed is composed of tschermakitic hornblende with an average chemical formula of $(\text{Ca}_{1.86}\text{Na}_{0.39}\text{K}_{0.08})(\text{Mg}_{1.81}\text{Fe}^{3+}_{0.56}\text{Fe}^{2+}_{1.84})(\text{Si}_{6.33}$

$\text{Al}_{1.67}\text{O}_{22}(\text{OH})_2$. Within the cumulate sample, there was little variation between amphibole species in cumulates versus amphibole grains scattered throughout the groundmass.

5.2.3 Accessory Phase Chemistry

Accessory phases comprise less than 5% of the modal abundance of a sample and include rare chromite and apatite as well as abundant ilmenite.

5.2.3.1 Chromite

Chromite was found in sample LOW17CB43 interstitial to amphibole phenocrysts within the groundmass, as well as very fine-grained inclusions within tremolite grains. Only two chromite grains were analyzed with a formula of $\text{Mg}_{0.02}\text{Al}_{0.2}\text{Ti}_{0.02}\text{Cr}_{1.07}\text{Fe}_2\text{O}_4$. The analyzed chromites exhibit Cr numbers ($\text{Cr\#} = \text{Cr}/[\text{Cr} + \text{Fe}^{3+}]$) of 38.08 and 45.47.

5.2.3.2 Ilmenite

Ilmenite was present in many samples throughout the field areas. It is often rounded to subhedral and scattered throughout the groundmass as well as associated with amphibole phases. The average chemical formula for ilmenite was $\text{Fe}_{1.37}\text{Ti}_{0.73}\text{Mn}_{0.14}\text{O}_3$.

5.2.3.3 Apatite

Apatite occurred in one sample as dispersed fine subhedral grains. Three apatite analyses produced an average chemical formula of $\text{Ca}_{5.22}(\text{P}_{3.66}\text{O}_4)_3(\text{OH})$.

5.3 Samarium-Neodymium Isotopes

Five mafic and five ultramafic samples were chosen for radiogenic isotope analyses to investigate the magmatic source of the rocks and to evaluate the presence and/or degree of crustal contamination (Table 5.1). One syenite sample was taken from the Falcon Island Stock. An age of 2719 Ma was used in order to re-calculate the ϵ_{Nd} of mafic and ultramafic samples, and an age of 2694 Ma was used for the syenite sample (Ayer and Davis, 1997). Full results for Sm-Nd isotope data is presented in Appendix C.

The ϵ_{Nd} values of the samples are from ultramafic rocks that exhibited primitive mantle pattern variations, for example, two samples have LREE depletion, two samples have

a distinct negative Nb anomaly, and two samples have similar Th and Nb values (Fig. 5.28). The samples with Nb depletions (LOW17CB62/68) have ϵ_{Nd} values of +1.07 and +1.63, samples with a LREE depletion and flat HREE pattern (LOW17CB28/69) have ϵ_{Nd} of +2.62 and +2.66, and the sample with equal Th and Nb with relatively flat HREE (LOW17CB92) has an ϵ_{Nd} of +2.14. Although there is strong variation between primitive mantle patterns, that variation is not reflected in the radiogenic isotope signatures.

Two mafic samples are low-Ti basalts (plot in the komatiitic basalt field on Jensen plot). One sample taken from Falcon Island exhibits LREE depletion and flat HREE (LOW17CB96) and has an ϵ_{Nd} of +1.50 and the other sample taken from Cliff Island has enriched Th and flat HREE (LOW17CB41) with an ϵ_{Nd} of +1.59. The high-Ti basalt (LOW17CB91) is LREE enriched relative to the other mafic and ultramafic samples with a moderate Th enrichment and has an ϵ_{Nd} of +0.95, lower than all other samples collected. Two calc-alkalic samples with similar Nb and Zr-Hf depletions as well as weakly fractionated HREEs have ϵ_{Nd} signatures of +1.71 (LOW17CB14) and +2.52 (LOW17CB22).

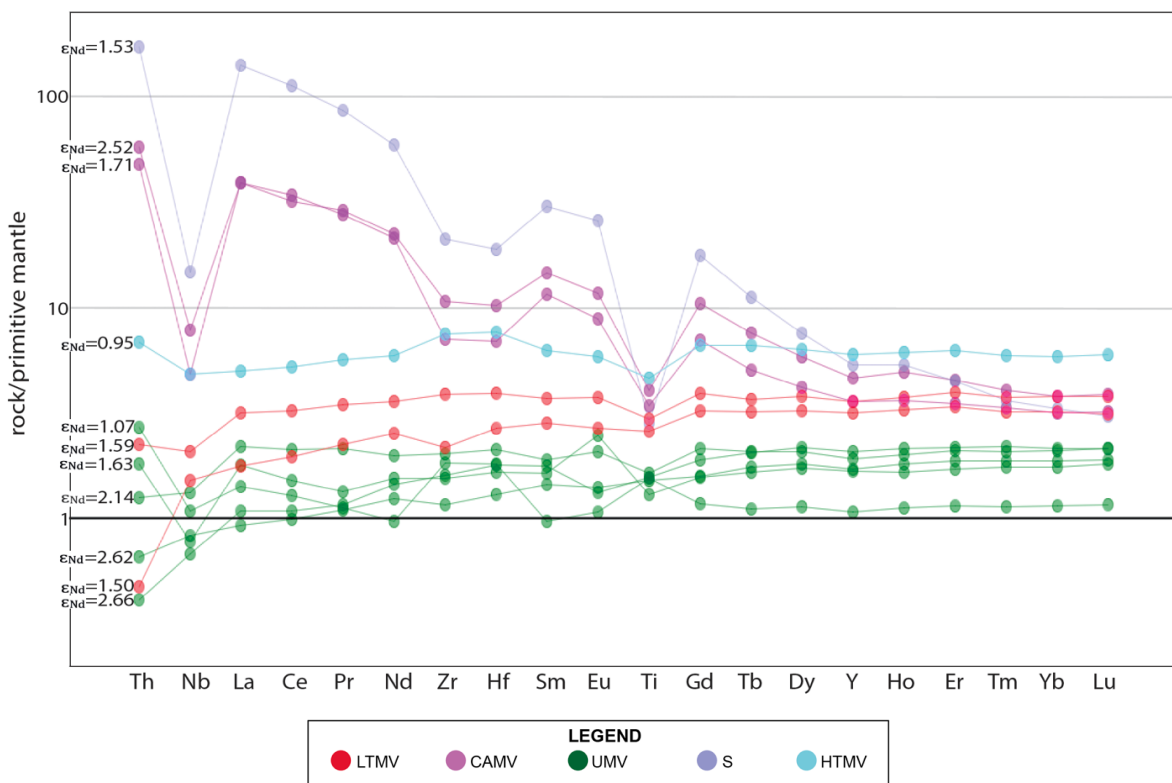


Figure 5.28. Primitive mantle normalized diagram of ultramafic samples and one mafic sample with corresponding ϵ_{Nd} values. Normalizing values from Sun and McDonough (1989).

One sample was taken from the Falcon Island Stock syenite (LOW17CB31) which shows similar primitive mantle patterns as the calc-alkalic mafic volcanic rocks sampled from Falcon Island. The ϵ_{Nd} signature of +1.53 is also similar to other samples.

Table 5.1. Results of radiogenic isotope analyses.

Sample	Rock Type	Age (Ma)	$^{143}\text{Nd}/^{144}\text{Nd}$ (current)	$^{143}\text{Nd}/^{144}\text{Nd}$ (initial)	ϵ_{Nd}
LOW17CB10	Metasedimentary	2719	0.511005	0.50924	1.83
LOW17CB14	Calc-Alkalic Volcanic	2719	0.511126	0.50920	1.71
LOW17CB22	Calc-Alkalic Volcanic	2719	0.511564	0.50924	2.52
LOW17CB28	Komatiite	2719	0.513397	0.50924	2.62
LOW17CB31	Syenite	2694	0.511027	0.50922	1.53
LOW17CB62	Komatiite	2719	0.512725	0.50916	1.07
LOW17CB68	Komatiite	2719	0.512736	0.50923	1.64
LOW17CB69	Komatiite	2719	0.512955	0.50920	2.66
LOW17CB91	High-Ti Tholeiite Volcanic	2719	0.512914	0.50916	0.95
LOW17CB92	Komatiite	2719	0.513596	0.50924	2.14
LOW17CB96	Low-Ti Tholeiite Volcanic	2719	0.512606	0.50922	1.50
LOW18CB41	Low-Ti Tholeiite Volcanic	2719	0.512869	0.50919	1.59

Chapter 6: Discussion

6.1 Mineralogy and Field Observations

The Upper Keewatin assemblage is comprised of a variety of volcanic units that include tholeiitic mafic to ultramafic volcanic rocks and calc-alkalic mafic volcanic rocks. Both the calc-alkalic and tholeiitic rocks contain varying amounts of metamorphic amphiboles and chlorite \pm plagioclase. These units are commonly weakly foliated amphibolites and schists with minor non-foliated amphibolites. Ultramafic rocks of komatiitic affinity are composed dominantly of chlorite with tremolite, talc and lesser anthophyllite. Rare secondary phases within ultramafic rocks include apatite, chromite, serpentine and enstatite.

6.1.1 Mafic to Ultramafic Volcanic Rocks

The mafic metavolcanic rocks, which comprise the majority of the field area, consist of high- and low-Ti tholeiites and rare calc-alkalic units that occur as a variety of amphibolites and chlorite-tremolite schists. When plotted on a Jensen plot, there is a visible correlation between geochemistry and petrography in which high-Ti tholeiites are commonly black amphibolites and low-Ti tholeiites commonly as grey amphibolites consisting of hornblende and minor tremolite (Fig. 6.1). The low-Ti and high-Mg tholeiitic samples transition from lighter to darker greys and finally black as they progress into the high-Fe tholeiitic basalt field where the high-Ti tholeiite samples reside. As samples transition into the komatiitic basalt field and become more Mg-rich, they typically exhibit moderate to strong schistosity, contain increased abundances of chlorite, and are therefore chlorite-tremolite schists (Fig. 6.1).

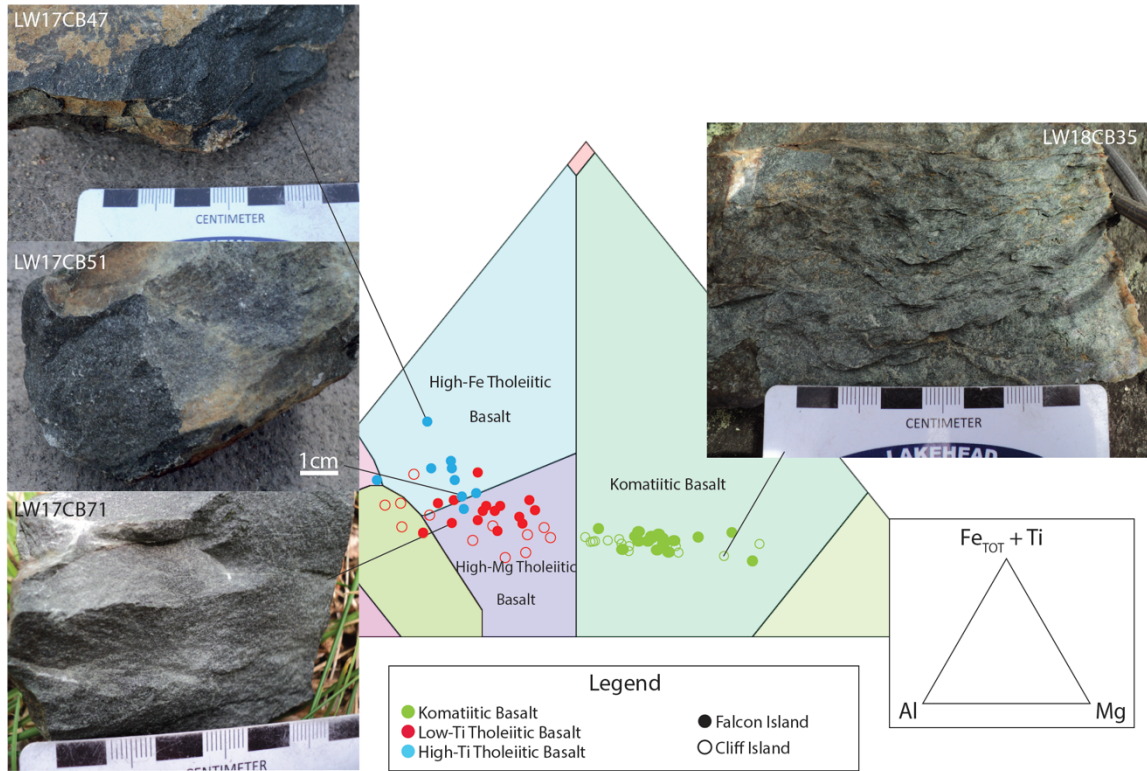


Figure 6.1. Jensen cation plot after Rollinson (2013) plotting tholeiitic mafic volcanic rocks and komatiitic basalts with corresponding hand sample photographs.

There is an increase in degree of foliation when samples transition from high-Fe and high-Mg tholeiitic basalt to komatiitic basalt (Fig. 6.2). Overall, the field area is comprised dominantly of weakly to moderately foliated units with only localized lenses of highly foliated and non-foliated samples (Fig. 6.2). High-Mg tholeiites are typically weakly to non-foliated amphibolites with rare moderately foliated schistose samples occurring in proximity to basaltic komatiites and komatiite samples. High-Fe tholeiites are black, non-foliated amphibolites that occur in small lenses throughout the field area. Basaltic komatiite samples range from weak to intensely foliated samples, generally the more Mg-rich samples contain stronger foliation and occur in proximity to ultramafic komatiite samples. Highly foliated samples also occur in minor lenses scattered throughout the field area. Komatiite samples are typically highly foliated; however, some samples show moderate foliation and are composed of increased amounts of amphibole compared to strongly foliated komatiites that contain dominantly chlorite and/or serpentine.

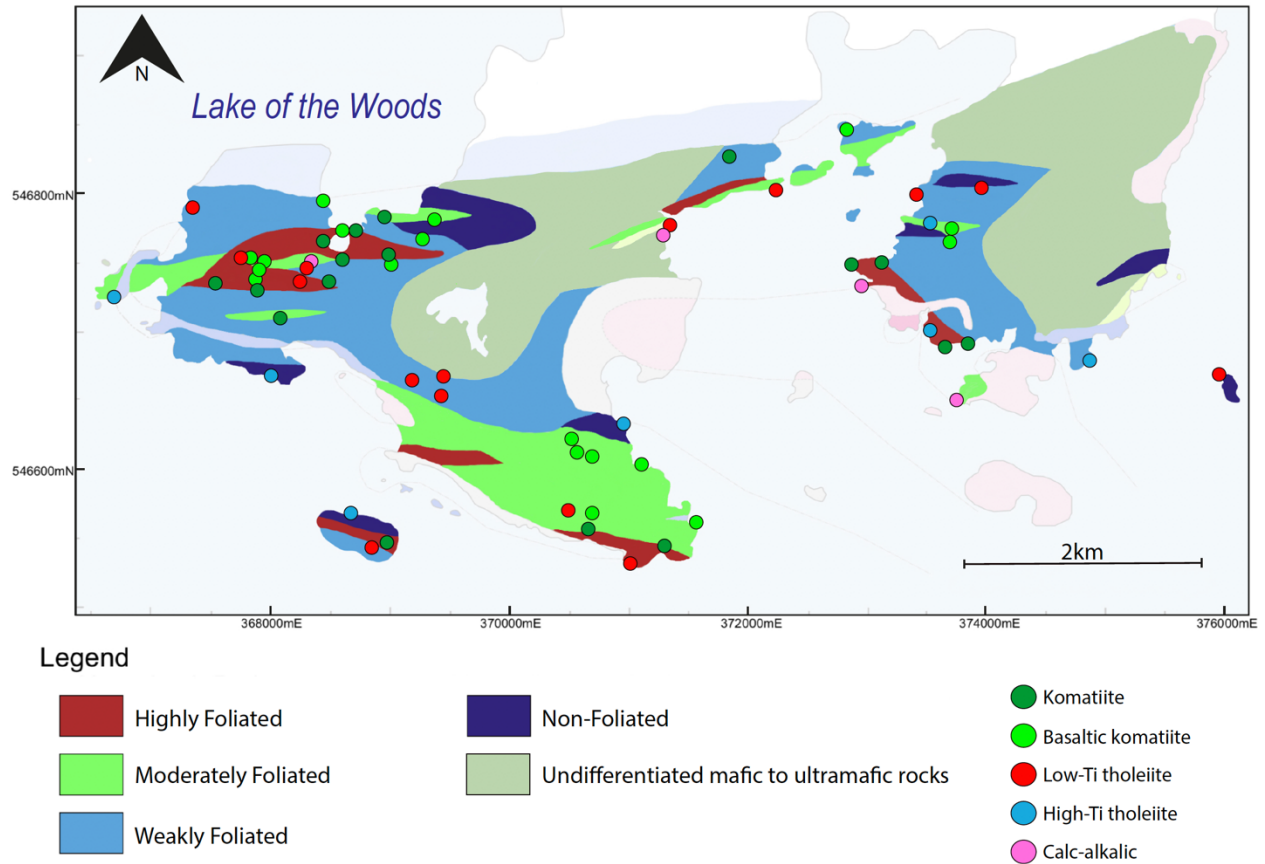


Figure 6.2. Geological map of Falcon Island with degree of foliation and geochemical classifications.

6.1.2 Textural Variability in Amphibolites

The amphibolites in the field area are often non-foliated to weakly foliated and consist dominantly of hornblende with minor actinolite and tremolite. The main variation between amphibolites is the habit of metamorphic amphiboles, for example, amphibolites that are Fe-rich and black in hand sample (Fig. 6.1) consist of fine-grained poikiloblastic hornblende that hosts quartz and plagioclase inclusions and are often randomly oriented throughout the sample. Poikiloblasts are porphyroblasts that incorporate numerous inclusions that typically grow at the same time but inclusions cease growing once enclosed by the poikiloblast (Vernon, 2004). Porphyroblasts are mechanically more resistant to deformation than the surrounding finer grained matrix and create a variation in the grain size between porphyroblasts and the surrounding matrix. Typically, porphyroblastic minerals will not nucleate in zones of active progressive shearing, but they will often nucleate and grow in zones of progressive shortening as syn-deformational growth (Bell et al., 1986). Since strain

is highly important during deformation, and strain in deformed rocks is extremely heterogeneous, it is possible that the strain heterogeneity caused the various forms of amphibole porphyroblasts in the amphibolites of this study.

6.1.3 Metamorphism and Deformation of Ultramafic Rocks

The metamorphism of ultramafic rocks can produce various mineral assemblages including serpentine, diopside, forsterite, tremolite, talc, anthophyllite, and enstatite depending on pressure and temperature conditions (Spear, 1993). The composition of metamorphic minerals in metamorphosed komatiites depends not only on the metamorphic conditions, but also on the bulk composition and primary mineralogy of the lava (Arndt, 1994). It is likely that the fluid phase involved in the metamorphism was predominantly H₂O as there is rare to no calcite present in ultramafic rocks, as would be expected if the fluid phase was CO₂ rich. Chlorite is produced in metamorphosed komatiite flows containing less than approximately 25 wt% MgO, serpentine in flows containing 25 to 35 wt% MgO, and serpentine-brucite in more magnesian flows (Arndt, 1994). The mineral assemblages present within the ultramafic samples in the field area contain chlorite, talc, serpentine and abundant amphibole phases. Samples that contain serpentine have MgO concentrations of 24 to 27.5 wt%, while chlorite-rich samples contain concentrations of MgO from 21.4 to 25.4 wt%. Chlorite-rich samples with higher concentrations of magnesium (MgO > 24 wt%) are accompanied by talc. Observations from ultramafic samples are consistent with typical metamorphic minerals of metamorphosed komatiites containing various concentrations of magnesium.

Tremolite cores analyzed in ultramafic samples in this study have Mg numbers ranging from 0.78 to 0.90 and when anthophyllite rims are present, they contain Mg numbers from 0.64 to 0.71 (Fig. 6.3). Similar to ultramafic rocks in the field area, metamorphosed komatiite flows of the Sula Mountains greenstone belt of the West African Archaean Craton contain 24 to 31 wt% MgO and exist as a variety of tremolite-chlorite and tremolite-chlorite-talc schists (Rollinson, 1999). The Sula Mountains komatiites typically have tremolite porphyroblasts that crosscut the foliation and have Mg numbers of 0.86 to 0.93 (Rollinson, 1999). The various opaque minerals include Cr-magnetite, ilmenite, pyrite

and arsenopyrite. It is probable that tremolite present in the samples formed as porphyroblasts rather than replacement of pyroxene in many or most cases, given that it overprints foliation. Samples in this study have coarser-grained subhedral tremolite as well as tremolite blades with similar grainsize as the chlorite matrix, therefore it is possible that amphiboles exist as both replacements and porphyroblasts.

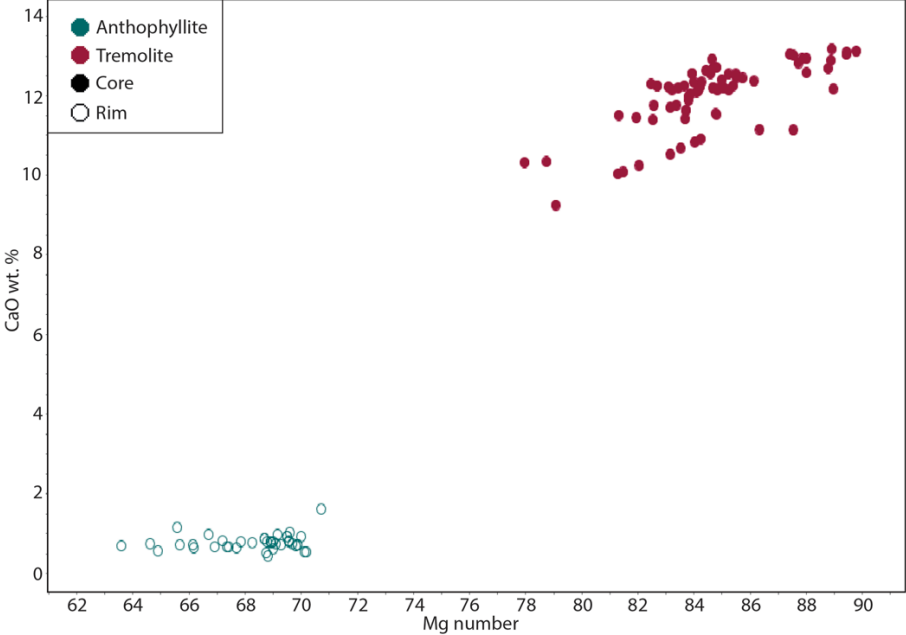


Figure 6.3. Amphibole porphyroblast mineral chemistry plotting CaO wt% versus Mg#.

The variation in amphibole species may also reflect the metamorphism of different portions of a differentiated flow where mineralogical differences would dictate the amphibole species present. For example, the metamorphism of komatiites and basalts from the Tungurcha greenstone belt in the Aldan Shield shows variation in mineral assemblages including actinolite-rich upper portions and tremolite- and anthophyllite-rich lower portions (Puchtel et al., 1993). The fine-grained zones of the flow, likely representing the upper chilled layer, is composed of short prismatic crystals of actinolite, talc, chrome magnetite and anthophyllite (Puchtel et al., 1993). Typically, the top of komatiitic flows contain abundant actinolite approximately 0.2 mm long and when progressing to the bottom of the flow crystals increase to 2 mm long and are dominantly tremolite and anthophyllite (Puchtel et al., 1993). If amphibole species present in the study reflected various facies of a komatiite flow, there would likely be a spatial correlation between amphibole species. As

individual flows were not observed in the field and there is no spatial correlation, it is likely that the various amphibole species are simply a reflection of chemistry of the host rock and do not represent zones of the flow.

Pyroxene grains analyzed in an ultramafic sample plot within the enstatite field (Fig. 5.26). They occur as randomly oriented thin needles typically 1mm in length, however, many needles are also very fine-grained (<1 mm). The pyroxene compositions are not consistent with mineral chemistry of many well-documented komatiitic flows as pyroxene spinifex typically consists of clinopyroxenes, although some authors suggest orthopyroxene is present within wet komatiite flows (Grove and Parman, 2004; Faure et al., 2006). It is also questionable why tremolite and anthophyllite are present in samples with abundant enstatite that is devoid of metamorphic amphiboles. In such samples it might be expected that the replacement amphiboles to effect pyroxenes present equally, i.e. all pyroxene grains would likely exhibit a degree of metamorphism to amphibole grains. It is possible the enstatite crystals are of metamorphic origin as enstatite is a common porphyroblast phase in ultramafic rocks at higher temperatures (Spear, 1993). In general, pyroxene in komatiites occurs in three dominant phases. Augite is the main component in pyroxene spinifex and also occurs as fine acicular grains in the matrix or as cumulus grains in differentiated flows (Arndt et al., 2008). Pigeonite is less abundant and is typically present in zoned pyroxenes that consist of pigeonite cores and augite rims (Arndt et al., 2008). Orthopyroxene, although rare, can occur in cumulate layers of differentiated flows, or in rare cases as cores of zoned needles in pyroxene textures (Bickle et al., 1993). Experimental evidence exists that shows pyroxene compositions of komatiites in the Barberton greenstone belt, South Africa, reflects crystallization from a hydrous magma that intruded as sills at shallow depths (Parman et al., 1997). Pyroxene grains in komatiites that reflect crystallization from anhydrous sources have a lower Wo (wollastonite) contents than pyroxenes of a hydrous source (Parman et al., 1997). Since the pyroxene species within ultramafic samples of this study differ from pyroxenes commonly documented in komatiitic flows, it is likely that these are secondary pyroxenes of metamorphic origin and do not reflect a primary texture. It is possible, however, that randomly oriented tremolite blades in this study represent relict pyroxene spinifex (Fig. 4.14).

6.2 Whole-Rock Geochemistry and Radiogenic Isotopes

The Long Bay group consists of many geochemically distinct units including ultramafic intrusive to volcanic rocks, high-Ti and low-Ti mafic tholeiitic volcanic rocks, calc-alkalic mafic volcanic rocks, and various felsic to intermediate intrusive and volcanic rocks. The Upper Keewatin Assemblage has been interpreted to consist of mafic to felsic metavolcanic rocks of calc-alkalic affinity, ultramafic to mafic metavolcanic rocks of komatiitic to tholeiitic affinity, and turbiditic metasedimentary rocks (Ayer and Davis, 1997).

6.2.1 High- and Low-Ti Tholeiitic Mafic Volcanic Rocks

The mafic volcanic rocks comprise the majority of Falcon Island and approximately half of the outcrop exposure at Cliff Island. Volcanic rocks are typically low-Ti tholeiitic mafic rocks with lenses of ultramafic volcanic rocks and lesser high-Ti tholeiitic and calc-alkalic volcanic rocks (Fig. 6.4). Ultramafic rocks are often surrounded by low-Ti tholeiitic units that occur between the ultramafic and high-Ti tholeiitic mafic rocks. Cliff Island consists of mainly low-Ti tholeiitic mafic volcanic rocks and intermediate volcanic rocks and therefore geochemical maps were not created.

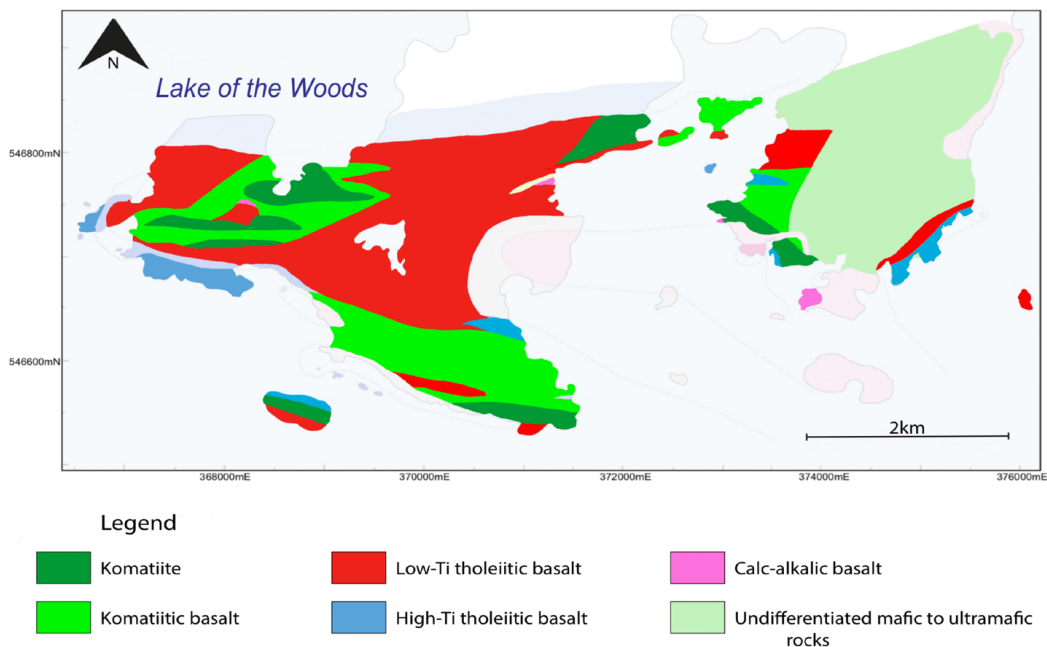


Figure 6.4. Geological map of Falcon Island showing distribution of various volcanic rocks.

The tholeiitic suite encompasses a range of major element concentrations. The SiO_2 contents for both low-Ti and high-Ti tholeiites range from 46 to 58 wt% and MgO from 4.4

to 13.4 wt%. The high-Ti tholeiites contain up to 18.4 wt% Fe₂O₃ and low-Ti tholeiites have from 7.6 to 14.7 wt% Fe₂O₃. Low-Ti tholeiites typically have higher metal abundances with Cr of 16 to 1083 ppm and Ni of 23 to 337 ppm, often with variable MgO concentrations (Fig. 6.5). The high-Ti samples however often have lower metal abundances with Cr <300 ppm and Ni <100 ppm. There is also no distinct variation between the two units based on other metals such as Pd, Pt and Au.

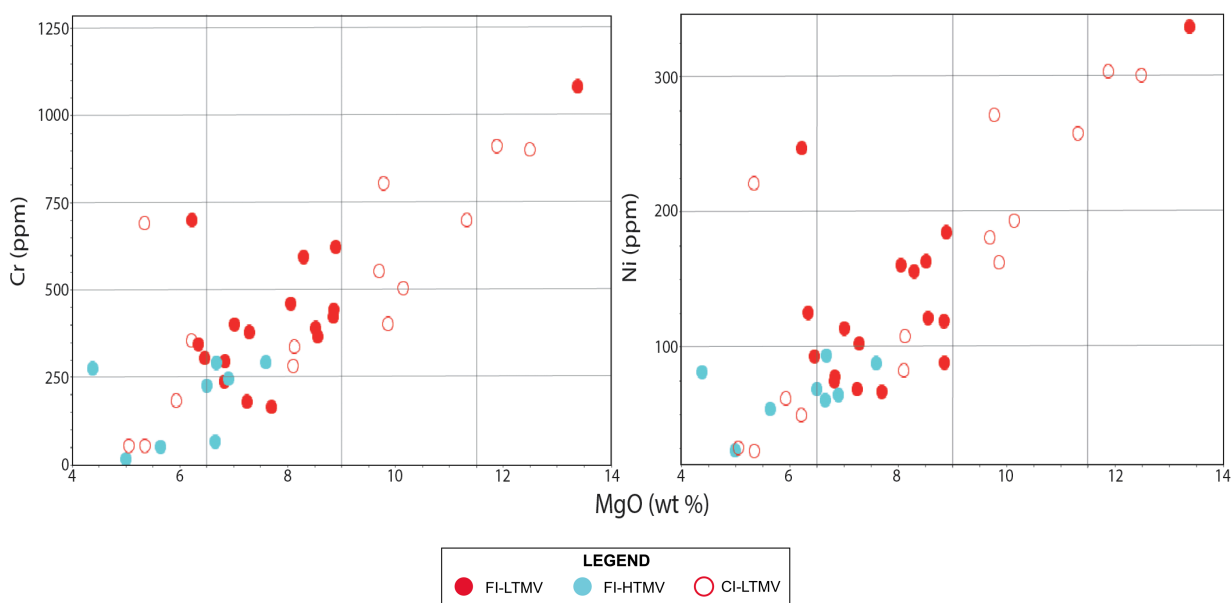


Figure 6.5. Bivariate plots of MgO vs metal abundances of tholeiitic volcanic rocks.

There is no distinct differentiation between the low- and high-Ti tholeiitic volcanic rocks when plotted on bivariate plots of Zr versus Nb, La, Ti, Th, Gd and Yb (Fig. 6.6). Samples show depleted concentrations of Nb relative to primitive mantle ratios, and often show scatter of La, Ti and Yb. The enrichment in Th is not generally accompanied by an enrichment in La, indicating it is not caused by LREE enrichment. Overall, trends are similar to that of the primitive mantle ratios.

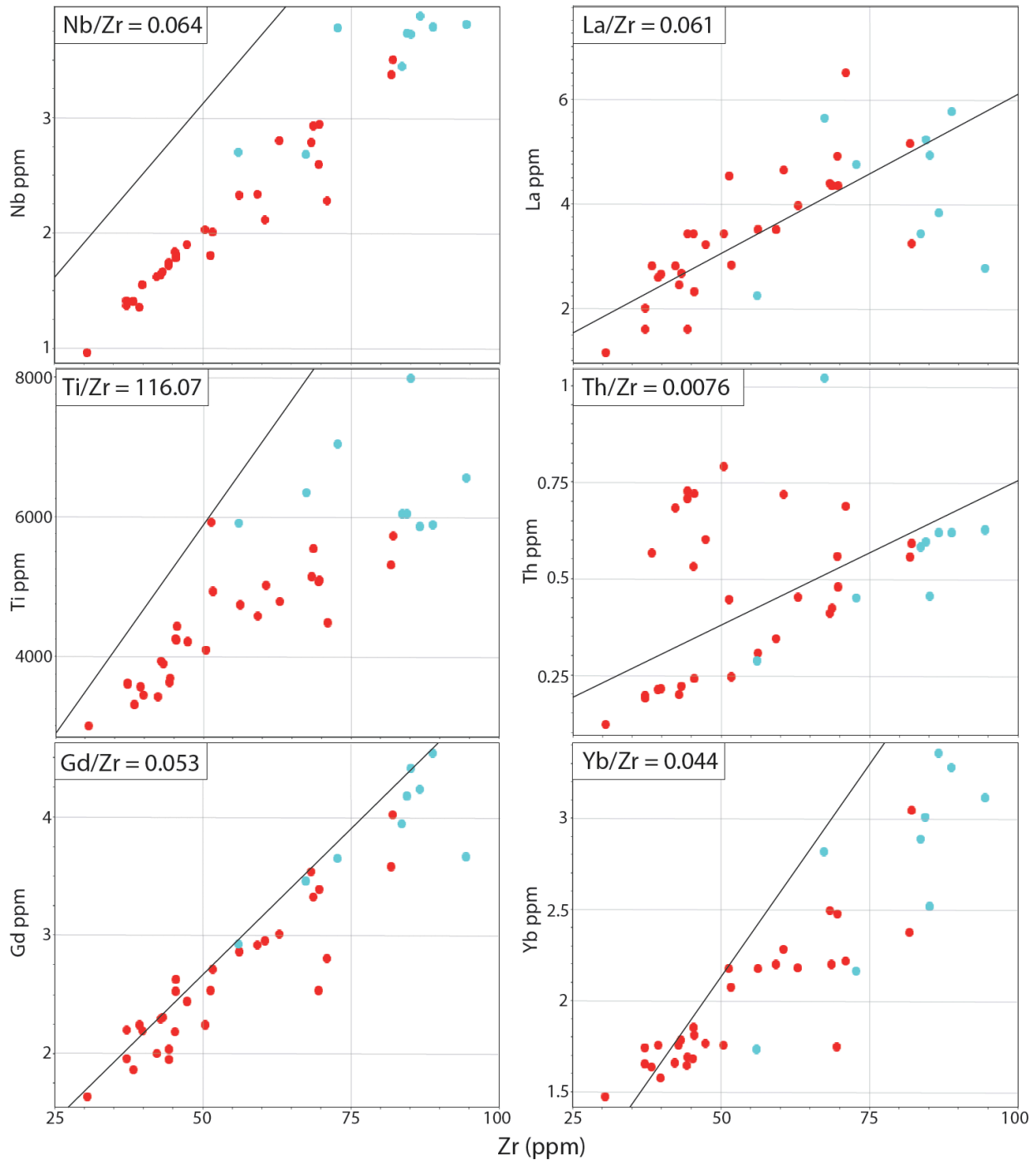


Figure 6.6. Bivariate diagrams of Zr versus Nb, La, Ti, Th, Gd and Yb with primitive mantle ratio trend lines.

The Th-Nb-LREE systematics of low-Ti tholeiites are much less complex than the komatiites and komatiitic basalts. In the following sections samples that show likely alteration effects (strong Eu anomalies and highly irregular LREEs) are omitted. Both high- and low-Ti tholeiites can be classified into samples with weak Nb depletions and moderate

to strong Nb depletions. As expected, samples with stronger Nb depletions often show increased fractionation (enrichment) of LREEs. The total range of $[\text{Nb}/\text{La}]_{\text{pm}}$ and $[\text{Th}/\text{La}]_{\text{pm}}$ values for low- and high-Ti tholeiites are 0.23 to 1.16 and 0.65 to 1.95, respectively. Typically, samples with stronger Nb depletions ($[\text{Nb}/\text{La}]_{\text{pm}} < 0.64$) have weakly to moderately fractionated LREEs ($[\text{La}/\text{Sm}]_{\text{pm}} = 1.06$ to 2.03; Fig. 6.7). Samples with weaker Nb depletions cluster at roughly $[\text{Th}/\text{La}]_{\text{pm}} = 0.8$ and $\text{La}/\text{Sm}_{\text{pm}} = 1$, with some high-Ti tholeiite outliers (Fig. 6.6). The remainder of samples with strong Nb depletions are scattered and contain variable $[\text{Th}/\text{La}]_{\text{pm}}$ values of 0.80 to 1.96. Overall, samples exhibit no correlation of $[\text{Th}/\text{La}]_{\text{pm}}$ and $\text{La}/\text{Sm}_{\text{pm}}$ but strong correlation of $[\text{Nb}/\text{La}]_{\text{pm}}$ and $\text{La}/\text{Sm}_{\text{pm}}$. Minimum and maximum values of $[\text{Th}/\text{La}]_{\text{pm}}$ and $[\text{Nb}/\text{La}]_{\text{pm}}$ occur in samples with less than 2 wt% LOI, and therefore it is not likely that alteration has affected the Th-Nb-LREE systematics. With the exception of one sample, all tholeiites have $[\text{La}/\text{Yb}]_{\text{pm}} \leq 2$, which is typical of Archean tholeiites from the Superior Province, indicating no significant REE fractionation has occurred (Kerrick et al., 1999).

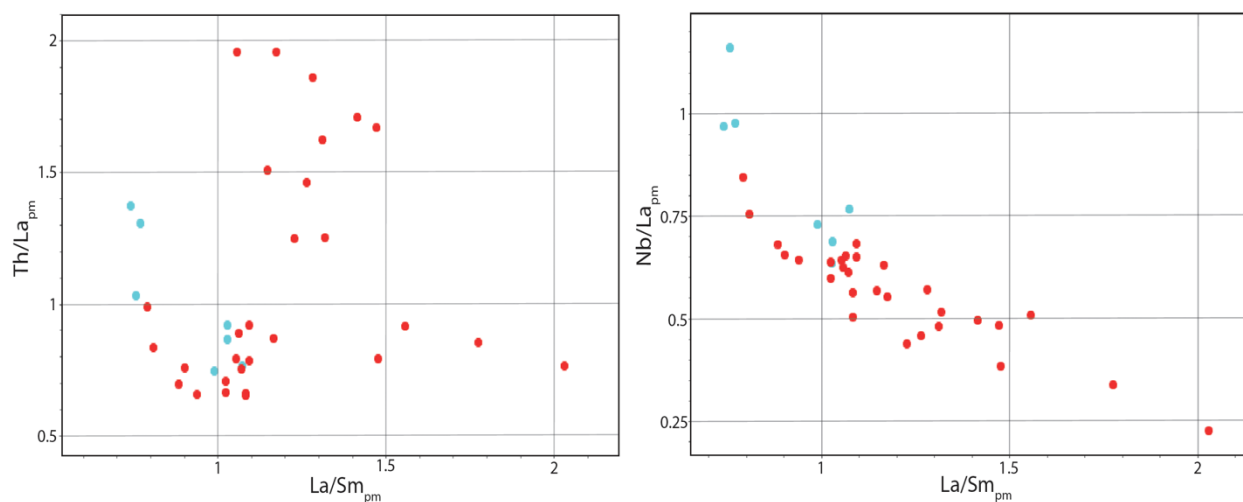


Figure 6.7. Diagram of $\text{La}/\text{Sm}_{\text{pm}}$ versus $[\text{Th}/\text{La}]_{\text{pm}}$ and $[\text{Nb}/\text{La}]_{\text{pm}}$. Normalizing values from Sun and McDonough (1989).

It is possible that compositional variances amongst the tholeiites can be attributed to fractional crystallization processes. The fractional crystallization of olivine could account for variable MgO concentrations, however since Nb and Th are not compatible in olivine, it is not likely that it could account for variable Th and Nb (Arndt, 1994). There is also no correlation between MgO (or Mg#) with $[\text{Th}/\text{La}]_{\text{pm}}$ or $[\text{Nb}/\text{La}]_{\text{pm}}$ (not shown). It is also possible for Fe-

Ti oxides to fractionate Nb, as well as Ti, however there is also no correlation between Ti/Ti^* and $[Th/La]_{pm}$ or $[Nb/La]_{pm}$ (Simons et al., 2017; Fig. 6.8). It is also not possible to explain variances in Th or La as a result of magnetite fractionation/accumulation as these elements are not compatible in magnetite (Kerrick et al., 1999). Combined, this suggests that fractionation was not the cause of the Th-Nb-LREE anomalies.

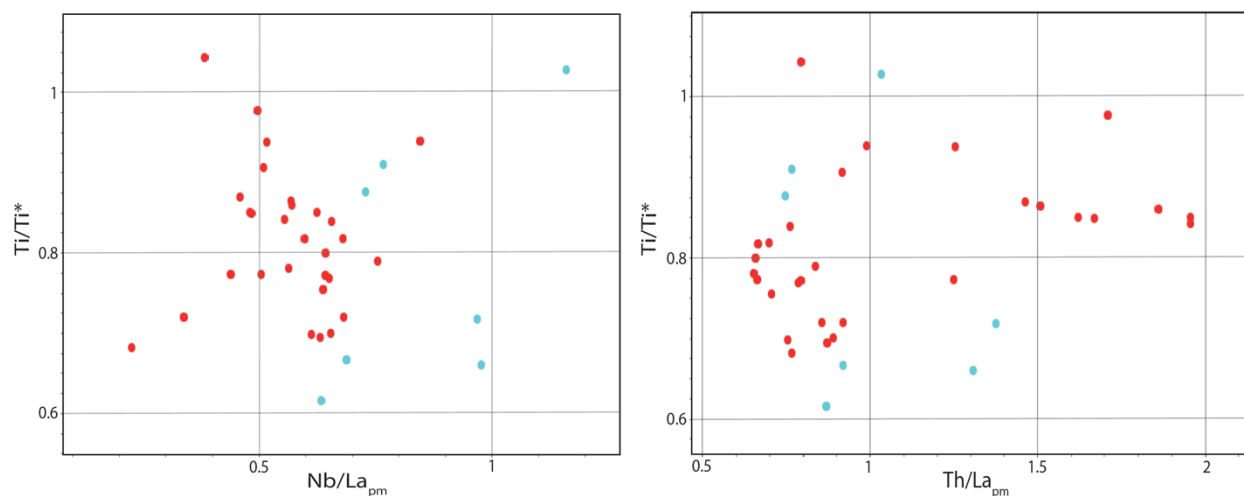


Figure 6.8. Bivariate plot of Ti/Ti^* versus $[Nb/La]_{pm}$ and $[Th/La]_{pm}$. Normalizing values after Sun and McDonough (1989).

When investigating the variation between the tholeiite units on a Nb-Th-Yb plot after Pearce (2014), it is evident that there is a distinction between tholeiites with weak and strong Nb depletions (Fig. 6.9). Low-Ti tholeiites with strong Nb depletions plot within the modern arc array and are weakly clustered. Whereas low- and high-Ti tholeiites with weak Nb depletions typically plot as a diagonal trend between the arc and MORB-OIB array. Constant Th-Nb can be interpreted to reflect varying degrees of melting of a subduction-modified source and subsequent fractional crystallization (Smithies et al., 2018). The constant Th-Nb trend that the tholeiites of this study define is consistent with that of the low-Ti tholeiites in the Abitibi greenstone belt which also have a constant Th-Nb trend at relatively low Nb/Th (Smithies et al., 2018). It is likely that the low $(Th/Yb)/(Nb/Yb)$ trends (constant Th/Nb) require a source that already possesses relatively constant Th/Nb ratios that is also high in Th. Greenstone belts with extensive lithological associations of mafic to felsic rocks with little range in Th/Nb ratios have been interpreted to represent a possible arc-subduction system that evolved beyond the initial stages (Smithies et al., 2018). Variable

Th-Nb trends often represent mixing between low Th/Nb mantle-derived melts and high Th/Nb crust resulting in high (Th/Yb)/(Nb/Yb); Pearce, 2008; Smithies et al., 2018). Greenstone belts with variable Th/Nb ratios are generally considered to be devoid of any subduction-derived influence and diagonal trends with variable Th addition are commonly attributed to contamination (Fig. 6.9; Pearce, 2008).

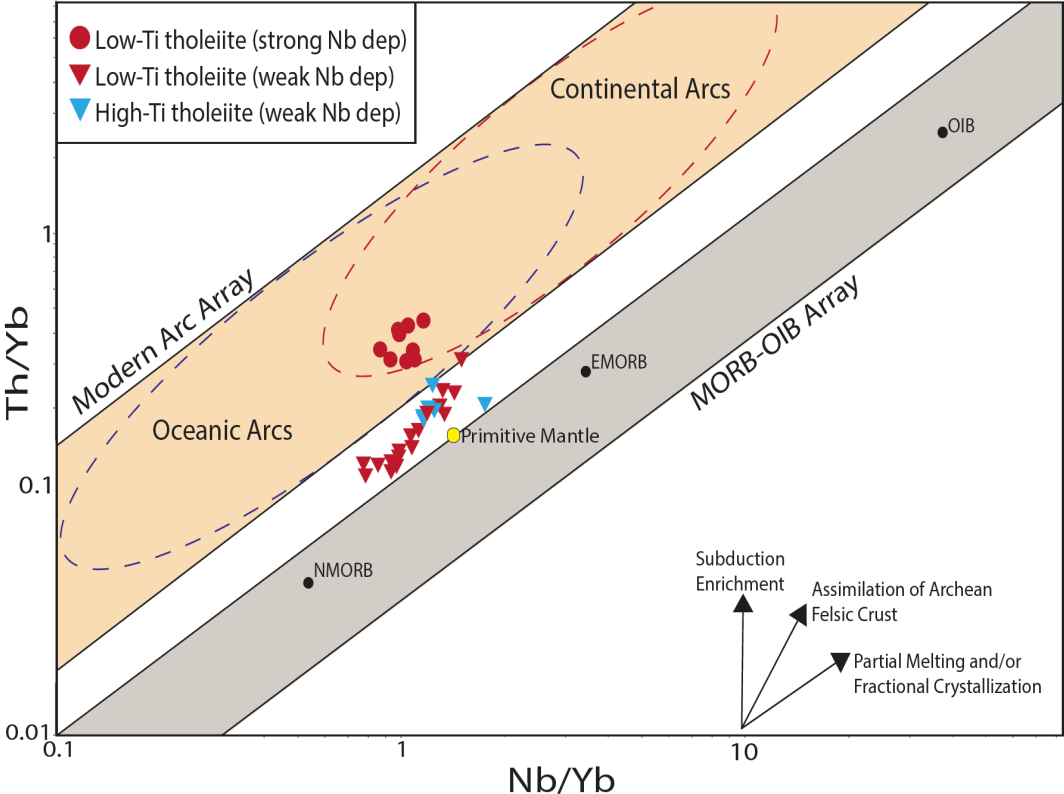


Figure 6.9. Diagram after Pearce (2014) plotting Th/Yb versus Nb/Yb of tholeiitic volcanic rocks.

The strongly depleted Nb samples cluster within the modern arc array and are distinct from the weakly depleted Nb samples. Based on the lack of a trend from the mantle array to the strongly Nb-depleted samples, their signatures are considered to be uncontaminated and indicative of subduction processes (i.e., they are “arc tholeiites”) and lack assimilation-fractional crystallization effects. Samples with weak Nb-depletions have relatively consistent Th/Nb ratios, with some outliers towards the top and bottom of the trend. This varies from strongly Nb depleted tholeiites as the weakly depleted tholeiites may represent initial partial melting and/or fractional crystallization trends with the addition of a contaminant as the melt progressed as the trend steepens towards higher Th/Yb and

Nb/Yb values. The trend most closely resembles the “crustally contaminated MORB ophiolite” trend discussed by Pearce (2008), who noted that such trends may develop from direct crustal contamination of MORB-style magmas or through contamination of the source mantle by adakite-style magmas generated by fusion of hydrated crust and sediments. The latter scenario may have been relatively common in the late Archean.

6.2.2 Calc-Alkalic Mafic Volcanic Rocks

The petrology and major element geochemistry between the tholeiitic and calc-alkalic rocks are broadly similar. The main variation between the two units is the abundance of light rare earth elements (Nd + Gd + La + Sm + Ce) and the nature of fractionation of the HREEs. Calc-alkalic rocks have total LREE concentrations of 87.4 to 143.4 ppm whereas tholeiitic rocks contain less than 50 ppm total LREE. Calc-alkalic rocks also have fractionated HREEs ($[Gd/Yb]_{pm} = 2.9$ to 3.9), suggesting these units originated from a deeper source than the tholeiitic mafic and ultramafic rocks in which garnet was a stable phase.

The calc-alkalic samples plot on a linear “wedge melting” trend (Pearce, 2008) within the continental arc domain on the modern arc array (Fig. 6.10). The trend of the samples follows the predicted trend for variable degrees of partial melting and/or fractional crystallization (Pearce, 2014).

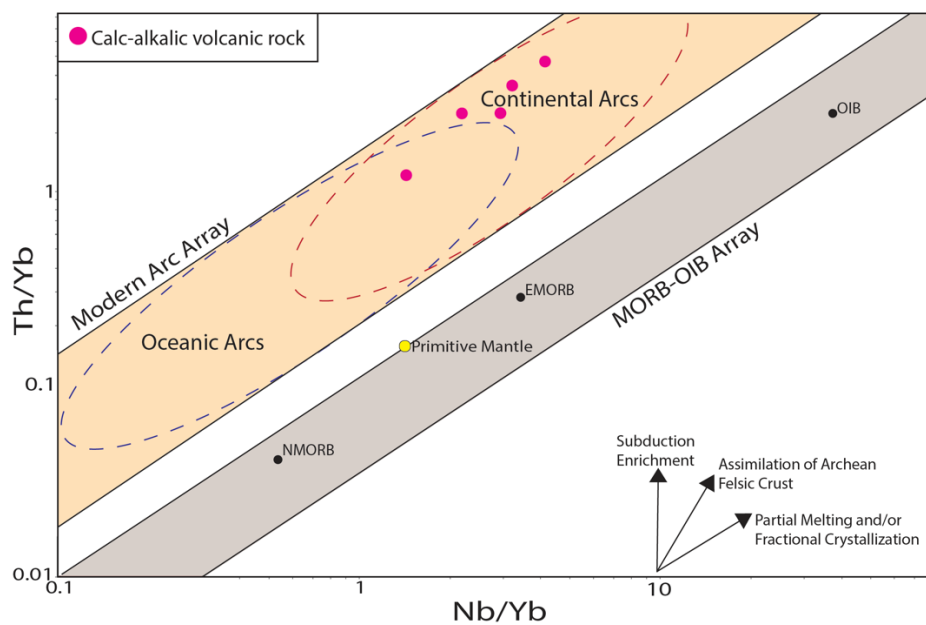


Figure 6.10. Diagram after Pearce (2014) plotting Th/Yb versus Nb/Yb of calc-alkalic mafic volcanic rocks.

6.2.3 Ultramafic Rock Discrimination

Komatiites are defined as having MgO >18 wt%, however other parameters can also be considered, such as high abundances of Ni and Cr and low abundances of Al, Si, Ti, and Zr (Arndt et al., 2008). Picrites, high-Mg volcanic rocks usually rich in olivine, have a lower abundance of SiO₂ and higher abundances of alkali elements and TiO₂ relative to komatiites (Arndt et al., 2008). Komatiites are distinguished from picrites, meimechites, boninites based mainly on Al₂O₃. Komatiites have lower concentrations of Al in comparison to other types of highly magnesian lavas, however TiO₂, Na₂O, K₂O, SiO₂ and FeO can also be used as discriminants when element mobility is not a factor (Arndt et al., 2008).

Komatiites generally have Cr and Ni concentrations of 2000 to 3000 ppm and 1000 to 1500 ppm, respectively (Hollings et al., 1999; Arndt et al., 2008). Ultramafic samples from the field area have Ni contents from 580 to 1311 ppm and Cr from 1734 to 3451 ppm (Fig. 6.11). The komatiitic basalts (low-Ti tholeiitic schists) plot as an intermediate phase between the high-Mg tholeiite and the komatiite samples. In komatiite flows with less than 25 wt% MgO, Cr typically increases with increasing MgO as a result of co-crystallization of olivine and chromite (Arndt et al., 2008). Olivine is the dominant Cr host until MgO values drop to 25 wt%, at which point chromite appears and hosts the majority of the Cr (Arndt et al., 2008). This is also seen in Ni values in which a linear trend often exists between Ni and MgO, in spite of the expected fractional crystallization patterns expected due to Ni being highly compatible in olivine (Arndt et al., 2008). Considering there is a positive linear correlation between both Cr and Ni (ppm) versus MgO wt%, it is likely that the co-crystallization of olivine and chromite is the driving force in metal abundances, apart from the few samples with >25 wt% MgO in which it is expected that olivine is the dominant host for Cr and Ni.

On the Jensen cation plot, many of the low-Ti tholeiitic samples plot within the komatiitic basalt field (Fig. 6.1). These samples are hornblende-chlorite-tremolite schists and weakly foliated amphibolites. Komatiitic basalts are distinguished from other basalts because of their genetic link to ultramafic members of the komatiitic magma series by field relationships, textural features and partly their chemical compositions (Arndt et al., 2008). Limited outcrop meant that clear field relationships were rarely observed. Typically,

komatiitic basalts will have MgO contents from 6 to 18 wt%, higher Al₂O₃ and lower Ni than their ultramafic counterparts as well as relatively low concentrations of TiO₂ and incompatible trace elements (Arndt et al., 2008; Dostal, 2008). Komatiitic basalts can host both olivine and/or pyroxene spinifex, however they contain dominantly pyroxene, often clinopyroxene, due to their lower MgO concentrations (Arndt et al., 2008; Dostal and Mueller, 2013).

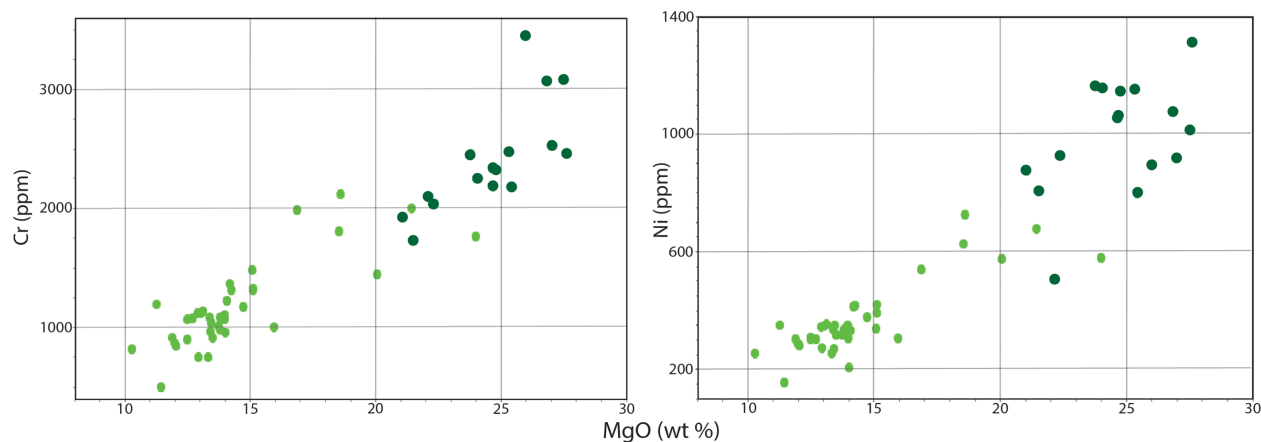


Figure 6.11. Bivariate diagram of MgO versus Cr and Ni. Dark green: komatiite. Light green: komatiitic basalts.

Komatiites can be classified into aluminum-depleted (ADK) and aluminum-undepleted (AUK) types based on multiple geochemical parameters. Aluminum-undepleted (Munro-type), as defined by Sossi et al. (2016) and references within, are characterized by chondritic Al₂O₃/TiO₂ ratios of ~20 and CaO/Al₂O₃ of ~1. The mobility of Ca during hydrothermal alteration and metamorphism can often produce low CaO/Al₂O₃ ratios and consequently should be interpreted with caution (Arndt et al., 2008). When CaO is plotted against LOI %, there is a negative correlation which suggests Ca loss during alteration (Fig. 6.12). The ratios of CaO/Al₂O₃ reside within the AUK range, and although Ca loss is likely in some samples, the Al₂O₃/TiO₂ and [Gd/Yb]_{pm} ratios are reliable and are consistent with classification as AUKs.

Aluminum-undepleted komatiites are also characterized by chondritic Al₂O₃/TiO₂ ratios of ~20 and unfractionated [Gd/Yb]_{pm} of ~1 (Sossi et al., 2016). The majority of samples for this study plot within the AUK field on a [Gd/Yb]_{pm} versus Al₂O₃/TiO₂ diagram with some points plotting at more Al-rich ratios (Fig. 6.13). Typically, points plot in the vicinity of CaO/Al₂O₃ ratios of 1 and plot within the AUK field (Fig. 6.13). The CaO/Al₂O₃ ratios are

strongly depth and pressure dependent due to the presence or lack of garnet in the residuum (Herzberg, 1995; Dostal, 2008). The unfractionated nature of the heavy rare earth elements suggests that the magma originated above the garnet stability field correlating to depths of origin at approximately 100 to 300km (5 to 6.5 GPa).

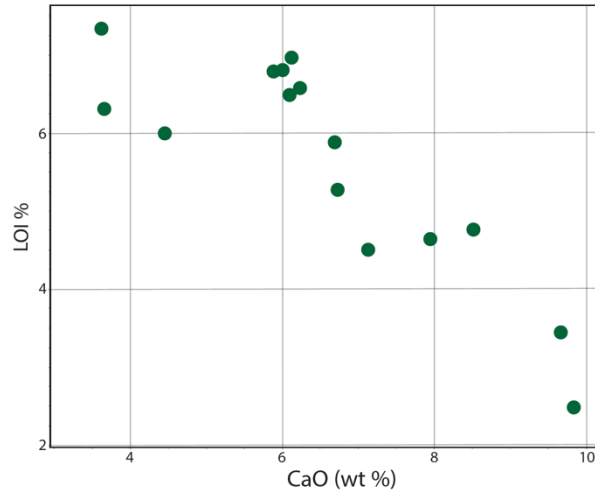


Figure 6.12. Bivariate diagram of CaO versus LOI for komatiite samples.

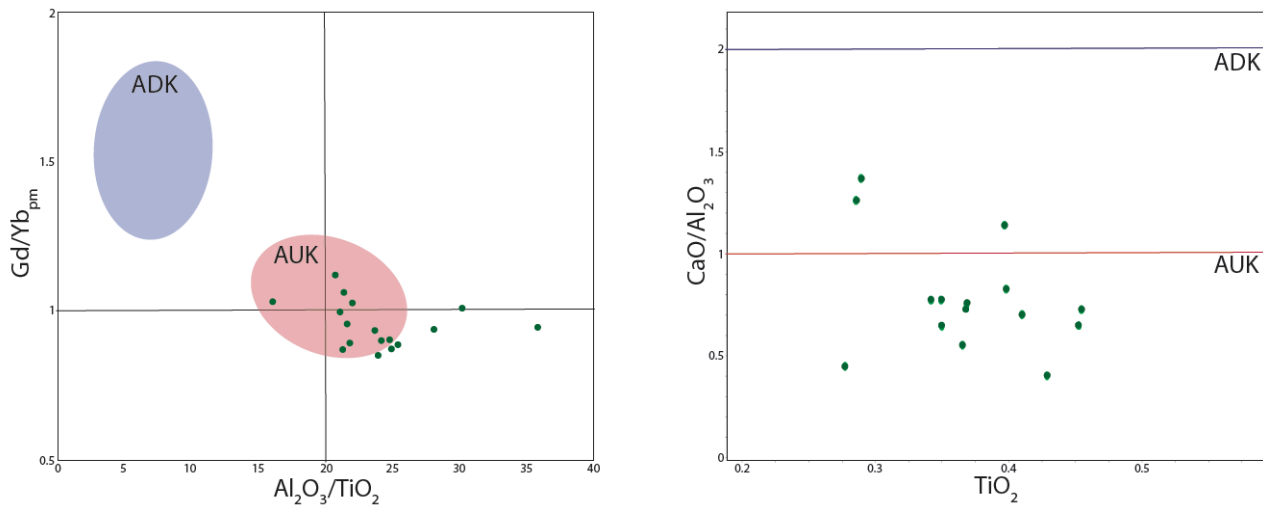


Figure 6.13. Komatiite classification diagrams. A) $\text{Al}_2\text{O}_3/\text{TiO}_2$ versus $\text{Gd}/\text{Yb}_{\text{pm}}$ (Modified from Dostal, 2008). Solid lines show primitive mantle ratios. Normalizing values after Sun and McDonough (1989). B) Bivariate diagram of $\text{CaO}/\text{Al}_2\text{O}_3$ versus TiO_2 . AUK and ADK classification after Arndt (2008).

Although the Abitibi greenstone belt (AGB) is not within the Wabigoon Terrane, the komatiites present in the AGB have similar eruption ages to the komatiites present in the Lake of the Woods greenstone belt. The Pyke Hill komatiites in the Kidd-Munro assemblage

have been assigned an age of 2718 to 2710 Ma whereas the komatiites in Boston Township are 2720 ± 2 Ma (Stone et al., 1995; Sproule et al., 2003). The komatiites of the LWGB, due to their intercalations with calc-alkalic material, are considered to be coeval with the calc-alkalic volcanism that has an eruption age of approximately 2719 Ma (Ayer and Davis, 1997). Komatiites of this study are compared to the Pyke Hill AUKs and Boston ADKs due to the similarity in eruption age (Fig. 6.14). Samples that show irregular LREEs, Zr-Hf anomalies, and enriched Th with Nb depletions have been omitted due to likely contamination and/or alteration. The komatiites of Pyke Hill have a typical AUK signature with LREE depletions and flat HREEs. The komatiites of the Boston Flow are typical ADKs with enriched LREEs and weakly fractionated HREEs. Figure 6.14 further suggests that komatiites within the field area are AUK type as they have very similar primitive mantle patterns to the AUKs of Pyke Hill.

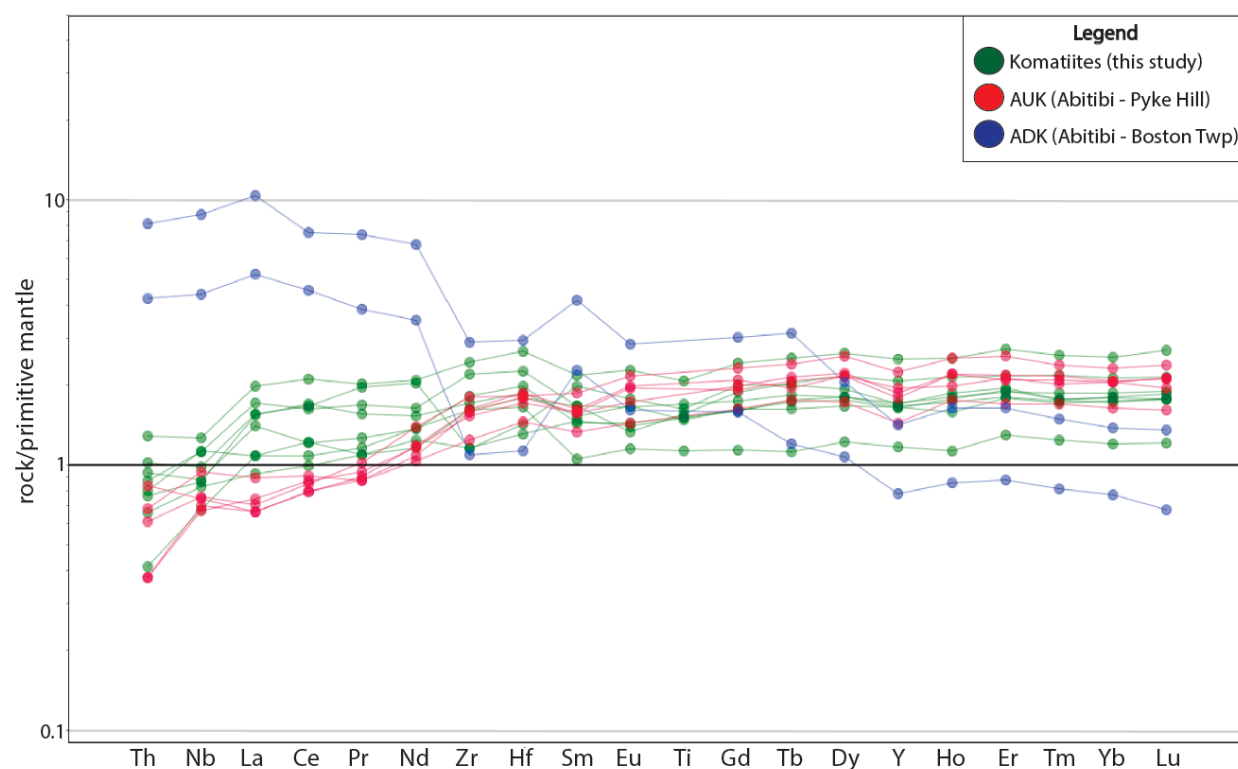


Figure 6.14. Primitive mantle diagram of komatiites from this study and komatiites from the Abitibi greenstone belt. Boston Creek Flow after Xie et al. (1993) and Pyke Hill komatiites after Fan and Kerrich (1997). Normalizing values after Sun and McDonough (1989).

6.2.4 Komatiites

The komatiites of the field area have similar major element geochemistry but variable trace element geochemistry (see Section 5.1.1). Three trace element patterns exist when samples are plotted on a primitive mantle diagram and each will be discussed in the following individual sections (Fig. 5.11).

6.2.4.1 N-MORB Pattern

Samples that have LREE depletions and flat HREE are typical of N-MORBs as they are derived from the upper depleted mantle. Typically, AUKs have N-MORB signatures as they form above the garnet stability zone from the depleted mantle. Samples that plot close to primitive mantle values imply that contamination, if it had occurred, was very minimal (Hollings and Kerrich, 1999). On bivariate plots with Zr versus Nb, La, Ti, Th, Gd and Yb, there is a clear trend in which units progress from komatiites to komatiitic basalts as element concentrations increase (Fig. 6.15). Overall, ultramafic rocks plot along primitive mantle ratio trends in most diagrams, except for Nb and Th, in which they plot below the PM ratio trendline. A linear trend exists amongst most samples that have a N-MORB (solid circles) or Th-Nb enrichment (solid diamonds) patterns on primitive mantle spider plots. The main deviation and scatter of points occurs on the Th and La diagrams, where the samples with Nb depletions (open circles) show strong deviation from the linear trend of Th/Zr and great scatter amongst La/Zr. These diagrams suggest that samples with N-MORB, as well as enriched Th-Nb, signatures have overall not been greatly affected by secondary processes.

6.2.3.2 Nb Depletion

In Archean terranes Al, Ti, the HFSEs (Th, Nb, Ta, Zr, Hf) and the REEs (excluding Eu) are broadly unaffected by alteration and metamorphic processes (Arndt and Nesbitt, 1982; Kerrich et al., 1999). There is a major variation in primitive mantle patterns of both komatiites and komatiitic basalts in terms of Nb, La and Th (Fig. 5.11). Figure 6.16 shows that samples with Nb depletions occur over a wide range of LOIs and do not always have Eu anomalies, and therefore it is unlikely that alteration has greatly affected the Th-Nb-LREE systematics. The lack of correlation between LOI and $[\text{Th}/\text{La}]_{\text{pm}}$ or Eu/Eu^* and $[\text{Nb}/\text{La}]_{\text{pm}}$

supports the interpretation that alteration and/or metamorphism are not the cause of Th-Nb-LREE variation (Fig. 6.16). This is consistent with observations from tholeiitic samples in Vermillion Lake (Western Wabigoon Terrane) where there also was no evidence that alteration or late-stage metamorphism had disturbed the Th-Nb-LREE systematics (Kerrick et al., 1999). Similar conclusions are assumed for komatiitic basalts of this study.

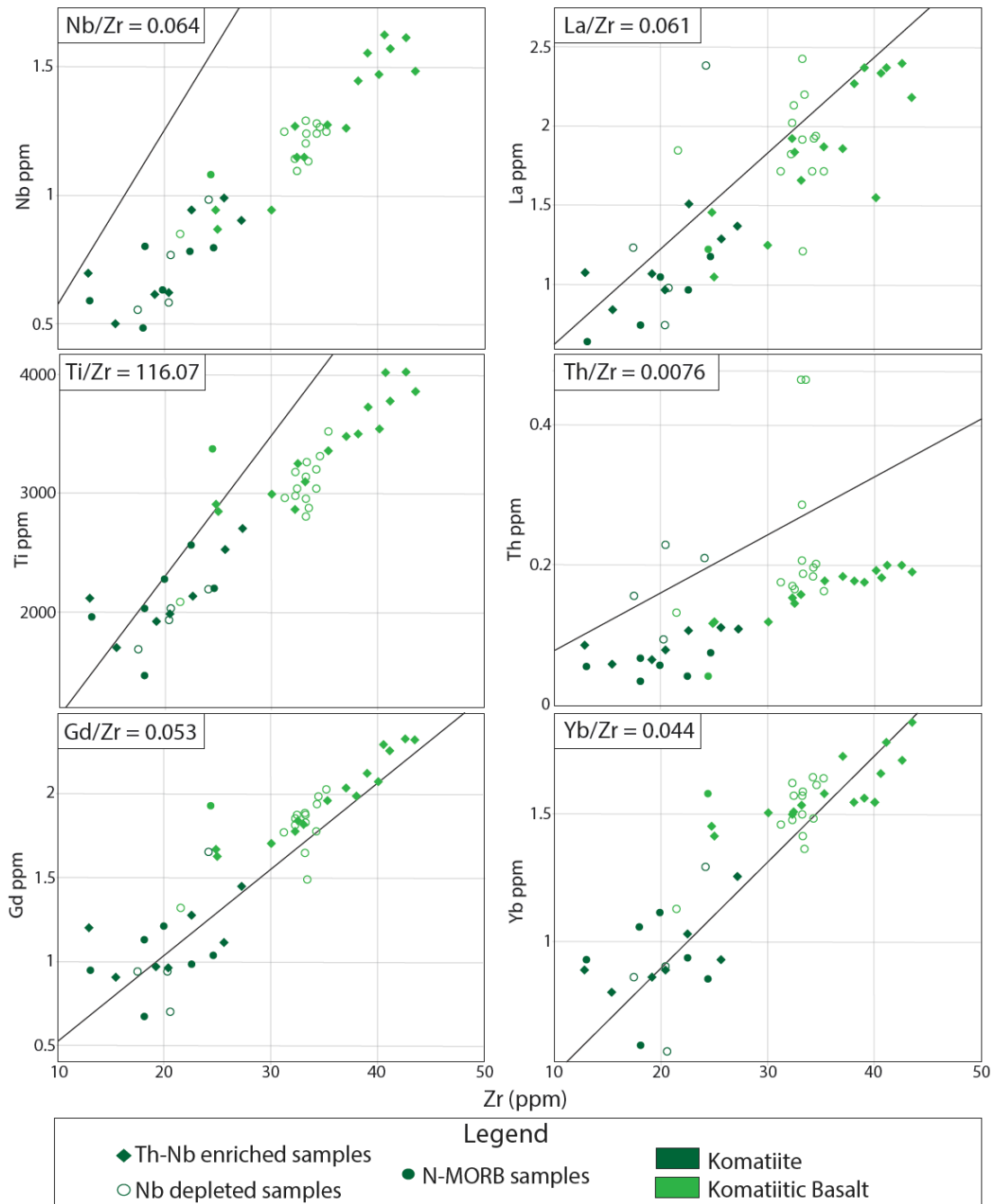


Figure 6.15. Bivariate diagrams of Zr (ppm) versus various trace elements for komatiites and komatiitic basalts. Trend line represents primitive mantle ratios after the normalizing values after Sun and McDonough (1989).

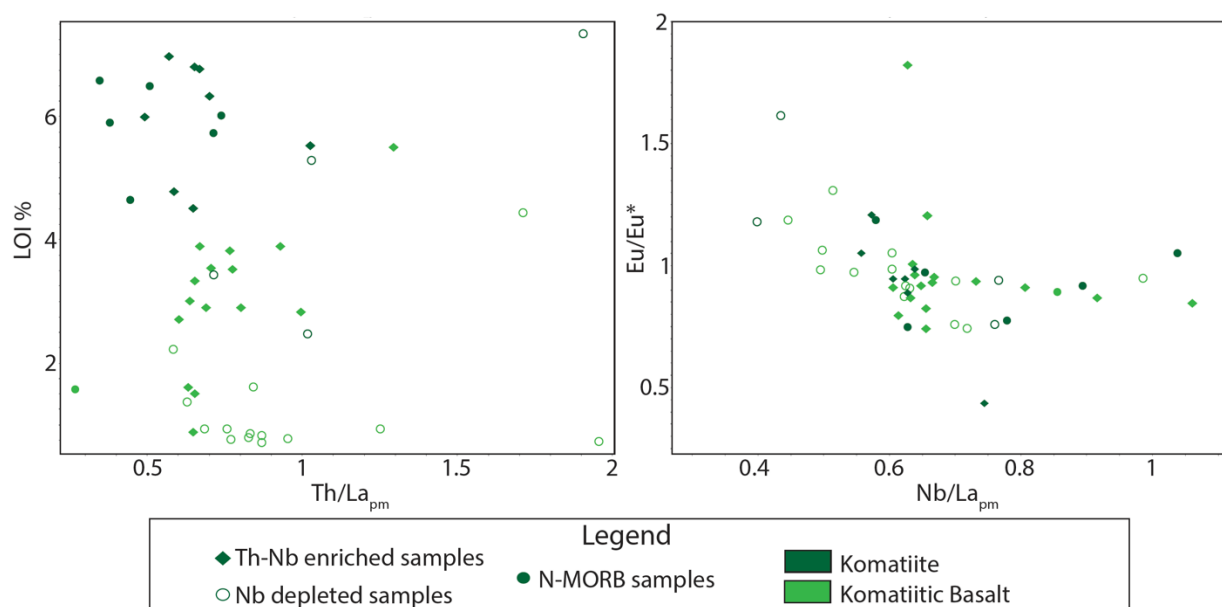


Figure 6.16. Bivariate diagrams of $[\text{Th}/\text{La}]_{\text{pm}}$ versus LOI % and $[\text{Nb}/\text{La}]_{\text{pm}}$ versus Eu/Eu^* . Normalizing values after Sun and McDonough (1989).

The ϵ_{Nd} values for mantle derived rocks in the Archean are typically from +2 to +4, therefore deviation to lower more negative values likely indicates contamination by older crustal material (Hollings et al., 1999). Since ultramafic samples in this study range from ϵ_{Nd} +1.07 to +2.66 and komatiitic basalts have ϵ_{Nd} of +1.49 and +2.14, it is not likely that contamination, if it has occurred, was by material that is significantly older than the ascending magmas. Figure 6.17 compares isotopic signatures from samples collected in this study with data reported for mafic and komatiite samples from the LWGB as well as komatiite samples from the Abitibi greenstone belt. Three komatiite and two komatiitic basalt samples from this study plot below the depleted mantle line and represent isotopically enriched signatures whereas the remaining two ultramafic samples plot above the depleted mantle line and represent a depleted signature. Komatiite samples from the Abitibi have ϵ_{Nd} ranges from +1.9 to +3.6, creating overlap between N-MORB and Th enriched komatiites from this study (Sproule et al., 2003). There is only one komatiite sample from the published LWGB dataset that has an ϵ_{Nd} of + 2.1, therefore it is difficult to provide a sufficient comparison of isotopic data from this study to published data (Ayer and Dostal, 2000). This study has demonstrated a greater range in ϵ_{Nd} for komatiites than has previously been documented.

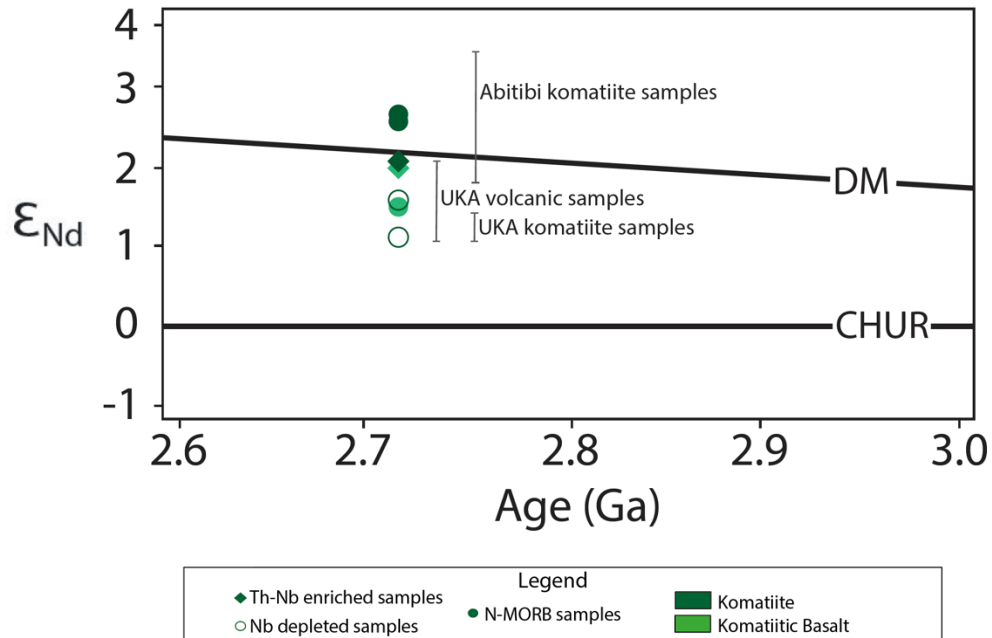


Figure 6.17. Komatiite and komatiitic basalt samples from this study compared to Abitibi komatiites (Sproule et al., 2003) and typical Upper Keewatin Assemblage komatiites (Ayer and Dostal, 2000).

A key component in establishing magma genesis is constraining the degree to which a mantle-derived magma is contaminated as it passes through continental crust. Magmas from crustal or mantle sources can mix in chambers or conduits, in which the walls, floors and roofs of magma chambers can become contaminated by melting and interacting with the surrounding material (Huppert and Sparks, 1985). Contamination has been recognized through enrichments in incompatible trace elements and deviation from expected radiogenic and stable isotopic ratios from the depleted mantle source of mid-ocean ridge basalts (Sparks, 1986). For example, contamination of mafic to ultramafic magmas by felsic crustal material results in an increase of SiO_2 , Th/Ce, Th/La, $[\text{La}/\text{Sm}]_{\text{pm}}$, LREEs combined with stronger negative Nb depletions (Hollings and Kerrich, 1999; Hollings et al., 1998). Contamination by crustal rocks will increase the abundances of incompatible elements, for example Th and the LREEs, with a smaller effect on Nb, Ta and Ti, and will result in a magma enriched in LREEs and Th with negative Nb, Ta and Ti anomalies (Jochum et al., 1993). Contamination by a substance with a strong geochemical contrast to the primary magma will be the most evident. The total amount of crust that can be potentially assimilated by ascending magma increases as melts become more primitive, hotter, and magnesian rich

(Sparks, 1986). Komatiites, for example, can become contaminated up to 50% by mass during magma ascent, whereas contamination post-eruption typically reaches a maximum at 10% when magmas are thermally eroding underlying rocks (Huppert and Sparks, 1985). The amount of contamination generally decreases with increasing flow rate; therefore, a very rapid ascent is critical to avoid substantial contamination (Huppert and Sparks, 1985). If contamination is fairly compositionally uniform then it likely occurred during magma ascent rather than post-eruption contamination (Hollings and Kerrich, 1999). In comparison to modern primitive basalts, ancient komatiites can assimilate approximately three times more than modern analogues (Sparks, 1986).

Elements, such as niobium, can be used to investigate a variety of processes. Firstly, Ti-bearing minerals such as rutile, sphene and ilmenite can fractionate Nb from other trace elements (Green, 1995). Garnet, amphibole and clinopyroxene can also fractionate Nb; however, the partitioning coefficients are very low and thus any involvement of these minerals in Nb fractionation would result in only minor changes (Green, 1995). Secondly, Nb depletions can also be caused by subduction processes. The oxidizing environment, caused by the addition of water to the mantle wedge, stabilizes minerals such as titanite, rutile, ilmenite and hornblende (Murphy, 2007). These minerals contain high abundances of high-field strength elements (Zr, Ti, Nb, Hf, Ta) and remain in the residue during partial melting, creating a depletion in HFSEs in arc magmas (Murphy, 2007). And finally, Nb depletions can reflect the end result of a magma interacting with a contaminant that has a Nb depletion.

The ultramafic samples in the Upper Keewatin Assemblage display multiple geochemical parameters indicative of some degree of contamination and/or variation in the source component (Fig. 6.18). The variation in the trace element chemistry of the komatiite units, with no variation amongst major element chemistry or mineralogy, suggests the possibility of a complex history. The ϵ_{Nd} values of komatiites do not decrease with increasing SiO_2 ; however, there is a negative correlation between ϵ_{Nd} and $[La/Sm]_{pm}$ ratios, suggesting progressive LREE enrichment with decreasing ϵ_{Nd} . Typically, ϵ_{Nd} would decrease and SiO_2 increase when contaminated by older crustal material (Halama et al., 2004). Positive ϵ_{Nd} values correlate to a depleted isotopic signature, and when contaminated by older crust, the values become isotopically enriched (negative). The lack of correlation between ϵ_{Nd} and SiO_2 and $[La/Sm]_{pm}$ suggests that if contamination had occurred it was not likely that the

contaminant was significantly older than the ascending magmas. The tholeiitic and komatiitic samples are suggested to occur as conformable intercalations with the calc-alkalic volcanic units of the Upper Keewatin Assemblage, therefore providing a potential source for contamination that is geochemically distinct, but does not present a strong isotopic contrast given their similar ages.

Samples of this study with pronounced Nb depletions ($Nb/Nb^* < 1$) are often enriched in Th, shown by increasing Th/La and Th/Ce ratios. This correlation is often consistent with crustal contamination signatures. Samples are weakly scattered on the $[La/Sm]_{pm}$ versus Nb/Nb^* diagram, but a handful of Nb-depleted komatiite samples have a weak correlation with increasing $[La/Sm]_{pm}$ and negative Nb anomalies. Finally, the overall Th enrichment within units with pronounced negative Nb anomalies is shown by decreasing $[Nb/Th]_{pm}$ ratios and increasing $[Th/Yb]_{pm}$ ratios, creating a trend that all samples with negative Nb anomalies follow. The only element that is consistently enriched in samples with strong Nb anomalies is Th. Some samples have apatite present, which can host Th as an accessory element; however, the samples that have apatite do not show a Th enrichment. Thorium, a lithophile element, is typically enriched in felsic material, especially granites, in comparison to more mafic and intermediate material. It would be expected that increased Th would occur in conjunction with increased SiO_2 ; however, there is no correlation between Th and SiO_2 .

In order to further assess contamination, quantitative modelling was used to evaluate the possibility of assimilation and fractional crystallization (AFC) or binary mixing to produce the Th-Nb-LREE variation. Since there is no correlation between decreasing ϵ_{Nd} and increasing SiO_2 , the contaminant was not likely a felsic unit (Fig. 6.18). Therefore, AFC modelling was undertaken with the mafic tholeiitic and calc-alkalic rocks as contaminants of a parent komatiite unit. A least altered komatiite sample with a typical N-MORB pattern was chosen as the parent rock (LOW17CB69), and a Nb-depleted sample with little variability in the LREEs and no Eu anomaly was chosen as the end-result comparison unit (LOW17CB57). Partitioning coefficients for ultramafic and mafic magmas, at a composition of 70 modal% olivine and 30 modal% pyroxene, after Rollinson (2013) and Arndt (2008) were utilized in the modelling (Table 6.1).

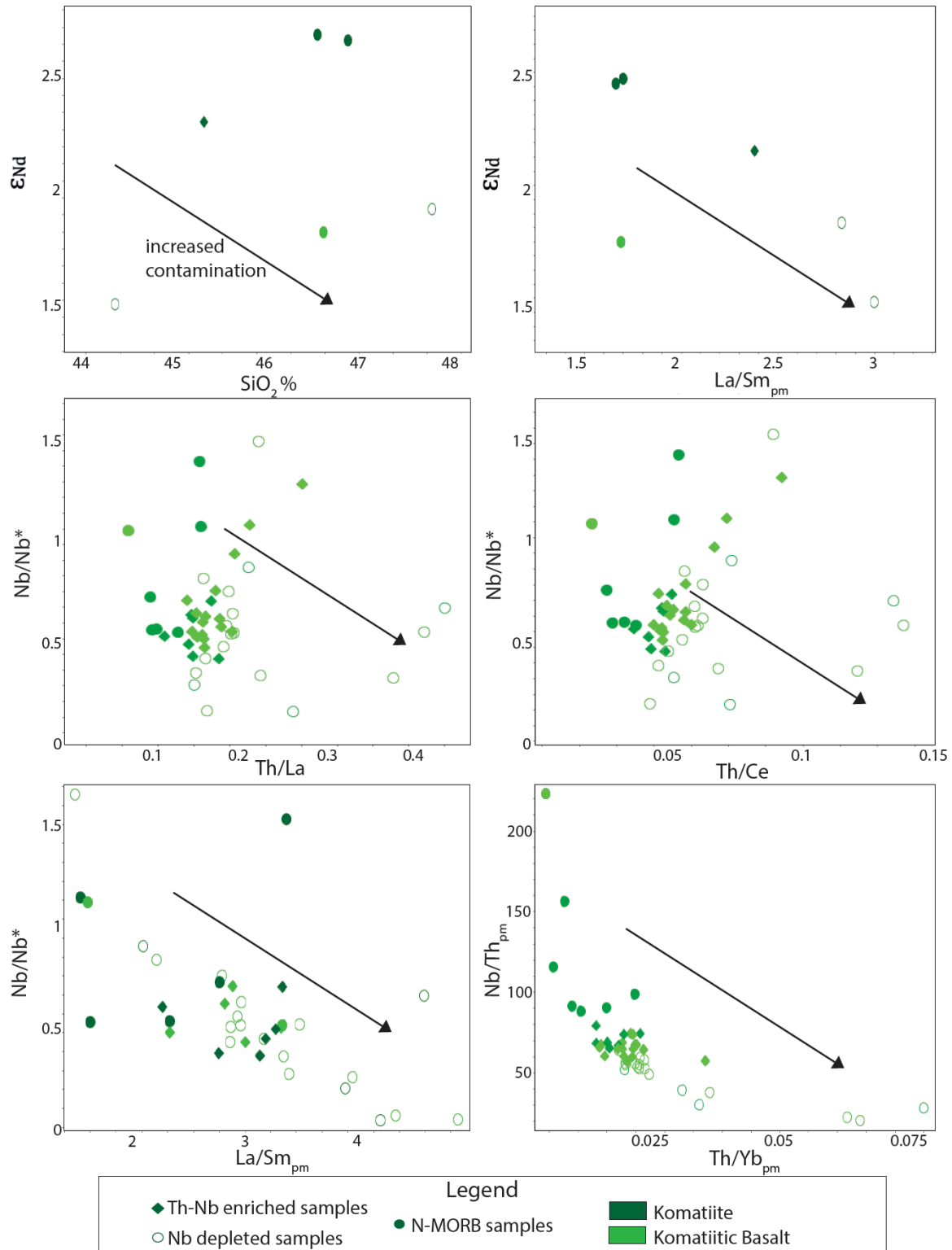


Figure 6.18. Komatiite Bivariate diagrams with trend lines (arrows) pointing in the general direction of increasing crustal contamination. Smaller points indicate increasing negative Nb depletion. A) ϵ_{Nd} vs SiO_2 , B) ϵ_{Nd} vs $[La/Sm]_{pm}$, C) Nb/Nb^* vs Th/La , D) Nb/Nb^* vs Th/Ce , E) Nb/Nb^* vs $[La/Sm]_{pm}$, F) $[Nb/Th]_{pm}$ vs $[Th/Yb]_{pm}$.

Table 6.1. Partitioning coefficients of ultramafic (bold) and mafic magmas (Rollinson (2013) and Arndt (2008)).

	Th	Nb	La	Ce	Nd	Sm	Zr	Hf	Eu	Ti	Dy	Y	Yb	Lu
Olivine	1	1	03	1	42	0.0011	0.001	0.013	75	0.02	0.0014	0.01	0.03	0.016
CPX	0.01	0.03	0.0536	0.0858	0.187	0.291	0.1	0.263	0.35	0.4	0.442	0.9	0.43	0.56

Contamination by Upper Keewatin Assemblage calc-alkalic mafic and tholeiitic volcanic rocks created patterns similar to komatiitic units with moderate Nb depletions. Patterns created by contamination of a calc-alkalic unit (LOW17CB81) that were the most comparable to a komatiite sample with a Nb depletion (LOW17CB57) occurred after the addition of 10% contaminant and 20% assimilation/fractional crystallization as well as the addition of 20% contaminant and 15% assimilation/fractional crystallization (Fig. 6.19). As the degree of contamination was increased, the strength of the negative Nb depletion also increased. Contamination >10% generally created Nb depletions that were larger than the Nb depletions in komatiite units. There is also discrepancy between the abundance of LREEs. When the modelled pattern has both the proper Nb depletion and abundance of HREEs, it is often LREE depleted relative to the komatiite unit (Fig. 6.19). As contamination by a calc-alkalic contaminant was likely ~10%, it is possible that contamination occurred at depth, as surficial thermal erosion, or a combination of both methods (Huppert and Sparks, 1985). Binary mixing demonstrates similar results to the AFC modelling as Nb depletions cannot be matched to that of the Nb-depleted komatiite (Fig. 6.20).

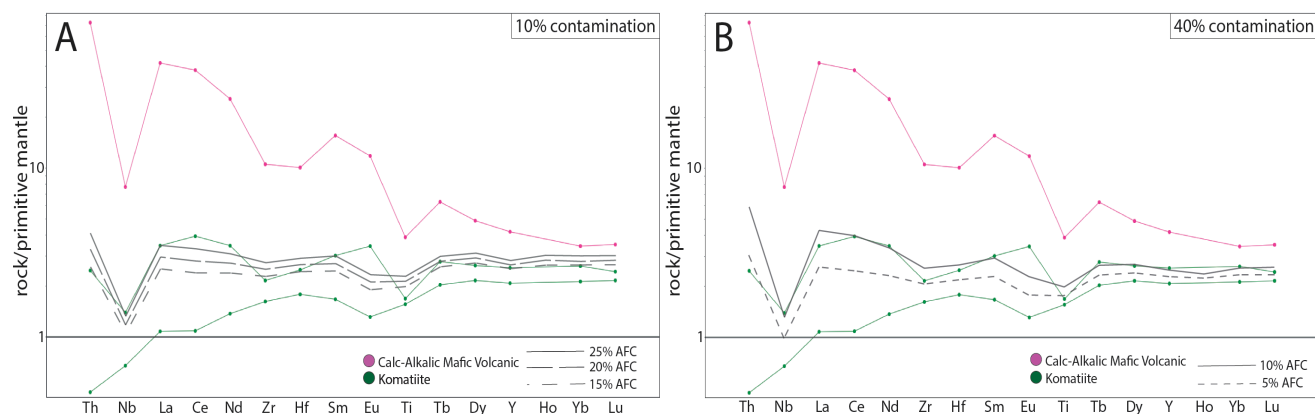


Figure 6.19. Results of AFC modelling plotted on primitive mantle normalized diagrams to produce Nb-depleted komatiites. A) Modelling at 10% contamination by a calc-alkalic mafic volcanic unit. B) Modelling at 40% contamination by a calc-alkalic mafic volcanic unit. Normalizing values after Sun and McDonough (1989).

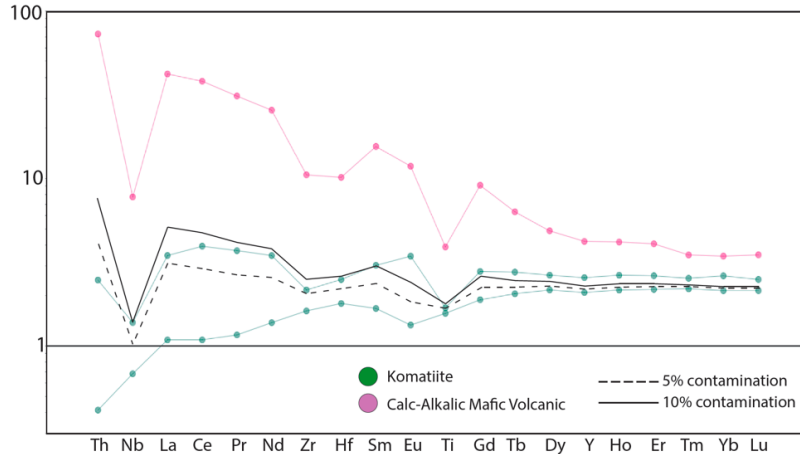


Figure 6.20. Binary mixing modelling on a primitive mantle normalized diagram to produce Nb-depleted komatiites. Mixing between a N-MORB komatiite sample and a calc-alkalic mafic volcanic unit.

Contamination by the low-Ti tholeiitic units that have distinct Nb depletions was also modelled. Similar results were observed with discrepancies between the HREE and LREE abundances. After the addition of 10% contaminant there were no comparable patterns as they lacked sufficient negative Nb anomalies (Fig. 6.21A). However, after 40% addition of contaminant there are slightly better comparisons with 20% assimilation/fractional crystallization yielding a pattern only slightly HREE enriched and LREE depleted compared to the proposed end result (Fig. 6.21B). Addition of ~40% contaminant suggests that contamination, if it occurred, was likely at depth and during emplacement. Binary mixing between the komatiite and low-Ti tholeiite produced similar Nb depletions after 25% contamination, however, LREE abundances are slightly lower than the Nb-depleted komatiites (Fig. 6.22). Simple mixing of komatiite and a strong Nb-depleted tholeiite at 25% contaminant produces similar concentrations of MgO, Ni and Cr, however mixing does not produce similar values with other major elements. As contamination reaches 40 to 50%, major element compositions become that of the komatiitic basalt samples (not shown).

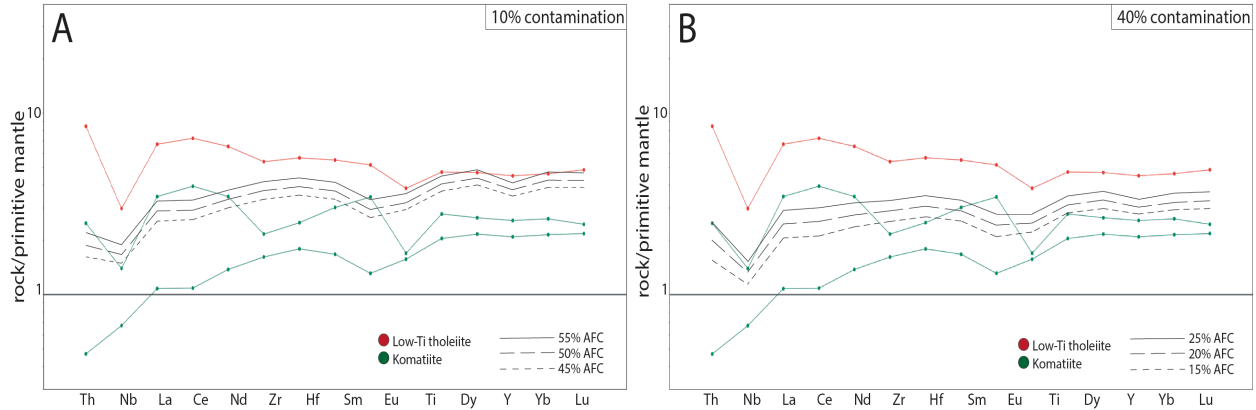


Figure 6.21. Results of AFC modelling plotted on primitive mantle normalized diagrams to produce Nb-depleted komatiites. A) Modelling at 10% contamination by a strong Nb-depleted tholeiitic mafic volcanic unit. B) Modelling at 40% contamination by a strong Nb-depleted tholeiitic mafic volcanic unit. Normalizing values after Sun and McDonough (1989).

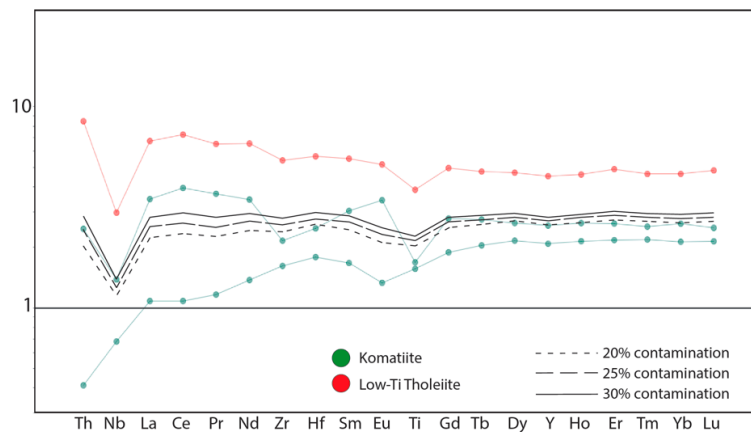


Figure 6.22. Binary mixing modelling on a primitive mantle normalized diagram to produce Nb-depleted komatiites. Mixing between a N-MORB komatiite sample and a strong Nb-depleted tholeiitic mafic volcanic unit.

Although enhanced mobility of Th, relative to Nb and Yb, can occur during medium- or high-grade metamorphism, the variation in Th/Yb and Th/Nb ratios within samples cannot be attributed to metamorphism since the samples should have experienced the same metamorphic grade. Variable Th/Yb and Nb/Yb trends, indicative of variable Th/Nb, likely reflect interaction between mantle-derived magmas and crust (Fig. 6.23A; Pearce, 2008). This would involve the interaction of low Th/Nb mantle-derived melts and high Th/Nb crust. The majority of samples have constant Th/Nb trends of approximately 0.12 over a range of SiO₂ of 43.7 to 50.8 wt%; however, samples that show strong negative Nb anomalies commonly exhibit enriched Th/Nb ratios up to 0.37 (Fig. 6.23B). Values of Th/Nb ratios are fairly consistent in the komatiites, komatiitic basalts and tholeiites in samples with weak Nb

depletions. Both high- and low-Ti tholeiites exhibit Th/Nb ratios of ~ 0.15 , similar to the average ratio of 0.12 seen in the komatiites and komatiitic basalts (not shown). The constant Th/Nb ratios in the tholeiitic mafic and ultramafic volcanic rocks, with the exception of units that have Nb depletions, are similar to observations by Smithies et al. (2018) in which they recognized constant and variable Th/Nb trends in the Yilgarn and Pilbara Craton and attributed it to two possible modes of greenstone belt formation. The two methods of greenstone belt formation include 1) possible arc-subduction interaction that evolved beyond the initiating stages of subduction, shown by constant Th/Nb over felsic to mafic lithologies, as well as 2) mantle-derived magmas interacting with the crust that produce variable Th/Nb ratios (Smithies et al., 2018).

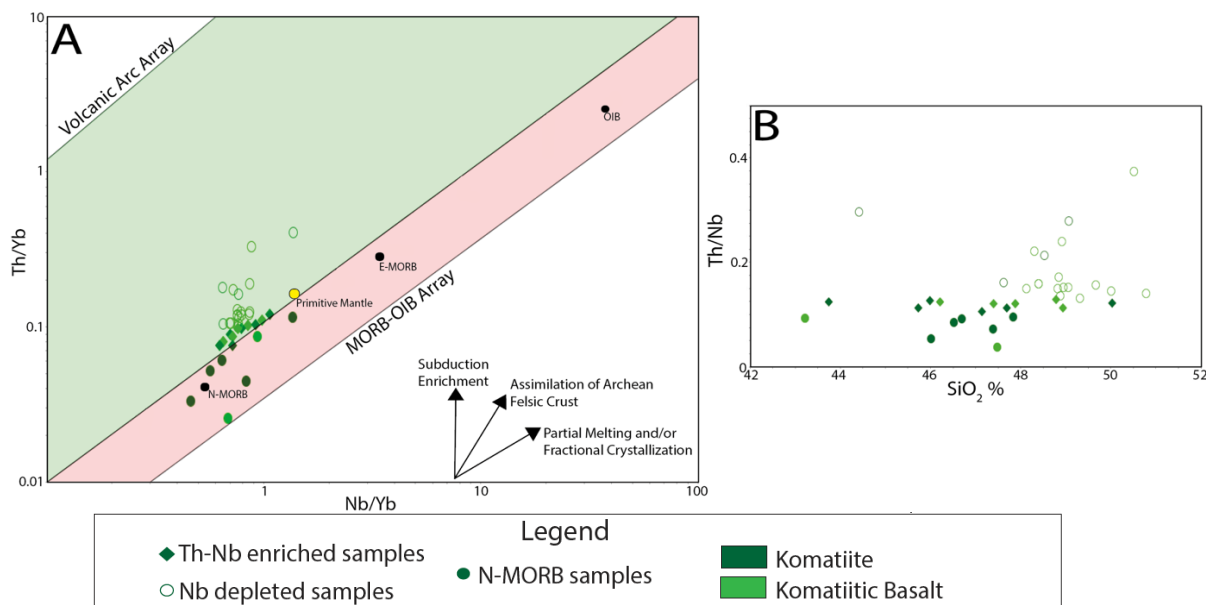


Figure 6.23. A) Diagram after Pearce (2008) of Th/Yb versus Nb/Yb. B) Th/Nb versus SiO₂ wt%.

Subduction-influenced magmatism can produce geochemical signatures similar to crustal contamination, including increased Th and strong Nb depletions. Figure 6.24 plots Ce/Nb versus Th/Nb with various end member sources consisting of a depleted MORB source mantle (DMM; high Ce/Nb), a recycled residual slab component (RSC) processed through a subduction zone (low Ce/Nb), and a subduction-derived component (SDC) complementary to RSC (high Th/Nb). Komatiites and komatiitic basalts with typical N-MORB patterns from this study show consistent Th/Nb ratios with variable Ce/Nb ratios less than

or near typical primitive mantle concentrations that plot consistently within a field defined by Archean tholeiites of the Superior Province (Fig. 6.24). Samples with enriched Th have similar Ce/Nb ratios as the N-MORB samples; however, they have slightly higher (+0.1) Th/Nb ratios. The samples with Nb depletions have strong variability amongst both Ce/Nb and Th/Nb ratios. Deviation towards higher Ce/Nb and Th/Nb ratios indicates a possible contribution from a subduction-derived source component (Fig. 6.24). The wide range in Th/Nb ratios suggests there is more than a singular process (e.g. alteration, contamination, partial melting) causing the Th enrichment (Saunders and Tarney, 1991).

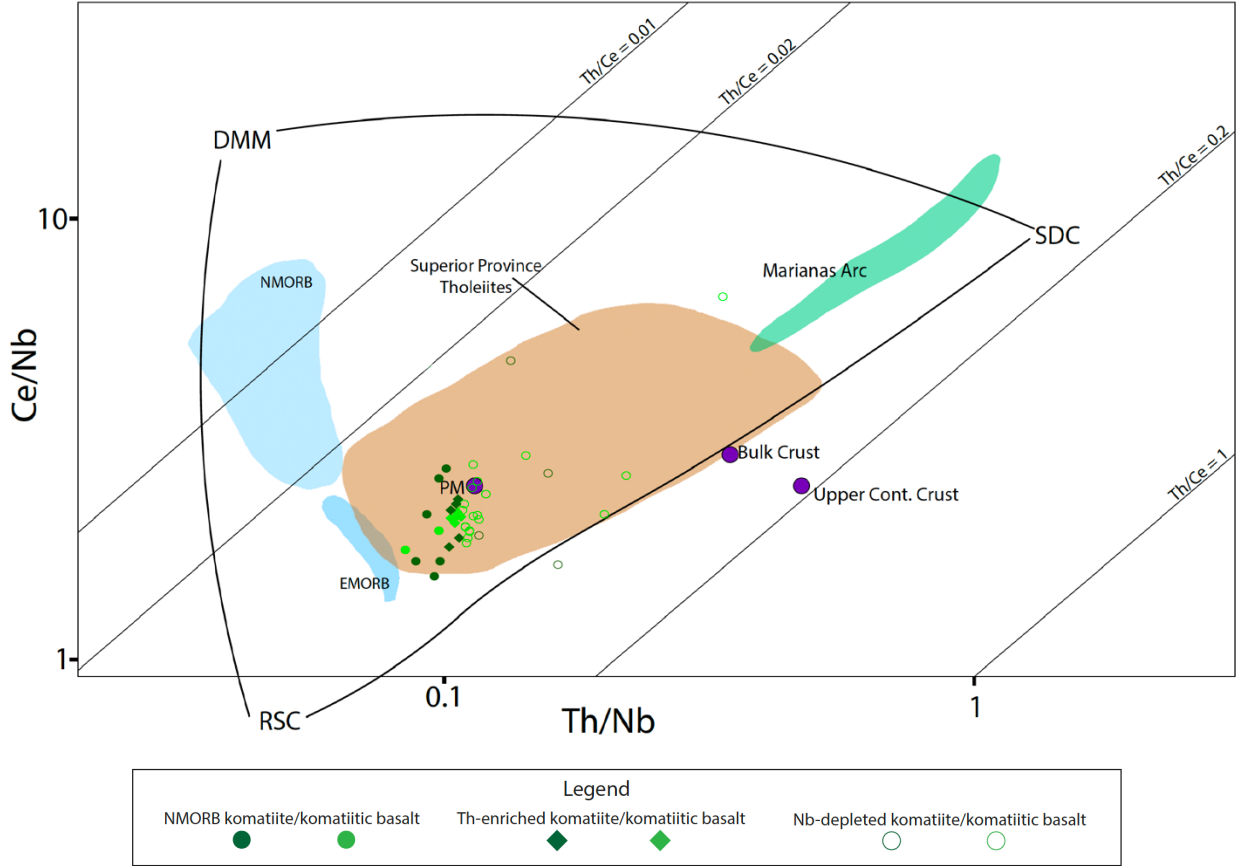


Figure 6.24. Plot of Ce/Nb versus Th/Nb. Data for Marianas Arc from Saunders and Tarney (1991). **N-MORB**: Normal MORB; **EMORB**: Enriched MORB; **PM**: Primitive Mantle; **SDC**: Subduction Derived Component, **DMM**: Depleted MORB Source Mantle, **RSC**: Recycled Residual Slab Component. Superior Province Tholeiites after Kerrich et al. (1999).

6.2.3.3 Th Enrichment

As discussed in Section 6.2.3.2, element mobility is not the likely source of the variation in Th abundances in the komatiites. The lack of correlation between samples with Th enrichments and LOI and Eu/Eu^* suggests alteration has not affected the Th abundances to cause the slight enrichment relative to komatiites with typical N-MORB signatures.

Numerical modelling was also utilized to test the possibility of contamination causing the enriched Th-Nb patterns of the komatiite units. Similar methods and partitioning coefficients as the modelling of the Nb depleted samples was applied to the modelling of Th-Nb enrichment. Contamination by calc-alkalic mafic volcanic rocks and tholeiitic samples with strong Nb depletions created patterns with Nb depletions that were too large ($\text{Nb}/\text{Nb}^* < 0.6$) to be comparable to komatiites with Th-Nb enrichments. Therefore, tholeiitic samples with moderate Nb depletions ($\text{Nb}/\text{Nb}^* > 0.6$) were used as potential contaminants.

The tholeiitic contaminant produced comparable patterns to the Th-enriched komatiite sample after the addition of 10% contaminant and 30% assimilation/fractional crystallization or by 40% contamination and 10% assimilation/fractional crystallization (Fig. 6.25).

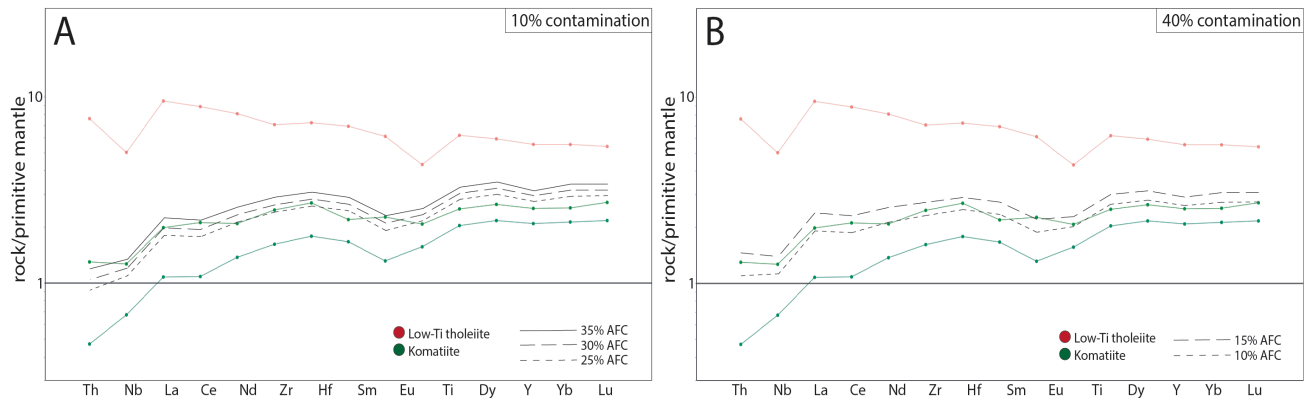


Figure 6.25. Results of AFC modelling plotted on primitive mantle normalized diagrams to produce Th-enriched komatiites. A) Modelling at 10% contamination by a weakly Nb-depleted tholeiitic mafic volcanic unit. B) Modelling at 40% contamination by a weakly Nb-depleted tholeiitic mafic volcanic unit. Normalizing values after Sun and McDonough (1989).

The modelling with 40% contamination yielded the best results as modelled patterns had similar HREEs and LREEs with only a slightly lower abundance of Th. The modelling with 10% however had comparable LREEs with higher abundances of HREEs, and therefore contamination at 40% is the ideal degree of contamination by a tholeiitic mafic volcanic rock with a moderate Nb depletion. Binary mixing produces similar results after 10 to 15%

contamination (Fig. 6.26). This suggests that contamination likely occurred during magma ascent rather than as a result of surficial thermal erosion.

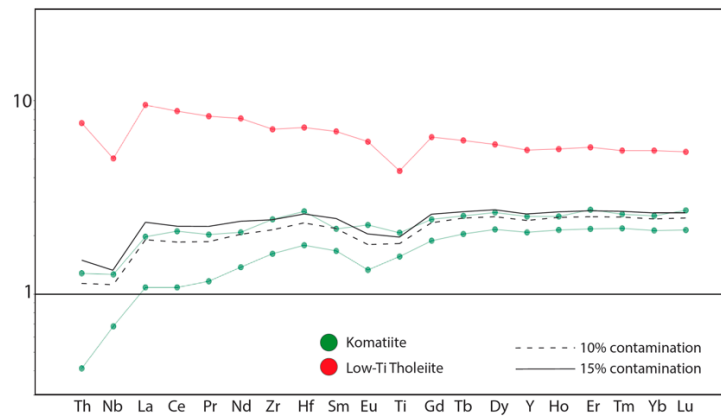


Figure 6.26. Binary mixing modelling on a primitive mantle normalized diagram to produce Th-enriched komatiites. Mixing between a N-MORB komatiite sample and a weakly Nb-depleted tholeiitic mafic volcanic unit.

Contamination by Lower Keewatin tholeiitic mafic volcanic rocks was also assessed as it is possible that the komatiitic magma interacted with the Lower Keewatin during its ascent. With the addition of 10% contaminant and 30% assimilation/fractional crystallization the pattern closely resembles that of the Th enriched komatiite sample (Fig 6.27). The same result was observed with 40% contamination and 10% assimilation/fractional crystallization (Fig. 6.27). The only variation between the komatiite sample and the modelled patterns is the strength of Th enrichment, as the modelled patterns are slightly Th-depleted in comparison to the komatiite pattern. Contamination up to 40% suggests it would have occurred during magma ascent.

6.2.5 Petrogenesis

The volcanism in the Upper Keewatin Assemblage consists of dominantly tholeiitic mafic to ultramafic volcanic rocks intercalated with minor calc-alkalic mafic volcanic rocks. The assemblage is also comprised of felsic to intermediate volcanic rocks, clastic sedimentary rocks, and various intrusive units. The tectonic setting to produce the Upper Keewatin Assemblage requires voluminous mafic magmatism with relatively sporadic ultramafic magmatism in a subaqueous setting given the widespread pillow basalts.

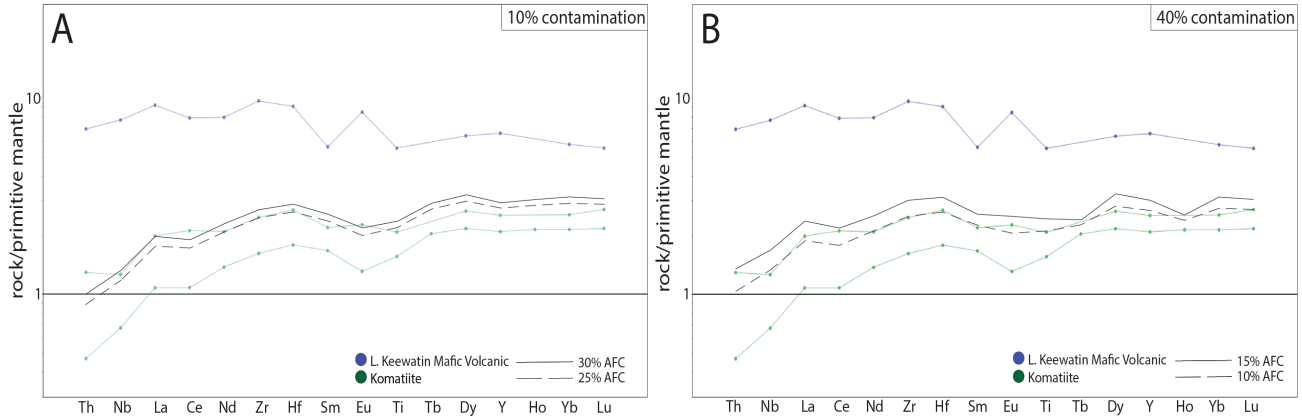


Figure 6.27. Results of AFC modelling plotted on primitive mantle normalized diagrams to produce Th-enriched komatiites. A) Modelling at 10% contamination by a tholeiitic mafic volcanic unit of the Lower Keewatin Assemblage. B) Modelling at 40% contamination by a tholeiitic mafic volcanic unit of the Lower Keewatin Assemblage. Normalizing values after Sun and McDonough (1989).

The komatiites within the UKA show evidence of complex Th-Nb-LREE systematics. The trace element variation within the komatiites cannot be explained by one process, but it is possible that the trace element geochemistry represents a combination of processes including contamination, binary mixing or assimilation and fractional crystallization and/or element mobility. Subduction zone influences will also be considered.

The major element and isotope geochemistry of the komatiites do not support contamination by an older felsic source. One komatiite from the literature has an ϵ_{Nd} signature of +1.3 and one komatiitic basalt of +1.2 (Ayer and Dostal, 2000). Komatiites from this study have ϵ_{Nd} ranging from +2.66 to +1.07, which fit within the typical range of Archean mantle derived rocks and were either uncontaminated or contaminated by material of similar composition and age (Hollings et al., 1999).

The AFC and binary mixing modelling suggest that contamination by the calc-alkalic mafic volcanic rocks would produce larger Th enrichments than seen in Nb-depleted komatiite samples with as little as 10% contaminant. The tholeiitic mafic volcanic contaminant with a strong Nb depletion produces a pattern similar to that of the Nb-depleted komatiite with binary mixing of 30% contaminant. The AFC modelling of this unit with the addition of 40% contaminant produces similar Nb depletions; however, with lower abundances of LREEs and higher abundances of HREEs. The komatiites with Nb depletions could have been contaminated by the strongly Nb-depleted tholeiitic mafic volcanic rocks. Modelling to produce komatiites with weak Th enrichments is much more promising.

Assimilation and fractional crystallization modelling with 40% addition of a contaminant and approximately 10% fractional crystallization produces a pattern very similar to that of the komatiite sample. Binary mixing also produces similar results at 10% contamination. The modelling suggests that Th-enriched komatiites may have been produced with 10% contamination by weakly Nb-depleted komatiites (binary mixing) upon eruption, or with 40% addition of contaminant and 10% fractional crystallization upon magma ascent.

When both mafic and ultramafic lithologies are plotted on the Pearce (2014) discrimination diagram, there are multiple lithological differentiations that can be observed (Fig. 6.28). Specifically, the tholeiitic mafic volcanic rocks, komatiitic basalts and komatiites show various trends. The low- and high-Ti tholeiites with moderate Nb depletions form a constant array with the komatiites and komatiitic basalts with Th enrichments. This linear trend shows a constant increase in Th/Yb and Nb/Yb ratios, and therefore constant Th/Nb. The komatiites and komatiitic basalts with Nb depletions are extremely scattered on this diagram as some plot along the constant Th/Nb array, and some plot in proximity to the strongly Nb depleted low-Ti tholeiites. This suggests that there is a relationship between Th-enriched komatiites/komatiitic basalts and weak to moderately Nb depleted low-Ti tholeiites.

As previously mentioned, AFC and binary mixing processes between the low-Ti tholeiite and komatiite parent can produce komatiites with Th enrichments. The constant Th/Nb array is consistent with partial melting and/or fractional crystallization processes, consistent with the possible contamination model for the Th enriched komatiite samples. Crustal contamination often creates a greater increase in Th/Nb as there is greater input of Th as it is concentrated in the crust. The samples towards the higher Th/Yb and Nb/Yb ratios have a slight steepening of the linear trend, and it is possible that the tholeiites did have some interaction with crustal material, resulting in slightly higher Th abundances. The Nb-depleted komatiites cannot be explained in this way as they do not form a linear trend and are highly scattered. Two komatiitic basalts and one komatiite cluster with the strongly Nb depleted tholeiites within the oceanic arc array, two komatiite and two komatiitic basalts samples occur with the strongly Nb depleted low-Ti tholeiite outlier, and the remainder occur within the linear array defined by the moderately Nb depleted tholeiites and Th-

enriched komatiites. The highly variable scatter is consistent with multiple processes affecting the Th and Nb of these samples.

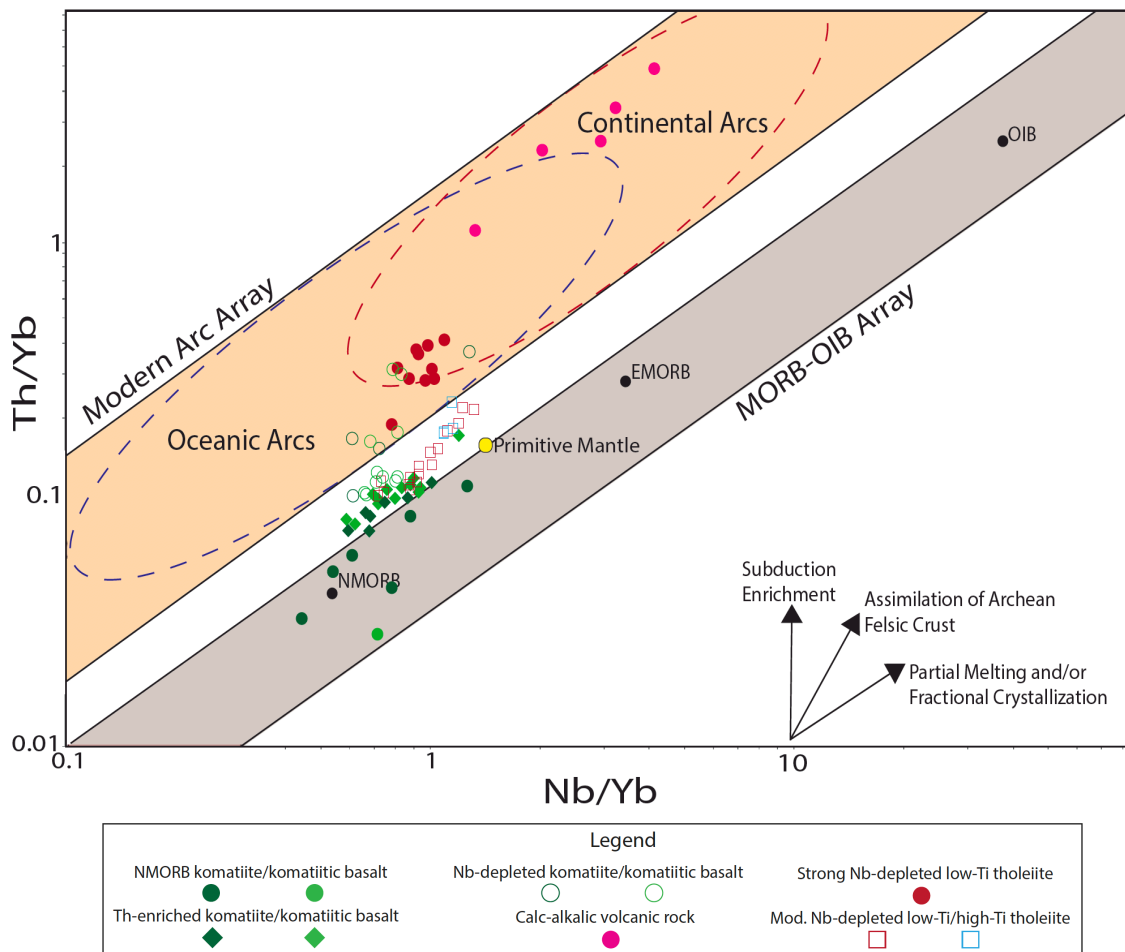


Figure 6.28. Diagram after Pearce (2014) plotting Th/Yb versus Nb/Yb of calc-alkalic mafic and tholeiitic mafic to ultramafic volcanic rocks.

The relationship between the units can be recognized on a Th/Nb versus Th diagram (Fig. 6.29). Komatiitic to tholeiitic rocks from Ayer (1997) are characterized by Th/Nb ratios of approximately 0.2, values that are fairly consistent with Th-enriched komatiites/komatiitic basalts as well as weakly to moderately Nb-depleted tholeiites in this study. The N-MORB komatiite samples typically have lower Th/Nb ratios and the Nb-depleted komatiite samples have higher ratios, similar to the lower ratios of the strongly Nb-depleted tholeiites. Niobium-depleted ultramafic rocks show a somewhat vertical trend, indicating an increase in Th/Nb ratios, with no great addition of Th, and therefore may have been the result of processes that created a Nb depletion without abundant addition of Th,

indicating potential subduction enrichment and/or partial melting with fractional crystallization that could be possibly occurring in conjunction with contamination.

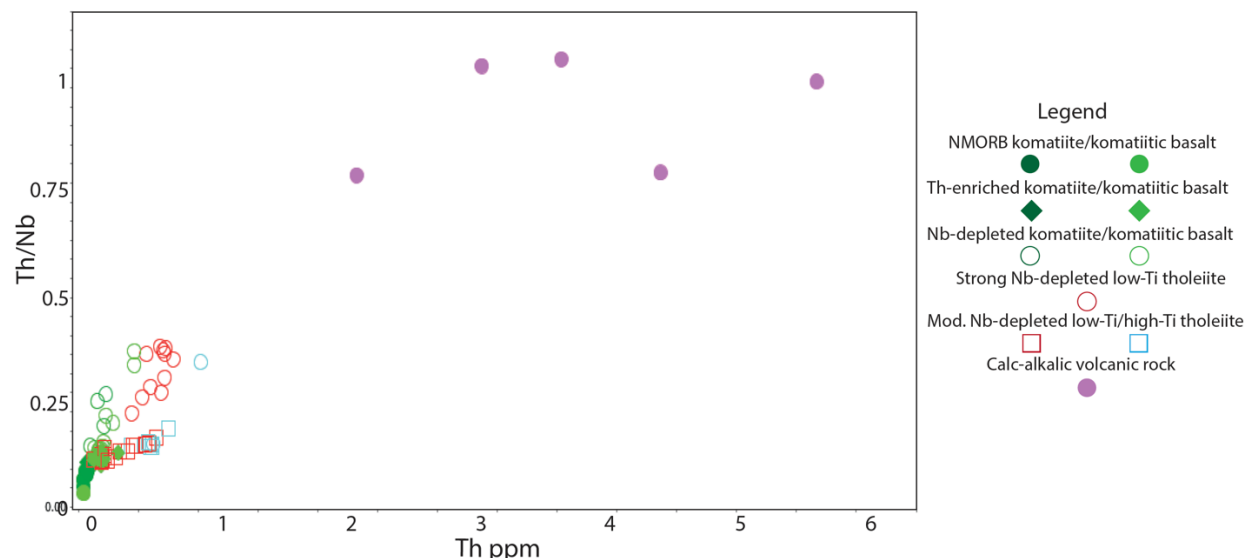


Figure 6.29. Th/Nb versus Th (ppm) of ultramafic and mafic volcanic rocks.

There is a distinct variation in the $^{147}\text{Sm}/^{144}\text{Nd}$ ratios of the study samples that plot with tholeiitic versus calc-alkalic affinities. Henry et al. (1997) established a series of mixing lines with trends defined by felsic intrusive and volcanic rocks, and intermediate and mafic volcanic rocks. Calc-alkalic samples plot along the felsic to intermediate volcanic trend line whereas tholeiitic affinity samples plot along the trend line defined by basalts (Fig. 6.30). Low Sm/Nd ratios may result from partial melting of the crustal endmember prior to mixing with mantle-derived magmas (Henry et al., 1997). The clear break between mixing lines b and c suggest that there was no interaction or mixing between the calc-alkalic rocks and tholeiitic mafic to ultramafic rocks (Fig. 6.30). This further supports the calc-alkalic AFC modelling is not successful in producing Nb-depleted komatiites.

6.2.6. Tectonic Environment

Trace element geochemistry suggests that the Upper Keewatin Assemblage formed in a complex geodynamic setting. Ayer and Davis (1997) proposed two models for the generation of the Lake of the Woods tholeiitic and calc-alkalic suites. They proposed that either there was an eruption of two suites from different geodynamic settings into a common depositional basin, or the two suites were derived from different magmatic sources in a

common geodynamic setting. They suggest that calc-alkaline volcanic rocks formed in a mature island arc setting whereas the tholeiites and komatiites may be the result of second-stage melting of the refractory mantle source from which the Lower Keewatin tholeiites were derived (Ayer and Davis, 1997).

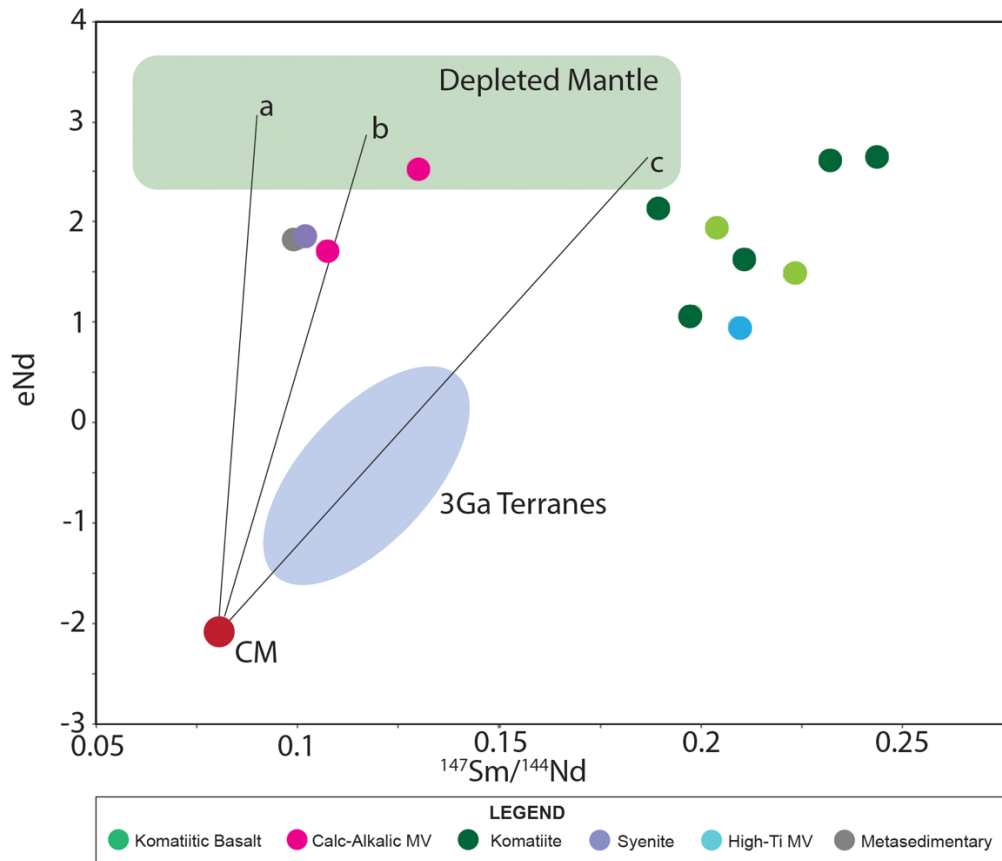


Figure 6.30. ϵ_{Nd} versus $^{147}\text{Sm}/^{144}\text{Nd}$ modified after Henry et al., (1997). Trend lines defined by granodiorites and diorites (a), intermediate to felsic rocks (b) and basalts (c). CM: Crustal endmember.

Dostal and Mueller (1997) proposed that the volcanic rocks of the Stoughton-Roquemaure (SRG) and Hunter Mine (HMG) Groups in the Abitibi greenstone belt show the effects of a plume impinging on a volcanic arc. The SRG consists of both ADK and AUK types, and proposed a heterogeneous plume to account for compositional variations encountered (Dostal and Mueller, 2013). The HMG consists of dominantly calc-alkalic felsic rocks, with minor basaltic and andesitic rocks (Dostal and Mueller, 1997). The volcanic rocks of the SRG and HMG show the effects of a mantle plume rising below and through an arc (Dostal and Mueller, 1997). Similar features are observed in the ultramafic to mafic rocks of Falcon Island

and Cliff Island in the Lake of the Woods Greenstone Belt. Calc-alkalic and tholeiitic mafic to ultramafic rocks are suggested to be intercalated from previous fieldwork conducted by Ayer (1997); however, these relationships were not observed in this study due to the lack of visible contacts in the field. Additionally, two models have been proposed for the generation of komatiites: the anhydrous melting of the mantle (mantle plume origin) as well as wet melting in which komatiites can be derived from a subduction zone setting (Grove et al., 1996; Parman et al., 1997; Parman et al., 2004). The subduction zone model suggests that komatiites could be produced by hydrous melting at shallower depths, and do not require temperatures as high as what is predicted for anhydrous melting (Parman et al., 1997; Arndt et al., 1998). This model is considered to account for prominent Nb-depletions present in many komatiite samples that lack evidence for contamination by older crustal material. The plume model for komatiite generation suggests that AUKs originate from depths of approximately 100 to 350km (above the garnet stability zone). Grove and Parman (2004) suggested that AUKs form at the core of the plume head and ADKs form in the plume tail. This contrasts with the model of Campbell et al. (1989) in which they suggest that basalts originate from the plume head and komatiites from the plume tail. The plume model is favoured by the author for the origin of komatiites in this study as insufficient evidence exists to suggest a subduction zone origin, as these studies often utilize primary mineral chemistry.

Low-Ti tholeiites that plot within the arc array in Figure 6.28 have stronger Nb depletions than tholeiites that plot along the MORB array, which may represent a fractionation effect by titanite, rutile, ilmenite or hornblende, present in the hydrated mantle wedge, however the weak to strongly Nb depleted tholeiites have a similar range of Ti depletions ($Ti/Ti^* = 0.6$ to 0.9). This suggests that magnetite and ilmenite fractionation did not occur in variable amounts between the two tholeiitic subdivisions and rather that hornblende, rutile and/or zircon were the main fractionating phases. Fractionation trends are observed while utilizing Al_2O_3/TiO_2 ratios versus both Al and Ti as this can track plagioclase and magnetite/ilmenite fractionation (Fig. 6.31). The linear trend observed in Figure 6.31A suggests magnetite fractionation occurred, whereas the scatter observed in Figure 6.31B does not support plagioclase fractionation. Typical basalts of subduction zone environments are often characterized by high Al_2O_3 (17 to 21 wt%), implying that plagioclase was not a liquidus phase and did not fractionate (Murphy, 2007). The low-Ti

tholeiites show a range of Al_2O_3/TiO_2 (14 to 25), similar to typical ranges of Superior Province tholeiitic suites ($Al_2O_3/TiO_2 = 10$ to 30) that have been interpreted to be the result of various fractionation effects (Hollings and Kerrich, 1999). Since weakly Nb depleted tholeiites (both high- and low-Ti) plot along the MORB array it is possible that minor fractionation or contamination produced the Nb depletion rather than subduction-related magmatism.

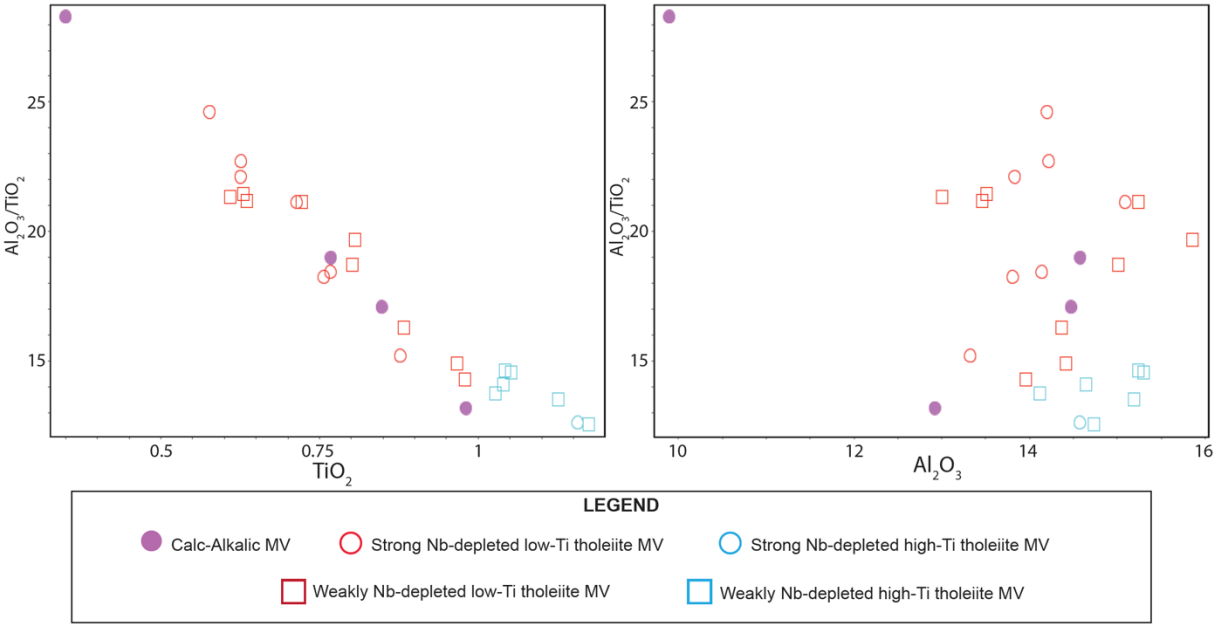


Figure 6.31. Bivariate diagrams of Al_2O_3/TiO_2 versus TiO_2 and Al_2O_3/TiO_2 versus Al_2O_3 of mafic volcanic rocks.

Although it is suggested that komatiites and most tholeiitic mafic volcanic rocks originated from plume-related magmatism, there are still abundant tholeiitic samples as well as the calc-alkalic rocks that have subduction-related signatures. As tholeiitic magmas are typically dominant in the early stages of oceanic island-arc genesis and calc-alkalic magmas are most common in mature oceanic arcs, it is possible that the island arc system in the Upper Keewatin Assemblage (UKA) represents a transition from a primitive to a mature arc system (Murphy, 2007). Typically, island arcs capped by mafic crust tend to be dominantly mafic to intermediate magmas, which suggests the presence of an island arc system to form the UKA (Murphy, 2006). It is therefore likely that tholeiitic mafic to intermediate volcanism with prominent Nb depletions originated from early stage subduction in an oceanic arc, whereas

the tholeiites with weak Nb depletions did not and will be discussed in a further section (Fig. 6.32).

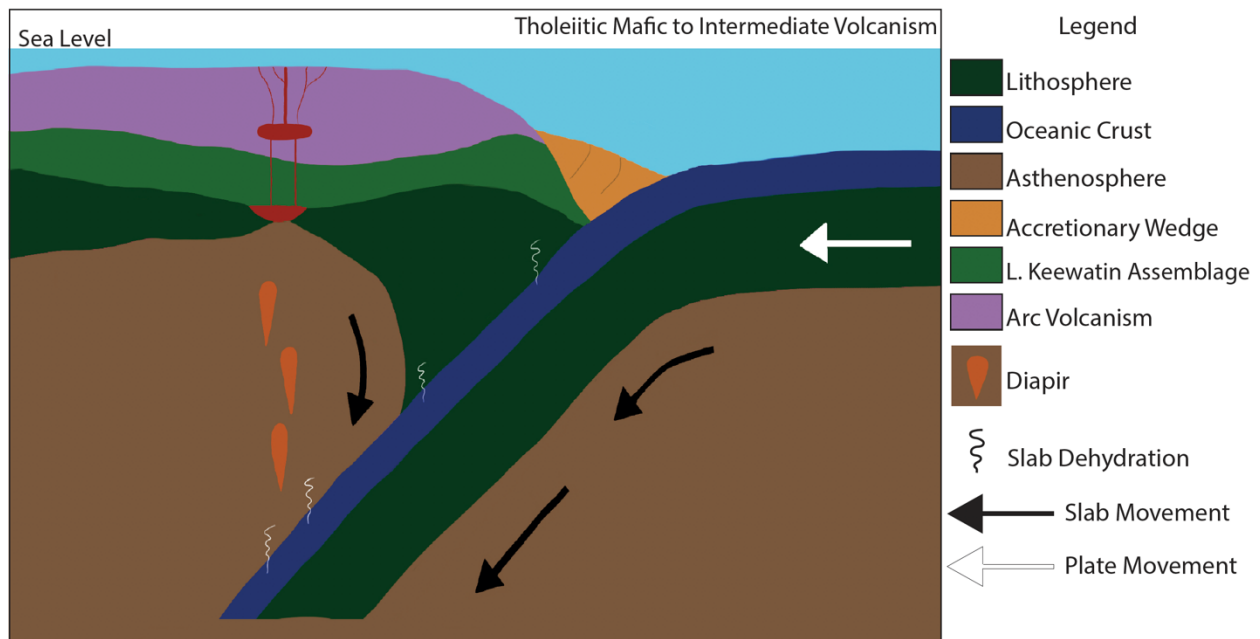


Figure 6.32. Reconstruction of the geodynamic setting for tholeiitic dominant magmatism.

Calc-alkalic volcanic rocks of this study display strongly enriched LREEs, negative HFSE anomalies and weak HREE fractionation, consistent with subduction related magmatism from within the garnet stability zone (Fig. 6.33). The tholeiites on the other hand have flat HREEs and do not have as strong a LREE enrichment as the calc-alkalic mafic volcanic rocks. This is consistent with a maturing of the island arc resulting in the progressive enrichment of LREEs, resulting in calc-alkalic magmatism (Murphy, 2007). With the gradual maturing of the subduction zone, the upper oceanic crust and mantle wedge cools and allows hydrous fluids to be subducted into the zone of arc magma generation (Savov et al., 2006). Although the garnet stability zone does not usually occur until depths of approximately 400 km, in mature arcs the effects of fluids are more profound and thus hydrated mantle melts can occur at significantly lower temperatures than the dry mantle (Ringwood, 1982). The addition of water weakens the bonds within crystal structures and requires less energy to break the bonds therefore magma can form at lower temperatures than under dry conditions (Murphy, 2007).

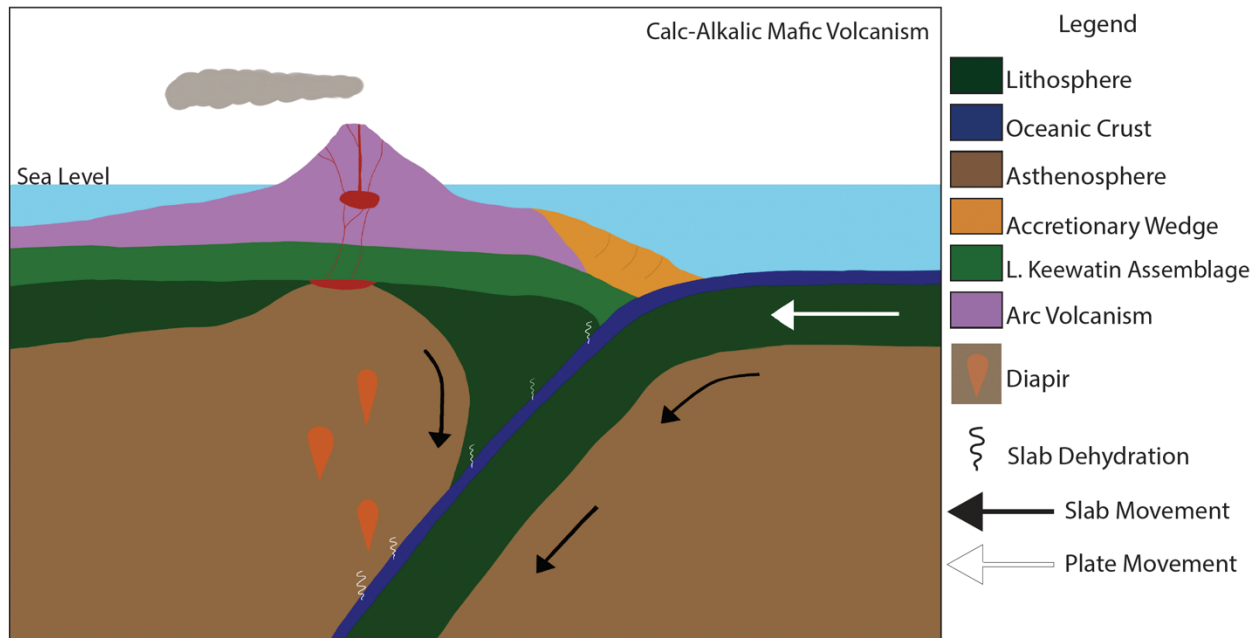


Figure 6.33. Reconstruction of the geodynamic setting for calc-alkalic dominant magmatism.

An idealized cross section through an intra-oceanic arc shows various lithologies present throughout the assemblage (Fig. 6.34). Typically, mafic cumulate rocks and sills occur at the base. Gabbroic intrusions of this study have similar primitive mantle patterns to the low-Ti tholeiites, and therefore it is possible they represent the interior of the arc plumbing system, as shown in Figure 6.35 (Murphy, 2006). Gabbro and cumulate samples are of tholeiitic affinity and therefore are likely sourced during arc initiation rather than sourced from within the mature arc system. Although samples of felsic intrusive units were not taken in this study, it is likely that they occurred as mid-crustal plutons in a mature arc setting in which magma differentiation occurred (Stern, 2002). Mafic flows and pillowed lavas occur at the base of the arc system, in which it is likely that tholeiitic flows and pillowed lavas occur from arc initiation and are then intercalated with calc-alkalic flows. As felsic and intermediate tuffs were mapped during this project but no samples taken for geochemistry, it is inferred that they may be of calc-alkalic affinity and occur interbedded with flows in the mature arc system.

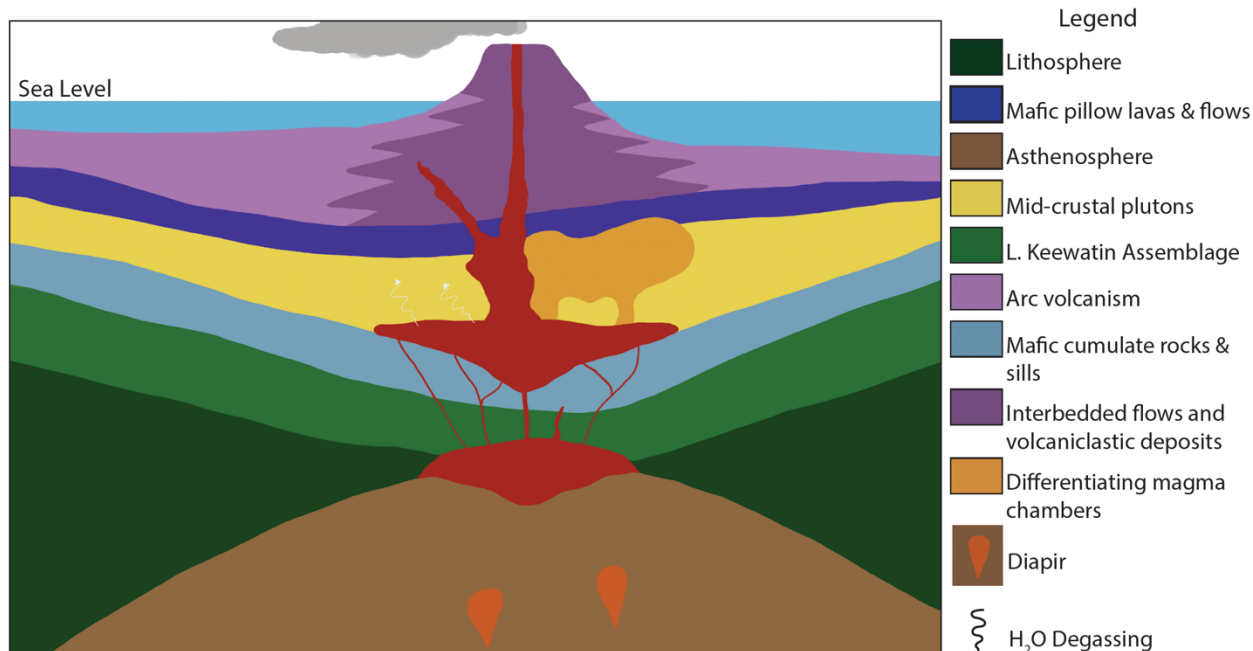


Figure 6.34. Idealized section through an oceanic arc.

The komatiites display various complex geochemical signatures based on the wide variety of primitive mantle patterns. As the assemblage is quite extensive, it is likely that multiple komatiite flows exist. It is possible that each geochemical signature present within the komatiites represents a different flow. Since complete stratigraphic sections were not observed in the field, it is difficult to determine which flow would have erupted first. It is proposed that AFC between the komatiite parent and weakly Nb-depleted low-Ti tholeiites produced the Th-enriched komatiites. On a primitive mantle normalized diagram, it is expected that parallel trends represent units derived from a similar source, with increasing element abundances indicating fractionation (Fig. 6.35; Murphy, 2007). There are slight parallels between Th-enriched komatiites and weakly Nb-depleted tholeiites, and perhaps the transition from the lowermost section when samples have parallel patterns to the samples at the uppermost section represent the interaction between the two suites. As the weakly Nb-depleted tholeiites plot along the MORB array, it is possible that these tholeiites were derived from the same source as the komatiites and some samples were contaminated which could explain the slight increase in Nb depletion and the increase in Th/Yb ratios observed on Figure 6.28. A plume interacting with a tholeiitic contaminant upon magma

ascent without contamination by the Lower Keewatin Assemblage is a plausible model (Fig. 6.36).

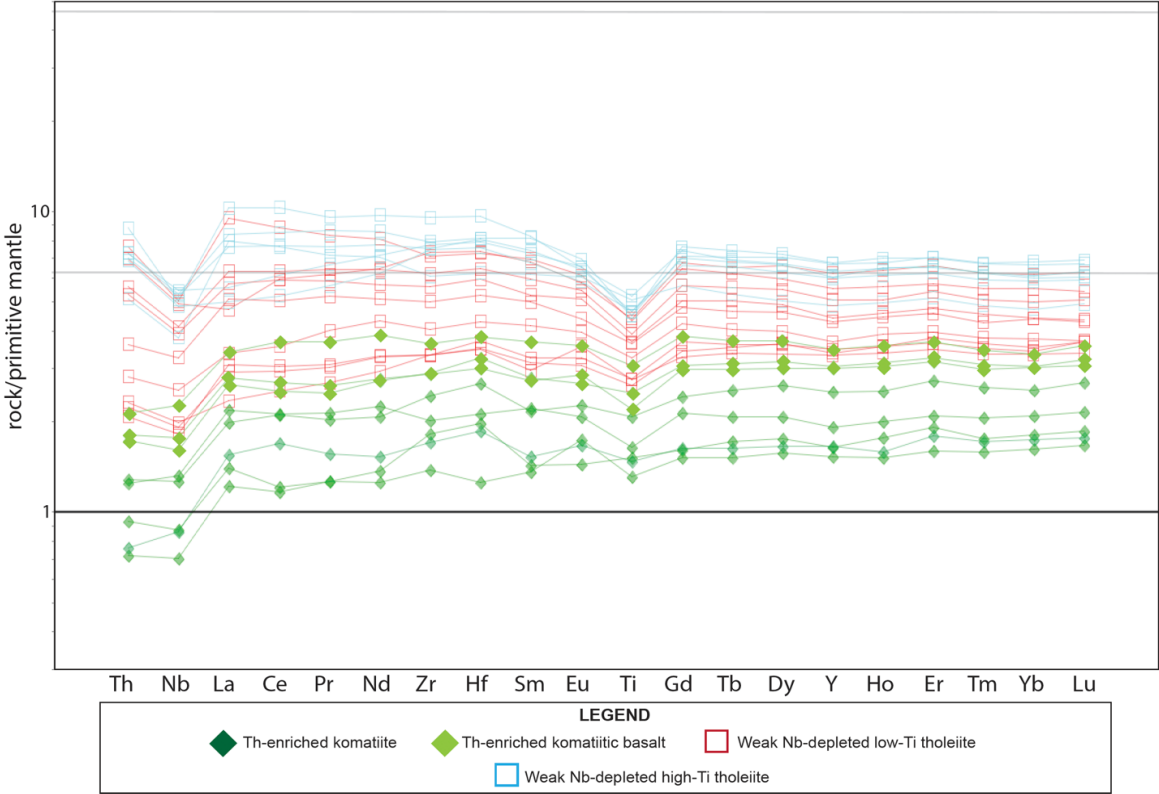


Figure 6.35. Primitive mantle normalized diagram



Figure 6.36. Reconstruction of plume-related komatiite and tholeiite magmatism.

Komatiites with Nb depletions were not perfectly replicated when AFC and binary mixing were explored, meaning there is not a single method that produced the geochemical signatures present. It is likely that contamination played a role; however, it is possible that greater fractionation occurred within the flow that produced Nb-depleted komatiites, and or secondary alteration/metamorphic effects have also affected the Th-Nb-LREE systematics. Island arcs are normally segmented into belts which can be terminated by deep-penetrating fractures that accommodate along-strike variations in the dip of the subduction zone (Murphy, 2007). Typically, magmatism in the vicinity of these fractures has chemical and isotopic features that are different from typical arc magmas and may reflect local upwelling of underlying asthenosphere (Murphy, 2006). Oceanic crust produced at slow spreading ridges is probably much more heterogeneous, with masses of unaltered crust (as wide as a few tens of kilometers) separated by major fault zones that penetrate the full thickness of the crust and result in substantial serpentinization of mantle rocks (Stern, 2002). If this is the case, it is possible that these fractures and/or fault zones could act as conduits for rising magmas as they exploit large scale crustal weaknesses. A komatiitic flow in this scenario may have interacted with subduction-derived fluids; however, this requires that the plume originated from underneath the subducting slab (Fig. 6.37). Kincaid et al. (2013) suggested that a plume rising in front of the trench may be stalled and bifurcated by subduction related flow, noting that factors that influence the relative sizes, positions and evolution of surface thermal expressions include the subduction style, plume location and plume buoyancy, and that –in very hot upwelling cases (approximately 600°C), the entire plume head ascended to the base of the surface plate. Fletcher and Wyman (2015) also suggest that some mantle plumes have closely interacted with subduction zones; however, the survival of a plume passing beneath a thicker mature trench is more problematic, likely due to the increase of thickness from a juvenile to mature trench. Although mantle-plume interactions have been commonly proposed for Archean sequences of intercalated calc-alkalic mafic to tholeiitic mafic and ultramafic rocks, the mechanisms involved have yet to be fully explained, and therefore although this scenario is possible, it is difficult to definitively conclude that this sequence of events occurred (Tomlinson et al., 1998; Hollings et al., 1999).

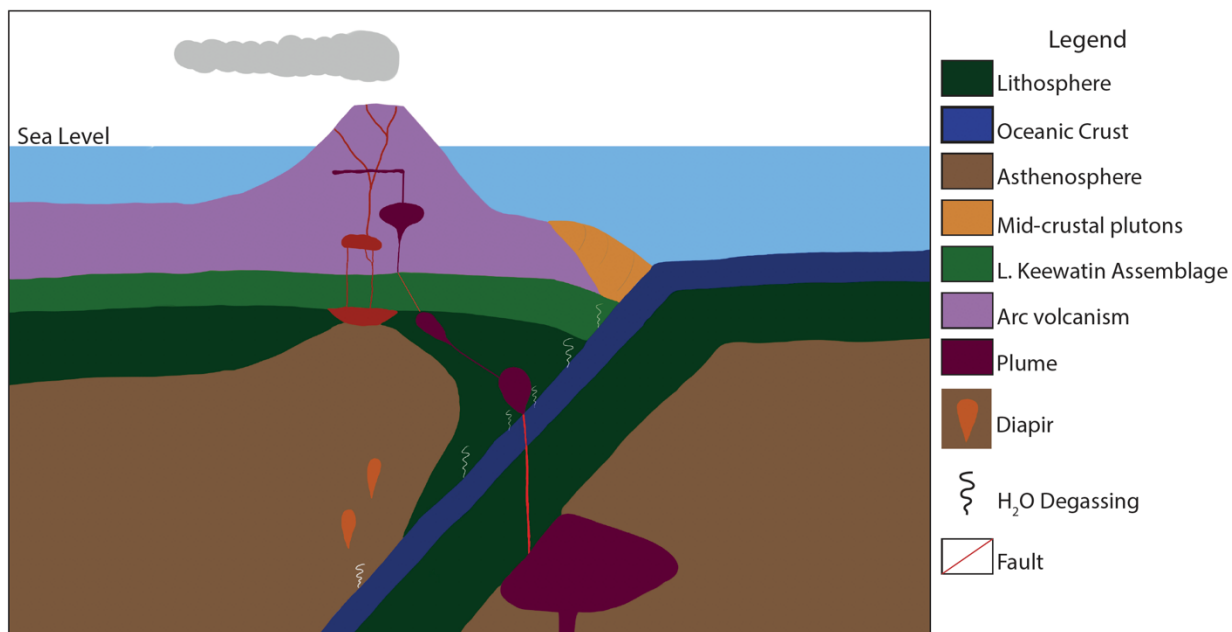


Figure 6.37. Reconstruction of possible pathways for an ascending plume.

Overall, the komatiites of the Lake of the Woods greenstone belt suggest a homogenous plume likely derived from partial melting of anhydrous mantle. The preferred model for belt evolution is an initial primitive oceanic arc with voluminous subaqueous tholeiitic magmatism, followed by dominantly calc-alkalic magmatism once the arc matured. Potential plume-arc interaction is probable as komatiite samples are commonly enriched in Th and display prominent Nb depletions whilst lacking signatures of contamination by older crustal material. Tholeiitic mafic volcanic rocks within the greenstone belt also originate from the ascending plume with weak Nb depletions likely from fractional crystallization. Although the exact geodynamics of the plume-arc interaction are unknown, geochemistry indicates it is plausible.

Chapter 7: Conclusions

The Lake of the Woods greenstone belt is comprised of three assemblages: the Lower Keewatin Assemblage (LKA), the Upper Keewatin Assemblage (UKA), and the Electrum Assemblage. The study area is located within the Long Bay Group of the Upper Keewatin Assemblage, in which ultramafic volcanic rocks were the focus. The UKA is composed of ultramafic to felsic volcanic rocks of tholeiitic and calc-alkalic affinity, that are commonly fine-grained and aphyric, with locally pillowed mafic and ultramafic flows. Lesser mafic and felsic intrusive units, as well as minor clastic metasedimentary rocks, occur sporadically throughout. Ultramafic rocks consist of both komatiites and komatiitic basalts with rare polyhedrally jointed flow tops; however, spinifex texture was not observed. Amphibole porphyroblasts are common throughout, typically as actinolite to tremolite in mafic volcanic rocks and tremolite to anthophyllite in ultramafic volcanic rocks. Trace amphibolites occur in scattered lenses throughout the field area that contain abundant poikiloblastic actinolite and tremolite. Overall, the field area is composed of dominantly anthophyllite-tremolite-chlorite and serpentine-tremolite-chlorite schists, as well as lesser talc-tremolite-chlorite schists.

The assemblage is composed of dominantly low-Ti tholeiitic with rare high-Ti tholeiitic basalts, Al-undepleted komatiites, and lesser low-Ti calc-alkalic basalts. The mafic volcanic rocks comprise the majority of Falcon and Cliff Island. Geochemically, low-Ti tholeiites can be subdivided into a weak to moderately Nb-depleted group and a strongly Nb-depleted group. The variation in negative Nb anomalies cannot be attributed to fractionation processes, therefore it is likely that the tholeiites were derived from different sources. Tholeiites with strong Nb depletions have trace element geochemistry consistent with rocks derived from an oceanic arc whilst weak to moderately Nb-depleted tholeiites form a trend along the MORB-OIB array. Tholeiites sourced from the oceanic arc are void of contamination, fractional crystallization, and subduction enrichment, however there are likely fractional crystallization and contamination effects on units along the plume-derived array. Calc-alkalic volcanic rocks have enriched LREEs and fractionated HREEs, consistent with subduction-derived magmatism with a magmatic source within the garnet stability zone. There is no variation between the calc-alkalic and tholeiitic rocks based on major element geochemistry and petrography. Based on Th, Nb, and Yb, the calc-alkalic rocks are suggested to be derived from a mature oceanic arc.

Complex trace element geochemistry suggests the various komatiite flows underwent various processes during eruption. Geochemically, based on trace element patterns, three varieties of komatiites exist within this study. Approximately half of the komatiite samples have typical N-MORB patterns in which they are LREE depleted with flat HREEs whereas the other majority of komatiites have progressive Th enrichment, to the extent that rare samples have weak to moderate negative Nb anomalies. Komatiites with N-MORB primitive mantle signatures are void of contamination and fractional crystallization effects. Numerical modelling was utilized to test the possibility of contamination causing enriched Th in numerous komatiite samples. It is possible that contamination by tholeiites with weak to moderate Nb depletions produced Th-enriched komatiite samples. This was typically observed with the addition of 40% contaminant accompanied by 10-15% fractional crystallization, likely upon magma ascent.

Komatiites with Nb-depletions require various processes to explain the Th-Nb-LREE systematics. It is clear that alteration and metamorphism cannot be attributed to the Th and Nb variation as there is no correlation between LOI and $[Th/La]_{pm}$ or Eu/Eu^* and $[Nb/La]_{pm}$. Contamination by older crustal material can also be ruled out as komatiites and komatiitic basalts with Nb depletions have ϵ_{Nd} values from +1.07 to +2.66. This is confirmed by a lack of negative correlation between ϵ_{Nd} and SiO_2 . Assimilation and fractional crystallization modelling was also used to assess possible contaminant for Nb-depleted komatiites. The AFC modelling conducted to produce Nb-depleted komatiites with a highly Nb-depleted tholeiitic contaminant showed similar results to the Th-enriched komatiites. After the addition of 40% tholeiitic contaminant and 20-25% fractional crystallization, similar Nb-depleted komatiite patterns were produced with slight discrepancies in LREE and HREE abundances. Along with tholeiitic contaminants, a calc-alkalic volcanic rock was also used. With contamination by a calc-alkalic sample from the UKA, Nb-depleted modelled patterns were similar when there was the addition of 10% calc-alkalic contaminant and ~20% fractional crystallization. This differs from other contamination trends in which the addition of 40% contaminant was required. Based on the contamination modelling, it is unlikely that contamination is the sole mechanism affecting the Th-Nb-LREE systematics. Subduction-influenced magmatism can produce geochemical signatures similar to crustal contamination, including increased Th and strong Nb depletions. Although Nb-depleted samples show signatures of subduction

enrichment relative to N-MORB komatiites, there is not sufficient evidence that indicates it is the only process producing negative Nb anomalies.

The tectonic setting to produce the Upper Keewatin Assemblage requires voluminous mafic magmatism with relatively sporadic ultramafic magmatism in a subaqueous setting given the widespread pillow basalts. Tholeiitic samples with weak to moderate Nb-depletions show consistent Th/Nb ratios as most Th-enriched komatiites and komatiitic basalts, suggesting that the interaction between these units is highly likely. Some deviation occurs in high-Ti tholeiites especially, and it is likely that a small population of tholeiitic rocks underwent minor contamination and have slightly elevated Th/Nb ratios. There is no consistency between Th/Nb ratios of Nb-depleted komatiites and tholeiites with large negative Nb anomalies, further suggesting a lack of interaction between the two units. Although it is suggested that komatiites and most tholeiitic mafic volcanic rocks originated from plume-related magmatism, there are still abundant tholeiitic samples as well as the calc-alkalic rocks that have subduction-related signatures. It is possible that highly Nb-depleted tholeiites represent the early stages of oceanic island-arc genesis and calc-alkalic volcanic rocks represent the maturing stages of the arc in which the magmatic source deepened to within the garnet stability zone. This represents a transition from primitive to mature arc system.

It is likely that multiple komatiitic flows exist within the assemblage. Trace element signatures of various komatiite samples suggests that three possible flows exist. The parallels of trace element geochemistry between Th-enriched komatiites and weakly Nb-depleted tholeiites suggests the two units may have been derived from a similar source. Minor tholeiites may have undergone subsequent contamination as there are tholeiites that plot along the MORB array that have a slight LREE enrichment and moderate Nb depletion relative to other tholeiitic units. An ascending plume with a tholeiitic contaminant and without contamination by the Lower Keewatin Assemblage was likely the source for N-MORB komatiites and Th-enriched komatiites.

Komatiites with Nb-depletions show signs of multiple processes that have resulted in the complex Th-Nb-LREE systematics observed. It is likely that contamination occurred, however it is possible that greater fractionation occurred within the flow that produced trace element variations. Deep-penetrating fractures can accommodate along-strike variations in

the dip of subduction zones, which typically segment island arcs into various belts. Large-scale crustal weaknesses would act as potential magma conduits for ascending plumes, resulting in a chemical and isotopic difference between the upwelling asthenosphere and arc magmatism. This could result in interaction between the rising plume and subduction-derived fluids, producing the Nb-depletions present in komatiite samples within the assemblage.

Overall, the Upper Keewatin Assemblage hosts a variety of lithologies with complex geochemistry that cannot be idealized into an exact petrogenetic sequence. The data from this study is consistent with arc-related magmatism with abundant plume magmatism that has likely undergone a degree of plume-arc interaction. Although methods commonly used in distinguishing subduction-related properties within komatiites could not be completed in this study, trace element geochemistry does suggest Nb-depletions present in komatiites are likely related to subduction-derived magmatism. With respect for accretionary processes along the southwestern margin of the Superior Province at $\sim 2.7\text{Ga}$, it is clear that subduction-related magmatism resulted in both calc-alkalic and tholeiitic magmatism and had subsequent interaction with a rising plume that generated AUKs and tholeiitic mafic volcanic rocks.

References

- Abbott, D., Burgess, L., Longhi, J., and Smith, W.H.F. 1994. An empirical thermal history of the Earth's upper mantle. *Journal of Geophysical Research: Solid Earth*, 99(7): 13,835-13,850.
- Aitken, B.G., and Echeverria, L.M. 1984. Petrology and geochemistry of komatiites and tholeiites from Gorgona Island, Columbia. *Contributions to Mineralogy and Petrology*, 86:94-105.
- Allegre, C.J. 1982. Genesis of Archean komatiites in a wet ultramafic subducted plate, in Arndt, N.T. and Nisbet, E.G. eds., *Komatiites*: London, George Allen and Unwin: 495-500.
- Arndt, N. 1994. Archean komatiites. In: K.C. Condie (ed.) *Archean Crustal Evolution*, 11-44. Amsterdam: Elsevier.
- Arndt, N. T. 1986. Differentiation of komatiite flows. *Journal of Petrology*, 27: 279-301.
- Arndt, N., Francis, D.M., and Hynes, A.J. 1979. Field characteristics and petrology of Archean and Proterozoic komatiites. *Canadian Mineralogy*, 17:147-163.
- Arndt, N., Ginibre, C., Chauvel, C., Albarède, F., Cheadle, M., Herzberg, C., Jenner, G., Lahaye, Y. 1998. Were komatiites wet? *Geology*, 26:739-742.
- Arndt, N.T., Leshner, M.C., and Barnes, S.J. 2008. *Komatiite*. Cambridge University Press, 488pp.
- Arndt NT, Nesbitt RW (1982) Geochemistry of Munro Township basalts. In: Arndt, N.T., and Nesbitt, E.G. (Eds.) *Komatiites*. George, Allen and Unwin, London: 309-329.
- Ayer, J.A. 1998. Petrogenesis and Tectonic Evolution of the Lake of the Woods Greenstone Belt, Western Wabigoon Subprovince, Ontario, Canada. PhD dissertation, Ottawa University, Canada, 278.
- Ayer, J.A. 1991. Geology of the Falcon Island area, District of Kenora; Ontario Geological Survey, Open File Report 5804: 142pp.
- Ayer, J.A., and Buck, S. 1989. Geology of the Chisholm Island area, Lake of the Woods, District of Kenora. Ontario Geological Survey, Open File Report 5710: 177pp.
- Ayer, J.A., and Davis, D.W. 1997. Late Archean evolution of differing convergent margin

assemblages in the Wabigoon Subprovince: Geochemical and geochronological evidence from the Lake of the Woods greenstone belt, Superior Province, northwestern Ontario; *Precambrian Research*, 81:155-178.

Ayer, J.A., and Dostal, J. 2000. Nd and Pb isotopes from the Lake of the Woods greenstone belt, northwestern Ontario: Implications for mantle evolution and the formation of crust in the southern Superior Province. *Canadian Journal of Earth Sciences*, 37:1677-1689.

Ayer, J.A., Johns, G.W. and Blackburn, C.E. 1991. Archean volcanology and sedimentology of the Lake of the Woods: The classic Keewatin greenstone belt; Geological Association of Canada–Mineral Association Canada–Society of Economic Geology, Joint Annual Meeting, Toronto '91, Field Trip B2 Guidebook: 59pp.

Beakhouse, G.P. 1991. Winnipeg River Subprovince, In *Geology of Ontario*. Edited by P.C. Thurston, H.R. Williams, R.H. Sutcliffe and G.M. Stott. Ontario Geological Survey, Special Volume 4, Part 1: 279-301.

Bedard, J.H. 2018. Stagnant lids and mantle overturns: Implications for Archean tectonics, magmagenesis, crustal growth, mantle evolution, and the start of plate tectonics. *Geoscience Frontiers*, 9(1): 19-49.

Bell, T. H., Fleming, P. D., and Rubenach, M. J. 1986. Porphyroblast nucleation growth and dissolution in regional metamorphic rocks as a function of deformation partitioning during foliation development. *Journal of Metamorphic Geology*, 4: 31-67.

Bickle, M.J., Arndt, N.T., Nisbet, E.G., Orpen, J.L., Martin, A., Keays, R.R., and Renner, R. 1993. Geochemistry of the igneous rocks of the Belingwe greenstone belt: alteration, contamination and petrogenesis. In: Bickle MJ, Nisbet EG (eds) *The geology of the Belingwe Greenstone Belt, Zimbabwe*. Balkema, Rotterdam: 175–214.

Blackburn, C.E., Johns, G.W., Ayer, J. and Davis, D.W. 1991. Wabigoon Subprovince; in Chapter 9, *Geology of Ontario*, Ontario Geological Survey, Special Volume 4, Part 1: 303-381.

Bleeker, W., 2002. Archean tectonics: a review, with illustrations from the Slave craton. In: Fowler, C.M.R., Ebinger, C.J., Hawkesworth, C.J. (Eds.), *The Early Earth: Physical, Chemical and Biological Development*, Special Publications, 199: 151–181.

Campbell, I.H., Griffiths, R.W., and Hill, R.I. 1989. Melting in an Archean mantle plume: Heads it is basalts and tails it is komatiites. *Nature*, 339:697-699.

Card, K.D., and Ciesielski, A., 1986. Subdivisions of the Superior Province of the Canadian Shield, *Geoscience Canada*, 13: 5-13.

Card, K.D., 1990. A review of the Superior Province of the Canadian Shield, a product of

- Archean accretion. *Precambrian Research*, 48: 99-156.
- Condie, K.C. 2016. A great thermal divergence in the mantle beginning 2.5Ga: Geochemical constraints from greenstone basalts and komatiites. *Geoscience Frontiers*, 7: 543-553.
- Corfu, F. and Davis, D.W. 1992. A U-Pb geochronological framework for the western Superior Province, Ontario. In *Geology of Ontario*. Edited by P.C. Thurston, H.R. Williams, R.H. Sutcliffe and G.M. Stott. Ontario Geological Survey, Special Volume 4, Part 2: 1335-1346.
- Dann, J.C. 2001. Vesicular komatiites, 3.5Ga Komati Formation, Barberton Greenstone Belt, South Africa: inflation of submarine lavas and origin of spinifex zones. *Bulletin of Volcanology*, 63: 462-481.
- Dann, J.C., and Grove, T.L. 2007. Volcanology of the Barberton greenstone belt, South Africa: Inflation and evolution of flow field, in van Kranendonk, M.J., Smithies, R.H., and Bennett, V.C., eds., *Precambrian Ophiolites and Related Rocks: Developments in Precambrian Geology*, 15, Elsevier, Amsterdam: 527-570.
- Davis, D.W., and Jackson, M. 1988. Geochronology of the Lumby Lake greenstone belt: a 3Ga complex within the Wabigoon Subprovince, northwest Ontario. *Geological Society of America Bulletin*, 100: 818-824.
- Davis, D.W. and Smith, P.M. 1991. Archean gold mineralization in the Wabigoon Subprovince, a product of crustal accretion: Evidence from U-Pb geochronology in the Lake of the Woods area, Superior Province, Canada; *Journal of Geology*, 99: 337-353.
- Devaney, J.R., and Williams, H.R. 1989. Evolution of an Archean Subprovince boundary: a sedimentological and structural study of part of the Wabigoon-Quetico boundary in northern Ontario. *Canadian Journal of Earth Sciences*, 26: 1013-1026.
- Donaldson, C. H. 1982. Spinifex-textured komatiites: a review of textures, compositions and layering. In: Arndt, N. T. & Nisbet, E. G. (eds) *Komatiites*. London: Allen & Unwin, 213-244.
- Dostal, J. 2008. Igneous Rock Associations 10. Komatiites. *Geoscience Canada*, 35(1):21-31.
- Dostal, J., and Mueller, W.U. 1997. Komatiitic flooding of a rifted Archean rhyolitic arc complex: Geochemical signatures and tectonic significance of the Stoughton-Roquemaure Group, Abitibi Greenstone belt. *Journal of Geology*, 105: 545-563.
- Dostal, J., and Mueller, W.U. 2013. Deciphering an Archean mantle plume: Abitibi greenstone belt, Canada. *Gondwana Research*, 23: 493-505.

- Easton, M. 2000. Metamorphism of the Canadian Shield, Ontario, Canada. I. The Superior Province. *The Canadian Mineralogist*, 38: 287-317.
- Fan, J., and Kerrich, R. 1997. Geochemical characteristics of aluminum depleted and undepleted komatiites and HREE-enriched low-Ti tholeiites, western Abitibi greenstone belt: A heterogeneous mantle plume-convergent margin environment. *Geochimica et Cosmochimica*, 61(22): 4723-4744.
- Faure, F.O., Arndt, N., Libourel, G. 2006. Formation of Spinifex Texture in Komatiites: an Experimental Study. *Journal of Petrology*, 47(8): 1591-1610.
- Fletcher, M., and Wyman, D.A. 2015. Mantle plume-subduction zone interactions over the past 60 Ma. *Lithos*, 233: 162-173.
- Fralick, P. 1997. Neoproterozoic evolution of the Wabigoon Subprovince: Evidence from the sedimentary record. In *Western Superior Transect 5th Annual Workshop*. Edited by R.M. Harrap and H.H. Helmstaedt. Lithoprobe Secretariat, The University of British Columbia, Vancouver, B.C., Lithoprobe Report 70: 97-99.
- Fralick, P.W., 2003. Geochemistry of clastic sedimentary rocks: ratio techniques. In: *Geochemistry of Sediments and Sedimentary Rocks: Evolutionary Considerations to Mineral-deposit Forming Environments*. In: Lentz, D.R., (Eds.), Geol. Assoc. Canada, St. John's, Newfoundland, Canada, *Geo Text* 4: 85-103pp.
- Fralick, P., and Davis, D.W. 1999. The Seine-Couchiching problem revisited: sedimentology, geochronology and geochemistry of sedimentary units in the Rainy Lake and Sioux Lookout areas. In *Western Superior Transect 5th Annual Workshop*. Edited by R.M. Harrap and H.H. Helmstaedt. Lithoprobe Secretariat, The University of British Columbia, Vancouver, B.C., Lithoprobe Report 70: 66-75.
- Galley, A., van Breemen, O., and Franklin, J. 2000. The relationship between intrusion-hosted Cu-Mo mineralization and VMS deposits of the Archean Sturgeon Lake mining camp, northwestern Ontario. *Economic Geology*, 95: 1543-1550.
- Green, J.C., Nicholls, I.A., Viljoen, M.J., and Viljoen, R.P. 1974. Experimental demonstration of the existence of peridotitic liquids in earliest Archean magmatism. *Geology*, 3: 11-14.
- Green, T.H. 1995. Significance of Nb/Ta as an indicator of geochemical processes in the crust-mantle system. *Chemical Geology*, 120: 347-359.
- Grove, T.L., de Wit, M.J., and Dann, J. 1997. Komatiites from the Komati type section, Barberton, South Africa. In: de Wit, M.J. and Ashwall, L.D. eds. *Greenstone Belts*, 422-437, Oxford Scientific Publications, Oxford.
- Grove, T.L., Gaetani, G.A., and de Wit, M.J. 1994. Spinifex textures in 3.49Ga Barberton

- Mountain Belt komatiites: Evidence for crystallization of water-bearing, cool magmas in the Archean: *Eos* (Transactions, American Geophysical Union), 75: 354.
- Grove, T.L., Gaetani, G.A., Parman, S., Dann, J., and de Wit, M.J. 1996. Origin of spinifex textures in 3.49Ga komatiite magmas from the Barberton Mountainland, South Africa: *Eos* (Transactions, American Geophysical Union), 77: 281.
- Grove, T.L., and Parman, S.W. 2004. Thermal evolution of the Earth as recorded by komatiites. *Earth Planet Science Letters*, 219(3-4): 173-187.
- Gurenko, A.A., Kamenetsky, V.S., and Kerr, A.C. 2016. Oxygen isotopes and volatile contents of the Gorgona komatiites, Columbia: A confirmation of the deep mantle origin of H₂O. *Earth and Planetary Science Letters*, 454: 154-165.
- Halama, R. 2004. Crustal contamination of mafic magmas: evidence from a petrological, geochemical and Sr-Nd-Os-O isotopic study of the Proterozoic Isortoq dike swarm, South Greenland, *Lithos*, 74(3-4): 199-232.
- Henry, P., Stevenson, R.K., and Garipey, C. 1997. Late Archean mantle composition and crustal growth in the Western Superior Province of Canada: Neodymium and lead isotopic evidence from the Wawa, Quetico, and Wabigoon subprovinces. *Geochimica et Cosmochimica Acta*, 62(1): 143-157.
- Hertzberg, C.T. 1992. Depth and degree of melting of komatiites. *Journal of Geophysical Research*, 97: 4521-4540.
- Hertzberg, C.T. 1995. 1995, Generation of plume magmas through time: An experimental perspective, *Chemical Geology*, 126: 1-16.
- Hill, R.E.T., Barnes, S.J., Gole, M.J., and Dowling, S.E. 1995. The volcanology of komatiites as deduced from field relationships in the Norseman-Wiluna greenstone belt, Western Australia. *Lithos*, 34: 159-188.
- Hollings, P., and Kerrich, R. 1999. Trace element systematics of ultramafic and mafic volcanic rocks from the 3 Ga North Caribou greenstone belt, northwestern Superior Province. *Precambrian Research*: 257-279.
- Hollings, P., Wyman, D., and Kerrich, R. 1998. Komatiite-basalt-rhyolite volcanic associations in Northern Superior Province greenstone belts: a significance of plume-arc interaction in the generation of the proto continental Superior Province. *Lithos*, 46: 137-161.
- Hollings, P., Wyman, D., and Kerrich, R., 1999. Komatiite-basalt-rhyolite volcanic association in Northern Superior Province greenstone belts: significance of plume-arc interaction in the generation of the proto continental Superior Province. *Lithos*, vol. 46, p. 137-161.

- Hou, T., Zhang, Z., Kusky, T., Du, Y., Liu, J., and Zhao, Z. 2011. A reappraisal of the high-Ti and low-Ti classification of basalts and petrogenetic linkage between basalts and mafic-ultramafic intrusions in the Emeishan Large Igneous Province, SW China. *Ore Geology Reviews*, 41(1): 133–143.
- Huppert, H.E., and Sparks, S.J. 1985. Cooling and contamination of mafic and ultramafic magmas during ascent through continental crust. *Earth and Planetary Science Letters*, 74: 371-386.
- Irvine T.N. and Baragar W.R.A., 1971, A guide to the chemical classification of the common volcanic rocks. *Canadian Journal Earth Sciences*, 8: 523-548.
- Jochum, K.P., Hofmann, A.W., and Seufert, H.M. 1993. Tin in mantle-derived rocks: constraints on Earth evolution. *Geochimica et Cosmochimica Acta*, 57: 3585-3595.
- Kawamoto, T., Hervig, R.L., and Holloway, J.R. 1996. Experimental evidence for a hydrous transition zone in the early Earth's mantle. *Earth and Planetary Science Letters*, 142:587-592.
- Kerrick, R., Polat, A., Wyman, D., and Hollings, P. 1999. Trace element systematics of Mg-, to Fe-tholeiitic basalt suites of the Superior Province: Implications for Archean mantle reservoirs and greenstone belt genesis. *Lithos*, 46: 163-187.
- Kincaid, C., Druken, K., Griffiths, R., and Stegman, D. 2013. Bifurcation of the Yellowstone plume driven by subduction-induced mantle flow. *Nature*, 6: 395–399.
- Kuno H., 1968, Differentiation of basalt magmas. In: Hess H.H. and Poldervaart A. (Eds.), *Basalts: The Poldervaart treatise on rocks of basaltic composition*, VOL. 2. Interscience, New York: 623-688.
- Le Maitre, R. W., Dubek, P., Keller, A., Lameyre, J., Le Bas, J., Sabine, M., Schmid, P., Sorensen, R., Streckeisen, H., and Wooley, A. 1989. *A Classification of Igneous Rocks and Glossary of Terms. Recommendations of the IUGS Commission on the Systematics of Igneous Rocks*. Oxford: Blackwell. Derived from work done in Le Bas, M. J., Le Maitre, R. W., Streckeisen, A. and Zanettin, B. 1986. A chemical classification of volcanic rocks based on the total alkali-silica diagram. *Journal of Petrology*, 27: 745-750.
- MacLean, W.H., and Barrett, T.J. 1993. Lithochemical techniques using immobile elements. *Journal of Geochemical Exploration*, 48: 109-133.
- Melnyk, M.J., Cruden, A.R., and Davis, D.W. 2000. Structural geometry and deformational chronology of the Kenora gneisses. In *Western Superior Transect 6th Annual Workshop*. Edited by R.M. Harrap and H.H. Helmstaedt. Lithoprobe Secretariat, The University of British Columbia, Vancouver, B.C., Lithoprobe Report 77: 82-89.

- Melnyk, M.J., Davis, D.W., Cruden, A.R., and Stern, R.A. 2006. U-Pb ages constraining structural development of an Archean terrane boundary in the Lake of the woods area, western Superior Province, Canada. *Canadian Journal of Earth Sciences*, 43.
- Middlemost, E.A.K. 1994. Naming materials in the magma/igneous rock system. *Earth-Science Reviews*, 37: 215-224.
- Murphy, J.B. 2006. *Igneous Rock Associations 7. Arc Magmatism I: Relationship Between Subduction and Magma Genesis*. Geoscience Canada, 33(4): 145-167.
- Murphy, J.B. 2007. *Igneous Rock Associations 8. Arc Magmatism II: Geochemical and Isotopic Characteristics*. Geoscience Canada, 34(1): 7-36.
- Nisbet, E.G., and Walker, D. 1982. Komatiites and the structure of the Archean mantle. *Earth and Planetary Science Letters*, 60:105-113.
- Ohtani, E. 1990. Majorite fractionation and genesis of komatiite in deep mantle. *Precambrian Research*, 48:195-202. Ontario Geological Survey 1992. *Bedrock geology of Ontario; Ontario Geological Survey, Maps 2541, 2542, 2543, scale 1:1 000 000 and Map 2545, Explanatory notes and legend*.
- Ontario Geological Survey 2011. *1:250 000 scale bedrock geology of Ontario; Ontario Geological Survey, Miscellaneous Release---Data 126-Revision 1*.
- Parman, S., Dann, K., Grove, T.L., and de Wit, M.J. 1997. Emplacement conditions of komatiite magmas from the 3.49Ga Komati Formation, Barberton Greenstone Belt, South Africa. *Earth and Planetary Science Letters*, 150:303-323.
- Parman, S.W., Grove, T.L., Dann, J.C., de Wit, M.J. 2004. A subduction origin for komatiites and cratonic lithospheric mantle. *South African Journal of Geology*, 107: 107-118.
- Pearce, J.A. 1983. Role of sub-continental lithosphere in magma genesis at active continental margins. In: Hawkesworth, C.J., Norry, M.J. (Eds.), *Continental Basalts and Mantle Xenoliths*. Shiva, Nantwich: 230-249pp.
- Pearce, J.A. 1996. A user's guide to basalt discrimination diagrams. In: Wyman, D.A. (Eds.) *Trace Element Geochemistry of Volcanic Rocks: Applications for Massive Sulphide Exploration*. Geological Association of Canada, Short Course Notes, 12: 79-113.
- Pearce, J.A. 2008. Geochemical fingerprinting of oceanic basalts with applications to ophiolite classification and the search for Archean oceanic crust, *Lithos*, 100: 14-48.
- Pearce, J. A. 2014. Immobile element fingerprinting of ophiolites. *Elements*, 10: 101-108.
- Percival, J.A. and Easton, R.M. 2007. *Geology of the Canadian Shield in Ontario: an update*;

- Ontario Geological Survey, Open File Report 6196, Geological Survey of Canada, Open File 5511, Ontario Power Generation, Report 06819-REP-01200-10158-R00, 65p.
- Percival, J.A., McNicoll, V., Brown, J.L., and Whalen, J.B. 2004. Convergent margin tectonics, central Wabigoon Subprovince, Superior Province, Canada. *Precambrian Research*, 132: 213-244.
- Percival, J.A., Sanborn-Barrie, M., Skulski, T., Stott, G.M., Helmstaedt, H., and White, D.J., 2006. Tectonic evolution of the western Superior Province from NARMAP and Lithoprobe studies. *Canadian Journal of Earth Sciences*, 43: 1085-1117.
- Percival, J.A., Skulski, T., Sanborn-Barrie, M., Stott, G.M., Leclair, A.D., Corkery, M.T., and Boily, M. 2012. Geology and tectonic evolution of the Superior Province, Canada. Chapter 6 In *Tectonic Styles in Canada: The LITHOPROBE Perspective*. Edited by J.A. Percival, F.A. Cook, and R.M. Clowes. Geological Association of Canada, Special Paper 49:321-378.
- Percival, J.A., Whalen, J.B., Tomlinson, K.Y., McNicoll, V., Stott, G.M. 2002. Geology and tectonostratigraphic assemblages, north-central Wabigoon Subprovince, Ontario. Ontario Geological Survey of Canada, Open File 4270; Ontario Geological Survey Map P.3447, scale 1:250,000.
- Perring, C.S., Barnes, S.J., and Hill, R.E.T. 1995. The physical volcanology of Archean komatiite sequences from Forestania, Southern Cross Province, Western Australia. *Lithos*, 34:189-207.
- Polat, A., 2008. The geochemistry of Neoproterozoic (ca. 2700 Ma) tholeiitic basalts, transitional to alkaline basalts, and gabbros, Wawa Subprovince, Canada: Implications for petrogenetic and geodynamic processes. *Precambrian Research*, 168(1): 83-105.
- Polat, A., and Kerrich, R. 2002. Nd-isotope systematics of ~2.7Ga adakites, magnesian andesites, and arc basalts, Superior Province: evidence for shallow crustal recycling at Archean subduction zones. *Earth and Planetary Science Letters*, 202(2): 345-360.
- Puchtel, I.s., Zhuravlev, D.Z., Samsonov, A.V., and Arndt, N.T. 1993. Petrology and geochemistry of metamorphosed komatiites and basalts from the Tungurcha greenstone belt, Aldan Shield. *Precambrian Research*, 62: 399-417.
- Ringwood, A.E. 1982. Phase transformations and differentiation in subducted lithosphere: implications for mantle dynamics, basalt petrogenesis, and crustal evolution. *Journal of Geology*, 90(6): 611-643.
- Rollinson, H. R. 1993. *Using Geochemical Data: Evaluation, Presentation, Interpretation*. London, Taylor and Francis: 352pp.

- Ross, P.-S., and Bédard, J. H., 2009. Magmatic affinity of modern and ancient subalkaline volcanic rocks determined from trace-element discriminant diagrams. *Canadian Journal of Earth Sciences*, 46: 823-839.
- Sanborn-Barrie, M. and Skulski, T. 2006. Sedimentary and structural evidence for 2.7 Ga continental arc–oceanic- arc collision in the Savant–Sturgeon greenstone belt, western Superior Province, Canada; *Canadian Journal of Earth Sciences*, 43: 995-1030.
- Saunders, A., and Tarney, J. 1991. Back-arc basins. In: Floyd, P.A. (Ed.), *Oceanic Basalts*. Blackie, London: 219-263.
- Savov, I.P., Vargas, R.H., Ryan, J.G., Spadea, P., and D’Antonio, M. 2006. Petrology and Geochemistry of West Philippine Basin Basalts and Early Palau-Kyushu Arc Volcanic Clasts from ODP Leg 195, Site 1201D: Implications for the Early History of the Izu-Bonin-Mariana Arc. *Journal of Petrology*, 47(2): 277-299.
- Shimizu, K.T., Komiya, S., Maruyama, S., and Hirose, K. 1997. Water content of melt inclusion in Cr-spinel of 2.7Ga komatiite from Belingwe Greenstone Belt, Zimbabwe: *Eos (Transactions, American Geophysical Union)*, 78:750.
- Shore, M., and Fowler, A.D. 1999. The origin of spinifex texture in komatiites. *Nature*, 397: 691-693.
- Simons, B., Andersen, J., Shail, R., and Jenner, F.E. 2017. Fractionation of Li, Be, Ga, Nb, Ta, In, Sb, W and Bi in the peraluminous Early Permian Variscan granites of the Cornubian Batholith: Precursor processes to magmatic-hydrothermal mineralisation. *Lithos* 278-281: 491-512.
- Skulski, T., Corkery, M.T., Stone, D., Whalen, J.B., and Stern, R.A. 2000. Geological and geochronological investigations in the Stull Lake – Edmund Lake greenstone belt and granitoid rocks of the northwestern Superior Province. In *Report of Activities 2000, Manitoba Industry, Trade and Mines*. Manitoba Geological Survey, 117-128.
- Smith, P.M. 1987. Geological Setting, Timing and Controls of Gold Mineralization at the Duport Deposit, Shoal Lake, Ontario. M.Sc. Thesis. University of Waterloo. Waterloo, Ont. 31pp (unpublished).
- Smithies, R.H., Ivanica, T.J., Lowrey, J.R., Morriss, P.A., Barnes, S.J., Wychea, S., and Lu, Y.J. 2018. Two distinct origins for Archean greenstone belts. *Earth and Planetary Science*, 486: 106-116.
- Sobolev, A.V., Asafov, E.V., Gurenko, A.A., Arndt, N.T., Batanova, V.G., Portnyagin, M.V., Garbe-Schönberg, D., Krashennnikov, S.P., 2016. Komatiites reveal a hydrous Archaean deep-mantle reservoir. *Nature* 531, 628-632.

- Sossi, P.A., Eggins, S.M., Nesbitt, R.W., Nebel, O., Hergt, J.M., Campbell, I.H., O'Neill, H.S.C., Van Kranendonk, M., and Davies, D.R. 2016. Petrogenesis and Geochemistry of Archean Komatiites. *Journal of Petrology*, 57(1):147-184.
- Sparks, R.S.J. 1986. The role of crustal contamination in magma evolution through geological time. *Earth and Planetary Science Letters*, 78(203): 211-223.
- Spear, F.S. 1993. *Metamorphic Phase Equilibria and Pressure-Temperature-Time Paths*: Washington, D.C., Mineralogical Society of America, 799pp.
- Sproule, R.A., Leshar, C.M., Houle, M.G., Keays, R.R., Ayer, J.A., and Thurston, P.C. 2003. Petrogenesis, and Metallogenesis of Komatiites in the Abitibi Greenstone Belt, Canada. Ontario Geological Survey, Open File Report 6073, p. 119.
- Stern, R.J. 2002. Subduction Zones. *Reviews of Geophysics*, 40(4): 1-42.
- Stone, W.E., Crocket, J.H., Dickin, A.P., and Fleet, M.E. 1995. Origin of Archean ferropicrites: geochemical constraints from the Boston Creek Flow, Abitibi greenstone belt, Ontario, Canada. *Chemical Geology*, 121(1-4), 51-71.
- Stott, G.M. 1997. The Superior Province, Canada. In *Greenstone Belts*. Edited by M.J. de Wit and L.D. Ashwal. Oxford Monograph on Geology and Geophysics, 35: 480-507.
- Stott, G.M., and Corfu, F. 1991. Uchi Subprovince. In *Geology of Ontario*. Edited by P.C. Thurston, H.R., Williams, R.H., Sutcliffe, and G.M., Stott. Ontario Geological Survey, Special Volume 4, Part 1: 145-238.
- Stott, G. M., Corkery, M.T., Percival, J.A., Simard, M., and Goutier, J., 2010. A revised terrane subdivision of the Superior Province. In: *Summary of Field Work and Other Activities, 2010*, Ontario Geological Survey, Open File Report 6260, p. 20-1 to 20-10.
- Stott, G.M., Davis, D.W., Parker, J.R., Straub, K.J., and Tomlinso, K.Y. 2002. Geology and tectonostratigraphic assemblages, eastern Wabigoon Subprovince, Ontario. Ontario Geological Survey of Canada, Open File Report 4285.
- Sushchevskaya, N.M., Evdokimov, A.N., Belyatsky, B.V., Maslov, V.A., and Kuz'min, D.V. 2008. Conditions of Quaternary Magmatism at Spitsbergen Island. *Geochemistry International*, 46(1): 1-16.
- Sun, S., and McDonough, W.F. 1989. Chemical and isotopic systematics of oceanic basalts: implications for mantle composition and processes. Geological Society, London, Special Publications Volume 42: 313-345.
- Tanaka, T., S. Togashi, H. Kamioka, H. Amakawa, H. Kagami, T. Hamamoto, M. Yuhara, Y.

- Orihashi, S. Yoneda, and H. Shimizu (2000), JNdi-1: A neodymium isotopic reference in consistency with LaJolla neodymium, *Chem. Geol.*, 168(3): 279– 281.
- Thurston, P.C. 2015. Greenstone Belts and Granite-Greenstone Terranes: Constraints on the Nature of the Archean World. *Geoscience Canada*, 42(4): 437-484.
- Tomlinson, K.Y., Hall, R.P., Hughes, D.J. and Thurston, P.C. 1996. Geochemistry and assemblage accretion of metavolcanic rocks in the Beardmore–Geraldton greenstone belt, Superior Province; *Canadian Journal of Earth Sciences*, 33: 1520-1533.
- Tomlinson, K.Y., Stevenson, R.K., Hughes, D.J., Hall, R.P., Thurston, P.C., and Henry, P. 1998. The Red Lake greenstone belt, Superior Province: evidence of plume-related magmatism at 3 Ga and evidence of an older enriched source. *Precambrian Research*, 89: 59-76.
- Tomlinson, K.Y., Stone, D., Stott, G.M. and Percival, J.A. 2004. Basement terranes and crustal recycling in the western Superior Province: Nd isotopic character of granitoid and felsic volcanic rocks in the Wabigoon Subprovince, N. Ontario, Canada; *Precambrian Research*, 132: 245-274.
- Turner, J.S., Huppert, H.E., and Sparks, R.S.J. 1986. Komatiites II Experimental and theoretical investigations of post-emplacement cooling and crystallization. *Journal of Petrology*, 27:397-437.
- Vernon, R. H. 2004. *A Practical Guide to Rock Microstructures*. Cambridge University Press, Cambridge, 594pp.
- Viljoen, M.J., and Viljoen, R.P. 1969. The geology and geochemistry of the lower ultramafic unit of the Onverwacht Group and a proposed new class of igneous rocks: *Geological Society of South Africa Special Publication*, 2:55-86. Whalen, J.B., Percival, J.A., McNicoll, V.J. and Longstaffe, F.J. 2004. Geochemical and isotopic (Nd-O) evidence bearing on the origin of late- to post-orogenic high-K granitoid rocks in the western Superior Province: Implications for late Archean tectonomagmatic processes; *Precambrian Research*, 132: 303-326.
- Whalen, J.B., McNicoll, V.J., Galley, A.G. and Longstaffe, F.J. 2004. Tectonic and metallogenic importance of an Archean composite high- and low-Al tonalite suite, Western Superior Province, Canada. *Precambrian Research*, 132: 275-301.
- Williams, H.R. 1991. Quetico Subprovince; in *Geology of Ontario*, Ontario Geological Survey, Special Volume 4, Part 1: 383-403.
- Wyman, D., Ayer, J.A. and Devaney, J.R. 2000. Niobium-enriched basalts from the Wabigoon Subprovince, Canada: Evidence for adakitic metasomatism above an Archean subduction zone. *Earth and Planetary Science Letters*, 179: 21-30.

- Wyman, D., and Kerrich, R. 2009. Plume and arc magmatism in the Abitibi subprovince: Implications for the origin of Archean continental lithospheric mantle. *Precambrian Research*, 168(1): 4-22.
- Xie, W., Kerrich, R., and Fan, J. 1993. HFSE/REE fractionations recorded in three komatiite-basalt sequences, Archean Abitibi greenstone belt: Implications for multiple plume sources and depths. *Geochemica et Cosmochimica*, 57: 4111-4118.

Appendix A
Field Sample Descriptions

Appendix A

- A) Mineral Abbreviations: **Ath**: Anthophyllite. **Trm**: Tremolite. **Ilm**: Ilmenite. **Chl**: Chlorite. **Srp**: Serpentine. **Pyrox**: Pyroxene. **Msc**: Muscovite. **Bt**: Biotite. **Amph**: Amphibole. **Kfsp**: K-feldspar. **Plag**: Plagioclase.
- B) The UTM co-ordinates are provided in Zone 15 using NAD83.
- C) Foliation and bedding orientation taken using Right Hand Rule.
- D) Stations beginning with LOW17 are stations marked during the field season of 2017 while stations beginning with LOW18 are stations taken during the field season of 2018.
- E) Blank dip spaces indicate dip measurements were unable to be taken.
- F) Lithological classification based on field observations.

Station	Northing	Easting	Description	Foliation	Lithology
LOW17CB01	5467226	375527	Very fine-grained, dark, highly foliated, micaceous (biotite defining foliation), moderately siliceous, qtz bands through <1mm , overall schist to phyllite	329/	Mafic to Intermediate MV (lapilli)
LOW17CB02	5467200	375484	Dark, very fine matrix with rounded knobby grains up to 3mm scattered throughout (robust relative to groundmass), locally highly magnetic, weak to mod sil, bt aligned with wk to mod foliation		Mafic to Intermediate MV (bedded)
LOW17CB03	5466814	375204	Very fine-grained, dark, mod to highly foliated, knobby grains ~3mm wide and elongated up to 1cm going with foliation, micaceous schist to phyllite, non-magnetic, very fine laths reflecting in groundmass		Cumulate
LOW17CB04	5466566	374891	Fine to medium-grained, mod-high foliated gneissic like bands (not continuous) siliceous vs darker bands (could be pyroxene with biotite), pyrox grains up to 1cm long elongated with foliation, non-magnetic	304/18	Gabbro
LOW17CB05	5466561	374883	Very fine-grained, dark, non-foliated, wk to mod siliceous, fine-grained subhedral pyrite	351/	Metasedimentary
LOW17CB06	5466519	374727	Dark fine-grained matrix with medium-grained knobby black grains up to 4mm wide, non-foliated, non-magnetic		Cumulate
LOW17CB07	5466495	374566	Grey, fine to very-fine grained, highly foliated, not gneissic like meta-gabbro 04, mod siliceous, non-magnetic	296/28	Metasedimentary
LOW17CB08	5466268	373755	Medium grained averaging ~3mm qtz, feldspar (plag with little to no Kfdsp), minor biotite + trace muscovite, weakly foliated with biotite & msc defining foliation, non-magnetic	36/74	Granodiorite
LOW17CB09	5467553	368633	Fgr to vfgr, grey, similar to previous mafic metavolcanic outcrops.		Mafic MV
LOW17CB10	5467554	368510	Grey, fine-grained, wk to no foliation, mod to high siliceous, minor bt ~1mm, trace fgr pyrite subhedral	264/68	Felsic to Intermediate MV (bedded)
LOW17CB11	5467477	368343	Very fine-grained, moderately foliated/siliceous, biotite and muscovite defining foliation, phyllite to schist like	296/68	Felsic to Intermediate MV (bedded)
LOW17CB12	5467334	368231	Fine to very fine-grained, highly foliated, wk siliceous, biotite defining foliation, schisty, slightly vesicular weathered surface 1-2mm wide, not as siliceous as 007	310/46	Felsic to Intermediate MV (bedded)

LOW17CB13	5467270	368192	Fine-grained, grey, wk siliceous, non-foliated, trace bt ~1mm, non-magnetic		
LOW17CB14	5467176	368123	White to grey, fine-grained, highly siliceous, minor bt with wk to no foliation, interbedded with 014		Mafic MV
LOW17CB15	5467242	368441	White, wk foliation, minor msc, dominantly quartz (possibly quartzite) fgr cubic pyrite ~1mm, non-magnetic		Felsic MV
LOW17CB16	5467256	368467	Grey, fine to slight medium-grained, wk to no foliation, mod to high siliceous, bt defining wk foliation, non-magnetic, could be felsic		Felsic MV
LOW17CB17	5467786	368345	Light grey, fine-grained, highly siliceous, minor bt defining foliation (sometimes in cumulates), non-magnetic, Ep alteration associated with fine veinlet of some sort	314/	Mafic MV
LOW17CB18	5468117	368427	Very fine-grained, green, highly chloritic, non-foliated		Felsic MV
LOW17CB19	5468092	368440	Very fine to fine-grained, weakly chloritic, wk to no foliation		Ultramafic MV
LOW17CB20	5467723	367237	Very fine to fine-grained, grey with wk chloritic tint, red K/Fe staining throughout, highly foliated, no biotite noticeable could be chlorite or muscovite following foliation, phyllite looking rather than schistose, highly magnetic throughout, fine-grained reflective laths ~1mm		Ultramafic to Mafic MV
LOW17CB21	5467349	366958	Very fine-grained matrix with medium-grained knobby grains ~5mm wide concentrated in a band 1.5cm wide, knobby grains slightly hexagonal "stop sign" shaped, knobby band follows foliation, wkly foliated, non-magnetic	341/70	Ultramafic MV
LOW17CB22	5467586	367178	Dark, very fine-grained matrix, highly foliated, wk siliceous, minor bt following foliation		Cumulate
LOW17CB23	5467359	367627	Fine-grained, dark, highly foliated, mod siliceous, very fine laths following foliation		Mafic MV
LOW17CB24	5467351	367719	Fine-grained, highly siliceous, biotite and trace feldspar(?) present, weak foliation, non-magnetic		Mafic MV
LOW17CB25	5467310	367817	Very fine-grained, mod to highly chloritic, highly foliated, wk siliceous, bt minor msc present, non-magnetic, minor qtz bands ~2mm following foliation direction		Granodiorite
LOW17CB26	5467262	367784	Very fine-grained, light grey to green, weak to no foliation, weakly chloritic, weak to moderate magnetism throughout		Mafic MV
LOW17CB27	5467187	367745	Very fine-grained, light grey, wkly/faintly chloritic, no foliation, lesser mica content than previously seen, locally moderately magnetic	278/61	Mafic MV

LOW17CB28	5467132	367773	Very fine-grained, dark and weakly chloritic, micaceous, wkly foliated, quartz rich band runs through sample ~1.5cm thick, non-magnetic		Mafic MV
LOW17CB29	5467100	367787	Fine-grained, wkly siliceous, micaeous (bt & likely chl), dark slightly green, fine-grained reflective laths in groundmass. Intruded by amphibolite syenite 1.5cm thick, some amphibole scattered into host rock groundmass. Intrusion is medium-grained with amph laths up to 1cm long and feldspar phases (both plag with minor kspar)	280/64	Mafic MV
LOW17CB30	5467091	367726	Medium-grained amphibole with trace biotite, black and beige-pink, feldspar plag and alkali phase likely monzonite, moderately magnetic locally		Syenite
LOW17CB31	5467156	367427	Fine to medium-grained, pyroxene plag and olivine, moderately foliated with bt defining foliation, moderately siliceous, non-magnetic, minor chloritic alteration		Syenite
LOW17CB32	5467225	366569	Fine-grained pink reaction rim of monzonite/syenite unit 031, high content of alkali feldspar + minor amphibole and biotite, non-foliated, non-magnetic		Syenite
LOW17CB33	5467031	366550	Fine-grained, dark, highly foliated, weakly siliceous, bt defining foliation, non-magnetic		Syenite
LOW17CB34	5466459	367882	Fine-grained, dark, highly foliated, weakly siliceous, bt defining foliation, non-magnetic	266/	Mafic MV
LOW17CB35	5466086	370921	Black and white, highly foliated, moderately siliceous, medium-grained, slightly gneissic-like bands, non-magnetic	288/67	Gabbro
LOW17CB36	5465800	371053	Grey, micaceous, bt defining wk foliation, wk siliceous, non-magnetic	266/76	Gabbro
LOW17CB37	5465362	371521	Dark, wk siliceous, non-foliated, minor biotite, fine-grained potential pyroxene acicular blades ~1mm some less, non-magnetic	210/	Mafic MV
LOW17CB38	5467368	368907	Dark with minor green, weakly chloritic, fine-grained, siliceous band in center ~7mm wide, wk to non-foliated, wk siliceous apart from band, minor fgr to vfgr pyrite subhedral grains	252/61	Ultramafic to Mafic MV
LOW17CB39	5467307	368921	Green, highly chloritic, fine-grained, fine to very fine-grained black acicular blades not always following foliation, foliation weak, wkly siliceous, non-magnetic	210/68	Mafic MV
LOW17CB40	5467665	368875	Fine-grained, grey to green, wkly siliceous, wk foliation, randomly oriented fine-grained black acicular blades ~1-2mm, non-magnetic	278/76	Ultramafic to Mafic MV
LOW17CB41	5467615	369301	Fine-grained, green, wk foliated, slightly micaceous, wk siliceous, non-magnetic, fine-grained black randomly oriented laths ~1-3mm long	288/58	Ultramafic to Mafic MV
LOW17CB42	5467523	369200	Grey, weakly chloritic, leucocratic, fine-grained white/grey/black?? laths randomly oriented ~1mm, slight pink staining (Fe/K?), non-magnetic, weak foliation,	282/65	Ultramafic to Mafic MV
LOW17CB43	5466813	368061	Fine-grained, moderately chloritic, wk siliceous, fine-grained black acicular laths randomly oriented, wk foliated, non-magnetic		Ultramafic to Mafic MV
LOW17CB44	5466858	367977	Fine to medium-grained, grey, wk foliated, weak pink/red staining, highly magnetic throughout, likely plag and pyroxene	286/46	Ultramafic to Mafic MV

LOW17CB45	5466310	369352	Fine-grained grey matrix with pyroxene medium-grained up to 3mm wide, slightly knobby surficial expression like previously seen, weakly chloritic, wk siliceous, non-magnetic	292/68	Mafic MV
LOW17CB46	5466448	369381	Very fine to fine-grained, grey, wk siliceous, mod to high foliated, non-magnetic		Cumulate
LOW17CB47	5466422	369112	Grey, wk foliation, fine-grained with laths in matrix up to 2mm long, both black and white reflective, non-magnetic, wk siliceous	281/64	Ultramafic to Mafic MV
LOW17CB48	5465040	370956	Light grey, fine-grained, siliceous, pink Fe/K staining, weakly chloritic, moderately foliated, no laths like previous sample 43, non-magnetic	270/56	Ultramafic to Mafic MV
LOW17CB49	5465163	371261	White and black, gneissic like banding, highly foliated and siliceous, non-magnetic, biotite and msc present	272/78	Ultramafic MV
LOW17CB50	5468117	371818	Fine-grained, grey, wk siliceous, non-foliated, non-magnetic	256/76	Metasedimentary
LOW17CB51	5465295	370608	Grey, weakly chloritic, non-foliated, wkly siliceous, non-magnetic		Mafic MV
LOW17CB52	5465425	370631	Fine-grained, weakly chloritic, grey-green, wkly foliated, non-magnetic, msc & bt		Mafic MV
LOW17CB53	5465435	370440	Highly chloritic, green, very fine-grained, non-foliated, non-magnetic	256/54	Ultramafic to Mafic MV
LOW17CB54	5467864	372223	Black/white, foliated, highly siliceous, fine-grained matrix with medium-grained elongate almost cumulate looking black up to 1.2cm in length possible amphibole?, kfdsp also concentrated in same cumulate like form, minor bt, meta-syenite/monzonite?		Ultramafic to Mafic MV
LOW17CB55	5467592	371316	Fine-grained, pink, wk foliation to non-foliated, minor bt, non-magnetic	266/70	Syenite
LOW17CB56	5467482	371294	Green-grey, fine to very fine-grained, wk foliation, minor biotite, non-magnetic, mod chloritic	284/48	Ultramafic to Mafic MV
LOW17CB57	5466719	374462	Highly chloritic, green, very fine to fine-grained, wk to mod foliation, biotite slightly coarser than groundmass concentrated in layers, trace acicular black needles ~5mm, non-magnetic	272/57	Ultramafic to Mafic MV
LOW17CB58	5466756	374552	Grey, weakly chloritic, non-foliated to wk foliated, very fine-grained, non-magnetic	238/48	Ultramafic to
LOW17CB59	5466709	373859	Grey, weakly chloritic, wk to mod foliation, fine to very fine-grained, non-magnetic, trace bt up to 2mm	291/64	Ultramafic to Mafic MV
LOW17CB60	5466673	373665	Various bands of pink/white/green coloration, very fine-grained, bands no greater than 7mm thick, on cut surface perpendicular to foliation, bands seem to bend around one another and go from grey to pink to green to white	294/54	Metasedimentary
LOW17CB61	5466788	373530	Fine to medium-grained, grey, wk siliceous minor qtz, non-foliated, trace chlorite alteration very fine-grained, minor biotite, non-magnetic, potential fine-grained gabbro		Ultramafic to Mafic MV
LOW17CB62	5467128	372939	Fine-grained grey, minor reddish coloration, reflective laths in groundmass up to 2mm in length, similar to other grey/red samples but darker grey, highly magnetic, wk to non-foliated, wk chlorite		Ultramafic to Mafic MV

LOW17CB63	5467302	372874	Grey, fine-grained, weakly chloritic, wk foliation, black acicular needles ~3-4mm long, generally randomly oriented, non-magnetic	278/68	Ultramafic to Mafic MV
LOW17CB64	5467317	373127	Fine-grained, grey, non to weak foliation, weak siliceous, minor black acicular fine-grained laths, non-magnetic	320/76	Ultramafic to Mafic MV
LOW17CB65	5467824	373416	Fine-grained, grey, weakly chloritic, non-foliated, non-magnetic, moderate black fine-grained acicular needles		Ultramafic to Mafic MV
LOW17CB66	5465979	370460	Green/grey, moderately chloritic, weak foliation, non-magnetic, siliceous band along foliation plane	277/57	Ultramafic to Mafic MV
LOW17CB67	5465879	370510	Very fine-grained, highly chloritic, foliated, trace red coloration, minor bt		Ultramafic to Mafic MV
LOW17CB68	5465853	370625	Fine-grained, grey, weakly chloritic, moderately magnetic, wk to non-foliated, minor bt	276/50	Ultramafic to Mafic MV
LOW17CB69	5467607	373522	Light grey, very fine-grained, moderately foliated, slight red coloration, non-magnetic, weak chlorite(?), minor bt	272/53	Ultramafic to Mafic MV
LOW17CB70	5467559	373722	Fine grained, grey, wkly siliceous, non-foliated, fine black acicular laths ~1-2mm, non-magnetic		Ultramafic to Mafic MV
LOW17CB71	5467484	373707	Grey, fine to very fine-grained, wk foliation, minor bt, non-magnetic, weakly chloritic	281/59	Ultramafic to Mafic MV
LOW17CB72	5465433	368560	Grey-green, weakly chloritic, wk to non-foliated, slightly micaceous, fine to very fine-grained, non-magnetic	288/60	Ultramafic to Mafic MV
LOW17CB73	5465199	368880	Grey, wk siliceous, very fine-grained, wk foliation, micaceous, trace chlorite (put with foliated grey samples)	232/76	Mafic MV
LOW17CB74	5465170	368755	Fine to medium-grained, moderately chloritic, non-foliated, biotite and msc present, non-magnetic		Mafic MV
LOW17CB75	5466467	376002	Grey, wk foliation, mod siliceous, fine-grained, bt defining foliation, non-magnetic	280/82	Mafic MV
LOW17CB76	5467881	373975	Grey, wk foliation, knobby grains up to 5mm wide, wk siliceous going w foliation, minor bt present, non-magnetic		Cumulate
LOW17CB77	5468320	372820	Grey, very fine-grained, wk to non-foliated, wkly micaceous, trace bt, moderate silicified, non-magnetic	290/55	Ultramafic to Mafic MV
LOW17CB78	5477792	363023	Green, highly chloritic, mod foliation, strongly magnetic, very fine black acicular laths ~1mm randomly oriented,		Ultramafic to Mafic MV
LOW17CB79	5478005	363199	Green, highly chloritic, mod foliation, non-magnetic, black acicular laths ~1mm less than previous sample		Ultramafic to Mafic MV
LOW17CB80	5478171	363084	Fine to medium-grained, grey, weakly to mod foliated, mod locally magnetic, wk foliated		Mafic MV

LOW17CB81	5467226	375527	Grey to green, wkly chloritic, mod to strongly foliated, micaceous, bt present throughout, minor very fine grained black acicular laths randomly oriented, non-magnetic		Ultramafic to Mafic MV
LOW17CB82	5467200	375484	Green, highly chloritic, wk to mod foliated, fine-grained bladed laths randomly oriented, non-magnetic		Ultramafic to Mafic MV
LOW17CB83	5466814	375204	Highly chloritic, light green to grey, black acicular needles 1-2mm randomly oriented and occur slightly sporadically, non-magnetic, wk foliation	262/64	Ultramafic to Mafic MV
LOW17CB84	5466566	374891	Fine-grained, grey, mod siliceous, mod to weak foliation, very weakly chloritic, some areas stronger foliated and micaceous, bt following foliation, non-magnetic,	264/46	Mafic MV
LOW17CB85	5466561	374883	Fine-grained, grey, wkly foliated, vfgr black acicular laths ~1mm or less, non-magnetic, laths randomly oriented	198/56	Ultramafic to Mafic MV
LOW17CB86	5466519	374727	Grey, wkly chloritic, non-foliated to wkly foliated, fine grained black laths, randomly oriented, non-magnetic	300/78	Ultramafic to Mafic MV
LOW17CB87	5466495	374566	Grey to green, wk to mod chloritic, trace fgr black acicular laths, fine-grained with medium grained crystals shining white in light seem anhedral to subhedral, non-		Ultramafic to Mafic MV
LOW17CB88	5466268	373755	Very fine grained, grey, wk foliation/siliceous, non-magnetic, trace qtz veinlets	260/86	Mafic MV
LOW17CB89	5467553	368633	Grey to green, foliation mod, wk siliceous, wk to mod chloritic, trace fgr black acicular laths, often following foliation, concentration of black laths in fine bands ~2mm wide, non-magnetic	170/66	Ultramafic to Mafic MV
LOW17CB90	5467554	368510	Grey to green, very fine to fine-grained, mod chloritic, wk to mod foliated, black acicular grains sporadically oriented 1-2mm, non-magnetic	278/43	Ultramafic to Mafic MV
LOW17CB91	5467477	368343	Grey, weakly chloritic, very fine to fine-grained, wkly foliated, wk to mod siliceous, non-magnetic	342/84	Mafic MV
LOW17CB92	5467334	368231	Green and red to grey, very fine to fine grained, highly chloritic and soft, mod foliated, weathered surface slightly knobby, strongly magnetic, red coloring rusty looking,	290/75	Ultramafic to Mafic MV
LOW17CB93	5467270	368192	Dark grey, wk foliated, minor green, trace very fine grained laths, non-magnetic		Ultramafic to Mafic MV
LOW17CB94	5467176	368123	Grey, very fine grained, wk to non-foliated, wk chloritic, minor qtz vugs ~1.5cm long, wk siliceous, non-magnetic		Mafic MV
LOW17CB95	5467242	368441	Very fine-grained, grey, mod chloritic, wk chloritic, non-magnetic, wk siliceous		Mafic MV
LOW17CB96	5467256	368467	Fine to medium-grained, dark, weakly chloritic, non-magnetic, wk to non-foliated, potential pyroxene grains ~1-2mm, weakly siliceous		Mafic to Ultramafic MV
LOW17CB97	5467786	368345	Grey, slightly chloritic, weakly siliceous, very fine to fine-grained, trace very fine black laths, non-magnetic		Mafic to Ultramafic MV

LOW17CB98	5468117	368427	Grey, non-foliated, very fine-grained, trace fgr biotite, slight mica sheen, trace fgr to vfgr subhedral Py, non-magnetic		Mafic to Ultramafic MV
LOW17CB99	5468092	368440	Fine to medium-grained, appears to be medium pyroxene blades in plag matrix		Mafic MV
LOW18CB01	5481550	388820	Fine to very fine-grained grey rock with weak to no silicification. No fabric or alteration visible. Outcrop 5 x 5m.		Mafic to ultramafic MV
LOW18CB02	5481427	389980	Grey to greenish (possible chl alteration), fgr, mod. siliceous. Outcrop shore ridge 15 x 3m.	092/86	Mafic to ultramafic MV
LOW18CB03	5483328	395095	Very fine-grained, grey, weakly siliceous shoreline outcrop	236/80	Mafic to ultramafic MV
LOW18CB04	5482873	394866	Fine-grained, grey, weak to no silicification. Outcrop is 15*3m with shore. Slight green tint	220/86	Mafic to ultramafic MV
LOW18CB05	5482829	394917	Slightly more schistose than previous sample. Slightly greener. Outcrop is 12*3m with shore.		Mafic to ultramafic MV
LOW18CB06	5482846	395119	Outcrop surface fairly green and 12*4m with shore. Grey to green likely from chlorite, fine-grained, weak to no silicification.	076/82	Mafic to ultramafic MV
LOW18CB07	5482805	395275	Gabbro or medium-grained metavolcanic. Blades ~1-3mm randomly oriented. Massive outcrop with no fabric 7*4m.		Mafic to ultramafic MV
LOW18CB08	5482923	395675	Green-grey schistose fine-grained sample. Outcrop on island shore 15*3m	276/	Mafic to
LOW18CB09	5483008	395302	Grey to greenish, fgr, highly foliated. Quartz veins follow foliation.	090/63	Mafic to ultramafic MV
LOW18CB10	5482506	388845	Massive shoreline outcrop with little to no foliation and no regular jointing. Very fine to fine-grained, grey with slight green tint, minor siliceous.		Mafic to ultramafic MV
LOW18CB11	5482731	389498	Small outcrop 6*2m, very fine-grained, minor siliceous		Mafic to ultramafic MV
LOW18CB12	5482779	389436	Similar to last stop, outcrop 10*4m going 100degrees. Weakly foliated.	276/	Mafic to ultramafic MV
LOW18CB13	5482517	389819	Fine-grained, moderate siliceous, grey with weak foliation		Mafic to ultramafic MV
LOW18CB14	5482691	389907	Very fine-grained to fine-grained, grey, weak siliceous, no fabric		Mafic to ultramafic MV
LOW18CB15	5482786	390447	Very fine to fine-grained, grey, moderate siliceous with slight foliation		Mafic to ultramafic MV
LOW18CB16	5481387	390210	Very fine to fine-grained, grey, weak siliceous, little to no fabric. Shoreline 15*3m.		Mafic to ultramafic MV

LOW18CB17	5483093	393486	Very fine-grained, dark grey. O/C shoreline 10*4m.		Mafic to ultramafic MV
LOW18CB18	5483032	392866	Contact with syenogranite at 264degrees. Splays into host ~30cm to 10m roughly 3cm to 15cm thick 60degrees off of the main intrusion. Offshoots at 210degrees. Host sampled, intrusion taken for TS. Host: fine-grained, dark grey, not siliceous. Intrusion: Abundant kspar, quartz, plag. Epidote alteration present.		Mafic to ultramafic MV
LOW18CB19	5483278	392755	Grey, fine-grained to very fine, weak to moderate siliceous, no fabric. O/C 6*3m.		Mafic to ultramafic MV
LOW18CB20	5483297	392557	O/C 4*5m. Grey, very fine-grained, weakly schistose, weak siliceous.		Mafic to ultramafic MV
LOW18CB21	5483449	395242	Highly foliated at approx.. 120degrees. Grey-greenish, weak siliceous. O/C 10*2m.	120/	Mafic to ultramafic MV
LOW18CB22	5483909	395824	Very fine-grained, grey with slight possible green tint, weak siliceous, little alteration. O/C 5*8m.	068/84	Mafic to ultramafic MV
LOW18CB23	5483757	395777	Light grey, mod foliation, mod siliceous. Possible mafic-interm. Very fine-grained.	068/81	Mafic to intermediate MV
LOW18CB24	5483883	395957	O/C 6*6m. Very fine-grained, weakly siliceous, little to no fabric.		Mafic to ultramafic MV
LOW18CB25	5482332	392360	Very fine-grained, dark grey, weak to no fabric. O/C 5*5m.		Mafic to ultramafic MV
LOW18CB26	5482444	392481	Very fine-grained, weakly siliceous, grey, no foliation. O/C 15*10m ~E-W.		Mafic to ultramafic MV
LOW18CB27	5482221	392602	O/C shore 10*4m. Potential contact between 1a and 2. Possible 2 with host sample (dominant sample).		Mafic to ultramafic MV
LOW18CB28	5481967	392036	O/C shore 10*7m. Layers of possible mafic and UM? UM green layers more foliated at ~E-W orientation. Very fine-grained 1a looking layers have chaotic quartz veining. Felsic layer? Host very fine-grained, grey-green, mod to high foliation. Felsic layer has chunk of host. Mafic layers ~1/2 meter (2 of them) also run east.		Mafic to ultramafic MV
LOW18CB29	5482310	391850	Very fine-grained, grey, weakly siliceous. O/C massive 60*20m. Weak foliation (O/C goes with foliation).	116/84	Mafic to ultramafic MV
LOW18CB30	5482382	391942	Very fine-grained, grey, weak to moderately siliceous, no fabric. O/C massive 20*15m.		Mafic to ultramafic MV
LOW18CB31	5482273	392070	Same old litho. O/C 6*4m E-W. Very fine-grained, grey, slight green powder, no fabric.		Mafic to ultramafic MV

LOW18CB32	5482121	391571	Grey, fine-grained to very fine, foliation weak to moderate 116/78. Weak to mod siliceous. O/C 10*20m with foliation.	116/78	Mafic to ultramafic MV
LOW18CB33	5482260	391310	Very fine-grained, weakly siliceous, little to no fabric. O/C 20*20m.		Mafic to ultramafic MV
LOW18CB34	5481707	392066	Fine-grained, grey, weakly siliceous. Slight phyllite surfaces. Weak alteration visible. O/C 8*3m.	080/88	Mafic to ultramafic MV
LOW18CB35	5481657	392100	Possible polygonal jointing. Greenish grey, mod foliated, potential foliation at 248/72 (hard because of fracturing). O/C point 15*5m.	248/72	Mafic to ultramafic MV
LOW18CB36	5481551	391768	Grey-greenish, weakly siliceous, chl alt potentially? Mod - strong foliation at 254/84. O/C 20*15m.	254/84	Mafic to ultramafic MV
LOW18CB37	5481462	391629	Potentially needles . Fine-grained, highly foliated like previous. Green-grey (dark). O/C 15*4m.		Mafic to ultramafic MV
LOW18CB38	5481454	391484	Fine-grained, mod to high foliated at 260/near vert. Mod-weak siliceous, grey-greenish.	260/89	Mafic to ultramafic MV
LOW18CB39	5481419	391357	Fine-grained greyish green (light), fairly siliceous, foliation moderate at 254/72. O/C shore ridge.	254/72	Mafic to ultramafic MV
LOW18CB40	5481391	391195	Grey to light greenish. Mod foliation like previous. O/C ridge continued.		Mafic to ultramafic MV
LOW18CB41	5482917	388860	Fine-grained grey to greenish (slight) - potential alteration. Mod to weak siliceous, wk foliation.		Mafic to ultramafic MV
LOW18CB42	5482903	389132	Very fine-grained, weak siliceous, grey. Pillowed UP 268 with selvages ~1.5cm then speckled with interior white with grains (photo 195). Pillows slightly deformed and range from ~10cm to ~1m in length.		Mafic to ultramafic MV
LOW18CB43	5483055	389461	O/C on island. Highly foliated, grey/greenish. Mod siliceous, very fine to fine-grained.	074/88	Mafic to ultramafic MV
LOW18CB44	5483035	390008	Highly foliated, grey-greenish. O/C 5*4m. Possible 1b medium-grained.		Mafic to ultramafic MV
LOW18CB45	5482441	393690	Very fine-grained, grey-greenish. Foliated moderate 060/84. Weak siliceous. O/C with shore 20*4m.	060/84	Mafic to ultramafic MV
LOW18CB46	5482760	393862	Medium grained, schistose, grey, mod siliceous, greenish. Possible diabase running 212. Contact not visible due to erosion.		Mafic to ultramafic MV

Appendix B

Whole-rock Geochemistry

	Detection Limit	LOW17 CB01	LOW17 CB02	LOW17 CB03	LOW17 CB04	LOW17 CB05	LOW17 CB06	LOW17 CB07	LOW17 CB10
Northing		5467226	5467200	5466814	5466566	5466561	5466495	5466268	5467553
Easting		375527	375484	375204	374891	374883	374566	373755	368633
Rock Type		LOTI tholeiite	HITI tholeiite	Gabbro	Amph cumulate	HITI tholeiite	Sedimentary	Calc-alkalic MV	Komatiite
SiO2_pct	0.04	51.23	49.71	46.94	49.13	50.71	65.53	49.88	44.58
TiO2_pct	0.01	0.96	1.11	2.15	1.21	1.17	0.4	0.76	0.38
Al2O3_pct	0.02	0.02	14.31	14.98	13.5	15.06	14.68	16.82	14.43
Fe2O3_pct	0.01	12.11	14.29	18.7	14.84	14.35	3.71	10.35	11.12
MnO_pct	0.002	0.195	0.206	0.251	0.215	0.209	0.052	0.185	0.169
MgO_pct	0.01	6.41	6.56	5.63	6.08	5.62	1.41	8.78	21.35
CaO_pct	0.006	12.262	7.905	9.738	9.806	8.336	4.892	11.188	7.601
Na2O_pct	0.02	1.38	2.7	2.63	2.64	4.05	4.43	2.86	0.8
K2O_pct	0.01	0.31	1.03	0.23	0.32	0.43	1.43	0.37	0.26
P2O5_pct	0.002	0.095	0.085	0.06	0.078	0.088	0.102	0.2	0.03
LOI		0.65	1.51	0.35	0.53	0.67	0.98	1.05	4.65
Sum		99.96	100.11	100.19	99.93	100.33	99.79	100.14	100.43
S_pct	0.003	0.046	0.212	0.005	<0.003	<0.003	0.031	0.01	0.005
CO2_pct	0.003	0.166	0.177	0.074	0.085	0.084	0.369	0.212	0.102
Ti_ppm	7	5581	6493	12500	7099	6762	2270	4380	2173
Cr_ppm	3	304	65	7	62	51	33	547	1945
Co_ppm	0.13	46.52	49.9	60.77	54.95	48.9	8.65	42.22	79.4
Ni_ppm	0.7	92.7	60	3.6	59.9	53.9	9	102.4	884.9
Rb_ppm	0.11	3.55	31.2	4.19	2.52	5.98	26.29	3.99	8.9
Sr_ppm	0.6	252.4	297.9	170.9	175.2	219.6	587.3	588.6	50
Cs_ppm	0.013	1.031	0.942	0.081	0.093	0.365	0.762	0.533	6.884
Ba_ppm	0.8	94.8	233.3	58.1	77.3	59.6	274.6	107.3	20.4
Sc_ppm	1.1	38.5	34	51.7	38.2	35.7	5.2	34.1	23.7
V_ppm	0.8	275	296	696	319	289	53	248	175
Ta_ppm	0.007	0.226	0.172	0.128	0.223	0.242	0.15	0.154	0.043
Nb_ppm	0.028	3.564	2.67	1.976	3.307	3.602	2.241	3.399	0.6
Zr_ppm	6	79	67	45	89	106	83	78	19
Hf_ppm	0.14	2.23	1.9	1.34	2.52	2.96	2.17	2.11	0.61
Th_ppm	0.018	0.646	0.429	0.277	0.607	0.743	1.201	3.992	0.055
U_ppm	0.011	0.171	0.117	0.071	0.147	0.164	0.296	0.73	0.075
Y_ppm	0.05	25.11	21.77	18.24	28.45	28.63	5.1	16.16	9.3
Cu_ppm	1.4	40.7	77.7	7.4	5.3	2.6	10	26	11.5
Zn_ppm	1.8	91.8	100.5	163.3	99.5	97.9	58.8	91.8	54.8
Mo_ppm	0.08	2.64	0.67	0.43	0.46	0.35	1.38	0.39	0.25
Tl_ppm	0.002	0.024	0.162	0.026	0.014	0.027	0.084	0.029	0.047
Pb_ppm	0.18	2.05	3.1	0.94	0.87	2.61	3.93	5	0.82
Sn_ppm	0.16	0.96	0.49	0.38	0.46	0.43	0.51	0.83	0.56

**Lithological classification based on whole-rock geochemistry and field observations.
MV: Metavolcanic rock. **LOTI:** Low-Ti tholeiitic rock. **HITI:** High-Ti tholeiitic rock.

	Detection Limits	LOW17 CB01	LOW17 CB02	LOW17 CB04	LOW17 CB06	LOW17 CB07	LOW17 CB10	LOW17 CB14	LOW17 CB19
Sb_ppm	0.04	0.04	<0.04	0.04	0.07	0.05	<0.04	0.12	<0.04
Ga_ppm	0.04	16.11	17.02	18.34	17.93	19.12	19.17	16.92	8.85
W_ppm	0.05	0.45	0.39	0.21	0.2	0.23	0.08	0.99	0.24
Bi_ppm	0.47	<0.47	<0.47	<0.47	<0.47	<0.47	<0.47	<0.47	<0.47
Be_ppm	0.04	0.46	0.44	0.29	0.6	0.73	0.59	0.9	0.19
Au_ppm		3.4	2.6	1.5	1.7	1.5	1.2	3.8	1.8
Pd_ppm	0.14	5.45	<0.14	<0.14	<0.14	<0.14	<0.14	2.58	6.35
Pt_ppm	0.06	8.81	<0.06	<0.06	<0.06	<0.06	<0.06	2.65	11.37
La_ppm	0.1	6.5	5.4	3.2	3.7	7	12.3	26.3	1
Ce_ppm	0.12	15.6	13.34	8.66	12.78	18.13	25.81	59.78	2.82
Pr_ppm	0.014	2.278	1.94	1.311	1.733	2.625	3.058	7.472	0.41
Nd_ppm	0.06	10.9	9.42	6.63	9.29	13.09	11.94	30.48	2.39
Sm_ppm	0.026	3.064	2.708	2.134	3.206	3.634	2.02	5.566	0.804
Eu_ppm	0.0031	1.0221	0.9982	0.8772	1.0405	1.089	0.6753	1.4652	0.3745
Gd_ppm	0.009	3.835	3.328	2.812	4.291	4.377	1.495	4.112	1.155
Tb_ppm	0.0023	0.6691	0.5643	0.4854	0.7345	0.7402	0.1926	0.5376	0.215
Dy_ppm	0.009	4.35	3.652	3.149	4.797	4.889	0.975	3.036	1.548
Ho_ppm	0.0025	0.9139	0.8036	0.6779	1.0298	1.0504	0.187	0.5887	0.34
Er_ppm	0.007	2.733	2.443	2.002	3.105	3.145	0.522	1.667	1.052
Tm_ppm	0.0019	0.4064	0.3546	0.2916	0.4529	0.4591	0.0719	0.2447	0.1541
Yb_ppm	0.009	2.708	2.295	1.988	3.006	2.933	0.471	1.54	1.059
Lu_ppm	0.002	0.399	0.359	0.3	0.459	0.446	0.071	0.235	0.155

	LOW17 CB20	LOW17 CB21	LOW17 CB22	LOW17 CB23	LOW17 CB24	LOW17 CB27	LOW17 CB28	LOW17 CB29	LOW17 CB31
Northing	5467554	546747	5467334	5467270	5467176	5467242	5467256	5467786	546817
Easting	368510	368343	368231	368192	368123	368441	368467	368345	368427
Rock Type	Komatiite basalt	Komatiite	Calc-alkalic MV	LOTI tholeiite	LOTI tholeiite	Komatiite	Komatiite	Komatiite basalt	Syenite
SiO2_pct	44.26	42.47	50.89	54.07	51.82	47.32	45.13	47.76	56.09
TiO2_pct	0.51	0.34	0.97	0.62	0.76	0.27	0.33	0.45	0.64
Al2O3_pct	9.18	10.53	7.41	12.78	13.71	14.01	6.39	7.9	11.51
Fe2O3_pct	11.64	10.93	11.08	10.77	11.96	9.45	10.53	10.85	7
MnO_pct	0.184	0.164	0.227	0.204	0.189	0.169	0.183	0.179	0.124
MgO_pct	17.75	25.48	9.31	6.95	7.63	22.5	23.27	13.4	2.62
CaO_pct	9.519	5.434	11.373	10.11	10.918	8.052	6.619	11.922	4.804
Na2O_pct	1.26	0.08	1.54	2.4	1.55	0.38	0.32	0.84	4.63
K2O_pct	0.09	0.02	0.29	0.23	0.17	0.03	0.03	0.67	5.76
P2O5_pct	0.032	0.027	0.456	0.056	0.066	0.024	0.029	0.067	0.599
LOI	3.33	6.77	0.94	0.61	0.74	4.78	5.72	1.72	0.78
Sum	99.37	99.48	99.94	99.79	99.84	99.7	100.39	99.54	99.81
S_pct	<0.003	0.019	<0.003	<0.003	<0.003	0.003	<0.003	0.019	0.038
CO2_pct	0.642	0.078	0.12	0.054	0.207	0.21	0.345	0.076	0.21
Ti_ppm	2810	1844	5222	3398	4179	1620	1850	2444	3645

	LOW17 CB20	LOW17 CB21	LOW17 CB22	LOW17 CB23	LOW17 CB24	LOW17 CB27	LOW17 CB28	LOW17 CB29	LOW17 CB31
Cr_ppm	1745	2297	496	400	164	2339	2064	996	38
Co_ppm	71.1	86.07	41.24	46.16	44.79	78.37	79.54	56.77	19
Ni_ppm	606.5	1221.7	87.6	113.1	66.6	1105.8	1000	311.5	14.6
Rb_ppm	0.72	0.26	3.88	1.9	2.33	0.49	0.99	29.1	151.54
Sr_ppm	23.6	78.9	239	74.5	80.5	28.7	23.2	116.4	>1560
Cs_ppm	0.606	0.056	0.746	0.342	0.406	0.302	1.414	1.162	11.78
Ba_ppm	10	12.4	72.4	66.4	40.2	7.1	4.8	89.8	>1740
Sc_ppm	30.8	18.6	30.2	41.9	41.6	20	20.7	31	9.7
V_ppm	211	135	242	261	289	121	143	204	102
Ta_ppm	0.057	0.035	0.307	0.123	0.137	0.028	0.034	0.062	0.46
Nb_ppm	0.912	0.582	5.491	1.611	1.888	0.476	0.557	0.934	10.348
Zr_ppm	24	19	118	42	47	14.7	12.28	31	233
Hf_ppm	0.79	0.57	3.11	1.27	1.39	0.37	0.38	0.9	5.73
Th_ppm	0.113	0.074	4.817	0.678	0.597	0.058	0.053	0.224	14.378
U_ppm	0.273	0.153	1.724	0.413	0.325	0.111	0.156	0.089	2.896
Y_ppm	12.17	6.96	20.88	14.04	15.45	6.63	7.35	11.16	24
Cu_ppm	6.7	578.5	33.3	9.8	6.5	10.8	4.7	72.3	40.8
Zn_ppm	72	65.8	92.8	72.7	77	58.4	71.3	68.2	89.8
Mo_ppm	0.42	0.97	0.48	0.95	0.73	0.3	0.38	2.38	1.33
Tl_ppm	0.006	0.16	0.032	0.015	0.018	0.002	0.005	0.098	0.813
Pb_ppm	1.1	4.03	3.46	2.37	1.16	0.42	0.45	0.84	23.58
Sn_ppm	0.56	<0.16	1.19	0.37	0.3	<0.16	0.16	0.27	1.55
Sb_ppm	<0.04	<0.04	0.24	0.09	0.11	<0.04	<0.04	0.04	0.15
Ga_ppm	10.13	7.34	15.59	13.26	14.33	6.61	7.53	10.85	17.34
W_ppm	0.18	0.36	0.92	1.38	0.34	0.09	0.19	0.41	0.52
Bi_ppm	0.55	<0.47	<0.47	<0.47	<0.47	<0.47	<0.47	<0.47	<0.47
Be_ppm	0.29	0.12	1.48	0.29	0.27	0.2	0.13	0.15	2.98
Au_ppm	1.6	3.3	2.6	40.2	8.8	1.8	1.5	2.3	2.1
Pd_ppm	5.71	6.07	2.3	7.29	9.79	7.45	5.09	8.75	0.98
Pt_ppm	9.22	7.28	3.36	7.43	7.5	3.34	4.58	10.83	1.87
La_ppm	1.4	0.9	26.5	2.8	3.2	0.8	0.6	2.1	95
Ce_ppm	3.46	2.01	55.9	7.22	8	1.97	1.66	4.82	196.21
Pr_ppm	0.587	0.326	7.848	1.057	1.166	0.333	0.285	0.691	23.295
Nd_ppm	3.15	1.73	34.19	5.1	5.63	1.62	1.58	3.35	89.75
Sm_ppm	1.126	0.594	7.197	1.541	1.803	0.575	0.615	1.092	15.089
Eu_ppm	0.8024	0.2258	1.9336	0.5171	0.6571	0.2783	0.2228	0.3437	4.2967
Gd_ppm	1.609	0.896	6.128	1.989	2.419	0.861	0.896	1.514	10.419
Tb_ppm	0.2943	0.1735	0.8108	0.3676	0.4189	0.1566	0.1786	0.2785	1.1905
Dy_ppm	2.104	1.205	4.238	2.495	2.835	1.104	1.257	1.928	5.487
Ho_ppm	0.4592	0.2704	0.7994	0.5459	0.5974	0.2372	0.2796	0.4243	0.8701
Er_ppm	1.392	0.855	2.143	1.669	1.79	0.732	0.85	1.331	2.126
Tm_ppm	0.2089	0.1215	0.2951	0.2517	0.2702	0.112	0.1303	0.1961	0.2644

	LOW17C B20	LOW17 CB21	LOW17C B22	LOW17C B23	LOW17C B24	LOW17C B27	LOW17C B28	LOW17C B29	LOW17 CB31
Yb_ppm	1.402	0.83	1.855	1.647	1.751	0.761	0.87	1.293	1.614
Lu_ppm	0.21	0.128	0.282	0.25	0.278	0.118	0.132	0.191	0.224

	LOW17 CB32	LOW17 CB34	LOW17 CB35	LOW17 CB36	LOW17 CB37	LOW17 CB38	LOW17 CB39	LOW17 CB40	LOW17 CB41
Northing	5468092	546773	5467349	5467586	5467359	5467351	5467310	5467262	546717
Easting	368440	367237	366958	367178	367627	367719	367817	367784	367745
Rock Type	Syenite	LOTI tholeiite	Gabbro	Gabbro	LOTI tholeiite	Komatiite basalt	Komatiite basalt	Komatiite basalt	Komatiit e basalt
SiO2_pct	52.06	51.02	50.22	51.67	52.38	50.07	47.57	47.74	49.5
TiO2_pct	0.83	0.87	1.4	1.09	0.63	0.53	0.53	0.57	0.54
Al2O3_pct	16.46	13.37	13.22	13.78	13.78	13.34	11.64	12.77	12.78
Fe2O3_pct	8.23	12.99	16.35	12.82	11.66	12.26	12.44	12.47	12.32
MnO_pct	0.141	0.231	0.236	0.209	0.227	0.207	0.2	0.214	0.22
MgO_pct	6.72	8.45	5.37	6.98	8.22	13.12	13.65	12.93	13.78
CaO_pct	8.472	8.952	8.51	7.872	11.411	8.635	9.883	10.071	8.672
Na2O_pct	4.68	3.13	2.82	3.8	0.96	1.98	1.24	1.62	1.71
K2O_pct	2.78	0.27	0.34	0.61	0.22	0.1	0.51	0.21	0.11
P2O5_pct	0.696	0.095	0.12	0.108	0.05	0.057	0.053	0.046	0.041
LOI	0.99	0.94	0.62	1	0.55	0.8	0.93	0.85	0.8
Sum	99.09	100.22	99.78	99.99	99.75	99.5	99.94	99.66	99.95
S_pct	0.06	0.003	0.004	0.003	<0.003	<0.003	<0.003	<0.003	<0.003
CO2_pct	0.13	0.126	0.103	0.219	0.098	0.215	0.088	0.077	0.125
Ti_ppm	4726	4968	8218	6181	3577	2933	2952	3170	3018
Cr_ppm	215	388	13	209	592	746	975	1129	1080
Co_ppm	32.78	47.57	49.51	41.49	52.9	60.59	64.12	67.54	65.43
Ni_ppm	59.8	162.2	23.3	46.5	155.4	253.2	316.4	350.3	325.4
Rb_ppm	408.8	4.01	3.99	26.98	1.71	1.21	26.17	3.17	1.34
Sr_ppm	1096.5	245.2	149.5	113.1	81.9	84.2	55.7	101.6	116.5
Cs_ppm	110.729	0.422	0.18	4.807	0.188	0.517	7.742	1.435	0.138
Ba_ppm	882.6	70.8	93.6	114.1	36.8	14.9	153.6	87.3	28.7
Sc_ppm	24.2	38.5	43.5	42.1	37.6	32.2	34	36.9	35.2
V_ppm	156	287	570	310	243	212	223	231	218
Ta_ppm	0.819	0.134	0.204	0.263	0.087	0.077	0.073	0.081	0.082
Nb_ppm	15.852	2.096	3.086	3.986	1.405	1.234	1.132	1.229	1.265
Zr_ppm	197	60	76	87	37	31	32	34	34
Hf_ppm	4.82	1.73	2.12	2.55	1.07	0.93	0.96	1.03	0.97
Th_ppm	11.204	0.711	0.951	0.623	0.196	0.174	0.169	0.195	0.183
U_ppm	3.515	0.545	0.237	0.417	0.128	0.095	0.17	0.123	0.098
Y_ppm	21.08	20.34	25.64	30.9	15.06	13.06	14.3	14.59	13.69
Cu_ppm	8.4	36.1	86.5	15	16	9.6	11.6	20.7	42.6
Zn_ppm	86.2	98.1	114.5	82.6	80.2	83.3	78.3	76.1	81.7
Mo_ppm	0.55	0.66	0.59	0.35	1.24	0.26	0.25	0.27	0.28

	LOW17 CB32	LOW17 CB34	LOW17 CB35	LOW17 CB36	LOW17 CB37	LOW17 CB38	LOW17 CB39	LOW17 CB40	LOW17 CB41
Tl_ppm	3.123	0.021	0.017	0.094	0.004	0.005	0.147	0.018	0.004
Pb_ppm	16.75	2.33	1.62	3.42	0.45	0.46	0.66	0.9	0.45
Sn_ppm	2.12	0.43	0.49	3.11	0.41	0.21	0.29	0.33	0.23
Sb_ppm	0.05	0.04	0.07	0.09	<0.04	<0.04	0.04	0.04	<0.04
Ga_ppm	14.91	15.08	18.48	15.28	13.84	11.46	12.27	11.84	10.96
W_ppm	0.17	0.2	0.11	0.57	0.31	0.1	0.19	0.12	0.1
Bi_ppm	<0.47	<0.47	<0.47	<0.47	<0.47	<0.47	<0.47	<0.47	<0.47
Be_ppm	3.41	0.39	0.44	1.67	0.15	0.14	0.13	0.18	0.22
Au_ppm	1.1	2	1.6	2.4	2.4	1.7	3.8	1.2	1.4
Pd_ppm	3.45	0.95	<0.14	2.85	4.49	2.26	4.02	2.03	3.03
Pt_ppm	4.39	2.37	0.64	6.18	9.59	6.25	8.14	6.18	7.15
La_ppm	60.4	4.6	3.6	4.6	1.6	1.7	2	1.9	1.7
Ce_ppm	134.29	12.76	11.83	11.79	4.46	4.27	5.09	4.84	4.6
Pr_ppm	17.226	1.787	1.834	2.101	0.738	0.65	0.772	0.758	0.689
Nd_ppm	70.84	8.78	9.51	10.96	3.96	3.53	3.96	3.94	3.49
Sm_ppm	12.37	2.424	2.844	3.332	1.308	1.166	1.261	1.331	1.214
Eu_ppm	2.9619	0.8607	0.9638	1.0478	0.5943	0.3564	0.4845	0.456	0.3546
Gd_ppm	8.529	2.926	3.599	4.554	1.949	1.756	1.833	1.92	1.764
Tb_ppm	0.9728	0.5092	0.6295	0.7785	0.3636	0.3145	0.3329	0.3434	0.3217
Dy_ppm	4.621	3.431	4.159	5.244	2.457	2.207	2.329	2.385	2.277
Ho_ppm	0.7496	0.746	0.9168	1.1109	0.5529	0.4713	0.5141	0.5213	0.4836
Er_ppm	1.933	2.327	2.759	3.415	1.657	1.463	1.574	1.613	1.478
Tm_ppm	0.239	0.3386	0.4093	0.49	0.2473	0.2175	0.2297	0.2396	0.2199
Yb_ppm	1.478	2.258	2.748	3.247	1.642	1.445	1.605	1.629	1.468
Lu_ppm	0.208	0.353	0.428	0.496	0.248	0.223	0.236	0.244	0.224

	LOW17 CB42	LOW17 CB43	LOW17 CB44	LOW17 CB45	LOW17 CB46	LOW17 CB47	LOW17 CB48	LOW17 CB51	LOW17 CB52
Northing	5467132	546710	5467091	5467156	5467225	5467031	5466459	5466086	546580
Easting	367773	367787	367726	367427	366569	366550	367882	370921	371053
Rock Type	Komatiite basalt	Komatiite	Komatiite basalt	Komatiite	Amph cumulate	HITI tholeiite	HITI tholeiite	HITI tholeiite	Komatiit e basalt
SiO2_pct	47.76	43.64	47.15	40.54	45.78	45.93	47.26	51.77	48.11
TiO2_pct	0.53	0.26	0.53	0.38	0.47	1.15	1.04	1.02	0.6
Al2O3_pct	12.09	11.94	9.31	11.92	7.88	9.43	14.49	15.12	14.03
Fe2O3_pct	11.85	11.75	12.15	13.23	14.01	18.31	13.84	12.11	12.14
MnO_pct	0.177	0.163	0.191	0.15	0.234	0.298	0.317	0.315	0.194
MgO_pct	13.63	24.39	13.85	24.85	18.49	4.97	7.51	6.46	13.17
CaO_pct	11.194	4.175	11.254	5.539	7.644	11.804	11.947	11.766	9.796
Na2O_pct	1.55	0.09	1.24	0.05	0.75	1.96	1.46	1.42	1.41
K2O_pct	0.17	0.02	0.12	0.03	0.07	0.41	0.25	0.37	0.16
P2O5_pct	0.085	0.006	0.062	0.034	0.096	0.121	0.103	0.093	0.044
LOI	0.77	6.01	0.89	6.79	2.68	0.61	0.93	0.71	1.14
Sum	99.82	100.33	99.52	99.94	99.83	100.08	99.82	100.12	99.73

	LOW17 CB42	LOW17 CB43	LOW17 CB44	LOW17 CB45	LOW17 CB46	LOW17 CB47	LOW17 CB48	LOW17 CB51	LOW17 CB52
S_pct	<0.003	<0.003	<0.003	0.036	0.003	<0.003	0.04	<0.003	<0.003
CO2_pct	0.093	0.089	0.237	0.132	0.135	0.054	0.416	0.097	0.15
Ti_ppm	2923	1383	2838	1972	2565	6295	5819	5807	3393
Cr_ppm	1078	3244	1211	2859	1095	16	291	225	1071
Co_ppm	61.18	99.97	61.99	98.56	83.14	58.78	48.87	42.84	67.08
Ni_ppm	333.5	842.4	329	1005.7	670.9	23.2	87.3	68.5	333.5
Rb_ppm	4.11	0.26	1.41	0.91	1.26	5.77	3.69	10.47	3.32
Sr_ppm	126.2	16.5	41.2	32.3	47.1	146.7	147.3	115.3	97.2
Cs_ppm	0.6	0.065	0.087	0.101	0.258	0.612	0.426	2.504	0.947
Ba_ppm	33.2	3	20.5	13.9	13	93.9	77.4	157.8	24.8
Sc_ppm	33.6	14.7	33.3	16.5	18.1	40	43	40.2	37.8
V_ppm	228	120	218	156	117	464	301	282	236
Ta_ppm	0.086	0.032	0.068	0.046	0.118	0.174	0.245	0.25	0.087
Nb_ppm	1.279	0.754	1.254	0.651	1.732	2.666	3.755	3.855	1.286
Zr_ppm	33	17	32	20.3	82	67	88	86	37
Hf_ppm	0.99	0.48	0.92	0.41	2.48	1.94	2.49	2.43	1.07
Th_ppm	0.283	0.064	0.152	0.081	0.993	1.013	0.612	0.614	0.175
U_ppm	0.207	0.304	0.103	0.023	0.206	0.396	0.185	0.336	0.368
Y_ppm	13.91	4.99	13.58	7.17	21.28	24	30.34	30.31	15.25
Cu_ppm	24.7	5.4	20.5	106.1	11.1	40.2	241.1	19.8	25.6
Zn_ppm	73.2	73.6	71.4	87	87.2	129.5	138.4	97	77.4
Mo_ppm	0.21	0.29	1.41	0.68	0.46	0.58	1.18	5.19	0.54
Tl_ppm	0.013	0.003	0.004	0.024	0.007	0.017	0.034	0.029	0.012
Pb_ppm	1.1	0.51	0.59	0.98	0.94	1.15	1.68	1.02	0.51
Sn_ppm	0.39	<0.16	0.41	0.22	0.31	0.5	0.79	0.81	0.37
Sb_ppm	<0.04	0.06	0.06	<0.04	0.2	0.04	0.06	<0.04	<0.04
Ga_ppm	12.57	8.97	11.96	7.8	8.96	19.34	17.53	15.92	12.88
W_ppm	0.09	0.37	0.09	0.45	0.31	1.28	0.56	0.67	0.07
Bi_ppm	<0.47	<0.47	<0.47	<0.47	<0.47	<0.47	<0.47	<0.47	<0.47
Be_ppm	0.37	0.1	0.19	0.15	0.25	0.39	0.46	0.44	0.23
Au_ppm	1.6	1.5	1.1	2.2	2	2	3.8	8.7	2.1
Pd_ppm	1.14	1.86	0.55	9.99	7.55	<0.14	6.24	2.13	5.1
Pt_ppm	5.12	3.46	4.62	10.22	3.03	0.32	10.22	7.38	8.4
La_ppm	2.4	0.7	1.9	1	6.2	5.6	5.7	3.8	2.1
Ce_ppm	5.83	2.03	4.74	2.75	14.6	10.3	14.95	10.83	5.36
Pr_ppm	0.936	0.284	0.721	0.505	2.062	2.203	2.355	1.825	0.845
Nd_ppm	4.41	1.47	3.72	2.56	9.25	10.42	11.51	9.59	4.43
Sm_ppm	1.338	0.439	1.204	0.818	2.54	2.862	3.585	3.188	1.375
Eu_ppm	0.676	0.1821	0.4775	0.2782	0.5586	1.1321	1.1552	1.0891	0.5107
Gd_ppm	1.863	0.636	1.758	1.115	3.131	3.435	4.495	4.203	2.016
Tb_ppm	0.3289	0.1141	0.3206	0.2011	0.5468	0.6066	0.7913	0.7535	0.3768
Dy_ppm	2.243	0.848	2.203	1.332	3.702	4.119	5.269	5.143	2.649

	LOW17 CB42	LOW17C B43	LOW17 CB44	LOW17 CB45	LOW17 CB46	LOW17 CB47	LOW17 CB48	LOW17 CB51	LOW17 CB52
Ho_ppm	0.4984	0.1735	0.4965	0.2864	0.802	0.9035	1.1358	1.1001	0.5746
Er_ppm	1.541	0.585	1.509	0.87	2.352	2.805	3.33	3.349	1.731
Tm_ppm	0.2213	0.0863	0.2195	0.122	0.3429	0.4105	0.4906	0.4944	0.2569
Yb_ppm	1.486	0.556	1.482	0.824	2.199	2.798	3.245	3.332	1.677
Lu_ppm	0.241	0.084	0.225	0.122	0.326	0.422	0.491	0.506	0.269

	LOW17 CB53	LOW17 CB54	LOW17 CB56	LOW17 CB57	LOW17 CB58	LOW17 CB59	LOW17 CB61	LOW17 CB62	LOW17 CB63
Northing	5465362	546738	5467307	5467665	5467615	5467523	5466813	5466858	546630
Easting	371521	368907	368921	368875	369301	369200	368061	367977	369352
Rock Type	Komatiite basalt	Komatiite	Komatiite basalt	Komatiite	Komatiite basalt	Komatiite basalt	Gabbro	Komatiite	LOTI tholeiite
SiO2_pct	48.22	44.99	48.09	46.46	48.15	47.83	50.19	40.65	51.04
TiO2_pct	0.37	0.33	0.53	0.38	0.55	0.53	0.45	0.32	0.57
Al2O3_pct	12.8	9.77	8.22	12.06	8.12	12.53	11.97	11.34	5.13
Fe2O3_pct	13.12	10.61	12.58	10.31	12.27	12.4	9.7	16.56	11.79
MnO_pct	0.232	0.174	0.193	0.197	0.2	0.202	0.194	0.22	0.189
MgO_pct	15.49	23.36	14.45	20.14	12.84	13.67	11.99	25.17	8.75
CaO_pct	8.421	6.355	8.371	9.254	10.203	9.664	12.545	3.308	10.201
Na2O_pct	1.29	0.39	1.51	0.77	1.65	1.48	2.02	0.05	2.04
K2O_pct	0.14	0.02	0.41	0.08	0.15	0.18	0.29	0.09	0.17
P2O5_pct	0.028	0.028	0.046	0.039	0.046	0.044	0.03	0.016	0.041
LOI	2.22	5.28	1.38	3.44	0.73	0.92	0.72	7.34	0.81
Sum	99.43	100.11	99.8	99.47	99.49	99.07	99.68	99.27	99.69
S_pct	<0.003	<0.003	<0.003	<0.003	<0.003	<0.003	<0.003	0.009	<0.003
CO2_pct	0.45	0.116	0.061	0.161	0.054	0.067	0.151	0.173	0.173
Ti_ppm	2046	1831	3002	2116	3105	3150	2618	1875	3282
Cr_ppm	983	2206	1159	1859	1113	1091	1384	2856	440
Co_ppm	66.08	85.94	70.04	72.65	64.05	67.76	48.84	138.4	47.96
Ni_ppm	298.6	1086.4	373.3	847.3	344.5	348.1	156	939.4	87.9
Rb_ppm	3.55	0.29	15.03	0.76	1.55	3.9	8.7	1.8	2.1
Sr_ppm	52.9	38.7	103.4	145.4	146.8	99	145.7	22	80.4
Cs_ppm	3.64	0.168	11.774	0.303	0.113	1.323	0.335	0.334	0.436
Ba_ppm	18.9	1.7	39.4	26.5	47.2	37.4	81.3	14	30.6
Sc_ppm	23.1	21.4	35.4	23.7	36.1	36.8	58.4	22.5	48.2
V_ppm	170	146	219	160	225	218	240	124	274
Ta_ppm	0.046	0.039	0.072	0.055	0.077	0.071	0.053	0.046	0.089
Nb_ppm	0.832	0.552	1.08	0.951	1.191	1.129	0.902	0.715	1.4
Zr_ppm	21	19.3	32	23.3	33	32	23	19	38
Hf_ppm	0.65	0.56	0.96	0.74	0.98	0.94	0.69	0.52	1.1
Th_ppm	0.13	0.089	0.164	0.203	0.204	0.169	0.264	0.212	0.562
U_ppm	0.038	0.113	0.17	0.245	0.136	0.168	0.103	1.121	0.209

	LOW17 CB53	LOW17 CB54	LOW17 CB56	LOW17 CB57	LOW17 CB58	LOW17 CB59	LOW17 CB61	LOW17 CB62	LOW17 CB63
Y_ppm	9.24	7.44	13.71	11.24	14.04	13.73	10.27	4.52	13.81
Cu_ppm	14.3	12.9	112.1	14.2	32.1	4.5	7.2	60.3	23.8
Zn_ppm	89.4	67.5	71	72.3	71.5	79.5	70.6	106.9	61.6
Mo_ppm	0.57	0.11	0.2	0.16	0.29	0.72	0.56	1.13	0.26
Tl_ppm	0.015	<0.002	0.064	0.007	0.007	0.014	0.029	0.045	0.008
Pb_ppm	0.54	0.4	1.31	0.76	0.91	0.95	0.79	1.35	0.7
Sn_ppm	0.46	0.28	0.36	0.44	0.32	0.52	0.34	0.16	0.42
Sb_ppm	0.08	<0.04	<0.04	<0.04	0.06	<0.04	0.26	0.09	<0.04
Ga_ppm	10.57	8.2	12.21	9.46	12.5	12.35	10.22	6.4	13.39
W_ppm	0.1	0.15	0.06	0.31	0.26	0.09	0.27	0.65	0.06
Bi_ppm	<0.47	<0.47	0.47	<0.47	<0.47	<0.47	<0.47	<0.47	<0.47
Be_ppm	0.16	0.12	0.25	0.63	0.21	0.19	0.16	0.09	0.3
Au_ppm	1.7	1.5	2.1	2.3	2.1	4.4	5.4	2	3.2
Pd_ppm	4.63	0.34	0.7	2.03	1.41	6.48	3.46	2.92	3.46
Pt_ppm	7.64	4.75	4.79	4.82	9.76	11.68	3.69	3.16	5.22
La_ppm	1.8	0.7	2.1	2.3	1.9	1.8	1.5	0.9	2.8
Ce_ppm	3.86	1.97	5.38	6.76	5.22	4.42	3.85	2.12	6.76
Pr_ppm	0.556	0.301	0.803	0.983	0.755	0.723	0.566	0.287	0.906
Nd_ppm	2.74	1.66	3.93	4.52	3.85	3.66	2.9	1.42	4.2
Sm_ppm	0.853	0.601	1.311	1.298	1.313	1.263	0.982	0.448	1.38
Eu_ppm	0.4077	0.1819	0.5005	0.5562	0.4976	0.5181	0.3656	0.1663	0.4776
Gd_ppm	1.29	0.898	1.841	1.597	1.812	1.794	1.401	0.651	1.846
Tb_ppm	0.2287	0.1703	0.3168	0.2871	0.3343	0.3284	0.2557	0.1106	0.3481
Dy_ppm	1.607	1.254	2.273	1.879	2.37	2.306	1.774	0.779	2.382
Ho_ppm	0.3658	0.2753	0.5028	0.4172	0.5176	0.5008	0.3806	0.1698	0.5294
Er_ppm	1.12	0.86	1.572	1.217	1.525	1.527	1.132	0.508	1.6
Tm_ppm	0.1597	0.1237	0.2238	0.1808	0.2357	0.2254	0.167	0.0781	0.2391
Yb_ppm	1.101	0.849	1.548	1.245	1.575	1.463	1.086	0.523	1.62
Lu_ppm	0.165	0.129	0.234	0.178	0.242	0.226	0.168	0.08	0.248

	LOW17 CB53	LOW17 CB54	LOW17 CB56	LOW17 CB57	LOW17 CB58	LOW17 CB59	LOW17 CB61	LOW17 CB62	LOW17 CB63
Northing	5465362	546738	5467307	5467665	5467615	5467523	5466813	5466858	546630
Easting	371521	368907	368921	368875	369301	369200	368061	367977	369352
Rock Type	Komatiite basalt	Komatiite	Komatiite basalt	Komatiite	Komatiite basalt	Komatiite basalt	Gabbro	Komatiite	LOTI tholeiite
SiO2_pct	48.22	44.99	48.09	46.46	48.15	47.83	50.19	40.65	51.04
TiO2_pct	0.37	0.33	0.53	0.38	0.55	0.53	0.45	0.32	0.57
Al2O3_pct	12.8	9.77	8.22	12.06	8.12	12.53	11.97	11.34	5.13
Fe2O3_pct	13.12	10.61	12.58	10.31	12.27	12.4	9.7	16.56	11.79
MnO_pct	0.232	0.174	0.193	0.197	0.2	0.202	0.194	0.22	0.189
MgO_pct	15.49	23.36	14.45	20.14	12.84	13.67	11.99	25.17	8.75
CaO_pct	8.421	6.355	8.371	9.254	10.203	9.664	12.545	3.308	10.201
Na2O_pct	1.29	0.39	1.51	0.77	1.65	1.48	2.02	0.05	2.04

	LOW17 CB53	LOW17C B54	LOW17 CB56	LOW17 CB57	LOW17 CB58	LOW17 CB59	LOW17 CB61	LOW17 CB62	LOW17 CB63
K2O_pct	0.14	0.02	0.41	0.08	0.15	0.18	0.29	0.09	0.17
P2O5_pct	0.028	0.028	0.046	0.039	0.046	0.044	0.03	0.016	0.041
LOI	2.22	5.28	1.38	3.44	0.73	0.92	0.72	7.34	0.81
Sum	99.43	100.11	99.8	99.47	99.49	99.07	99.68	99.27	99.69
S_pct	<0.003	<0.003	<0.003	<0.003	<0.003	<0.003	<0.003	0.009	<0.003
CO2_pct	0.45	0.116	0.061	0.161	0.054	0.067	0.151	0.173	0.173
Ti_ppm	2046	1831	3002	2116	3105	3150	2618	1875	3282
Cr_ppm	983	2206	1159	1859	1113	1091	1384	2856	440
Co_ppm	66.08	85.94	70.04	72.65	64.05	67.76	48.84	138.4	47.96
Ni_ppm	298.6	1086.4	373.3	847.3	344.5	348.1	156	939.4	87.9
Rb_ppm	3.55	0.29	15.03	0.76	1.55	3.9	8.7	1.8	2.1
Sr_ppm	52.9	38.7	103.4	145.4	146.8	99	145.7	22	80.4
Cs_ppm	3.64	0.168	11.774	0.303	0.113	1.323	0.335	0.334	0.436
Ba_ppm	18.9	1.7	39.4	26.5	47.2	37.4	81.3	14	30.6
Sc_ppm	23.1	21.4	35.4	23.7	36.1	36.8	58.4	22.5	48.2
V_ppm	170	146	219	160	225	218	240	124	274
Ta_ppm	0.046	0.039	0.072	0.055	0.077	0.071	0.053	0.046	0.089
Nb_ppm	0.832	0.552	1.08	0.951	1.191	1.129	0.902	0.715	1.4
Zr_ppm	21	19.3	32	23.3	33	32	23	19	38
Hf_ppm	0.65	0.56	0.96	0.74	0.98	0.94	0.69	0.52	1.1
Th_ppm	0.13	0.089	0.164	0.203	0.204	0.169	0.264	0.212	0.562
U_ppm	0.038	0.113	0.17	0.245	0.136	0.168	0.103	1.121	0.209
Y_ppm	9.24	7.44	13.71	11.24	14.04	13.73	10.27	4.52	13.81
Cu_ppm	14.3	12.9	112.1	14.2	32.1	4.5	7.2	60.3	23.8
Zn_ppm	89.4	67.5	71	72.3	71.5	79.5	70.6	106.9	61.6
Mo_ppm	0.57	0.11	0.2	0.16	0.29	0.72	0.56	1.13	0.26
Tl_ppm	0.015	<0.002	0.064	0.007	0.007	0.014	0.029	0.045	0.008
Pb_ppm	0.54	0.4	1.31	0.76	0.91	0.95	0.79	1.35	0.7
Sn_ppm	0.46	0.28	0.36	0.44	0.32	0.52	0.34	0.16	0.42
Sb_ppm	0.08	<0.04	<0.04	<0.04	0.06	<0.04	0.26	0.09	<0.04
Ga_ppm	10.57	8.2	12.21	9.46	12.5	12.35	10.22	6.4	13.39
W_ppm	0.1	0.15	0.06	0.31	0.26	0.09	0.27	0.65	0.06
Bi_ppm	<0.47	<0.47	0.47	<0.47	<0.47	<0.47	<0.47	<0.47	<0.47
Be_ppm	0.16	0.12	0.25	0.63	0.21	0.19	0.16	0.09	0.3
Au_ppm	1.7	1.5	2.1	2.3	2.1	4.4	5.4	2	3.2
Pd_ppm	4.63	0.34	0.7	2.03	1.41	6.48	3.46	2.92	3.46
Pt_ppm	7.64	4.75	4.79	4.82	9.76	11.68	3.69	3.16	5.22
La_ppm	1.8	0.7	2.1	2.3	1.9	1.8	1.5	0.9	2.8
Ce_ppm	3.86	1.97	5.38	6.76	5.22	4.42	3.85	2.12	6.76
Pr_ppm	0.556	0.301	0.803	0.983	0.755	0.723	0.566	0.287	0.906
Nd_ppm	2.74	1.66	3.93	4.52	3.85	3.66	2.9	1.42	4.2
Sm_ppm	0.853	0.601	1.311	1.298	1.313	1.263	0.982	0.448	1.38

	LOW17 CB53	LOW17C B54	LOW17 CB56	LOW17 CB57	LOW17 CB58	LOW17 CB59	LOW17 CB61	LOW17 CB62	LOW17 CB63
Eu_ppm	0.4077	0.1819	0.5005	0.5562	0.4976	0.5181	0.3656	0.1663	0.4776
Gd_ppm	1.29	0.898	1.841	1.597	1.812	1.794	1.401	0.651	1.846
Tb_ppm	0.2287	0.1703	0.3168	0.2871	0.3343	0.3284	0.2557	0.1106	0.3481
Dy_ppm	1.607	1.254	2.273	1.879	2.37	2.306	1.774	0.779	2.382
Ho_ppm	0.3658	0.2753	0.5028	0.4172	0.5176	0.5008	0.3806	0.1698	0.5294
Er_ppm	1.12	0.86	1.572	1.217	1.525	1.527	1.132	0.508	1.6
Tm_ppm	0.1597	0.1237	0.2238	0.1808	0.2357	0.2254	0.167	0.0781	0.2391
Yb_ppm	1.101	0.849	1.548	1.245	1.575	1.463	1.086	0.523	1.62
Lu_ppm	0.165	0.129	0.234	0.178	0.242	0.226	0.168	0.08	0.248

	LOW17 CB64	LOW17 CB65	LOW17 CB66	LOW17 CB67	LOW17 CB68	LOW17 CB69	LOW17 CB70	LOW17 CB71	LOW17 CB72
Northing	5466448	546642 2	5465040	5465163	5468117	5465295	5465425	5465435	546784
Easting	369381	369112	370956	371261	371818	370608	370631	370440	372223
Rock Type	LOTI tholeiite	LOTI tholeiite	LOTI tholeiite	Komatiite	Komatiite	Komatiite	Komatiite basalt	LOTI tholeiite	LOTI tholeiite
SiO2_pct	50.19	52.47	51.76	42.71	47.51	44.38	49.76	50.43	49.24
TiO2_pct	0.62	0.75	0.63	0.42	0.28	0.32	0.49	0.7	0.87
Al2O3_pct	14.03	14.08	13.68	13.91	8.94	6.94	8.11	12	14.79
Fe2O3_pct	11.85	11.95	11.79	10.99	10.42	11.06	12.43	10.86	12.63
MnO_pct	0.219	0.195	0.24	0.162	0.181	0.188	0.22	0.192	0.209
MgO_pct	8.76	7.18	7.21	23.52	20.82	23.07	13.2	6.7	7.94
CaO_pct	10.481	10.444	10.246	5.79	9.508	6.261	8.815	11.746	11.63
Na2O_pct	2.56	2.17	2.91	0.23	1.06	0.18	1.34	2.29	1.5
K2O_pct	0.19	0.18	0.22	0.03	0.07	0.03	0.21	0.26	0.29
P2O5_pct	0.053	0.056	0.054	0.027	0.027	0.049	0.036	0.058	0.085
LOI	0.66	0.69	0.74	6.58	2.48	5.89	0.74	0.81	0.91
Sum	99.74	99.79	99.77	99.75	99.56	99.88	99.37	98.88	99.54
S_pct	<0.003	<0.003	0.003	<0.003	0.003	<0.003	<0.003	<0.003	0.011
CO2_pct	0.053	0.227	0.292	0.171	0.127	0.287	0.13	0.072	0.166
Ti_ppm	3602	4222	3664	2395	1647	1909	2784	4058	5043
Cr_ppm	421	180	377	2314	1691	2199	957	294	458
Co_ppm	50.36	45.74	50.34	84.29	67.76	82.67	62.68	46.64	53.5
Ni_ppm	118.7	68.4	102.2	1078.5	787.7	991.7	269.4	77.6	159.3
Rb_ppm	3	4.2	2.2	<0.8	0.8	2.3	7.3	6.8	5.9
Sr_ppm	138.2	185.2	148.9	23.6	69.2	16.4	71.8	104.2	101.8
Cs_ppm	0.341	0.983	0.375	0.24	0.07	0.867	1.134	3.226	1.35
Ba_ppm	37.4	30.4	108.9	2.3	24.4	25.9	48.4	58.5	49
Sc_ppm	46.1	42.2	45.4	23.1	20.2	22.3	42.6	46	38.9
V_ppm	268	284	269	173	129	167	240	283	265
Ta_ppm	0.114	0.13	0.115	0.037	0.027	0.022	0.077	0.136	0.186
Nb_ppm	1.709	1.825	1.732	0.727	0.542	0.456	1.232	2.014	2.918
Zr_ppm	44	45	44	21	17	17	33	50	69

	LOW17C B64	LOW17C B65	LOW17C B66	LOW17C B67	LOW17C B68	LOW17C B69	LOW17C B70	LOW17C B71	LOW17 CB72
Hf_ppm	1.22	1.31	1.25	0.66	0.5	0.52	0.95	1.41	1.97
Th_ppm	0.702	0.527	0.722	0.039	0.151	0.033	0.46	0.783	0.473
U_ppm	0.288	0.411	0.697	0.156	0.144	0.169	0.196	0.266	0.118
Y_ppm	14.72	15	14.52	7.23	7.47	8.9	12.45	15.92	22.97
Cu_ppm	19.6	28.1	42.5	86.4	13.6	14.2	14.4	19.5	108.6
Zn_ppm	84	81.6	92.9	69	60.5	78.1	114.8	89.2	92.8
Mo_ppm	0.38	0.63	0.93	0.51	0.38	0.47	0.34	0.32	0.46
Tl_ppm	0.015	0.015	0.013	0.002	0.006	0.005	0.037	0.036	0.037
Pb_ppm	1.64	0.96	3.64	0.69	1.32	0.5	2.29	1.46	1.06
Sn_ppm	0.53	0.39	0.83	0.17	0.25	0.45	0.48	0.49	0.52
Sb_ppm	0.04	0.07	0.04	0.13	<0.04	<0.04	<0.04	<0.04	<0.04
Ga_ppm	14.17	14.19	11.73	8.66	6.91	7.62	11.48	14.47	15.09
W_ppm	0.13	0.18	0.43	0.55	0.34	0.59	0.05	0.31	0.11
Bi_ppm	<0.47	<0.47	0.65	<0.47	<0.47	<0.47	<0.47	<0.47	<0.47
Be_ppm	0.29	0.39	0.32	0.16	0.2	1.04	0.28	0.42	0.33
Au_ppm	2.2	3.4	2	2.6	2.8	1.9	2.3	2.3	4
Pd_ppm	4.86	5.62	2.74	0.42	3.01	0.72	8.41	3.78	6.84
Pt_ppm	7.58	6.61	6.73	4.65	5.5	4.62	6.07	7.15	10.4
La_ppm	3.4	3.4	1.6	0.9	1.2	0.7	1.9	3.4	4.3
Ce_ppm	8.19	7.79	4.93	2.19	2.62	1.81	4.88	8.14	11.13
Pr_ppm	1.062	1.164	0.806	0.339	0.36	0.302	0.746	1.137	1.757
Nd_ppm	5.15	5.49	4.25	1.79	1.79	1.75	3.46	5.62	8.59
Sm_ppm	1.493	1.668	1.427	0.646	0.639	0.697	1.162	1.715	2.614
Eu_ppm	0.5504	0.6229	0.5054	0.1953	0.4039	0.2109	0.4124	0.593	0.9061
Gd_ppm	2.023	2.166	1.934	0.92	0.914	1.06	1.633	2.224	3.356
Tb_ppm	0.3697	0.4087	0.3509	0.1837	0.1741	0.2075	0.3006	0.3944	0.5977
Dy_ppm	2.489	2.711	2.482	1.233	1.241	1.496	2.058	2.758	4.005
Ho_ppm	0.5456	0.5786	0.5401	0.2624	0.2656	0.3315	0.4584	0.5789	0.8281
Er_ppm	1.635	1.685	1.706	0.805	0.8	0.98	1.402	1.833	2.578
Tm_ppm	0.245	0.2536	0.2437	0.1211	0.1265	0.1521	0.2041	0.2664	0.3718
Yb_ppm	1.631	1.669	1.674	0.875	0.839	0.99	1.401	1.739	2.451
Lu_ppm	0.243	0.259	0.248	0.126	0.131	0.149	0.217	0.272	0.373

	LOW17 CB73	LOW17 CB74	LOW17 CB76	LOW17 CB77	LOW17 CB78	LOW17 CB79	LOW17 CB80	LOW17 CB81	LOW17 CB82
Northing	5467592	546742	5466719	5466756	5466709	5466673	5466788	5467128	546732
Easting	371316	371294	374462	374552	373859	373665	373530	372939	372874
Rock Type	LOTI tholeiite	Calc- alkalic MV	Amph cumulate	Int MV	Komatiite	Komatiite	HITI tholeiite	Calc- alkalic MV	Komatiite
SiO2_pct	48.16	53.35	49.41	56.78	40.23	44.51	47.21	48.98	44.85
TiO2_pct	0.96	0.34	1.15	0.93	0.34	0.4	1.06	0.82	0.43
Al2O3_pct	14.16	13.69	9.62	14.84	16.47	10.26	8.43	15.13	14

	LOW17 CB73	LOW17 CB74	LOW17 CB76	LOW17 CB77	LOW17 CB78	LOW17 CB79	LOW17 CB80	LOW17 CB81	LOW17 CB82
Fe2O3_pct	14.41	7.19	14.41	7.43	13.96	12.56	15.49	10	12.27
MnO_pct	0.261	0.134	0.214	0.154	0.165	0.196	0.334	0.153	0.208
MgO_pct	6.69	14.47	6.56	3.8	22.32	23.72	6.46	9.55	20.28
CaO_pct	10.957	8.035	10.016	9.696	5.679	3.4	7.691	8.234	6.74
Na2O_pct	2.31	2.51	1.98	2.49	0.09	0.04	2.89	2.8	0.46
K2O_pct	0.51	1.46	0.21	0.39	0.02	0.02	0.4	1.78	0.04
P2O5_pct	0.101	0.135	0.082	0.081	0.024	0.047	0.101	0.404	0.05
LOI	1.35	1.92	0.68	0.95	6.49	6.32	2.62	2.38	4.51
Sum	99.46	99.52	99.56	99.27	99.83	99.93	99.45	99.34	99.43
S_pct	0.003	<0.003	0.005	0.088	<0.003	<0.003	0.003	0.003	0.005
CO2_pct	0.087	0.178	0.205	0.142	0.248	0.24	0.171	0.127	0.147
Ti_ppm	5637	1916	6797	5489	2056	2359	6372	4933	2576
Cr_ppm	235	2226	49	652	1650	2040	285	1048	1907
Co_ppm	44.39	48.23	51.44	62.08	100.95	106.74	52.65	39.86	89.53
Ni_ppm	73.7	369.5	65.9	226.2	542.6	748.2	91.5	163.8	647.2
Rb_ppm	19.7	38.5	4	9.3	<0.8	0.8	12.3	57.7	<0.8
Sr_ppm	170.3	454.6	148.1	182.3	6.3	2.6	177.7	>1560	9.4
Cs_ppm	1.462	7.713	0.511	1.45	0.709	1.13	2.739	4.635	2.173
Ba_ppm	75.6	280.8	48.6	130.1	2.7	4.5	364.6	805.1	14
Sc_ppm	40.9	27.7	36.6	41.5	20.7	24	47.1	28.2	28.7
V_ppm	293	113	298	270	172	163	318	194	180
Ta_ppm	0.234	0.167	0.164	0.183	0.044	0.048	0.253	0.309	0.05
Nb_ppm	3.459	2.853	2.695	2.905	0.745	0.926	3.709	5.391	0.86
Zr_ppm	81	69	62	68	23	24	92	115	26
Hf_ppm	2.24	1.83	1.81	1.98	0.65	0.7	2.62	3.05	0.79
Th_ppm	0.583	3.302	0.392	0.418	0.069	0.104	0.61	6.019	0.104
U_ppm	0.169	1.274	0.088	0.099	0.039	0.138	0.146	1.504	0.073
Y_ppm	28.04	7.59	21.93	20.12	7.11	7.47	25.91	18.6	10.93
Cu_ppm	30.2	12.1	32.8	118.4	17.6	7.4	17.6	59.6	25.4
Zn_ppm	107.1	65.5	110.7	85.4	92.6	92.1	142.9	96.8	85.3
Mo_ppm	0.67	0.16	0.41	1.01	0.18	0.11	0.65	0.3	0.29
Tl_ppm	0.076	0.199	0.022	0.033	0.003	0.005	0.057	0.316	0.002
Pb_ppm	1.28	3.7	0.7	1.41	0.48	0.34	0.9	11.94	0.38
Sn_ppm	0.83	0.56	0.68	0.66	<0.16	<0.16	0.84	0.99	0.2
Sb_ppm	<0.04	0.04	<0.04	<0.04	0.05	0.09	0.04	0.09	<0.04
Ga_ppm	15.97	11	18.47	17.39	11.51	9.33	17.42	17.02	9.68
W_ppm	0.37	0.3	0.07	0.17	0.11	0.39	0.72	0.64	0.08
Bi_ppm	<0.47	<0.47	<0.47	<0.47	<0.47	<0.47	<0.47	<0.47	<0.47
Be_ppm	0.58	0.88	0.46	0.41	0.26	1.24	0.72	1.93	0.27
Au_ppm	1.9	2.2	1.7	2.6	2.1	5	6.3	3.9	3.6
Pd_ppm	3.38	3.37	<0.14	10.81	4.9	8.44	4.63	2.14	3.9
Pt_ppm	8.5	11.17	<0.06	13.05	5.33	11.23	7.6	2.99	6.09

	LOW17 CB83	LOW17 CB84	LOW17 CB85	LOW17 CB86	LOW17 CB87	LOW17 CB88	LOW17 CB89	LOW17 CB90	LOW17 CB91
Northing	5467317	546784	5465979	5465879	5465853	5467607	5467559	5467484	546543
Easting	373127	373416	370460	370510	370625	373522	373722	373707	368560
Rock Type	Komatiite	LOTI tholeiite	Komatiite basalt	Komatiite basalt	Komatiite basalt	HITI tholeiite	Komatiite basalt	Komatiite basalt	HITI tholeiite
SiO2_pct	44.05	48.8	47.73	47.46	47.75	52.34	48.48	48.21	51.75
TiO2_pct	0.31	0.79	0.66	0.57	0.54	1.03	0.59	0.54	1.03
Al2O3_pct	9.29	8.71	15.55	13.69	12.51	12.24	15.06	12.7	11.88
Fe2O3_pct	10.28	9.96	11.65	11.56	11.86	12.55	12.1	12.09	11.69
MnO_pct	0.167	0.171	0.197	0.17	0.189	0.251	0.212	0.205	0.257
MgO_pct	22.45	6.22	13.15	13.9	13.94	4.33	11.06	12.27	6.84
CaO_pct	7.132	14.261	8.625	9.769	9.272	11.077	10.72	11.315	10.165
Na2O_pct	0.3	1.88	1.59	1.99	1.94	1.83	2.18	1.53	2.53
K2O_pct	0.03	0.35	0.19	0.1	0.1	0.26	0.22	0.2	0.23
P2O5_pct	0.006	0.077	0.049	0.04	0.041	0.101	0.045	0.04	0.099
LOI	5.98	1.5	1.6	1.61	1.52	0.52	0.76	0.92	0.77
Sum	99.73	99.62	99.26	99.87	99.58	99.4	99.23	99.35	99.91
S_pct	<0.003	<0.003	0.003	0.003	<0.003	0.003	<0.003	0.003	0.003
CO2_pct	0.116	0.104	0.174	0.229	0.089	0.12	0.143	0.134	0.352
Ti_ppm	1809	4706	3945	3262	3196	6002	3491	3228	5984
Cr_ppm	2118	341	902	1346	1294	275	1183	1059	244
Co_ppm	85.72	42.69	64.23	68.5	71.79	45.51	65.99	65.45	47.2
Ni_ppm	1089.7	123.6	311.6	408.4	412.2	81.2	347.2	305.8	64.1
Rb_ppm	1.8	13.2	3.8	1.4	1.7	4.2	12.6	16.5	3
Sr_ppm	29.8	258.5	96.9	99.4	104.5	175	326.4	91.6	136.7
Cs_ppm	2.717	3.044	1.023	1.051	1.316	0.791	3.296	2.115	1.142
Ba_ppm	2.7	72.9	28.7	21.5	22	41.7	64.6	41.8	116.9
Sc_ppm	20.6	38.3	40.4	37.9	38.1	41.6	39.2	37.5	41.8
V_ppm	154	231	242	226	216	292	235	218	296
Ta_ppm	0.027	0.175	0.098	0.081	0.074	0.246	0.073	0.073	0.23
Nb_ppm	0.578	2.764	1.595	1.244	1.129	3.716	1.236	1.227	3.418
Zr_ppm	18	62	40	34	32	84	35	33	83
Hf_ppm	0.54	1.81	1.16	1.03	0.99	2.49	1.04	0.98	2.33
Th_ppm	0.061	0.444	0.179	0.198	0.145	0.592	0.162	0.186	0.578
U_ppm	0.126	0.192	0.203	0.14	0.14	0.278	0.127	0.205	0.259
Y_ppm	7.07	19.84	15.52	14.5	13.65	27.45	14.85	13.7	27.06
Cu_ppm	15.5	72.5	28.2	26.3	3.3	10.6	6.1	24.4	6
Zn_ppm	80.8	65.8	74.8	70.5	79.3	102.6	75.3	86.4	99.4
Mo_ppm	0.1	0.59	0.37	0.27	0.48	1.48	0.61	0.43	1.08

	LOW17 CB83	LOW17C B84	LOW17 CB85	LOW17 CB86	LOW17 CB87	LOW17 CB88	LOW17 CB89	LOW17 CB90	LOW17 CB91
Tl_ppm	0.011	0.086	0.009	0.004	0.003	0.016	0.068	0.068	0.017
Pb_ppm	0.98	2.96	0.76	0.89	0.7	1.73	4.74	1.2	1.59
Sn_ppm	0.2	0.57	0.38	0.31	0.42	0.84	0.3	0.26	0.62
Sb_ppm	<0.04	0.17	<0.04	<0.04	<0.04	<0.04	0.05	0.08	<0.04
Ga_ppm	9.1	16.17	13.19	12.08	11.73	17.37	13.05	12.33	17.05
W_ppm	0.28	1.42	0.12	0.07	0.06	0.9	0.19	0.63	0.34
Bi_ppm	<0.47	1.99	<0.47	<0.47	<0.47	0.77	0.5	<0.47	0.58
Be_ppm	0.37	0.62	0.3	0.27	0.28	0.62	0.38	0.35	0.56
Au_ppm	2.3	2.2	3.5	2.4	5.8	5.5	2.7	2.8	7.2
Pd_ppm	0.9	5.85	4.34	2.95	4.26	0.94	8.79	4.12	7.17
Pt_ppm	2.79	10.38	7.13	5.28	8.88	6.62	15.28	7.35	10.12
La_ppm	1	3.9	2.3	1.9	1.8	5.2	1.7	1.2	3.4
Ce_ppm	2.83	10.35	6.43	4.82	4.42	13.59	4.97	3.87	9.21
Pr_ppm	0.405	1.595	0.999	0.732	0.679	2.102	0.798	0.684	1.55
Nd_ppm	1.95	7.61	5.18	3.74	3.64	10.42	4.12	3.54	8.38
Sm_ppm	0.64	2.307	1.606	1.304	1.223	3.269	1.411	1.251	2.971
Eu_ppm	0.2637	0.8438	0.5929	0.4718	0.4425	1.0676	0.5166	0.4709	0.9725
Gd_ppm	0.914	2.963	2.253	1.949	1.807	4.155	2.008	1.851	3.907
Tb_ppm	0.1657	0.5375	0.3944	0.3517	0.3326	0.7316	0.3585	0.3172	0.7032
Dy_ppm	1.151	3.542	2.684	2.41	2.294	4.871	2.543	2.349	4.602
Ho_ppm	0.2447	0.7411	0.5759	0.5288	0.5069	1.0578	0.5477	0.5053	0.9983
Er_ppm	0.81	2.251	1.745	1.682	1.542	3.116	1.66	1.562	2.968
Tm_ppm	0.1192	0.3309	0.251	0.2505	0.2253	0.4623	0.2455	0.2254	0.4346
Yb_ppm	0.806	2.143	1.627	1.585	1.486	2.991	1.626	1.553	2.864
Lu_ppm	0.123	0.318	0.26	0.244	0.234	0.466	0.247	0.228	0.436

	LOW17 CB92	LOW17 CB93	LOW17 CB94	LOW17 CB95	LOW17 CB96	LOW17 CB97	LOW17 CB98	LOW17 CB99	LOW18 CB02
Northing	5465199	546510	5466467	5467881	5468320	5477792	5478005	5478171	548147
Easting	368880	368755	376002	373975	372820	363023	363199	363084	389980
Rock Type	Komatiite	LOTI tholeiite	LOTI tholeiite	LOTI tholeiite	Komatiite basalt	HITI tholeiite	HITI tholeiite	HITI tholeiite	Komatiit e basalt
SiO2_pct	42.2	50.09	48.59	51.68	46.36	49.27	48.83	49.63	48.18
TiO2_pct	0.34	0.71	0.62	0.79	0.57	1.22	1	1.35	0.6
Al2O3_pct	14.51	7.48	15	13.3	14.79	10.96	13.5	14.09	13.28
Fe2O3_pct	11.39	11.26	12.56	12.09	12.61	15.54	13.63	15.96	11.24
MnO_pct	0.185	0.198	0.211	0.281	0.2	0.227	0.312	0.372	0.173
MgO_pct	24.93	8.42	8.75	6.13	14.74	6.45	6.65	3.29	13.01
CaO_pct	5.643	10.284	12.972	11.258	10.089	9.629	10.303	10.095	9.117
Na2O_pct	0.06	2.14	1.25	1.25	1.82	2.28	2.45	1.93	1.11
K2O_pct	0.02	0.24	0.13	0.19	0.26	0.17	0.16	0.24	0.17
P2O5_pct	0.04	0.055	0.046	0.068	0.034	0.092	0.07	0.109	0.045
LOI	6.97	0.91	0.6	0.38	1.58	1.01	1.85	2.51	2.84
Sum	99.6	99.36	99.11	99.01	99.4	99.41	99.36	99.54	99.91

	LOW17 CB92	LOW17 CB93	LOW17 CB94	LOW17 CB95	LOW17 CB96	LOW17 CB97	LOW17 CB98	LOW17 CB99	LOW18 CB02
S_pct	0.005	<0.003	0.049	0.044	0.005	0.015	0.018	0.047	0.019
CO2_pct	0.175	0.176	0.127	0.151	0.131	0.732	1.288	2.324	<0.023
Ti_ppm	1985	4191	3588	4717	3314	6957	5794	7770	3442
Cr_ppm	2358	365	620	698	1294	76	104	82	1064
Co_ppm	91.96	49.27	59.89	62.05	71.1	58.06	57.81	52.43	185.9
Ni_ppm	854.3	120.4	184	246.4	414.5	81.6	99.9	56.9	339.7
Rb_ppm	<0.8	3.5	1.4	3.2	23.4	2	1.6	1.6	1.87
Sr_ppm	38.5	115.2	117.4	122.3	84.9	131.5	134.7	210.8	93.9
Cs_ppm	0.892	1.773	0.706	0.423	27.395	0.107	0.038	0.046	0.108
Ba_ppm	8.6	42.2	69.2	67.8	28.6	39.8	78.6	41.2	42
Sc_ppm	22	40.4	40.3	40	38.5	34.3	39.3	33.7	34.7
V_ppm	119	256	258	261	236	322	314	328	215.5
Ta_ppm	0.05	0.113	0.086	0.144	0.051	0.25	0.171	0.239	0.091
Nb_ppm	0.878	1.801	1.363	2.319	1.064	3.744	2.65	3.633	1.426
Zr_ppm	21	45	37	56	24	72	55	83	39
Hf_ppm	0.61	1.32	1.14	1.62	0.81	2.05	1.56	2.37	1.05
Th_ppm	0.099	0.238	0.188	0.306	0.04	0.446	0.281	0.443	0.185
U_ppm	3.793	0.178	0.049	0.079	0.125	0.106	0.072	0.122	0.061
Y_ppm	8.13	16.62	15.69	19.54	14.12	21.18	17.65	25.04	13.88
Cu_ppm	54.6	50.5	70.6	76.6	10.5	176.1	86.9	47.2	91.5
Zn_ppm	84.5	81.5	81.9	83.7	78.8	115.7	89.5	120.1	78.5
Mo_ppm	0.75	0.53	0.92	0.99	0.94	0.4	0.42	1.14	0.44
Tl_ppm	0.004	0.011	0.013	0.03	0.135	0.012	0.01	0.007	0.007
Pb_ppm	1.14	0.85	0.66	0.86	1.79	1.46	0.92	2.55	0.58
Sn_ppm	<0.16	0.42	0.37	0.46	0.26	0.61	0.63	0.9	0.33
Sb_ppm	<0.04	0.1	<0.04	<0.04	<0.04	0.04	0.06	0.08	0.05
Ga_ppm	7.5	14.56	13.53	15.09	11.45	18.44	17.78	20.34	12.27
W_ppm	0.27	0.07	0.16	0.15	0.18	0.16	0.17	0.39	0.09
Bi_ppm	0.95	<0.47	<0.47	<0.47	0.73	<0.47	<0.47	<0.47	<0.47
Be_ppm	0.68	0.41	0.27	0.27	0.79	0.62	0.4	0.44	0.18
Au_ppm	1.9	2.2	3.5	9	3	5.2	5.9	3.8	6.4
Pd_ppm	15.56	4.42	7.69	7.31	5.18	2.05	8.85	0.34	18.88
Pt_ppm	6.08	9.3	12.24	11.76	12.35	3.9	12.59	0.83	14.92
La_ppm	1.4	2.3	2	3.5	1.2	4.7	2.2	4.8	1.5
Ce_ppm	3.5	6.26	5.2	8.93	3.43	12.13	5.17	12.41	4.08
Pr_ppm	0.548	1.097	0.833	1.434	0.609	1.847	0.883	1.955	0.764
Nd_ppm	2.84	5.8	4.43	6.92	3.4	9.17	4.77	9.99	3.93
Sm_ppm	0.914	1.84	1.434	2.21	1.204	2.832	1.879	3.137	1.368
Eu_ppm	0.3234	0.6623	0.5452	0.7361	0.4412	1.0191	0.7833	0.9448	0.4707
Gd_ppm	1.185	2.505	2.183	2.849	1.89	3.614	2.871	4.296	2.012

	LOW17 CB92	LOW17 CB93	LOW17 CB94	LOW17 CB95	LOW17 CB96	LOW17 CB97	LOW17 CB98	LOW17 CB99	LOW18 CB02
Tb_ppm	0.2085	0.4322	0.3877	0.4994	0.3389	0.6098	0.4995	0.7147	0.3503
Dy_ppm	1.419	2.908	2.645	3.386	2.356	3.912	3.236	4.54	2.298
Ho_ppm	0.3049	0.6367	0.58	0.7284	0.5261	0.8111	0.6599	0.941	0.5158
Er_ppm	0.934	1.887	1.805	2.193	1.604	2.346	1.918	2.757	1.523
Tm_ppm	0.142	0.2791	0.2671	0.315	0.2322	0.3283	0.2646	0.381	0.2275
Yb_ppm	0.956	1.835	1.73	2.164	1.554	2.139	1.699	2.45	1.499
Lu_ppm	0.148	0.273	0.271	0.317	0.228	0.314	0.246	0.348	1.5

	LOW18 CB03	LOW18 CB05	LOW18 CB08	LOW18 CB09	LOW18 CB10	LOW18 CB12	LOW18 CB13	LOW18 CB15	LOW18 CB17
Northing	5483328	5482829	5482923	5483008	5482506	5482779	5482517	5482786	548309
Easting	395095	394917	395675	395302	388845	389436	389819	390447	393486
Rock Type	LOTI tholeiite	Komatiite basalt	Komatiite basalt	Int MV	LOTI tholeiite	Komatiite basalt	LOTI tholeiite	LOTI tholeiite	LOTI tholeiite
SiO2_pct	48.67	48	47.3	58.72	48.59	47.78	48.95	48.33	51.12
TiO2_pct	0.66	0.55	0.48	0.33	0.6	0.62	0.65	0.61	0.72
Al2O3_pct	13.8	12.23	12.15	9.15	16.37	13.67	15.54	13.6	16.43
Fe2O3_pct	11.72	11.97	12.22	8.53	10.22	11.65	10.47	11.51	10.82
MnO_pct	0.217	0.187	0.185	0.157	0.165	0.19	0.166	0.171	0.189
MgO_pct	9.48	12.46	13.33	9.82	9.65	11.7	9.94	11.52	5.89
CaO_pct	10.73	9.535	8.208	7.56	10.665	10.191	10.558	9.318	10.655
Na2O_pct	1.57	1.53	1.41	1.17	1.41	1.68	1.55	1.76	3.27
K2O_pct	0.09	0.09	0.08	0.09	0.12	0.09	0.14	0.09	0.17
P2O5_pct	0.05	0.045	0.039	0.03	0.048	0.048	0.05	0.046	0.085
LOI	2.94	3.81	4.44	4.38	2.07	2.71	2.01	3.7	1.14
Sum	100.04	100.55	99.99	100.04	99.98	100.45	100.11	100.8	100.53
S_pct	0.034	0.016	<0.003	0.007	0.031	0.006	0.123	0.043	0.049
CO2_pct	0.703	0.833	0.783	1.728	0.058	0.242	0.31	0.03	0.042
Ti_ppm	3782	3226	2750	1840	3376	3624	3847	3543	4378
Cr_ppm	811	1130	1137	818	400	880	500	924	141
Co_ppm	83.6	98.7	99.6	65.2	59.5	70	62.9	70.7	49.4
Ni_ppm	264.1	332	291.2	243.5	159.5	280.1	190.2	293.3	61.3
Rb_ppm	0.54	0.57	0.93	1.59	1.33	0.81	1.8	0.71	1.2
Sr_ppm	94	139.7	72.4	150	86.6	106.4	94.3	129.4	196.1
Cs_ppm	0.057	0.041	0.103	0.07	0.105	0.053	0.117	0.041	0.056
Ba_ppm	23	38	34	50	40	31	24	46	59
Sc_ppm	36	32	38	22	31	34	36	33	35
V_ppm	231	215	238	140	205	229	232	220	250
Ta_ppm	0.104	0.075	0.076	0.044	0.096	0.092	0.101	0.09	0.102
Nb_ppm	1.616	1.223	1.083	0.706	1.523	1.509	1.604	1.462	1.765
Zr_ppm	42	34	32	20	39	38	42	38	45

	LOW18 CB03	LOW18 CB05	LOW18 CB08	LOW18 CB09	LOW18 CB10	LOW18 CB12	LOW18 CB13	LOW18 CB15	LOW18 CB17
Hf_ppm	1.18	0.98	0.93	0.56	1.1	1.1	1.19	1.08	1.27
Th_ppm	0.214	0.17	0.444	0.12	0.21	0.171	0.195	0.182	0.711
U_ppm	0.054	0.043	0.107	0.036	0.057	0.052	0.061	0.043	0.153
Y_ppm	15.27	13.35	11.31	8.53	14.46	14.16	15.63	13.76	16.37
Cu_ppm	42.9	72.7	22.9	67.3	35.6	84.7	202.8	102.8	58.4
Zn_ppm	76.9	79.1	81.7	53.6	68.2	78	67.6	77.9	82.7
Mo_ppm	0.45	0.26	0.24	0.71	0.36	0.78	0.45	0.37	4.25
Tl_ppm	0.003	0.002	0.005	0.005	0.006	0.005	0.038	0.004	0.007
Pb_ppm	0.38	0.29	0.92	0.62	0.5	0.8	1.55	0.77	1.49
Sn_ppm	0.4	0.32	0.39	0.25	0.34	0.34	0.36	0.33	0.38
Sb_ppm	<0.04	0.06	0.06	0.04	<0.04	0.05	<0.04	<0.04	0.05
Ga_ppm	13.17	10.94	11.29	10	14.14	12.76	13.7	11.66	15.76
W_ppm	0.05	0.06	0.14	0.08	<0.05	0.17	0.19	0.1	0.09
Bi_ppm	<0.47	<0.47	<0.47	<0.47	<0.47	<0.47	<0.47	<0.47	<0.47
Be_ppm	0.24	0.17	0.23	0.11	0.2	0.2	0.2	0.26	0.31
Au_ppm	1.7	2.2	1.5	2.5	2.4	2.5	7.3	4.1	1.3
Pd_ppm	11.44	7.72	4.64	4.18	9.28	12.42	15.94	9.95	<0.14
Pt_ppm	12.93	9.17	5.89	7.51	12.28	14.18	13.22	12.27	0.57
La_ppm	2.6	1.8	2.1	1.4	2.6	2.3	2.4	2.3	7.5
Ce_ppm	6.67	4.54	5.18	3.24	6.54	5.86	6.54	5.95	17.45
Pr_ppm	1.052	0.733	0.736	0.498	1.003	0.936	1.045	0.959	2.469
Nd_ppm	5.35	3.69	3.26	2.51	4.92	4.66	5.23	4.79	10.57
Sm_ppm	1.641	1.27	0.959	0.801	1.553	1.447	1.653	1.449	2.388
Eu_ppm	0.5696	0.3743	0.4067	0.3705	0.5687	0.4896	0.5592	0.4481	0.7769
Gd_ppm	2.239	1.879	1.421	1.185	2.145	2.063	2.247	2.08	2.598
Tb_ppm	0.3975	0.3398	0.2673	0.2092	0.3521	0.3585	0.3956	0.3703	0.4332
Dy_ppm	2.562	2.201	1.893	1.431	2.44	2.349	2.676	2.433	2.806
Ho_ppm	0.5656	0.5047	0.4307	0.3197	0.5319	0.517	0.5803	0.5325	0.6078
Er_ppm	1.701	1.517	1.329	0.979	1.586	1.573	1.75	1.599	1.812
Tm_ppm	0.2473	0.2353	0.2008	0.1411	0.2374	0.2388	0.2659	0.238	0.2651
Yb_ppm	1.73	1.519	1.299	0.935	1.541	1.516	1.717	1.567	1.787
Lu_ppm	2.6	1.8	2.1	1.4	2.6	2.3	2.4	2.3	7.5

	LOW18 CB18	LOW18 CB19	LOW18 CB20	LOW18 CB21	LOW18 CB22	LOW18 CB23	LOW18 CB36	LOW18 CB28	LOW18 CB31
Northing	5483032	5483278	5483297	5483449	5483909	5483757	5481551	5481967	548223
Easting	392866	392755	392557	395242	395824	395777	391768	392036	392070
Rock Type	LOTI tholeiite	LOTI tholeiite	Int MV	LOTI tholeiite	LOTI tholeiite	LOTI tholeiite	Komatiite basalt	Komatiite basalt	Komatiite basalt
SiO2_pct	51.64	54.9	57.47	46.16	51.96	45.57	48.15	48.07	45.81
TiO2_pct	0.92	0.77	0.85	0.74	0.88	0.59	0.57	0.64	0.65

	LOW18 CB18	LOW18 CB19	LOW18 CB20	LOW18 CB21	LOW18 CB22	LOW18 CB23	LOW18 CB36	LOW18 CB28	LOW18 CB31
Al2O3_pct	15.1	15.72	15.95	13.68	15.28	12.93	12.97	14.03	14.15
Fe2O3_pct	11.04	11.61	8.86	10.52	11.62	11.45	11.88	11.82	12.56
MnO_pct	0.159	0.203	0.143	0.183	0.212	0.181	0.189	0.188	0.188
MgO_pct	6.1	4.98	5.29	8.8	5.22	11.64	12.29	11.78	13.52
CaO_pct	9.606	6.694	4.337	8.655	10.638	9.262	9.107	9.415	8.556
Na2O_pct	2.6	3.48	4.81	1.83	1.71	1.46	1.56	1.69	1.2
K2O_pct	0.93	0.15	0.1	0.12	0.12	0.05	0.13	0.14	0.11
P2O5_pct	0.093	0.079	0.076	0.065	0.075	0.046	0.045	0.05	0.048
LOI	0.96	1.41	2.23	8.8	1.92	7.55	2.89	2.88	3.9
Sum	99.2	100	100.16	99.63	99.72	100.85	99.93	100.81	100.85
S_pct	0.126	0.005	0.004	0.01	0.096	0.012	0.007	0.017	0.017
CO2_pct	0.039	0.029	0.481	4.931	0.29	3.861	0.265	0.027	0.16
Ti_ppm	5250	4419	4947	4172	5040	3542	3376	3666	3864
Cr_ppm	335	40	227	538	695	867	1059	855	1060
Co_ppm	43.6	51.7	49.2	69.7	69.5	78.7	78.3	73.1	82.8
Ni_ppm	49	25	79.3	165.1	217.1	279.2	295	273.5	331
Rb_ppm	32.27	0.87	1.84	2.69	0.85	0.84	1.3	2.46	2.55
Sr_ppm	505.5	232.5	259.4	90.7	132.3	71.8	103.8	91.7	106.7
Cs_ppm	7.075	0.07	0.218	0.077	0.072	0.072	0.039	0.084	0.078
Ba_ppm	98	38	78	43	17	23	24	29	38
Sc_ppm	39	33	28	34	39	32	35	34	33
V_ppm	264	228	195	243	271	225	227	232	237
Ta_ppm	0.205	0.145	0.164	0.138	0.194	0.092	0.084	0.097	0.098
Nb_ppm	3.344	2.25	2.54	2.134	2.736	1.465	1.225	1.526	1.548
Zr_ppm	81	70	68	54	67	39	36	40	41
Hf_ppm	2.2	1.94	1.85	1.53	1.88	1.06	1.03	1.15	1.16
Th_ppm	0.55	0.678	0.544	0.314	0.401	0.176	0.179	0.196	0.191
U_ppm	0.183	0.175	0.131	0.078	0.102	0.042	0.049	0.05	0.053
Y_ppm	21.16	19.9	16.44	18.01	22.64	13.58	14.63	14.7	15.41
Cu_ppm	75.9	12.9	<1.4	130.9	79.6	127.6	33.5	73.3	41
Zn_ppm	87.5	111.8	63.1	91.6	88.5	79.6	74.4	75.8	84.2
Mo_ppm	2.6	1.68	0.78	0.23	1.12	0.18	0.18	0.28	0.29
Tl_ppm	0.194	0.004	0.007	0.011	0.006	0.004	0.005	0.008	0.009
Pb_ppm	5.69	1.44	0.82	0.77	0.96	0.44	0.63	0.54	0.58
Sn_ppm	13.15	0.48	0.45	0.9	0.62	0.33	0.28	0.39	0.36
Sb_ppm	1.02	0.04	0.05	<0.04	0.07	<0.04	<0.04	<0.04	<0.04
Ga_ppm	17.26	18.19	13.34	13.73	16.55	11.42	12.23	13.29	13.12
W_ppm	0.31	0.16	0.23	0.15	0.19	0.1	<0.05	0.06	<0.05
Bi_ppm	<0.47	<0.47	<0.47	<0.47	<0.47	<0.47	<0.47	<0.47	<0.47
Be_ppm	0.46	0.42	0.33	0.33	0.33	0.22	0.17	0.17	0.18
Au_ppm	2.2	0.7	<0.6	5.9	1.8	3.7	1.4	2.9	1.2
Pd_ppm	5.98	2.39	1.53	8.56	9.65	9.37	10.34	10.88	12

	LOW18 CB18	LOW18 CB19	LOW18 CB20	LOW18 CB21	LOW18 CB22	LOW18 CB23	LOW18 CB36	LOW18 CB28	LOW18 CB31
Pt_ppm	8.47	2.27	1.95	11.12	11.89	11.3	10.02	12.8	12.58
La_ppm	5.1	6.4	4.8	3.2	4.3	2.1	1.8	2.3	2.3
Ce_ppm	13.33	14.2	11.28	8.56	11.14	5.65	4.43	6.08	6.27
Pr_ppm	2.018	2.007	1.544	1.298	1.818	0.91	0.724	0.97	1.021
Nd_ppm	9.8	8.75	6.87	6.21	8.65	4.5	3.7	4.83	5.01
Sm_ppm	2.829	2.33	1.993	1.963	2.595	1.479	1.251	1.623	1.611
Eu_ppm	0.9523	0.863	0.6161	0.6689	0.8858	0.4841	0.4252	0.5993	0.5702
Gd_ppm	3.546	2.763	2.477	2.656	3.469	2.027	1.975	2.191	2.235
Tb_ppm	0.6027	0.5063	0.439	0.4878	0.6198	0.3603	0.3515	0.4063	0.3994
Dy_ppm	3.824	3.266	2.871	3.166	3.789	2.439	2.475	2.673	2.737
Ho_ppm	0.8286	0.7387	0.633	0.6821	0.8536	0.5279	0.5561	0.5848	0.5783
Er_ppm	2.385	2.246	1.856	2.046	2.566	1.593	1.664	1.729	1.736
Tm_ppm	0.3503	0.3348	0.2688	0.3084	0.4036	0.2321	0.2516	0.2628	0.2558
Yb_ppm	2.35	2.184	1.707	2.002	2.445	1.505	1.675	1.731	1.64
Lu_ppm	5.1	6.4	4.8	3.2	4.3	2.1	1.8	2.3	2.3

	LOW18 CB33	LOW18 CB35	LOW18 CB37	LOW18 CB38	LOW18 CB39	LOW18 CB41	LOW18 CB42	LOW18 CB44	LOW18 CB45
Northing	5482260	5481657	5481462	5481454	5481419	5482917	5482903	5483035	548241
Easting	391310	392100	391629	391484	391357	388860	389132	390008	393690
Rock Type	LOTI tholeiite	Komatiite basalt	LOTI tholeiite	Komatiite basalt	Komatiite basalt	Komatiite basalt	Calc- alkalic MV	LOTI tholeiite	Komatiite basalt
SiO2_pct	51.73	47.03	45.28	47.35	48.33	49.27	49.18	50.11	49.17
TiO2_pct	0.99	0.48	0.48	0.52	0.5	0.66	0.83	0.59	0.59
Al2O3_pct	15.33	11.02	15.33	12.19	12.14	13.56	12.63	15.63	12.83
Fe2O3_pct	14.19	11.49	12.4	12.17	11.63	11.69	10.53	10.58	11.36
MnO_pct	0.23	0.175	0.181	0.197	0.179	0.185	0.217	0.167	0.21
MgO_pct	5.37	16.25	10.84	14.68	14.68	11.1	8.25	7.9	12.65
CaO_pct	9.24	8.812	8.253	8.823	8.613	8.5	12.14	8.376	8.737
Na2O_pct	2.7	1.03	2.8	1.15	1.23	2	2.18	3.34	2.08
K2O_pct	0.54	0.08	0.13	0.11	0.08	0.08	0.97	0.49	0.09
P2O5_pct	0.067	0.04	0.052	0.041	0.036	0.051	0.328	0.048	0.044
LOI	0.64	3.9	5.07	3.5	3.53	3.53	3.22	3.56	3.01
Sum	101.07	100.59	100.91	100.91	101.15	100.7	100.59	100.86	100.87
S_pct	0.006	0.006	0.01	0.006	0.005	0.004	0.004	0.01	0.006
CO2_pct	0.377	0.194	1.974	0.074	<0.023	0.487	1.949	1.219	0.039
Ti_ppm	5880	2739	2850	2988	2880	3720	4935	3439	3396
Cr_ppm	48	2011	716	1330	1546	525	386	337	773
Co_ppm	50.6	79.6	70.8	80.4	72.4	66.7	49.8	52.7	69.3
Ni_ppm	22.9	519.9	245.8	380.7	326.9	150.9	75.4	104.4	264.7
Rb_ppm	15.18	0.96	1.5	2.13	0.62	0.88	42.84	17.17	1.41

	LOW18 CB33	LOW18 CB35	LOW18 CB37	LOW18 CB38	LOW18 CB39	LOW18 CB41	LOW18 CB42	LOW18 CB44	LOW18 CB45
Sr_ppm	135.6	97.5	139.1	64.7	57	131.6	316.1	163	99.6
Cs_ppm	0.795	0.059	0.052	0.093	0.054	0.045	0.761	0.731	0.045
Ba_ppm	212	33	29	20	22	20	592	186	24
Sc_ppm	43	32	29	33	31	35	32	33	30
V_ppm	356	201	222	207	204	240	255	240	212
Ta_ppm	0.108	0.054	0.059	0.072	0.059	0.091	0.141	0.084	0.085
Nb_ppm	1.796	0.835	0.915	1.106	0.91	1.429	2.584	1.31	1.401
Zr_ppm	51	24	29	32	29	42	75	38	37
Hf_ppm	1.42	0.7	0.84	0.92	0.86	1.17	2	1.08	1.03
Th_ppm	0.442	0.115	0.115	0.153	0.115	0.184	2.249	0.205	0.173
U_ppm	0.111	0.034	0.033	0.042	0.031	0.055	0.607	0.057	0.049
Y_ppm	18.8	11.86	12.45	13.21	12.37	15.69	18.11	15.8	13.65
Cu_ppm	15.4	43.5	<1.4	42.6	51.2	49.4	3.6	34.8	20.7
Zn_ppm	91.5	69.2	102.7	76.5	66.6	68.9	75.6	57.5	97
Mo_ppm	1.43	0.18	0.13	0.19	0.11	0.14	0.18	0.47	0.26
Tl_ppm	0.062	0.003	0.005	0.006	0.003	0.003	0.148	0.05	0.005
Pb_ppm	0.92	0.35	1.39	0.45	0.42	0.83	3.65	0.92	0.62
Sn_ppm	0.3	0.24	0.68	0.23	0.25	0.34	0.63	0.32	0.35
Sb_ppm	<0.04	0.04	<0.04	<0.04	0.04	<0.04	<0.04	<0.04	<0.04
Ga_ppm	17.95	10.83	14.35	11.73	12.15	13.37	12.2	15.65	11.69
W_ppm	<0.05	<0.05	0.15	0.06	<0.05	0.05	0.12	0.12	0.06
Bi_ppm	<0.47	<0.47	<0.47	<0.47	<0.47	<0.47	<0.47	<0.47	<0.47
Be_ppm	0.31	0.12	0.36	0.14	0.13	0.25	0.77	0.24	0.26
Au_ppm	0.9	1.7	<0.6	1.1	1.4	0.6	<0.6	2.5	0.7
Pd_ppm	<0.14	6.66	3.37	8.21	9.48	5.74	3.21	8.58	10
Pt_ppm	0.27	6.75	8.08	9.37	10.53	9.13	3.96	11.12	11.11
La_ppm	4.5	1	1.1	1.6	1.2	2.1	16.4	2.5	2.2
Ce_ppm	10.29	2.8	3	4.13	3.2	5.56	37.51	5.94	5.62
Pr_ppm	1.496	0.478	0.52	0.658	0.523	0.921	5.237	0.906	0.866
Nd_ppm	6.71	2.41	2.58	3.26	2.64	4.45	21.69	4.59	4.26
Sm_ppm	1.97	0.971	1.009	1.15	1.093	1.604	4.75	1.492	1.47
Eu_ppm	0.7684	0.3679	0.6369	0.4348	0.4106	0.6048	1.3939	0.6262	0.4373
Gd_ppm	2.518	1.569	1.552	1.757	1.642	2.242	4.292	2.161	1.919
Tb_ppm	0.4369	0.2994	0.3042	0.3216	0.3	0.3829	0.5784	0.3883	0.3413
Dy_ppm	3.122	2.052	2.077	2.159	2.159	2.702	3.333	2.6	2.299
Ho_ppm	0.6971	0.4551	0.453	0.4851	0.4626	0.5948	0.6724	0.5913	0.5076
Er_ppm	2.076	1.336	1.385	1.526	1.445	1.829	1.942	1.766	1.536
Tm_ppm	0.3208	0.2013	0.2071	0.223	0.2206	0.2667	0.272	0.2653	0.2305
Yb_ppm	2.161	1.357	1.396	1.478	1.45	1.792	1.799	1.692	1.502
Lu_ppm	4.5	1	1.1	1.6	1.2	2.1	16.4	2.5	2.2

	LOW18 CB46	LOW18 CB48
Northing	5482760	5482382
Easting	393862	390626
Rock Type	Komatiite basalt	LOTI tholeiite
SiO2_pct	42.69	51.16
TiO2_pct	0.59	0.81
Al2O3_pct	10.69	14.64
Fe2O3_pct	14.14	11.26
MnO_pct	0.21	0.183
MgO_pct	18.98	8.02
CaO_pct	7.158	10.977
Na2O_pct	0.07	1.73
K2O_pct	0.04	0.15
P2O5_pct	0.058	
LOI	5.5	1.28
Sum	100.31	100.32
S_pct	0.003	0.052
CO2_pct	0.041	0.125
Ti_ppm	3416	4859
Cr_ppm	1440	281
Co_ppm	100.4	51.1
Ni_ppm	543.8	81.7
Rb_ppm	0.62	0.82
Sr_ppm	4	96.3
Cs_ppm	0.074	0.039
Ba_ppm	<8	38
Sc_ppm	26	43
V_ppm	191	287
Ta_ppm	0.121	0.118
Nb_ppm	2.09	1.981
Zr_ppm	48	51
Hf_ppm	1.29	1.36
Th_ppm	0.304	0.242
U_ppm	0.113	0.063
Y_ppm	15.54	19
Cu_ppm	<1.4	52.7
Zn_ppm	102.8	70.2
Mo_ppm	0.16	0.73
Tl_ppm	0.002	0.012

	LOW18 CB46	LOW18 CB48
Pb_ppm	0.24	1.1
Sn_ppm	0.47	0.44
Sb_ppm	<0.04	<0.04
Ga_ppm	12.94	15.01
W_ppm	0.08	0.23
Bi_ppm	<0.47	<0.47
Be_ppm	0.22	0.26
Au_ppm	<0.6	1.4
Pd_ppm	5.56	12.28
Pt_ppm	6.82	15.2
La_ppm	1.9	2.8
Ce_ppm	5.07	7.69
Pr_ppm	0.825	1.227
Nd_ppm	4.24	6.19
Sm_ppm	1.553	2.047
Eu_ppm	0.5096	0.7316
Gd_ppm	2.169	2.678
Tb_ppm	0.3894	0.4681
Dy_ppm	2.532	3.219
Ho_ppm	0.5593	0.6997
Er_ppm	1.694	2.042
Tm_ppm	0.2491	0.3013
Yb_ppm	1.637	2.044
Lu_ppm	1.9	2.8

Appendix C

Samarium-Neodymium Isotope Data

Sample	Nd (ppm)	Sm (ppm)	Nd ¹⁴³ /Nd ¹⁴⁴	Nd ¹⁴³ /Nd ¹⁴⁴ (initial)	Sm ¹⁴⁷ /Nd ¹⁴⁴	ε _{Nd}	Age	Model Age (TDM2)
CBO-28	1.68	0.64	0.513397	0.50924	0.2318	2.622	2719	2061
CBO-62	1.31	0.43	0.512725	0.50916	0.1974	1.074	2719	3960
CBO-62 (DUP)	1.30	0.42	0.512736	0.50923	0.1967	2.391	2719	3701
CBO-68	2.11	0.73	0.512955	0.50919	0.2109	1.636	2719	
CBO-69	1.97	0.79	0.513596	0.50924	0.2435	2.656	2719	2264
CBO-92	2.69	0.84	0.512606	0.50922	0.1891	2.143	2719	3358
CBO-96	3.42	1.26	0.513183	0.50919	0.2233	1.499	2719	519
LOW17CB10	11.55	1.92	0.511005	0.50920	0.1003	1.831	2719	2868
LOW17CB14	28.66	5.10	0.511126	0.50920	0.1075	1.711	2719	2889
LOW17CB22	30.07	6.45	0.511564	0.50924	0.1297	2.523	2719	2863
LOW17CB31	79.49	13.37	0.511027	0.50922	0.1017	1.533	2694	2874
LOW18CB41	4.86	1.64	0.512869	0.50921	0.2040	1.938	2719	4411
LOW18CB41 (DUP)	5.06	1.70	0.512867	0.50919	0.2030	1.588	2719	4029
LOW17CB91	8.00	2.77	0.512914	0.50916	0.2094	0.946	2719	

Appendix D

Mineral Chemistry

Major element compositions of primary and secondary minerals in ultramafic samples.

Mineral	Enstatite	Tremolite	Anthophyllite	Chlorite	Serpentine	Chromite	Talc
No. of analyses	33	112	62	25	6	2	8
SiO ₂	58.2	55.5	55.4	28.7	39.5		59.4
TiO ₂						1.4	
Al ₂ O ₃	1.3	1.3	rare	17		7.1	0.38
FeO	14.4	6	17	9.9	16	47	6.3
MnO	0.5	0.28	0.54		0.38		
MgO	25.4	20.7	22.4	26	26.4	0.7	26.7
CaO	0.6	12.4	0.76		0.5		
K ₂ O							
Na ₂ O		0.4					
Cr ₂ O ₃		rare		0.78		37.5	
Total	100.4	96.6	96.1	82.4	82.8	93.7	92.8

	LOW17CB043									
Site	1									2
Point	A	B	C	D	E	F	G	H	I	A
Mineral	Amph	Amph	Amph	Amph	Amph	Amph	Amph	Amph	Amph	Amph
K2O										
MgO	17.66	17.23	18.08	18.28	18.91	19.63	19.37	23.02	18.38	17.99
Al2O3	1.21	1.34	0.78	2.79	1.08			16.53	3.26	1.5
SiO2	48.21	47.69	49.03	49.48	51.97	49.78	49.65	25.24	46.66	49.49
CaO	10.11	10.74	11.31	9.16	11.31	0.53	0.69		10.28	11.28
FeO	6.51	5.52	5.11	8.64	6.23	15.57	15.91	8.83	6.39	5.55
Na2O	0.31			0.57					0.3	
Cr2O3				0.3				0.88	0.45	
MnO						0.27	0.36			
TiO2										
V2O5										
ZnO										
NiO										
MoO3										
CoO										
CuO										
SO3										
P2O5										
IrO2										
La2O3										
Total	84.01	82.52	84.31	89.22	89.5	85.78	85.98	74.5	85.72	85.81
Si	7.731	7.798	7.726	7.754	7.763	8.005	8.001	8.005	8.015	7.732
Al iv	0.269	0.202	0.274	0.246	0.166					0.215
Al vi	0.062	0.106	0.026	0.040					0.047	
Ti										
Cr										
Fe3+	0.352	0.156	0.404	0.408	0.829					0.859
Fe2+	0.442	0.546	0.341	0.352		2.119	2.077	2.130	2.030	
Mn						0.049	0.046	0.050	0.050	
Mg	4.144	4.192	4.229	4.200	4.258	4.695	4.733	4.673	4.709	4.241
Ni										
Zn										
Ca	1.880	1.927	1.863	1.851	1.724	0.127	0.142	0.137	0.110	1.685
Na	0.095	0.086	0.119	0.096						
K										
Ba										
Sr										
Pb										
F										
Cl										
OH*	2.000	2.000	2.000	2.000	2.000	2.000	2.000	2.000	2.000	2.000
O	23.000	23.000	23.000	23.000	23.000	23.000	23.000	23.000	23.000	23.000
Total	16.975	17.013	16.981	16.947	16.740	16.995	16.999	16.995	16.961	16.731

	LOW17CB043									
Site	2									
Point	B	C	D	E	F	G	H	I	J	K
Mineral	Chl	Amph	Chl	Chl	Chl	Chl	Amph	Chl	Amph	Amph
K2O										
MgO	17.26	19.05	17.42	18.79	17.55	16.85	19.15	18.1	19.42	21.91
Al2O3	0.74	1.22	1.43	0.83	0.83	0.71	1.78	1		
SiO2	47.1	51.78	47.95	51.04	47.66	46.85	51.61	50.29	49.64	55.19
CaO	10.74	10.53	10.7	11.1	10.28	10.51	10.25	11.38	0.95	1.61
FeO	5.2	6.88	5.75	5.85	5.93	5.45	7.47	5.54	15.78	16.19
Na2O							0.3			
Cr2O3										
MnO	0.24								0.51	0.4
TiO2										
V2O5										
ZnO										
NiO										
MoO3										
CoO										
CuO										
P2O5										
IrO2										
La2O3										
Total	81.28	89.46	83.25	87.61	82.25	80.37	90.56	86.31	86.3	95.3
Si	4.0563	7.732	4.0318	4.0781	4.0562	4.0805	7.631	4.0787	7.970	8.001
Al iv	0.085	0.215	0.1603	0.0884	0.0942	0.0825	0.310	0.1081		
Al vi										
Ti	0		0	0	0	0		0		
Cr	0		0	0	0	0		0		
Fe3+	0.8957	0.859	0.967	0.9348	1.0094	0.9494	0.924	0.8986		
Fe2+									2.119	1.963
Mn	0.0413		0	0	0	0		0		0.049
Mg	2.9729	4.241	2.9295	3.0026	2.9872	2.9352	4.221	2.9359	0.069	4.735
Ni	0		0	0	0	0		0	4.648	
Zn	0		0	0	0	0		0		
Ca	1.8499	1.685	1.7994	1.7738	1.7498	1.8308	1.624	1.8459		0.250
Na	0		0	0	0	0	0.086	0		
K	0		0	0	0	0		0		
Ba	0		0	0	0	0		0	0.163	
Sr										
Pb										
F	0		0	0	0	0		0		
Cl	0		0	0	0	0		0		
OH*	8	2.000	8	8	8	8	2.000	8		2.000
O	10	23.000	10	10	10	10	23.000	10	23	23.000
Total	17.901	16.731	17.888	17.878	17.897	17.878	16.795	17.867	16.970	16.999

	LOW17CB043									
Site	2									3
Point	L	M	N	O	P	Q	R	S	T	A
Mineral	Amph	Amph	Amph	Ilm	Hem	Chl	Chl	Amph	Amph	Amph
K2O										
MgO	21.22	21.42	21.27		1.9	25.85	25.41	22.05	22.04	20.04
Al2O3						18.03	17.27	0.48		1.5
SiO2	53.69	53.31	53.55		4.39	27.98	27.76	54.79	55.35	55.21
CaO	0.71	0.93	0.8					0.55	0.76	11.88
FeO	16.77	16.36	17.04	40.53	68.99	9.59	9.33	16.75	17.1	6.91
Na2O										
Cr2O3						1.09	0.98			
MnO	0.37	0.5	0.44	6.08				0.42	0.36	
TiO2				53.37						
V2O5				0.23						
ZnO										
NiO										
MoO3										
CoO										
CuO										
SO3										
P2O5										
IrO2										
La2O3										
Total	92.76	92.52	93.1	100.21	75.28	82.54	80.75	95.04	95.61	95.54
Si	8.013	7.969	7.974	0	0.0875	0.0808	1.7538	7.963	8.008	7.748
Al iv				0	0	0	1.5068	0.037		0.248
Al vi								0.045		
Ti				0.8007	0	0	0			
Cr				1.0676	0	0	0			
Fe3+		0.062	0.053	1.2161	2.7493	0.3532	1.1696			0.683
Fe2+	2.093	1.983	2.069					2.036	2.069	0.128
Mn	0.047	0.063	0.055	0.1824	0	0	0	0.052	0.044	
Mg	4.721	4.773	4.721	0	0.0757	0.9521	3.1854	4.777	4.754	4.193
Ni				0	0	0	0			
Zn				0	0	0	0			
Ca	0.114	0.149	0.128	0	0	0	0	0.086	0.118	1.786
Na				0	0	0	0			
K				0	0	0	0			
Ba				0	0	0	0			
Sr										
Pb										
F				0	0	0	0			
Cl				0	0	0	0			
OH*	2.000	2.000	2.000			8	8	2.000	2.000	2.000
O	23.000	23.000	23.000	3	3	10	10	23.000	23.000	23.000
Total	16.987	17.000	17.000	3.2669	2.9125	9.3862	15.616	16.996	16.992	16.786

	LOW17CB043									
Site	3									
Point	B	C	D	E	F	G	H	I	J	K
Mineral	Amph	Amph	Chl	Chl	Amph	Amph	Amph	Ilm	Amph	Chl
K2O										
MgO	20.13	18.98	18.6	19.06	19.37	21.43	21.82		19.34	25.65
Al2O3	1.5	2.03	1.3	1.65	1.44		0.3		1.79	17.55
SiO2	55.2	53.05	51.26	51.48	54.11	54.07	54.64		52.93	28.22
CaO	12.14	12.21	10.94	10.22	12.21	0.63	0.77		12.18	
FeO	6.42	6.16	6.46	7.35	6.47	17.16	17.53	40.73	6.14	9.58
Na2O		0.28								
Cr2O3				0.23						0.95
MnO							0.46	6.06		
TiO2								53.8		
V2O5										
ZnO										
NiO										
MoO3										
CoO										
CuO										
SO3										
P2O5										
IrO2										
La2O3										
Total	95.39	92.71	88.56	89.99	93.6	93.29	95.52	100.59	92.38	81.95
Si	7.771	7.759	1.5673	2.8554	7.808	7.999	7.927	0	7.731	1.742
Al iv	0.229	0.241	1.3001	0.0966	0.192		0.051	0	0.269	1.4444
Al vi	0.020	0.108			0.053				0.039	
Ti			0	0				0.8023		0
Cr			0	0				1.0697		0
Fe3+	0.547	0.227	1.0535	0.7197	0.364	0.001	0.095	0.2192	0.418	5.0284
Fe2+	0.208	0.526			0.416	2.122	2.032		0.332	
Mn			0	0		0.051	0.057	0		0.7481
Mg	4.225	4.138	2.8692	2.0722	4.167	4.726	4.719	0.5684	4.211	0
Ni			0	0				0		0
Zn			0	0				0		0
Ca	1.831	1.913	1.2353	1.1386	1.888	0.100	0.120	0	1.906	0
Na		0.079	0	0				0		0
K			0	0				0		0
Ba			0	0				0		0
Sr										
Pb										
F			0	0				0		0
Cl			0	0				0		0
OH*	2.000	2.000	8	8	2.000	2.000	2.000		2.000	8
O	23.000	23.000	10	10	23.000	23.000	23.000	3	23.000	10
Total	16.831	16.993	16.025	14.882	16.888	17.000	17.000	2.6596	16.906	16.963

	LOW17CB043									
Site	3			4						
Point	L	M	N	A	B	C	D	E	F	G
Mineral	Chl	Amph	Hem	Amph	Amph	Amph	Amph	Amph	Chl	Hem
K2O										
MgO	25.92	19.84	5.13	20.13	20.96	19.67	20.07	19.1	18.73	0.86
Al2O3	16.97	1.97	1.91	1.34	1.45	1.2	1.36	1.05	0.87	
SiO2	28.96	53.45	7.74	55.33	56.11	53.19	55.45	51.69	50.78	5.37
CaO		10.08	0.22	12.25	12.54	11.53	12.44	10.92	11.37	0.21
FeO	9.21	8.04	74.93	6.14	6.48	6.29	5.96	6.37	5.57	81.01
Na2O				0.28						
Cr2O3	0.67	0.31				0.29				
MnO					0.26					
TiO2			0.37							0.37
V2O5										
ZnO										
NiO										
MoO3										
CoO										
CuO										
SO3										
P2O5										
IrO2										
La2O3										
Total	81.73	93.69	90.3	95.47	97.8	92.17	95.28	89.13	87.32	87.82
Si	1.7863	7.626	0.1291	7.814	7.702	7.733	7.839	7.750	2.9077	0.0921
Al iv	1.3957	0.331	0.0425	0.186	0.235	0.206	0.161	0.186	0.0664	0
Al vi				0.037			0.066			
Ti	0		0						0	0
Cr	0	0.035	0			0.033			0	0
Fe3+	1.1818	0.959	0.3072	0.366	0.673	0.703	0.327	0.799	0.6379	2.7791
Fe2+				0.360	0.071	0.062	0.378			
Mn	0		0		0.030				0	0
Mg	3.1643	4.220	0.8647	4.238	4.289	4.263	4.230	4.269	2.145	0.0295
Ni	0		0						0	0
Zn	0		0						0	0
Ca	0	1.541	0.0073	1.854	1.844	1.796	1.884	1.754	1.3021	0.0072
Na	0		0	0.077					0	0
K	0		0						0	0
Ba	0		0						0	0
Sr										
Pb										
F	0		0						0	0
Cl	0		0						0	0
OH*	8	2.000		2.000	2.000	2.000	2.000	2.000	8	
O	10	23.000	3	23.000	23.000	23.000	23.000	23.000	10	3
Total	16.528	16.712	11.351	16.930	16.844	16.796	16.884	16.758	15.059	2.9079

	LOW17CB043									
Site	4								5	
Point	H	I	J	K	L	M	N	O	A	B
Mineral	Amph	Amph	Amph	Amph	Amph	Chl	Chl	Amph	Amph	Amph
K2O										
MgO	22.01	22.23	21.61	21.46	18.49	25.5	25.29	19.22	20.31	20.49
Al2O3		0.35			3.35	18.13	17.56	1.94	1.16	1.61
SiO2	55.16	55.22	54.6	54.13	51.07	28.05	28.1	53.09	56.03	56.08
CaO	0.69	0.55	0.81	1.02	12.22			12.09	12.18	12.54
FeO	16.97	16.83	16.86	16.71	6.71	9.75	9.42	6.48	6.36	6.2
Na2O					0.51					
Cr2O3					0.34	1.04	0.96			
MnO	0.45	0.47	0.47	0.41						
TiO2										
V2O5										
ZnO										
NiO										
MoO3										
CoO										
CuO										
SO3										
P2O5										
IrO2										
La2O3										
Total	95.28	95.65	94.35	93.73	92.69	82.47	81.33	92.82	96.04	96.92
Si	8.007	7.975	8.010	7.997	7.505	1.7223	1.7482	7.716	7.833	7.780
Al iv		0.025			0.495	1.4843	1.4566	0.284	0.167	0.220
Al vi		0.034			0.085			0.048	0.024	0.043
Ti						0	0			
Cr					0.040	0	0			
Fe3+				0.007	0.377	1.1973	1.1721	0.471	0.495	0.449
Fe2+	2.060	2.033	2.068	2.058	0.448			0.317	0.249	0.270
Mn	0.055	0.057	0.058	0.051		0	0			
Mg	4.763	4.786	4.726	4.726	4.051	3.1315	3.1467	4.164	4.233	4.238
Ni						0	0			
Zn						0	0			
Ca	0.107	0.085	0.127	0.161	1.924	0	0	1.883	1.824	1.864
Na					0.145	0	0			
K						0	0			
Ba						0	0			
Sr										
Pb										
F						0	0			
Cl						0	0			
OH*	2.000	2.000	2.000	2.000	2.000	8	8	2.000	2.000	2.000
O	23.000	23.000	23.000	23.000	23.000	10	10	23.000	23.000	23.000
Total	16.993	16.995	16.990	17.000	17.069	15.536	15.524	16.883	16.824	16.864

LOW17CB043										
Site	5									
Point	C	D	E	F	G	H	I	J	K	L
Mineral	Amph	Amph	Amph	Amph	Amph	Ilm	Chl	Amph	Chl	Amph
K2O										
MgO	20.99	20.33	20.73	20.1	21.57		25.58	21.72	26.65	21.19
Al2O3	0.66	0.7	1.79	0.91			17.77		18.66	1.57
SiO2	56.36	55.11	56.26	54.66	54.62		28.15	54.73	28.67	56.49
CaO	10.03	11.54	12.34	12.36	0.76			0.98		11.98
FeO	8.62	6.51	7.05	5.77	17.2	45.85	9.71	17.26	9.79	7.32
Na2O										
Cr2O3							1.07		1.09	
MnO					0.43	2.79		0.4		
TiO2						53.81				
V2O5										
ZnO										
NiO										
MoO3										
CoO										
CuO										
SO3										
P2O5										
IrO2										
La2O3										
Total	96.66	94.19	98.17	93.8	94.58	102.45	82.28	95.09	84.86	98.55
Si	7.774	7.814	7.685	7.850	8.004	0	1.7332	7.976	1.7112	7.673
Al iv	0.107	0.117	0.288	0.150		0	1.4588		1.485	0.251
Al vi				0.004						
Ti						0.7878	0		0	
Cr						1.0505	0		0	
Fe3+	0.994	0.749	0.730	0.343		1.3426	1.1957	0.049	1.1687	0.829
Fe2+		0.023	0.076	0.350	2.108			2.055		
Mn					0.053	0.0817	0	0.049	0	
Mg	4.316	4.297	4.221	4.303	4.712	0	3.1499	4.719	3.1813	4.291
Ni						0	0		0	
Zn						0	0		0	
Ca	1.482	1.753	1.806	1.902	0.119	0	0	0.153	0	1.743
Na						0	0		0	
K						0	0		0	
Ba						0	0		0	
Sr										
Pb										
F						0	0		0	
Cl						0	0		0	
OH*	2.000	2.000	2.000	2.000	2.000		8	2.000	8	2.000
O	23.000	23.000	23.000	23.000	23.000	3	10	23.000	10	23.000
Total	16.675	16.753	16.806	16.902	16.996	3.2626	15.537	17.000	15.546	16.787

	LOW17CB043									
Site	5						6			
Point	M	N	O	P	Q	R	A	B	C	D
Mineral	Amph	Ilm	Amph	Chr	Chr	Chl	Amph	Amph	Amph	Amph
K2O										
MgO	19.3		21.68	0.62	0.76	25.93	19.88	19.67	19.94	19.88
Al2O3	0.87		0.3	6.4	7.71	18.6	2.01	1.83	1.79	1.71
SiO2	53.66		55.24		0.41	27.83	55.29	54.55	54.3	54.71
CaO	12.3		0.79				12.55	12.58	12.22	12.19
FeO	5.97	42.86	17.53	50.76	43.4	9.84	6.79	5.87	6.26	6.41
Na2O							0.35	0.31	0.43	0.35
Cr2O3	0.27			34.69	40.22	1.17				
MnO		5.18	0.48							
TiO2		54.55		1.84	0.92					
V2O5				0.8						
ZnO				0.92	1.15					
NiO										
MoO3										
CoO										
CuO										
SO3										
P2O5										
IrO2										
La2O3										
Total	92.37	102.59	96.02	96.03	94.57	83.37	96.87	94.81	94.94	95.25
Si	7.769	0	7.978	0	0.0088	1.6691	7.731	7.798	7.726	7.754
Al iv	0.148	0	0.022	0.181	0.2201	1.4873	0.269	0.202	0.274	0.246
Al vi			0.030				0.062	0.106	0.026	0.040
Ti		0.7976		0.039	0.0197	0				
Cr	0.031	0		1.4713	1.7221	0.1403				
Fe3+	0.467	1.2533		2.1529	1.8583	1.1803	0.352	0.156	0.404	0.408
Fe2+	0.419		2.117				0.442	0.546	0.341	0.352
Mn		0.1515	0.059	0	0	0				
Mg	4.166	0	4.668	0.0263	0.0325	3.1102	4.144	4.192	4.229	4.200
Ni		0		0	0	0				
Zn		0		0	0	0				
Ca	1.908	0	0.122	0	0	0	1.880	1.927	1.863	1.851
Na		0		0	0	0	0.095	0.086	0.119	0.096
K		0		0	0	0				
Ba		0		0	0	0				
Sr										
Pb										
F		0		0	0	0				
Cl		0		0	0	0				
OH*	2.000		2.000			8	2.000	2.000	2.000	2.000
O	23.000	3	23.000	4	4	10	23.000	23.000	23.000	23.000
Total	16.908	2.2024	16.996	3.8705	3.8615	15.5873	16.975	17.013	16.981	16.947

LOW17CB043										
Site	6									
Point	E	F	G	H	I	J	K	L	M	N
Mineral	Amph	Ilm	Amph	Amph	Amph	Amph	Ilm	Chl	Ilm	Amph
K2O										
MgO	20.63		21.6	21.99	21.59	22.39		26.17		21.95
Al2O3	1.02					0.28		17.8		4.6
SiO2	56.07		54.9	55.42	55.13	56.82		28.71	0.46	49.52
CaO	11.62		0.81	0.92	0.88	0.73			0.43	5.19
FeO	7.16	43.29	17.38	17.2	17.54	17.21	43.37	9.49	40.32	11.25
Na2O										
Cr2O3								0.94		
MnO		3.52	0.4	0.38	0.41	0.42	4.39		7.42	
TiO2		53.32					54.47		54.07	
V2O5							0.45			
ZnO										
NiO										
MoO3										
CoO										
CuO										
SO3										
P2O5										
IrO2										
La2O3										
Total	96.5	100.13	95.09	95.91	95.55	97.85	102.68	83.11	102.7	92.51
Si	7.763	0	8.005	8.001	8.005	8.015	0	1.747	0.0067	7.237
Al iv	0.166	0					0	1.4442	0	0.763
Al vi						0.047				0.030
Ti		0.7988					0.7992	0	0.793	
Cr		0					0	0	0	
Fe3+	0.829	1.297					1.2727	1.1549	1.1828	0.733
Fe2+			2.119	2.077	2.130	2.030				0.642
Mn		0.1055	0.049	0.046	0.050	0.050	0.1288	0	0.2177	
Mg	4.258	0	4.695	4.733	4.673	4.709	0	3.1849	0	4.782
Ni		0					0	0	0	
Zn		0					0	0	0	
Ca	1.724	0	0.127	0.142	0.137	0.110	0	0	0	0.813
Na		0					0	0	0	
K		0					0	0	0	
Ba		0					0	0	0	
Sr										
Pb										
F		0					0	0	0	
Cl		0					0	0	0	
OH*	2.000		2.000	2.000	2.000	2.000		8		2.000
O	23.000	3	23.000	23.000	23.000	23.000	3	10	3	23.000
Total	16.740	2.2012	16.995	16.999	16.995	16.961	2.2008	15.531	2.2002	17.000

LOW17CB062										
Site	1								2	
Point	1	2	3	4	6	7	8	9	12	13
Mineral	Mt	Mt	Px	Px	Ilm	Mt	Mt	Srp	Px	Amph
K2O										
MgO		0.92	25.02	25.66	1.32	3.98	14.32	13.1	24.88	22.85
Al2O3						1.37	5.41			0.54
SiO2		1.89	57.54	58.77		3.32	9.95	38.89	57.82	57.68
CaO			0.64	0.76				1.49	0.79	11.13
FeO	89.57	84.64	14.39	14.49	45.91	91.01	77.89	21.3	14.18	5.8
Na2O										
Cr2O3	5.33									
MnO			0.53	0.53	1.93				0.37	
TiO2	0.59				55.25		0.91			
V2O5	0.42									
ZnO										
NiO		0.79						1.01		
MoO3		0.63								
CoO										
CuO										
SO3										
P2O5										
IrO2										
La2O3										
Total	95.91	88.87	98.12	100.21	104.41	99.68	108.48	75.79	98.04	98
Si	0	0.0432	1.759	1.759	0	0.0666	0.1834	1.3001	1.769	7.823
Al iv	0	0			0	0.0367	0.133	0		0.086
Al vi										
Ti	0.0124	0			0.7937	0	0.0168	0		
Cr	0.2233	0			0	0	0	0		
Fe3+	3.752	3.8715	0.880	0.868	1.3191	3.6521	2.8721	1.4242	0.868	0.658
Fe2+										
Mn	0	0	0.032	0.032	0.0555	0	0	0	0.023	
Mg	0	0.0421	1.530	1.536	0.0379	0.1597	0.528	0.8759	1.523	4.620
Ni	0	0			0	0	0	0		
Zn	0	0			0	0	0	0		
Ca	0	0	0.039	0.046	0	0	0	0.0996	0.048	1.617
Na	0	0			0	0	0	0		
K	0	0			0	0	0	0		
Ba	0	0			0	0	0	0		
Sr										
Pb										
F	0	0			0	0	0	0		
Cl	0	0			0	0	0	0		
OH*								4		2.000
O	4	4	6.000	6.000	3	4	4	5	6.000	23.000
Total	3.9876	3.9568	4.241	4.241	2.2063	3.9151	3.7333	7.6999	4.231	16.805

LOW17CB062										
Site	2								3	
Point	14	15	16	18	19	21	22	23	25	26
Mineral	Amph	Chl	Amph	Chl	Mt	Amph	Mt	Px	Chl	Chl
K2O										
MgO	21.31	30.14	22.44	30.3	3.47	28.57	0.65	26.17	30.2	30.13
Al2O3	2.41	17.45	1.64	15.42				1	14.86	15.93
SiO2	55.36	31.14	56.51	31.77	6.94	50.17	2.43	56.74	32.78	31.6
CaO	12.93		11.15			1.51		0.68		
FeO	5.18	7.22	6.33	6.82	85.77	12.21	86.32	14.16	7.45	6.78
Na2O	0.54		0.44							
Cr2O3		0.57	0.33	0.45					0.27	0.47
MnO						0.31		0.52		
TiO2										
V2O5										
ZnO										
NiO							4.33			
MoO3										
CoO										
CuO										
SO3							4.77			
P2O5										
IrO2										
La2O3										
Total	97.73	86.52	98.84	84.76	96.18	92.77	98.5	99.27	85.56	84.91
Si	7.632	1.5656	7.642	1.8741	0.1443	7.206	0.0544	1.715	1.9156	1.8608
Al iv	0.368	1.1698	0.261	1.2128	0		0	0.040	1.1579	1.2507
Al vi	0.023									
Ti		0		0	0		0		0	0
Cr		0.0573	0.035	0.0531	0		0		0.0316	0.0554
Fe3+	0.381	0.726	0.716	0.8046	3.5671	1.467	3.8622	0.856	0.8707	0.7985
Fe2+	0.216									
Mn		0		0	0	0.038	0	0.031	0	0
Mg	4.379	3.0307	4.524	3.5748	0.1443	6.118	0.0291	1.582	3.5297	3.5485
Ni		0		0	0		0		0	0
Zn		0		0	0		0		0	0
Ca	1.910	1.3002	1.616	0	0	0.232	0	0.041	0	0
Na	0.144	0	0.115	0	0		0		0	0
K		0		0	0		0		0	0
Ba		0		0	0		0		0	0
Sr										
Pb										
F		0		0	0		0		0	0
Cl		0		0	0		0		0	0
OH*	2.000	8	2.000	8		2.000			8	8
O	23.000	10	23.000	10	4	23.000	4	6.000	10	10
Total	17.054	15.85	16.909	15.519	3.8557	17.060	3.9456	4.265	15.505	15.514

LOW17CB062										
Site	3									
Point	27	28	29	30	31	32	33	34	36	38
Mineral	Amph	Px	Amph	Amph	Amph	Px	Amph	Px	Amph	Px
K2O										
MgO	21.77	25.24	21.34	29.83	21.61	24.63	22.75	24.87	14.79	25.69
Al2O3	1.43		2.73	11.61	1.63		1.45			
SiO2	56.59	58.74	56.32	40.49	56.35	58.35	58.6	57.78	43.47	58.26
CaO	13.09	0.75	13.01		12.89	0.87	12.68	0.73	1.75	0.39
FeO	4.58	14.49	5.41	9.08	4.82	14.06	5.13	14.84	25.01	13.98
Na2O			0.57		0.33		0.3			
Cr2O3				0.32						
MnO		0.7				0.74		0.62		0.63
TiO2										
V2O5										
ZnO										
NiO									0.91	
MoO3										
CoO										
CuO										
SO3										
P2O5										
IrO2										
La2O3										
Total	97.46	99.92	99.38	91.33	97.63	98.65	100.91	98.84	85.93	98.95
Si	7.780	1.764	7.637	5.904	7.750	1.774	7.746	1.754	7.359	1.766
Al iv	0.220		0.363	1.995	0.250		0.226			
Al vi	0.012		0.073		0.015					
Ti										
Cr				0.037						
Fe3+	0.352	0.870	0.360	1.107	0.348	0.855	0.567	0.901	1.236	0.848
Fe2+	0.174		0.253		0.207				2.183	
Mn		0.042				0.045		0.038		0.038
Mg	4.462	1.516	4.314	6.484	4.431	1.498	4.483	1.510	3.766	1.558
Ni									0.126	
Zn										
Ca	1.928	0.045	1.890		1.900	0.053	1.796	0.044	0.330	0.024
Na			0.150		0.088		0.077			
K									0.045	
Ba										
Sr										
Pb										
F										
Cl										
OH*	2.000		2.000	2.000	2.000		2.000		2.000	
O	23.000	6.000	23.000	23.000	23.000	6.000	23.000	6.000	23.000	6.000
Total	16.928	4.236	17.040	17.527	16.988	4.226	16.896	4.246	17.045	4.234

LOW17CB062										
Site	3								3	
Point	39	40	41	42	43	44	45	47	48	49
Mineral	Amph	Px	Chl	Mt	Mt	Px	Px	Iddingsite	Olv	Olv
K2O			0.3					0.41		
MgO	24.94	26.29	30.39	8.17	6.83	25.2	25.33	20.45	14.18	11.83
Al2O3			15.63	2.64	2.32					
SiO2	58.35	58.96	31.74	5.18	4.49	58.65	58.15	42.49	30.09	25.69
CaO	0.84	0.4				0.49	0.56	1.3	0.51	0.5
FeO	14.73	13.79	6.53	87.91	89.44	14.62	13.94	22.61	49.62	58.89
Na2O										
Cr2O3			0.43							
MnO	0.48	0.49				0.55	0.55			
TiO2										
V2O5										
ZnO										
NiO								0.8		
MoO3										
CoO										
CuO										
SO3										
P2O5										
IrO2										
La2O3										
Total	99.34	99.93	85.02	103.9	103.08	99.51	98.53	88.06	94.4	96.91
Si	8.001	1.770	1.8828	0.0997	0.0871	1.768	1.771	2.4462	0.6375	0.5302
Al iv			1.2362	0.0678	0.06			0	0	0
Al vi										
Ti			0	0	0			0	0	0
Cr			0	0	0			0	0	0
Fe3+		0.828	0.7747	3.3844	3.4707	0.882	0.849	2.6033	2.1025	2.4307
Fe2+										
Mn	1.565	0.029	0	0	0	0.033	0.033	0	0	0
Mg	0.056	1.579	3.6054	0.3145	0.265	1.519	1.542	2.3546	0.6008	0.4883
Ni	5.318		0	0	0			0	0	0
Zn			0	0	0			0	0	0
Ca		0.024	0	0	0	0.030	0.034	0.1497	0.0216	0.0206
Na			0	0	0			0	0	0
K			0	0	0			0	0	0
Ba	0.058		0	0	0			0	0	0
Sr										
Pb										
F			0	0	0			0	0	0
Cl			0	0	0			0	0	0
OH*	2.00									
O	23	6.000	10	4	4	6.000	6.000	10	4	4
Total	16.999	4.230	7.4991	3.8664	3.8829	4.232	4.229	7.5538	3.3625	3.4698

	LOW17CB062									
Site	3			4						
Point	50	51	52	53	54	55	56	57	60	61
Mineral	Px	Px	Px	Px	Mt	Mt	Px	Srp	Px	Srp
K2O										
MgO	24.82	24.84	25.29	25.26		7.31	25.31	29.9	25.88	28.04
Al2O3						3.12				
SiO2	57.82	57.79	58.29	58.64		5.56	58.77	40.67	58.89	40.23
CaO	0.59	0.61	0.72	0.86			0.8	0.23	0.57	0.25
FeO	14.53	14.25	14.65	14.37	88.22	86.29	14.3	14.14	14.47	15.33
Na2O										
Cr2O3					5.61					
MnO	0.47	0.56	0.61	0.45			0.64		0.4	0.3
TiO2					0.88					
V2O5										
ZnO										
NiO										
MoO3										
CoO										
CuO										
SO3										
P2O5										
IrO2										
La2O3										
Total	98.23	98.05	99.56	99.58	94.71	102.28	99.82	84.94	100.21	84.15
Si	1.766	1.768	1.756	1.767	0	0.1087	1.766	1.197	1.763	1.1952
Al iv					0	0.0813		0		0
Al vi										
Ti					0.0198	0		0		0
Cr					0	0		0		0
Fe3+	0.888	0.872	0.883	0.866	3.9605	3.3747	0.860	0.8324	0.866	0.9109
Fe2+										
Mn	0.029	0.034	0.037	0.027	0	0	0.038	0	0.024	0.0178
Mg	1.516	1.520	1.524	1.522	0	0.2859	1.521	1.7601	1.550	1.6661
Ni					0	0		0		0
Zn					0	0		0		0
Ca	0.036	0.037	0.043	0.052	0	0	0.048	0.0135	0.034	0.0149
Na					0	0		0		0
K					0	0		0		0
Ba					0	0		0		0
Sr										
Pb										
F					0	0		0		0
Cl					0	0		0		0
OH*										
O	6	6	6	6	4	4	6	5	6	5
Total	4.234	4.232	4.244	4.233	3.9802	3.8506	4.234	3.803	4.237	3.8048

	LOW17CB062									
Site	4								5	
Point	62	63	66	67	68	69	70	71	72	77
Mineral	Chl	Amph	Px	Px	Amph	Srp	Mt	Mt	Amph	Amph
K2O										
MgO	29.06	22.07	25.68	25.63	22.14	29.09	4.42		22.28	20.79
Al2O3	7.17	1.7			1.36		1.65		1.71	2.36
SiO2	38.14	57.24	59.47	58.48	57.82	39.46	3.1	0.67	58.08	54.09
CaO	12.84	13.18	0.67	0.47	13.03	0.19			13.11	12.58
FeO		4.91	14.42	14.25	4.67	15.69	87.68	86.57	4.52	5.05
Na2O		0.36							0.33	0.46
Cr2O3	0.26							5.3		
MnO			0.66	0.53						
TiO2								1		
V2O5								0.45		
ZnO										
NiO										
MoO3										
CoO										
CuO										
SO3										
P2O5										
IrO2										
La2O3										
Total	87.47	99.46	100.9	99.36	99.02	84.43	96.85	93.99	100.03	95.33
Si	2.1802	7.739	1.768	1.766	7.803	1.1684	0.064	0.0152	7.957	7.636
Al iv	0.5465	0.261			0.197	0	0.0454	0	0.043	0.364
Al vi		0.010			0.019				0.233	0.029
Ti	0					0	0	0.0227		
Cr	0.0297					0	0	0		
Fe3+	0	0.337	0.857	0.861	0.411	0.9292	3.6213	3.9243		0.404
Fe2+		0.218			0.117				0.518	0.192
Mn	0		0.039	0.032		0	0	0		
Mg	3.3223	4.434	1.527	1.548	4.454	1.7227	0.1826	0	4.246	4.375
Ni	0					0	0	0		
Zn	0					0	0	0		
Ca	1.4679	1.909	0.040	0.028	1.884	0.0113	0	0	1.847	1.903
Na	0	0.094				0	0	0	0.122	0.126
K	0					0	0	0		
Ba	0					0	0	0		
Sr										
Pb										
F	0					0	0	0		
Cl	0					0	0	0		
OH*	8	2.000			2.000				2.000	2.000
O	10	23.000	6	6	23.000	5	4	4	23.000	23.000
Total	15.547	17.004	4.232	4.234	16.884	3.8316	3.9133	3.9621	16.966	17.029

	LOW17CB062									
Site	5									
Point	78	80	81	82	83	84	85	86	87	88
Mineral	Chl	Srp	Px	Px	Px	Px	Px	Mt	Px	Px
K2O										
MgO	30.49	25.26	25.09	25.29	25.26	25.42	25.08		25.22	25.12
Al2O3	16.34									
SiO2	31.53	38.75	58.22	58.07	58.6	58.04	58.09		57.97	58.32
CaO		0.38	0.54	0.74	0.62	0.7	0.6		0.7	0.68
FeO	6.75	17.47	14.56	14.39	14.82	14.29	14.38	82.68	14.39	14.92
Na2O										
Cr2O3	0.48							6.72		
MnO		0.55	0.58	0.62	0.57	0.39	0.58		0.48	0.48
TiO2								1.35		
V2O5								0.4		
ZnO										
NiO										
MoO3										
CoO										
CuO										
SO3										
P2O5										
IrO2										
La2O3										
Total	85.59	82.41	98.99	99.11	99.87	98.84	98.73	91.15	98.76	99.52
Si	1.8419	1.1755	1.764	1.758	1.760	1.762	1.765	0	1.761	1.758
Al iv	1.2727	0						0		
Al vi										
Ti	0	0						0.0298		
Cr	0.0561	0						0.2962		
Fe3+	0.7886	1.0599	0.883	0.871	0.890	0.867	0.874	3.6443	0.874	0.900
Fe2+										
Mn	0	0.0334	0.035	0.038	0.034	0.024	0.035	0	0.029	0.029
Mg	3.5623	1.5326	1.521	1.531	1.518	1.543	1.524	0	1.532	1.514
Ni	0	0						0		
Zn	0	0						0		
Ca	0	0.0231	0.033	0.045	0.037	0.042	0.036	0	0.043	0.041
Na	0	0						0		
K	0	0						0		
Ba	0	0						0		
Sr										
Pb										
F	0	0						0		
Cl	0	0						0		
OH*	8									
O	10	5	6.000	6.000	6.000	6.000	6.000	4	6.000	6.000
Total	15.522	3.8245	4.236	4.242	4.240	4.238	4.235	3.9702	4.239	4.242

LOW17CB062										
Site	5									
Point	89	90	91	92	93	94	98	99	100	102
Mineral	Mt	Mt	Mt	Px	Px	Px	Amph	Amph	Amph	Px
K2O										
MgO		0.59	0.73	25.77	24.94	25.5	21.47	21.34	21.4	25.09
Al2O3		0.79		1.33			2.91	3	2.96	
SiO2		0.41	0.38	55	58.07	58.04	56.1	55.82	56.07	58.7
CaO				0.63	0.61	0.52	13.04	12.82	12.93	0.74
FeO	89.25	84.91	87.4	13.77	14.59	14.93	5.51	5.33	5.27	14.7
Na2O							0.67	0.66	0.6	
Cr2O3	4.83	4.87	4.52							
MnO				0.59	0.62	0.65				0.58
TiO2	1.04	3.81	2.49							
V2O5	0.59	0.43	0.37							
ZnO										
NiO										
MoO3										
CoO										
CuO										
SO3										
P2O5										
IrO2										
La2O3										
Total	95.71	95.81	95.89	97.09	98.83	99.64	99.7	98.97	99.23	99.81
Si	0	0.0086	0.008	1.699	1.763	1.747	7.597	7.589	7.603	1.764
Al iv	0	0.0221	0	0.055			0.403	0.411	0.397	
Al vi							0.062	0.069	0.076	
Ti	0.0219	0.0799	0.0521							
Cr	0.2031	0.2042	0.1893							
Fe3+	3.7532	3.5609	3.66	0.851	0.886	0.899	0.381	0.434	0.406	0.884
Fe2+							0.223	0.172	0.192	
Mn	0	0	0	0.036	0.038	0.039				0.035
Mg	0	0.0247	0.0306	1.593	1.514	1.536	4.335	4.325	4.326	1.508
Ni	0	0	0							
Zn	0	0	0							
Ca	0	0	0	0.039	0.037	0.031	1.892	1.867	1.879	0.044
Na	0	0	0				0.176	0.174	0.158	
K	0	0	0							
Ba	0	0	0							
Sr										
Pb										
F	0	0	0							
Cl	0	0	0							
OH*							2.000	2.000	2.000	
O	4	4	4	6.000	6.000	6.000	23.000	23.000	23.000	6.000
Total	3.9781	3.9005	3.9399	4.273	4.237	4.253	17.068	17.041	17.036	4.236

	LOW17CB062						LOW17CB067			
Site	5						1			
Point	103	104	105	106	107	108	1	2	3	4
Mineral	Px	Px	Px	Srp	Px	Amph	Amph	Amph	Amph	Amph
K2O										
MgO	25.31	25.29	26.26	32.74	25.16	23.04	17.82	18.6	17.97	17.74
Al2O3			1.51	0.99		1.1	4.34	3.28	4.32	4.95
SiO2	59.16	59.3	56.67	38.9	58.85	58.99	52.13	52.82	51.94	51.6
CaO	0.7	0.72	0.55		0.7	12.17	12.03	12.32	12.11	12.09
FeO	14.97	14.56	14.86	12.43	14.38	5.1	9.24	8.49	8.72	9.2
Na2O						0.26	1.39	1.17	1.38	1.61
Cr2O3										
MnO	0.61	0.63	0.44	0.27	0.62					
TiO2										
V2O5										
ZnO										
NiO										
MoO3										
CoO										
CuO										
P2O5										
IrO2										
La2O3										
Total	100.75	100.5	100.29	85.33	99.71	100.66	96.95	96.68	96.44	97.19
Si	1.762	1.770	1.695	1.1397	1.771	7.799	7.403	7.503	7.411	7.325
Al iv			0.060	0.0387		0.171	0.597	0.497	0.589	0.675
Al vi							0.130	0.052	0.137	0.153
Ti				0						
Cr				0						
Fe3+	0.892	0.869	0.889	0.7283	0.865	0.564	0.423	0.372	0.368	0.400
Fe2+							0.674	0.637	0.673	0.692
Mn	0.036	0.038	0.026	0.0158	0.037					
Mg	1.507	1.510	1.571	1.9184	1.514	4.541	3.773	3.939	3.822	3.754
Ni				0						
Zn				0						
Ca	0.042	0.043	0.033	0	0.042	1.724	1.830	1.875	1.851	1.839
Na				0		0.067	0.383	0.322	0.382	0.443
K				0						
Ba				0						
Sr										
Pb										
F				0						
Cl				0						
OH*						2.000	2.000	2.000	2.000	2.000
O	6.000	6.000	6.000	5	6.000	23.000	23.000	23.000	23.000	23.000
Total	4.238	4.230	4.275	3.841	4.229	16.866	17.213	17.197	17.233	17.282

	LOW17CB067									
Site	1					2				
Point	5	6	7	8	9	10	11	12	13	14
Mineral	Amph	Amph	Amph	Amph	Amph	Amph	Amph	Amph	Amph	Amph
K2O										
MgO	17.65	18.63	17.46	17.4	19.5	18.27	17.86	18.58	17.42	18.93
Al2O3	4.71	3.06	5.08	5.07	1.36	4.11	4.14	3.22	4.56	4.85
SiO2	51.8	53.31	51.12	51.01	55.78	52.51	52.15	53.39	50.79	50.42
CaO	11.84	12.09	12.05	12.02	12.65	12.36	11.88	12.09	12.11	10.1
FeO	9.3	8.11	9.18	9.04	7.23	8.58	8.79	8.44	9.16	9.61
Na2O	1.54	1.05	1.58	1.59	0.42	1.29	1.41	1.11	1.47	1.06
Cr2O3										
MnO		0.29	0.32			0.26	0.3			
TiO2										
V2O5										
ZnO										
NiO										
MoO3										
CoO										
CuO										
SO3										
P2O5										
IrO2										
La2O3										
Total	96.84	96.54	96.79	96.13	96.94	97.38	96.53	96.83	95.51	94.97
Si	7.364	7.549	7.296	7.329	7.839	7.421	7.331	7.452	7.364	7.549
Al iv	0.636	0.451	0.704	0.671	0.161	0.579	0.669	0.530	0.636	0.451
Al vi	0.154	0.060	0.151	0.187	0.065	0.106	0.017		0.154	0.060
Ti										
Cr										
Fe3+	0.451	0.434	0.431	0.341	0.172	0.377	1.033	0.985	0.451	0.434
Fe2+	0.655	0.526	0.665	0.745	0.678	0.637			0.655	0.526
Mn		0.047	0.039			0.031	0.036			0.047
Mg	3.741	3.933	3.715	3.727	4.086	3.849	3.743	3.866	3.741	3.933
Ni										
Zn										
Ca	1.803	1.834	1.843	1.850	1.905	1.872	1.789	1.808	1.803	1.834
Na	0.425	0.288	0.437	0.443	0.114	0.353	0.384	0.300	0.425	0.288
K										
Ba										
Sr										
Pb										
F										
Cl										
OH*	2.000	2.000	2.000	2.000	2.000	2.000	2.000	2.000	2.000	2.000
O	23.000	23.000	23.000	23.000	23.000	23.000	23.000	23.000	23.000	23.000
Total	17.228	17.123	17.280	17.293	17.019	17.225	17.002	16.941	17.228	17.123

	LOW17CB067									
Site	2			3						
Point	15	16	18	19	21	20	22	23	24	25
Mineral	Amph	Amph	Ap	Amph	Ap	Ap	Amph	Amph	Amph	Amph
K2O										
MgO	18.95	18.8		18.98		11.74	17.78	16.9	18.33	17.37
Al2O3	4.76	2.47		2.77		5.11	4.54	6.09	4.3	5.16
SiO2	50.38	54.15		54.22		19.4	51.81	49.95	52.02	50.94
CaO	10.14	12.08	55.97	12.29	56.12	30.27	12	11.96	12.07	11.95
FeO	9.41	8.16	0.49	8.39	0.31	5.86	8.84	9.57	8.63	9.07
Na2O	0.96	1.01		0.94		0.37	1.54	1.87	1.42	1.68
Cr2O3										
MnO		0.38								
TiO2										
V2O5										
ZnO										
NiO										
MoO3										
CoO										
CuO										
SO3										
P2O5			39.78		40.81	22.82				
IrO2			3.97		3.3					
La2O3										
Total	94.6	97.05	100.21	97.59		95.57	96.51	96.34	96.77	96.17
Si	7.196	7.540	0	7.502	0	1.2227	7.284	7.070	7.291	7.201
Al iv	0.801	0.405	0	0.452	0	0.4294	0.716	0.930	0.709	0.799
Al vi							0.036	0.086	0.001	0.060
Ti			0		0	0				
Cr			0		0	0				
Fe3+	1.124	0.950	0	0.971	0	0.7387	1.039	1.133	1.012	1.072
Fe2+										
Mn		0.045	0		0	0				
Mg	4.035	3.903	0	3.915	0	1.4798	3.727	3.566	3.830	3.660
Ni			0		0	0				
Zn			0		0	0				
Ca	1.552	1.802	7.0145	1.822	6.9477	3.8155	1.808	1.814	1.813	1.810
Na	0.266	0.273	0	0.252	0	0	0.420	0.513	0.386	0.460
K			0		0	0				
Ba			0		0	0				
Sr										
Pb			4.9855		5.0523	2.8765				
F, Cl			0		0	0				
P			0		0	0				
OH*	2.000	2.000	1	2.000	1	1	2.000	2.000	2.000	2.000
O	23.000	23.000	12	23.000	12	12	23.000	23.000	23.000	23.000
Total	16.974	16.918	13	16.913	13	11.563	17.030	17.112	17.041	17.063

	LOW17CB067								LOW17CB076	
Site	3								1	
Point	26	27	28	29	30	31	32	34	3	4
Mineral	Amph	Amph	Amph	Amph	Amph	Amph	Amph	Ap	Amph	Amph
K2O									0.36	0.57
MgO	18.44	17.09	18.57	17.56	18.72	17.05	18.91		9.23	8.02
Al2O3	3.05	5.96	3.46	5.01	2.74	5.48	2.54		12.62	14.2
SiO2	53.39	50.83	53.48	50.89	54.13	50.26	54.71	0.34	43.07	40.83
CaO	12.02	12.16	12.04	11.79	12.23	11.97	12.22	56.11	11.6	11.36
FeO	8.11	9.47	8.54	9.21	7.99	9.4	8.22	0.4	17.72	17.98
Na2O	0.96	1.78	1.16	1.6	0.88	1.79	0.87		1.38	
Cr2O3										
MnO							0.28		0.28	
TiO2									0.5	0.6
V2O5										
ZnO										
NiO										
MoO3										
CoO										
CuO										
SO3										
P2O5								40.47		
IrO2								3.32		
La2O3										
Total	95.97	97.29	97.25	96.06	96.69	95.95	97.75	100.64	96.76	93.56
Si	7.504	7.115	7.432	7.201	7.546	7.137	7.554	0	6.426	6.244
Al iv	0.496	0.885	0.567	0.799	0.450	0.863	0.413	0	1.574	1.756
Al vi	0.009	0.099		0.036		0.054			0.645	0.803
Ti								0	0.056	0.069
Cr								0		
Fe3+	0.953	1.109	0.993	1.090	0.931	1.116	0.949	0	0.641	0.581
Fe2+									1.570	1.719
Mn							0.033	0	0.035	
Mg	3.864	3.566	3.847	3.704	3.890	3.609	3.892	0	2.053	1.828
Ni								0		
Zn								0		
Ca	1.810	1.824	1.793	1.787	1.827	1.821	1.808	6.9716	1.854	1.861
Na	0.262	0.483	0.313	0.439	0.238	0.493	0.233	0	0.399	0.400
K								0	0.069	0.111
Ba								0		
Sr										
Pb								5.0284		
F								0		
Cl								0		
OH*	2.000	2.000	2.000	2.000	2.000	2.000	2.000		2.000	2.000
O	23.000	23.000	23.000	23.000	23.000	23.000	23.000	12	23.000	23.000
Total	16.898	17.080	16.944	17.056	16.882	17.093	16.882	12	17.322	17.373

	LOW17CB076									
Site	1			3	4					
Point	5	6	7	8	9	10	11	12	13	14
Mineral	Amph	Fds	Qtz	Amph	Amph	Fds	Ilm	Ilm	Amph	Amph
K2O	0.64			0.44	0.36				0.48	0.57
MgO	7.94			9.13	8.69				8.66	8.54
Al2O3	14.97	25.65		13.11	12.9	26.76			13.56	14.02
SiO2	42.04	54.71	102.6	43.79	41.67	55.98			42.64	42.5
CaO	11.7	8.68		11.72	11.22	9.7			11.53	11.59
FeO	18.57			18.58	17.34		47.31	46.74	17.9	18.27
Na2O	1.52	6.4		1.25	1.24	5.97			1.51	1.5
Cr2O3										
MnO					0.39		1.54	1.54		0.34
TiO2	0.45			0.69	0.52		54.74	54.87	0.53	0.47
V2O5										
ZnO										
NiO										
MoO3										
CoO										
CuO										
SO3										
P2O5										
IrO2										
La2O3										
Total	97.83	95.44	102.6	98.71	94.33	98.41	103.59	103.15	96.81	97.8
Si	6.254	2.293	1	6.403	6.311	2.2754	0	0	6.379	6.302
Al iv	1.746	1.4334	0	1.597	1.689	1.4503	0	0	1.621	1.698
Al vi	0.879			0.662	1.830				0.770	0.752
Ti	0.050	0	0	0.076	0.059	0	1.5	1.5	0.060	0.052
Cr		0	0			0	0	0		
Fe3+	0.477	0	0	0.675		0	0	0	0.507	0.620
Fe2+	1.833			1.597	4.500				1.733	1.645
Mn		0	0		0.295	0	0	0		0.043
Mg	1.761	0	0	1.990	0.007	0	0	0	1.931	1.888
Ni		0	0			0	0	0		
Zn		0	0			0	0	0		
Ca	1.865	0.7276	0	1.836	0.005	0.7885	0	0	1.848	1.841
Na	0.438	1.0729	0	0.354	0.341	0.9706	0	0	0.438	0.431
K	0.121	0	0	0.082	0.008	0	0	0	0.092	0.108
Ba		0	0			0	0	0		
Sr										
Pb		0	0			0	0	0		
F		0	0			0	0	0		
Cl		0	0			0	0	0		
OH*	2.000			2.000	2.000				2.000	2.000
O	23.000	8	2	23.000	23.000	8	3	3	23.000	23.000
Total	17.425	5.5268	1	17.272	17.044	5.4848	1.5	1.5	17.378	17.380

LOW17CB076										
Site	4			5	6					
Point	15	16	19	20	21	22	23	25	27	28
Mineral	Fds	Fds	Amph	Amph	Amph	Fds	Fds	Fds	Amph	Amph
K2O			0.4	0.48					0.56	0.42
MgO			8.95	9.04	8.56				8.55	7.79
Al2O3	26.29	26.05	13.39	14.61	13.43	24.81	25.42	28.25	13.78	14.34
SiO2	57.39	57.01	42.35	43.37	42.06	55.07	54.58	53.8	42.74	40.75
CaO	8.66	9.04	11.39	11.94	11.5	8.25	9.27	11.57	11.47	11.51
FeO		0.3	18.09	18.73	17.84				18.21	18.25
Na2O	6.3	6.43	1.28	1.43	1.45	6.54	6.04	5	1.52	1.45
Cr2O3										
MnO				0.33	0.28					
TiO2			0.58	0.5	0.56				0.72	0.62
V2O5										
ZnO										
NiO										
MoO3										
CoO										
CuO										
SO3										
P2O5										
IrO2										
La2O3										
Total	98.64	98.83	96.43	100.43	95.68	94.67	95.31	98.62	97.55	95.13
Si	2.3273	2.3074	7.999	6.264	6.341	2.3268	2.2906	2.1821	6.350	6.233
Al iv	1.4215	1.4058	0.001	1.736	1.659	1.3977	1.4224	1.5277	1.650	1.767
Al vi			0.022	0.751	0.728				0.763	0.818
Ti	0	0			0.064	0	0	0	0.080	0.071
Cr	0	0				0	0	0		
Fe3+	0	0.0243		0.801	0.665	0	0	0	0.530	0.522
Fe2+			5.419	1.461	1.584				1.733	1.812
Mn	0	0	0.252	0.040	0.036	0	0	0		
Mg	0	0	1.177	1.946	1.924	0	0	0	1.894	1.776
Ni	0	0				0	0	0		
Zn	0	0				0	0	0		
Ca	0.7024	0.7318	0.121	1.848	1.858	0.6972	0.7781	0.9386	1.826	1.886
Na	1.0219	1.041		0.400	0.424	1.1053	1.014	0.8112	0.438	0.430
K	0	0		0.088		0	0	0	0.106	0.082
Ba	0	0				0	0	0		
Sr										
Pb	0	0				0	0	0		
F	0	0				0	0	0		
Cl	0	0				0	0	0		
OH*			2.000	2.000	2.000				2.000	2.000
O	8	8	23.000	23.000	23.000	8	8	8	23.000	23.000
Total	5.473	5.5102	16.990	17.337	17.281	5.527	5.5051	5.4596	17.370	17.398

	LOW17CB076									
Site	6			7						
Point	29	30	31	32	33	34	37	38	39	40
Mineral	Amph	Amph	Fds	Fds	Ilm	Ilm	Amph	Amph	Amph	Amph
K2O	0.47	0.43					0.28	0.49	0.36	0.52
MgO	8.66	8.7					8.32	8.33	8.7	8.36
Al2O3	14.06	13.69	27.05	26.87			12.8	12.3	13.29	12.33
SiO2	42.49	42.8	57.29	56.76	0.32	0.41	40.77	40.43	42.8	40.42
CaO	11.62	11.68	9.7	9.55			11.12	11.09	11.6	11.52
FeO	17.94	17.69			46.91	47.33	17.14	17.6	18.39	18.25
Na2O	1.39	1.28	6.67	6.34			1.43	1.35	1.42	1.24
Cr2O3										
MnO					1.25	1.44	0.36			
TiO2	0.55	0.64			55.47	55.89	0.41	0.65	0.61	0.6
V2O5										
ZnO										
NiO										
MoO3										
CoO										
CuO										
SO3										
P2O5										
IrO2										
La2O3										
Total	97.18	96.91	100.71	99.52	103.95	105.07	92.63	92.24	97.17	93.24
Si	6.321	6.382	2.2754	2.2814	0.0046	0.0059	6.370	6.367	6.376	6.321
Al iv	1.679	1.618	1.4325	1.44	0	0	1.630	1.633	1.624	1.679
Al vi	0.786	0.788					0.727	0.650	0.709	0.594
Ti	0.062	0.072	0	0	0.8004	0.7979	0.048	0.077	0.068	0.071
Cr			0	0	0	0				
Fe3+	0.576	0.502	0	0	1.3538	1.3514	0.595	0.577	0.598	0.604
Fe2+	1.656	1.704					1.644	1.741	1.693	1.783
Mn			0	0	0.0361	0.0411	0.048			
Mg	1.921	1.934	0	0	0	0	1.938	1.956	1.932	1.949
Ni			0	0	0	0				
Zn			0	0	0	0				
Ca	1.852	1.866	0.7705	0.7677	0	0	1.861	1.871	1.851	1.930
Na	0.401	0.370	1.0597	1.0193	0	0	0.433	0.412	0.410	0.376
K	0.089	0.082	0	0	0	0	0.056	0.098	0.068	0.104
Ba			0	0	0	0				
Sr										
Pb			0	0	0	0				
F			0	0	0	0				
Cl			0	0	0	0				
OH*	2.000	2.000					2.000	2.000	2.000	2.000
O	23.000	23.000	8	8	3	3	23.000	23.000	23.000	23.000
Total	17.342	17.318	5.5381	5.5083	2.1949	2.1963	17.350	17.382	17.330	17.410

	LOW17CB076						LOW17CB079			
Site	7						2			
Point	41	42	43	44	45	46	A	B	C	D
Mineral	Amph	Amph	Ilm	Ilm	Fds	Fds	Amph	Amph	Tlc	Tlc
K2O	0.35	0.51								
MgO	8.84	8.11					20.02	19.3	27.43	26.36
Al2O3	13.41	14.28			25.75	26.33	1.23	0.97		
SiO2	42.38	41.37		0.31	55.61	57	54.81	53.45	61.4	54.97
CaO	11.64	11.42			8.66	8.7	12.68	11.41		
FeO	18.02	18.3	46.04	46.45			6.46	6.71	5.24	10.07
Na2O	1.39	1.54			6.7	6.68				
Cr2O3										0.43
MnO		0.3	1.31	1.45						
TiO2	0.6	0.57	54.07	53.73						
V2O5										
ZnO										
NiO										
MoO3										
CoO										
CuO										
SO3										
P2O5										
IrO2										
La2O3										
Total	96.63	96.4	101.42	101.94	96.72	98.71	95.2	91.84	94.07	91.83
Si	6.341	6.234	0	0.0046	2.2998	2.3098	7.718	7.779	3.2635	3.0071
Al iv	1.659	1.766	0	0	1.4199	1.4226	0.204	0.166	0	0
Al vi	0.706	0.769								
Ti	0.068	0.065	0.7997	0.7906	0	0			0	0
Cr			0	0	0	0			0	0
Fe3+	0.616	0.633	1.3619	1.367	0	0	0.761	0.817	0.557	1.1018
Fe2+	1.639	1.673								
Mn		0.038	0.0387	0.0427	0	0			0	0
Mg	1.972	1.822	0	0	0	0	4.203	4.188	2.9159	2.884
Ni			0	0	0	0			0	0
Zn			0	0	0	0			0	0
Ca	1.866	1.844	0	0	0.7163	0.7051	1.913	1.779	0	0
Na	0.403	0.450	0	0	1.1084	1.0828			0	0
K	0.067	0.098	0	0	0	0			0	0
Ba			0	0	0	0			0	0
Sr										
Pb			0	0	0	0			0	0
F			0	0	0	0			0	0
Cl			0	0	0	0			0	0
OH*	2.000	2.000					2.000	2.000	2	2
O	23.000	23.000	3	3	8	8	23.000	23.000	10	10
Total	17.336	17.392	2.2003	2.2048	5.5444	5.5203	16.799	16.729	8.7365	8.9929

	LOW17CB079									
Site	2				3					
Point	E	F	G	H	A	B	C	D	E	F
Mineral	Amph	Amph	Tlc	Amph						
K2O										
MgO	20.15	19.93	27.3	19.94	20	21.99	19.9	20.96	19.43	19.86
Al2O3	0.91	1.05	0.39	0.74	1.48		1.36		0.74	
SiO2	55.07	55.52	61.06	55.19	55.08	55.55	55.84	54.07	53.44	52.29
CaO	12.47	12.06		7.17	12.34	0.51	12.92	0.79	9.25	0.64
FeO	6.3	7.02	4.94	12.02	6.66	17.81	6.44	17.71	9.17	18.09
Na2O										
Cr2O3										
MnO				0.27	0.24	0.48		0.36		0.54
TiO2										
V2O5										
ZnO										
NiO										
MoO3										
CoO										
CuO										
SO3										
P2O5										
IrO2										
La2O3										
Total	94.9	95.58	93.69	95.33	95.8	96.34	96.46	93.89	92.03	91.42
Si	7.768	7.770	3.2586	7.732	7.707	7.643	7.752	7.641	7.751	7.611
Al iv	0.151	0.173	0.0278	0.122	0.244		0.223		0.127	
Al vi										
Ti			0							
Cr			0							
Fe3+	0.743	0.822	0.5273	1.408	0.779	2.049	0.748	2.093	1.112	2.202
Fe2+										
Mn			0		0.028	0.056		0.043		0.067
Mg	4.237	4.158	2.9139	4.164	4.172	4.510	4.119	4.416	4.201	4.309
Ni			0							
Zn			0							
Ca	1.885	1.808	0	1.076	1.850	0.075	1.922	0.120	1.438	0.100
Na			0							
K			0							
Ba			0							
Sr										
Pb			0							
F			0							
Cl			0							
OH*	2.000	2.000	2	2.000	2.000	2.000	2.000	2.000	2.000	2.000
O	23.000	23.000	10	23.000	23.000	23.000	23.000	23.000	23.000	23.000
Total	16.785	16.732	8.7275	16.503	16.781	16.333	16.763	16.312	16.629	16.288

	LOW17CB079									
Site	3				4					
Point	G	H	I	J	A	D	E	F	G	H
Mineral	Tlc	Chl	Ilm	Amph	Amph	Amph	Amph	Amph	Chl	Amph
K2O										
MgO	26.77	23.29		22.19	20.26	21.29	19.39	20.83	23.09	20.12
Al2O3	0.48	17.06		9.36	1.12				17.35	1.07
SiO2	60.18	27.16	0.41	44.44	55.57	54.9	54.6	54.62	27.47	55.48
CaO				4.07	12.71	0.67	0.7	0.68		8.04
FeO	5.07	13.19	38.09	11.53	6.47	18.34	19.78	18.37	13.27	11.66
Na2O										
Cr2O3		0.74		0.35					0.64	
MnO			9.24		0.27	0.41	0.73	0.54		0.33
TiO2			53.33							
V2O5										
ZnO										
NiO										
MoO3										
CoO										
CuO										
SO3										
P2O5										
IrO2										
La2O3										
Total	92.5	81.44	101.07	91.94	96.4	95.61	95.2	95.04	81.82	96.7
Si	3.253	1.6828	0.0067	6.497	7.733	7.775	7.777	7.625	1.6919	7.636
Al iv	0.0346	1.4093	0	1.503	0.184	0.197	0.205		1.4248	
Al vi				0.109						
Ti	0	0	0.8711						0	
Cr	0	0	0						0	
Fe3+	0.5481	1.6344	1.2444	1.410	0.753	0.815	0.774	2.130	1.6346	2.148
Fe2+										
Mn	0	0	0		0.032			0.048	0	0.064
Mg	2.8941	2.886	0	4.836	4.203	4.128	4.072	4.408	2.8443	4.341
Ni	0	0	0						0	
Zn	0	0	0						0	
Ca	0	0	0	0.637	1.895	1.805	1.906	0.100	0	0.102
Na	0	0	0						0	
K	0	0	0						0	
Ba	0	0	0						0	
Sr										
Pb	0	0	0						0	
F	0	0	0						0	
Cl	0	0	0						0	
OH*	2	8		2.000	2.000	2.000	2.000	2.000	8	2.000
O	10	10	3	23.000	23.000	23.000	23.000	23.000	10	23.000
Total	8.7297	15.613	2.1222	16.992	16.799	16.720	16.734	16.310	15.596	16.290

	LOW17CB079									
Site	4			5						
Point	I	J	K	A	B	C	D	E	F	G
Mineral	Ilm	Amph	Ilm							
K2O										
MgO		18.91	19.88	19.61	19.62	20.14	20.86	20.29	20.87	0.36
Al2O3		1.26		1.1	0.89	0.76				
SiO2		53.12	53.69	55.23	54.18	55.18	54.14	54.88	53.44	0.32
CaO		12.15	0.56	11.76	12.46	12.14	0.68	1.15	0.65	
FeO	37.99	6.8	19.16	6.98	5.93	6.22	18.03	18.98	17.75	36.74
Na2O										
Cr2O3										
MnO	8.95		0.73				0.53	0.75	0.36	8.96
TiO2	53.76									52.74
V2O5	0.31									0.19
ZnO										
NiO										
MoO3										
CoO										
CuO										
SO3										
P2O5										
IrO2										
La2O3										
Total	101.01	92.24	94.02	94.68	93.08	94.44	94.24	96.05	93.07	99.31
Si	0	7.723	7.610	7.793	7.790	7.808	7.652	7.618	7.622	0
Al iv	0	0.216		0.183	0.151	0.127				0
Al vi										
Ti	0.8008									0.8036
Cr	0									0
Fe3+	1.1318	0.827	2.271	0.824	0.713	0.736	2.131	2.203	2.117	1.1197
Fe2+										
Mn	0.2666		0.088					0.088	0.043	0.2731
Mg	0	4.098	4.201	4.125	4.205	4.249	4.395	4.199	4.437	0
Ni	0									0
Zn	0									0
Ca	0	1.893	0.085	1.778	1.919	1.841	0.103	0.171	0.099	0
Na	0									0
K	0									0
Ba	0									0
Sr										
Pb	0									0
F	0									0
Cl	0									0
OH*		2.000	2.000	2.000	2.000	2.000	2.000	2.000	2.000	
O	3	23.000	23.000	23.000	23.000	23.000	23.000	23.000	23.000	3
Total	2.1992	16.756	16.254	16.703	16.778	16.760	16.282	16.280	16.319	2.1964

	LOW17CB079								
Site	5						6		
Point	H	I	J	K	L	M	A	B	C
Mineral	Talc	Talc	Amph	Amph	Chl	Amph	Amph	Amph	Amph
K2O									
MgO	26.29	23.69	19.63	19.81	23.82	19.67	19.51	19.65	19.69
Al2O3			0.77		17.42	1.38	1.45	1.44	1.61
SiO2	59.24	54.21	55.08	53.9	29.64	55.25	53.77	55.29	54.64
CaO		1.44	12.4	0.75	0.19	11.75	11.7	12.2	12.55
FeO	4.61	9.83	6.18	19.34	13.52	7.4	7.05	6.95	6.4
Na2O									
Cr2O3					0.7				
MnO				0.67					
TiO2									
V2O5									
ZnO									
NiO									
MoO3									
CoO									
CuO									
SO3									
P2O5									
IrO2									
La2O3									
Total	90.14	89.17	94.06	94.47	85.29	95.45	93.48	95.53	94.89
Si	3.286	3.0397	7.829	7.607	1.752	7.742	7.702	7.744	7.712
Al iv	0	0	0.129		1.3729	0.228	0.245	0.238	0.268
Al vi									
Ti	0	0			0				
Cr	0	0			0				
Fe3+	0.5114	1.1024	0.735	2.283	1.5983	0.867	0.845	0.814	0.755
Fe2+									
Mn	0	0		0.080	0				
Mg	2.9166	2.6567	4.159	4.168	2.8159	4.109	4.166	4.103	4.143
Ni	0	0			0				
Zn	0	0			0				
Ca	0	0.1615	1.888	0.113	0.0225	1.764	1.796	1.831	1.898
Na	0	0			0				
K	0	0			0				
Ba	0	0			0				
Sr									
Pb	0	0			0				
F	0	0			0				
Cl	0	0			0				
OH*	2	2	2.000	2.000	8	2.000	2.000	2.000	2.000
O	10	10	23.000	23.000	10	23.000	23.000	23.000	23.000
Total	8.714	8.9603	16.740	16.251	15.562	16.710	16.753	16.730	16.776

	LOW17CB079									
Site	6							8		
Point	E	F	G	H	I	J	K	A	B	C
Mineral	Amph	Amph	Amph	Amph	Ilm	Chl	Amph	Amph	Amph	Amph
K2O										
MgO	21.99	21.09	20.73	20.68		23.48	19	20.31	23.32	20.88
Al2O3						16.88	1.18	1.25		
SiO2	54.97	55.22	55.47	55.5		27.72	53.55	56.9	58.45	53.27
CaO	0.44	0.83	0.72	0.72			10.34	12.63	0.82	0.77
FeO	17.76	18.36	18.92	19.28	38.92	12.75	9.14	6.68	18.19	17.31
Na2O										
Cr2O3						0.7				
MnO	0.51	0.47	0.56	0.68	8.71				0.4	0.5
TiO2					54.23					
V2O5										
ZnO										
NiO										
MoO3										
CoO										
CuO										
SO3										
P2O5										
IrO2										
La2O3										
Total	95.67	95.97	96.4	96.86	101.86	81.53	93.21	97.77	101.18	92.73
Si	7.621	7.642	7.648	7.627	0	1.7147	7.695	7.781	7.651	7.628
Al iv					0	1.3922	0.200	0.201		
Al vi										
Ti					0.7986	0				
Cr					0	0				
Fe3+	2.059	2.125	2.181	2.216	1.1463	1.5774	1.098	0.764	1.991	2.073
Fe2+										
Mn	0.060	0.055	0.065	0.079	0.2565	0			0.044	0.061
Mg	4.545	4.351	4.261	4.237	0	2.9049	4.070	4.140	4.551	4.457
Ni					0	0				
Zn					0	0				
Ca	0.065	0.123	0.106	0.106	0	0	1.592	1.850	0.115	0.118
Na					0	0				
K					0	0				
Ba					0	0				
Sr										
Pb					0	0				
F					0	0				
Cl					0	0				
OH*	2.000	2.000	2.000	2.000		8	2.000	2.000	2.000	2.000
O	23.000	23.000	23.000	23.000	3	10	23.000	23.000	23.000	23.000
Total	16.350	16.296	16.262	16.265	2.2014	15.589	16.656	16.737	16.353	16.336

	LOW17CB079									
Site	8			9						
Point	D	E	F	A	B	C	D	E	F	G
Mineral	Talc	Talc	Amph							
K2O										
MgO	27.2	28.34	21.59	16.83	17.22	17.43	17.41	17.32	17.87	17.16
Al2O3		0.28	1.21	0.85	1.07	0.96	0.83	0.52		0.97
SiO2	60.26	63.79	58.98	47.09	48.8	48.17	48.17	48.13	48.51	48.51
CaO			11.45	10.07	11.27	10.85	9.22	11	0.78	8.68
FeO	4.51	5.35	8.48	6.73	5.88	6.22	7.58	5.68	17.87	9.1
Na2O										
Cr2O3										
MnO									0.57	0.33
TiO2										
V2O5										
ZnO										
NiO										
MoO3										
CoO										
CuO										
SO3										
P2O5										
IrO2										
La2O3										
Total	91.97	97.76	101.71	81.57	84.24	83.63	83.21	82.65	85.6	84.75
Si	3.2761	3.2626	7.743	7.752	7.727	7.727	7.763	7.801	7.595	7.693
Al iv	0	0.0191	0.187	0.167	0.177	0.177	0.171	0.099		0.181
Al vi										
Ti	0	0								
Cr	0	0								
Fe3+	0.4904	0.5473	0.931	0.872	0.849	0.849	0.921	0.770	2.340	1.207
Fe2+										
Mn	0	0		0.032						
Mg	2.9575	2.8989	4.226	4.120	4.051	4.051	4.009	4.185	4.171	4.057
Ni	0	0								
Zn	0	0								
Ca	0	0	1.611	1.786	1.955	1.955	1.826	1.910	0.131	1.475
Na	0	0								
K	0	0								
Ba	0	0								
Sr										
Pb	0	0								
F	0	0								
Cl	0	0								
OH*	2	2	2.000	2.000	2.000	2.000	2.000	2.000	2.000	2.000
O	10	10	23.000	23.000	23.000	23.000	23.000	23.000	23.000	23.000
Total	8.7239	8.7279	16.698	16.729	16.759	16.759	16.690	16.765	16.236	16.613

LOW17CB079										
Site	9		10							
Point	H	A	B	C	D	E	F	G	H	I
Mineral	Amph	Amph	Amph	Amph	Amph	Chl	Chl	Chl	Amph	Amph
K2O										
MgO	17.55	18.88	18.23	18.32	18.16	22.01	22.5	24	19.09	18.42
Al2O3	0.87	0.97	1.01	0.72	0.98	16.47	15.48	17.37	0.7	0.84
SiO2	49.04	52.96	51.84	52.34	52.43	26.18	27.04	28.34	53.71	52.49
CaO	9.92	11.39	12.24	11.78	11.51				12.25	10.32
FeO	7.31	7.12	6.81	7.05	7.44	13.01	12.69	13.05	6.65	9.28
Na2O										
Cr2O3						0.7	0.62	0.84		
MnO		0.26								
TiO2										
V2O5										
ZnO										
NiO										
MoO3										
CoO										
CuO										
SO3										
P2O5										
IrO2										
La2O3										
Total	84.69	91.58	90.13	90.21	90.52	78.37	78.33	83.6	92.4	91.35
Si	7.748	7.752	7.727	7.727	7.763	1.6853	1.7398	1.7122	7.790	7.708
Al iv	0.162	0.167	0.177	0.177	0.171	1.4137	1.328	1.3992	0.120	0.145
Al vi										
Ti						0	0	0		
Cr						0	0	0		
Fe3+	0.966	0.872	0.849	0.849	0.921	1.675	1.633	1.5768	0.807	1.140
Fe2+										
Mn		0.032				0	0	0		
Mg	4.133	4.120	4.051	4.051	4.009	2.8338	2.8954	2.9	4.127	4.032
Ni						0	0	0		
Zn						0	0	0		
Ca	1.679	1.786	1.955	1.955	1.826	0	0	0	1.904	1.624
Na						0	0	0		
K						0	0	0		
Ba						0	0	0		
Sr										
Pb						0	0	0		
F						0	0	0		
Cl						0	0	0		
OH*	2.000	2.000	2.000	2.000	2.000	8	8	8	2.000	2.000
O	23.000	23.000	23.000	23.000	23.000	10	10	10	23.000	23.000
Total	16.688	16.729	16.759	16.759	16.690	15.608	15.596	15.588	16.747	16.649

LOW17CB079									
Site	11								
Point	A	B	C	D	E	F	G	H	I
Mineral	Amph	Amph	Amph	Amph	Amph	Ilm	Ilm	Ilm	Ilm
K2O									
MgO	18.98	18.46	19.28	18.88	19.92	0.33	0.78	1.16	
Al2O3	1.23	1.19						0.45	
SiO2	52.74	51.19	50.32	51.18	51.48	0.41	0.94	1.43	
CaO	12.04	11.41	0.69	2.35	0.98			0.2	
FeO	6.51	6.5	17.86	16.69	17.73	35.36	34.4	33.11	33.51
Na2O	0.31								
Cr2O3									
MnO			0.47	0.47	0.39	10.08	7.81	5.9	10.06
TiO2						51.13	52.74	52.82	51.54
V2O5									
ZnO									
NiO									
MoO3									
CoO									
CuO									
SO3									
P2O5									
IrO2									
La2O3									
Total	91.81	88.75	88.62	89.57	90.5	97.31	96.67	95.07	95.11
Si	7.711	7.726	7.588	7.978	7.577	0	0	0.0032	0
Al iv	0.212	0.212				0	0	0.0097	0
Al vi									
Ti						0.7942	0.8332	0.8526	0.8128
Cr						0	0	0	0
Fe3+	0.796	0.820	2.252	2.176	2.182	1.0985	1.0869	1.0689	1.057
Fe2+									
Mn					0.049	0.3131	0.2468	0.1905	0.3173
Mg	4.137	4.154	4.334	4.387	4.370	0	0	0.0145	0
Ni						0	0	0	0
Zn						0	0	0	0
Ca	1.886	1.845	0.111	0.392	0.155	0	0	0	0
Na	0.088					0	0	0	0
K						0	0	0	0
Ba						0	0	0	0
Sr									
Pb						0	0	0	0
F						0	0	0	0
Cl						0	0	0	0
OH*	2.000	2.000	2.000	2.000	2.000				
O	23.000	23.000	23.000	23.000	23.000	3	3	3	3
Total	16.829	16.757	16.286	16.934	16.332	2.2058	2.1668	2.1394	2.1872